The development and application of a new algorithm for ocean geoid recovery.

Jonathan Frank Kirby

A thesis submitted in fulfilment of the requirements
for the degree of Doctor of Philosophy
to the
University of Edinburgh
1996

Declaration

This thesis has been composed by myself and it has not been submitted in any previous application for a degree. The work reported within was executed by myself, unless otherwise stated.

Abstract

The thesis describes and tests a method to combine satellite measurements of the geoid height with shipboard and terrestrial measurements of the freeair gravity anomaly using Fourier transform techniques. Fast Fourier transforms enable very large data sets to be processed quickly, but require the data to be available on a complete and regular grid. New methods were devised that grid altimeter and marine gravity data, and which remove the long-wavelength errors associated with these measurements.

Satellite altimeter data distributed along widely spaced groundtracks were differenced along track to reduce long-wavelength orbit errors (acknowledging that this underestimates the true slope), and any repeat track observations were averaged to reduce time-dependent oceanographic noise. The ascending and descending along-track slopes were then gridded separately, using a kernel designed to extrapolate the observations smoothly into the gaps between tracks, at maximum computer efficiency. The spectral properties of the gridding operation were analysed by calculation of a transfer function. Then, using linear vector geometry, grids of along-track slopes were transformed to grid-easting and -northing deflections of the vertical. Vertical deflection grids from any number of satellite missions can then be combined, and converted using Fourier techniques to give a grid of the geoid height. A grid of the freeair anomaly was also generated.

The effect of datum errors in the shipboard gravity data was reduced by processing not gravity but along-track gravity gradient. An incomplete grid of freeair gravity anomalies was generated from the observed along-track gravity slopes, constrained by and improving the altimeter-derived freeair anomaly grid. This method produces a smoothed field, owing to the nature of the interpolation algorithm. Land gravity measurements were interpolated directly onto a separate grid as there was no similar long-wavelength error in the data.

The combination algorithm performed a weighted superposition of the geoid height and freeair anomaly grids in an iterative process, until the solution converged and self-consistency was achieved.

The algorithms were first tested on a simulated dataset, extracted from accurate, high-resolution and self-consistent geoid and freeair anomaly models of the British Isles and North Sea. The geometry of real altimeter tracks from an area of equal size in the North Atlantic were superimposed on the British geoid, and simulated readings interpolated. A simulated shipboard dataset was created in a similar fashion, using the British freeair anomaly. These track data were then gridded and combined using the algorithms. The accuracy of the gridding and combination algorithms were assessed by comparing the simulated data with values interpolated from the generated grids at the equivalent spatial location. The standard deviation between the simulated ship freeair anomalies and the values interpolated from the altimeter-only freeair anomaly grid was 10.50 mgal; that between the simulated freeair anomalies and the values interpolated from the combined freeair anomaly grid was 4.54 mgal, showing an improvement upon the altimeter-only solution.

A 5 km gridded model of the gravity field of the North Atlantic was then created from Geosat/ERM and Topex/Poseidon altimeter data, and marine and land freeair anomaly datasets. The accuracy of the gridding and combination algorithms were assessed by comparing the along-track slopes of the altimeter data with the slope values interpolated from the generated grid. This removed the effect of orbit error. The standard deviation between the Geosat data and the altimeter geoid grid was 6.95 μrad; that for the Topex data was 6.75 μrad. Comparing the satellite data with the combined geoid, the standard deviations were 6.81 μrad for Geosat and 6.56 μrad for Topex. The standard deviation between the ship data and the altimeter freeair anomaly field was 13.4 mgal; that between the ship data and the combined field was 10.2 mgal, showing a slight improvement in accuracy. This field also compared favourably with a field generated by Sandwell et al. (1995), using very densely distributed ERS-1 data.

Analyses of the isostatic admittance and coherence were made on four areas extracted from the North Atlantic study area. Estimates of the elastic plate thickness and Moho depth were found from the generated gravity field and the Sandwell field, using the ETOPO5 relief model. Neither gravity model gave estimates that agreed with the values obtained from previous studies. Furthermore, the results returned from a one-dimensional admittance analysis upon gravity and bathymetry data collected by a ship did not show agreement with the values in the literature either. While this suggests a fault in the admittance algorithm, it could also be due to inaccurate data or faults in the theoretical isostasy models.

Estimates of the elastic plate thickness from the coherence analysis generally did not agree with the values from previous studies. I suggest that a bathymetry grid that is partially derived from satellite altimeter data should not be used to calculate admittances, as a degree of correlation exists between the bathymetry and gravity field. Furthermore, I would propose the investigation of non-radially-symmetric theoretical isostasy models to enable a thorough two-dimensional analysis.

Acknowledgements

I am indebted to my supervisors, Roger Hipkin and Roger Scrutton. Roger has been both helpful and supportive, and a source of much interesting discussion. I have learned a lot about gravity and geodesy from him. And Roger has always been ready to take an interest in my work and provide help and information on the more geological matters. Both have been instrumental in enabling me to gain first-rate field geophysical experience, for which I am very grateful.

Thanks also to Anton Ziolkowski for his input, and to Donna Blackman.

I am grateful to me Mum and Dad for their support, and never saying, "you should have a bluddy job."

I would also like to thank Shane Voss and Ian Chisholm, the computer officers, for all their help and patience; and all the secretarial staff for their help.

Thanks goes to the British National Space Centre for their funding of this project, and the NERC special topics section for their helpful administration.

And to the Bureau Gravimetrique International for their kind supply of data.

And the rogues gallery of Teenage-fanclub Trev, Roadrunner Rodney, young-shaver Sharpy and Glastonbury Dave for giving it a good hard read, beachy Janet for surreal encouragement and daft jokes, raver Al, reggae Ned, doolally Tom, footy Phil & Mayfield Road lads for blethers on the beautiful game, Sandra, Damian and Rachel, and everyone else who made for a smashin' time.

This thesis was writen with the assistance of beer & tabs & probably coffee.

Contents

List of Figures

List of Tables

List of symbols

Mathematical functions

$\tilde{a}(\vec{k}) \equiv \mathcal{F}\{a(\vec{x})\}$	two dimensional forward Fourier transform of $a(\vec{x})$
$\langle A \rangle$	denotes average around equal-area annuli in the wavenumber domain

Mathematical symbols

$a_\circ$	Witch kernel halfwidth	(km)	[L]
a'	latitude dependent $a_\circ$	(km)	[L]
D	flexural rigidity	(Nm)	[$\mathrm{ML^2T^{-2}}$]
E	Young's modulus	(10^{11} $\mathrm{Nm^{-2}}$)	[$\mathrm{ML^{-1}T^{-2}}$]
f	Moho to surface loading ratio	( )	[ ]
$\vec{g}$	gravity field vector	($\mathrm{ms^{-2}}$)	[$\mathrm{LT^{-2}}$]
Δg	freeair gravity anomaly	(mgal)	[$\mathrm{LT^{-2}}$]
Δg_B	Bouguer gravity anomaly	(mgal)	[$\mathrm{LT^{-2}}$]
G	gravitational constant (6.672×10^{-11}	$\mathrm{N\ m^2\ kg^{-2}}$)	[$\mathrm{L^3M^{-1}T^{-2}}$]
G_B	Fourier transform of Bouguer anomaly	(mgal $\mathrm{km^2}$)	[$\mathrm{L^3T^{-2}}$]
G_F	Fourier transform of freeair anomaly	(mgal $\mathrm{km^2}$)	[$\mathrm{L^3T^{-2}}$]
h	ellipsoidal normal	(m)	[L]
J	function of principal radii of curvature of the Earth	($\mathrm{km^{-1}}$)	[$\mathrm{L^{-1}}$]
$\vec{k}$	circular wavenumber vector (k_x, k_y)	($\mathrm{km^{-1}}$)	[$\mathrm{L^{-1}}$]
N	geoid height above reference ellipsoid	(m)	[L]
Q	ratio of Witch kernel halfwidth to search radius	( )	[ ]
Q_B	Bouguer isostatic admittance function	(mgal $\mathrm{m^{-1}}$)	[$\mathrm{T^{-2}}$]
R_e	mean Earth radius	(km)	[L]
$R_\circ$	Witch kernel search radius	(km)	[L]
R'	latitude dependent $R_\circ$	(km)	[L]
T	disturbing gravitational potential	(J $\mathrm{kg^{-1}}$)	[$\mathrm{L^2T^{-2}}$]

T_e	elastic plate thickness	(km)	[L]
U	normal (ellipsoidal) gravitational potential	(J kg^{-1})	[L^{2}T^{-2}]
W	total gravitational potential	(J kg^{-1})	[L^{2}T^{-2}]
$\vec{x}$	space vector (x, y)	(km)	[L]
z	spatial vector normal to and positive upwards from a flat-Earth plane	(km)	[L]
z_m	depth to Moho	(km)	[L]

α_d	RMS fit of admittance and coherence data to theoretical curves		
$\delta\omega(\vec{x})$	Witch gridding kernel	( )	[ ]
$\vec{\gamma}$	ellipsoidal (normal) gravity field	(ms^{-2})	[LT^{-2}]
γ^2	isostatic coherence	( )	[ ]
ϵ_a	ascending along-track geoid slope	(μrad)	[ ]
ϵ_d	descending along-track geoid slope	(μrad)	[ ]
η	east vertical deflection	(μrad)	[ ]
λ	wavelength	(km)	[L]
ξ	north vertical deflection	(μrad)	[ ]
ρ	density	(kg m^{-3})	[ML^{-3}]
σ	load	(kg m^{-2})	[ML^{-2}]
σ_p	Poisson's ratio	(0.25)	[ ]
Σ	Fourier transform of load	(kg m^{-2}km^2)	[M]
$\Phi(\phi)$	latitude-dependent function in satellite data gridding algorithm	( )	[ ]
ω	weighting grids generated from gridding algorithms	( )	[ ]
ω_e	rotational angular velocity of Earth	(s^{-2})	[T^{-2}]

Abbreviations

1-D	one-dimension(al)
2-D	two-dimension(al)
DFT	discrete Fourier transform
ERM	Exact Repeat Mission for the Geosat altimeter
FFT	fast Fourier transform
FZ	fracture zone
GM	Geodetic Mission for the Geosat altimeter
IFC	Iterative Fourier Combination
LSC	least squares collocation
Ma	million years ago
RMS	root mean square
s.d.	standard deviation

Chapter 1

Introduction

1.1 The gravity field of the Earth

Geodesy, the study of the figure of the Earth, and gravimetry, the study of its gravity field, are intrinsically related disciplines. Determination of the shape and size of the Earth can, given its density distribution, provide information on its gravity field. Conversely, measurements of the gravity field can improve models of both the internal density distribution and the the physical shape of the Earth.

The Earth's gravity field is highly variable from place to place: the largest difference in the acceleration due to gravity is between the equator and the poles, with the field over 5100 mgal larger at the latter. The regional perturbations to this field are considerably less than this and arise from irregular density distributions within the body of the Earth.

The force acting on a body at rest on the Earth's surface is the resultant of the gravitational force arising from the mass distribution, and the centripetal force due to the Earth's rotation. This system can be expressed in terms of a total potential, W, that satisfies the generalised Poisson equation:

$$\nabla^2 W = -4\pi G\rho + 2\omega_e^2 \quad , \tag{1.1}$$

where ∇^2 is the Laplacian operator, ρ is the local density of the Earth, ω_e its angular velocity of rotation, and G is the gravitational constant. The aim of physical geodesy is determination of the function W. The surfaces $W = W_0$, where W_0 is a constant, are called *equipotential surfaces.* To a good approximation, the ocean surface follows an equipotential surface. This particular surface was proposed as the mathematical figure of the Earth by Gauss, and was later termed the *geoid* [Heiskanen and Moritz (1967)].

A model Earth can be represented as an oblate ellipsoid rotating about its minor axis. This is the *reference ellipsoid.* The external potential of this figure, the *normal potential* U, is completely determined by the shape of the ellipsoid, its total mass, and angular velocity [*ibid.*]. The total potential, W, can now be expressed in terms of perturbations to the normal potential by a small *disturbing* potential, T:

$$W = U + T \quad . \tag{1.2}$$

T is the potential due to anomalous densities within the Earth, and is not dependent upon its rotation. Therefore, as U can be determined mathematically, it is necessary only to measure T to determine W completely. This can be achieved through geodetic and gravimetric methods.

A useful property of T, and one which assists its computation, is that outside the attracting masses of the solid Earth, where $\rho \approx 0$, T satisfies Laplace's equation,

$$\nabla^2 T = 0 \quad . \tag{1.3}$$

The solutions to eq.1.3 are called *harmonic* functions. These functions are analytic, *i.e.* they are continuous and have continuous derivatives of any order, but only outside the attracting masses. Within the body of the Earth T satisfies Poisson's equation.

The gravity field at any point is defined as the gradient vector of the potential W,

$$\vec{g} = -\vec{\nabla} W \quad . \tag{1.4}$$

It is the total acceleration (gravitational plus centripetal) experienced by a unit mass, and is normal to the equipotential surface passing through the point. The direction of the gravity vector is the direction a plumb line would hang, the *vertical*; thus equipotential surfaces are, by definition, horizontal everywhere. The *orthometric height*, H, of a point above sea level is the distance measured along the vertical from the geoid to the point.

Similarly to eq.1.4, the gradient vector of the normal potential is the *normal gravity*:

$$\vec{\gamma} = -\vec{\nabla} U \quad . \tag{1.5}$$

Consider the situation in fig 1.1, where the geoid is compared with a reference ellipsoid of the same potential, W_0. The distance from a point P on the geoid

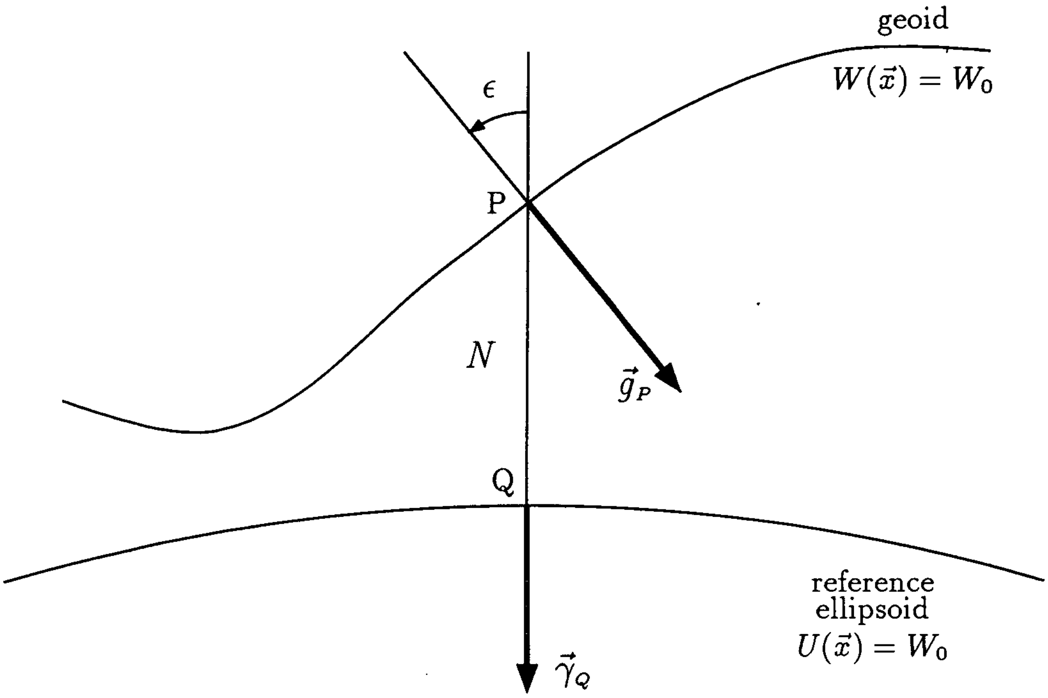

Figure 1.1. The geoid and reference ellipsoid, showing the geoid height, N, and deflection of the vertical, ϵ.

projected along the ellipsoidal normal to a point Q on the ellipsoid is called the *geoid height*, N. The *gravity anomaly* is defined as the difference in magnitude of the gravity vector at P and the normal gravity at Q:

$$\Delta g = |\vec{g}_P| - |\vec{\gamma}_Q| \quad . \tag{1.6}$$

The angle ϵ in fig 1.1 is the *deflection of the vertical*, discussed later.

The first of two important formulae in physical geodesy is *Bruns formula*, which relates the geoid height to the disturbing potential [Heiskanen and Moritz (1967)]:

$$N = \frac{T}{\gamma} \quad . \tag{1.7}$$

The second is the *geodetic boundary condition*, the so-called fundamental equation of physical geodesy [*ibid.*]:

$$\frac{\partial T}{\partial h} - \frac{1}{\gamma}\frac{\partial \gamma}{\partial h}T + \Delta g = 0 \quad , \tag{1.8}$$

where h is measured along the ellipsoidal normal. The equation relates the unknown potential, T, to the measured quantity Δg, with

$$\frac{\partial\gamma}{\partial h} = -2\gamma J - 2\omega_e^2 \quad , \tag{1.9}$$

where J is a function of the principal radii of curvature of the Earth [see Heiskanen and Moritz (1967), p 70].

Since Δg is known only on the geoid, eq.1.8 is a boundary condition, but can be used to determine T everywhere outside the Earth. [In fact Δg is known only on the topographic surface of the Earth: corrections such as the freeair or Bouguer correction must be applied to determine its value on the geoid (sea level).] Once the disturbing potential, T, is known, the geoid height can be computed using Bruns' formula (eq.1.7).

The deflection of the vertical

The deflection of the vertical, shown in fig 1.1 as ϵ, is the negative of the geoid slope in the direction of s:

$$\epsilon = -\frac{dN}{ds} \quad . \tag{1.10}$$

It is often resolved into north-south and east-west components:

$$\eta = -\frac{\partial N}{\partial x} = -\frac{1}{R_e \cos\phi}\frac{\partial N}{\partial \lambda} \qquad \xi = -\frac{\partial N}{\partial y} = -\frac{1}{R_e}\frac{\partial N}{\partial \phi} \quad , \tag{1.11}$$

where x and y are the local rectangular coordinates in the plane approximation, (λ, ϕ) are the geodetic longitude and latitude, and R_e is the mean Earth radius [Heiskanen and Moritz (1967)]. It is often quoted as an angle in micro-radians (μrad).

1.2 The Fourier method

In Fourier analysis, well-behaved, non-periodic functions are represented by combinations of sine and cosine functions of many different frequencies [Kanasewich (1981)]. This method is particularly suited to solving partial differential equations, such as the geodetic boundary condition.

With the advent of the fast Fourier transform (FFT), it is now possible to process large datasets very quickly, provided they exist on a regular grid.

1.2.1 The Fourier transform and techniques for calculation

The Fourier analysis of a potential field involves the use of two-dimensional Fourier transforms, and calculates the spectrum as a function of wavenumber (spatial frequency). Throughout this work $\vec{k} = (k_x, k_y)$ will denote the circular wavenumber vector (unless otherwise indicated), where:

$$k \equiv |\vec{k}| = \frac{2\pi}{\lambda} \tag{1.12}$$

where λ is wavelength, with:

$$|\vec{k}| = \sqrt{k_x^2 + k_y^2} \ . \tag{1.13}$$

To calculate the two-dimensional forward Fourier transform of a function $a(\vec{x})$, let

$$k_x = 2\pi u \ , \qquad\qquad k_y = 2\pi v \tag{1.14}$$

in eq.1.13. Then

$$\mathcal{F}\left\{a(x,y)\right\} \equiv \tilde{a}(u,v) = \int\!\!\int_{-\infty}^{\infty} a(x,y) e^{-2\pi i(ux+vy)}\, dx\, dy \ . \tag{1.15}$$

The inverse Fourier transform of the function $\tilde{a}$ returns the original function:

$$\mathcal{F}^{-1}\left\{\tilde{a}(u,v)\right\} \equiv a(x,y) = \int\!\!\int_{-\infty}^{\infty} \tilde{a}(u,v) e^{2\pi i(ux+vy)}\, du\, dv \ . \tag{1.16}$$

The above are continuous Fourier transforms. When dealing with finite arrays of data, the discrete Fourier transform (DFT) must be used. For a function a known only at a finite number of points (M in the x direction and N in the y direction) on a regular grid with sampling intervals Δx, Δy, the forward DFT is written:

$$\tilde{a}(m\,\Delta u, n\,\Delta v) = \Delta x\,\Delta y \sum_{j=0}^{M-1}\sum_{l=0}^{N-1} a(j\,\Delta x, l\,\Delta y) \exp\left[-2\pi i\left(\frac{mj}{M} + \frac{nl}{N}\right)\right] \tag{1.17}$$

and the inverse DFT:

$$a(j\,\Delta x, l\,\Delta y) = \Delta u\,\Delta v \sum_{m=0}^{M-1}\sum_{n=0}^{N-1} \tilde{a}(m\,\Delta u, n\,\Delta v) \exp\left[2\pi i\left(\frac{mj}{M} + \frac{nl}{N}\right)\right] \ . \tag{1.18}$$

The spectrum is also discrete with wavenumber spacings:

$$\Delta u = \frac{2\pi}{M\,\Delta x} \qquad \Delta v = \frac{2\pi}{N\,\Delta y} \tag{1.19}$$

up to the Nyquist wavenumbers:

$$u_N = \pm\frac{2\pi}{2\,\Delta x} \qquad v_N = \pm\frac{2\pi}{2\,\Delta y}\ . \tag{1.20}$$

The Nyquist wavenumbers are the highest wavenumbers that can be resolved by the data [Schwarz et al. (1990), Bracewell (1965)].

The FFT utilizes a very fast form of eqs 1.17 & 1.18 [Kanasewich (1981)], and can compute Fourier transforms in times of the order of $MN\ln(MN)$, compared to $(MN)^2$ for the conventional DFT.

When using any discrete transform however, the finite extent of datasets causes 'spectral leakage'. This arises from the inability of the transform to resolve wavelengths longer than the dataset side length, and from discontinuities arising at the dataset edges due to its periodicity [Schwarz et al. (1990)]. The errors caused by this leakage may be reduced by certain techniques; those used in this study are discussed in Appendix D.

1.2.2 Fourier techniques in gravity field calculations

Given measurements of the gravity anomaly reduced to the geoid, we wish to find the disturbing potential and thus the geoid height. This involves the solution of the geodetic boundary condition (eq.1.8) over the area where measurements of the gravity anomaly exist.

Consider an area small enough (of side of the order of a few thousand kilometres) to reduce coordinate distortion due to the curvature of the Earth, and project the ellipsoidal surface onto a plane $(\vec{x}, z) \equiv (x, y, z)$. This is the *flat-Earth approximation.* The coordinates x and y are grid eastings and northings respectively; the z coordinate is a good approximation to the ellipsoidal normal h, taken to be positive upwards from the surface. An example of such a projection is the Lambert conical conformal, used in this thesis and described in Appendix A.

Now, the disturbing potential, T, is a harmonic function satisfying Laplace's equation (eq.1.3), which in rectangular Cartesian coordinates is

$$\frac{\partial^2 T}{\partial x^2} + \frac{\partial^2 T}{\partial y^2} + \frac{\partial^2 T}{\partial z^2} = 0 \ . \tag{1.21}$$

The solution to this equation may be written

$$T(\vec{x}, z) = \frac{1}{2\pi} \int\!\!\int_{-\infty}^{\infty} \tilde{T}(\vec{k}, 0)\, e^{-kz} e^{i\vec{k}\cdot\vec{x}}\, d^2\vec{k} \tag{1.22}$$

for all mass sources below the plane $z = 0$.

Now take the Fourier transform of the geodetic boundary condition (eq.1.8), at the surface of the Earth with h along the plane normal, z. The transform of the derivative term is obtained from eq.1.22, giving after rearrangement:

$$\widetilde{\Delta g} = \left(k - 2J - \frac{2\omega_e^2}{\gamma} \right) \tilde{T} \ . \tag{1.23}$$

Now, despite γ and J having a spatial dependence, this is only weak and they can be treated as constants in the Fourier transformation; and as $\omega_e \approx 7.29 \times 10^{-5} s^{-1}$, this term can be omitted from eq.1.23 without significant errors occurring. Furthermore, $2J \approx 2/R_e \approx 3 \times 10^{-7} m^{-1}$, and if there are no very long wavelengths present in the data (greater than a couple of thousand kilometres), then this term can be left out as well, giving, with the substitution of Bruns' formula (eq.1.7):

$$\widetilde{\Delta g} = \gamma k \widetilde{N} \ . \tag{1.24}$$

This formula allows a fast and simple transformation between freeair anomaly and geoid height, and is central to the heterogeneous gravity data conversion method in this thesis.

Fourier analysis also yields simple relationships between the gravity anomaly, the disturbing potential and all their derivatives. For example, the Fourier-domain relationship between freeair anomaly and the components of the deflection of the vertical is:

$$\widetilde{\Delta g} = \frac{i\gamma}{k} \left(k_x \tilde{\eta} + k_y \tilde{\xi} \right) \ , \tag{1.25}$$

while that between the freeair anomaly and its vertical gradient is

$$\mathcal{F}\left\{ \frac{\partial \Delta g}{\partial z} \right\} = -k\, \widetilde{\Delta g} \ . \tag{1.26}$$

The equations can also be used in the Fourier combination of heterogeneous gravity data. For the implementation of FFTs, all data must be available on a regular grid.

1.3 Geopotential models

While computation of the normal potential must be performed in ellipsoidal coordinates if high accuracy is required, it is often convenient to work in a spherical coordinate system and sometimes sufficient when solving for the disturbing potential to make a spherical approximation. Here, the ellipsoidal normal, h, is approximated to the spherical radius vector, r. This generates errors of the order of the ellipsoid flattening ($\approx 1/298$) only. The spherical approximation to the geodetic boundary condition (eq.1.8) is:

$$\frac{\partial T}{\partial r} + \frac{2}{r} T + \Delta g = 0 \quad . \tag{1.27}$$

If we wish to solve Laplace's equation for the Earth as a whole, it is simplest to use spherical polar coordinates. Eq.1.3 becomes:

$$r^2 \frac{\partial^2 T}{\partial r^2} + 2r \frac{\partial T}{\partial r} + \frac{\partial^2 T}{\partial \theta^2} + \cot\theta \frac{\partial T}{\partial \theta} + \frac{1}{\sin^2\theta} \frac{\partial^2 T}{\partial \lambda^2} = 0 \tag{1.28}$$

where r is the geocentric distance, θ the geocentric colatitude, and λ the longitude. This equation can be solved by separating the radial and angular parts. This gives a series of radial solutions, called *solid spherical harmonics*:

$$R(r) = r^n \text{ and } \frac{1}{r^{n+1}} \quad . \tag{1.29}$$

The r^n solutions represent functions that are harmonic inside a certain sphere, while the $1/r^{n+1}$ solutions represent functions that are harmonic outside the sphere. The angular solutions form a series of *surface spherical harmonics*:

$$Y_n(\theta, \lambda) = \sum_{m=0}^{n} P_n^m(\cos\theta)(a_{nm} \cos m\lambda + b_{nm} \sin m\lambda) \tag{1.30}$$

where (n, m) are the harmonic degree and order respectively, $P_n^m(\cos\theta)$ are associated Legendre functions, and a_{nm}, b_{nm} are harmonic coefficients.

For the particular instance of the Earth, several adjustments to the general harmonic solutions may be made. First, we are only concerned with the exterior solid harmonics (eq.1.29). Second, an analysis of the lower degree harmonics implies that there are no first degree terms in the expansion of the potential T if the origin $r = 0$ is the centre of the Earth [Heiskanen and Moritz (1967)]. Furthermore, the (0,0) term is equal to GM_e, and the $n = 2$ harmonics can be expressed as functions of the Earth's moments and products of inertia [*ibid.*]. Thus, the spherical harmonic expansion of the disturbing potential is written

$$T(r,\theta,\lambda) = \frac{GM_e}{r}\sum_{n=2}^{\infty}\left(\frac{R_e}{r}\right)^n Y_n(\theta,\lambda) \tag{1.31}$$

where the surface harmonics Y_n are given by eq.1.30. Then, using Bruns formula (eq.1.7) and the approximate relation $\gamma \approx GM_e/r^2$, the geoid height is given from eq.1.31, for $r \geq R_e$ as

$$N(r,\theta,\lambda) = r\sum_{n=2}^{\infty} Y_n(\theta,\lambda) \quad . \tag{1.32}$$

The geodetic boundary condition (eq.1.27) may now be used to determine the expansion of the gravity anomaly:

$$\Delta g(r,\theta,\lambda) = \frac{GM_e}{r^2}\sum_{n=2}^{\infty}(n-1)\left(\frac{R_e}{r}\right)^n Y_n(\theta,\lambda) \quad . \tag{1.33}$$

The gravity anomaly, Δg, is not a harmonic function, but $r\Delta g$ is in the space outside the generating masses of the potential [Rapp and Pavlis (1990)].

The values of $N(R_e,\theta,\lambda)$ and $\Delta g(R_e,\theta,\lambda)$ around the Earth depend upon the values of the harmonic coefficients a_{nm}, b_{nm}. These may be determined from satellite measurements of the geoid height, perturbations of satellite orbits, and all surface gravity data. However, the calculation of the coefficients requires gravity data to be available globally [*ibid.*]. The maximum degree and order of expansion of a particular geopotential model will depend upon the data density. The smallest resolvable wavelength of a harmonic model is given by

$$\lambda_{min} = \frac{2\pi R_e}{\sqrt{n_{max}(n_{max}+1)}} \tag{1.34}$$

where n_{max} is the maximum degree of the model [Cazenave et al. (1992)].

The use of Fourier transform techniques in converting between heterogeneous data can generate errors if very long wavelengths are present in the data [Schwarz et al. (1990)]. These are typically reduced using the *remove-restore* method,

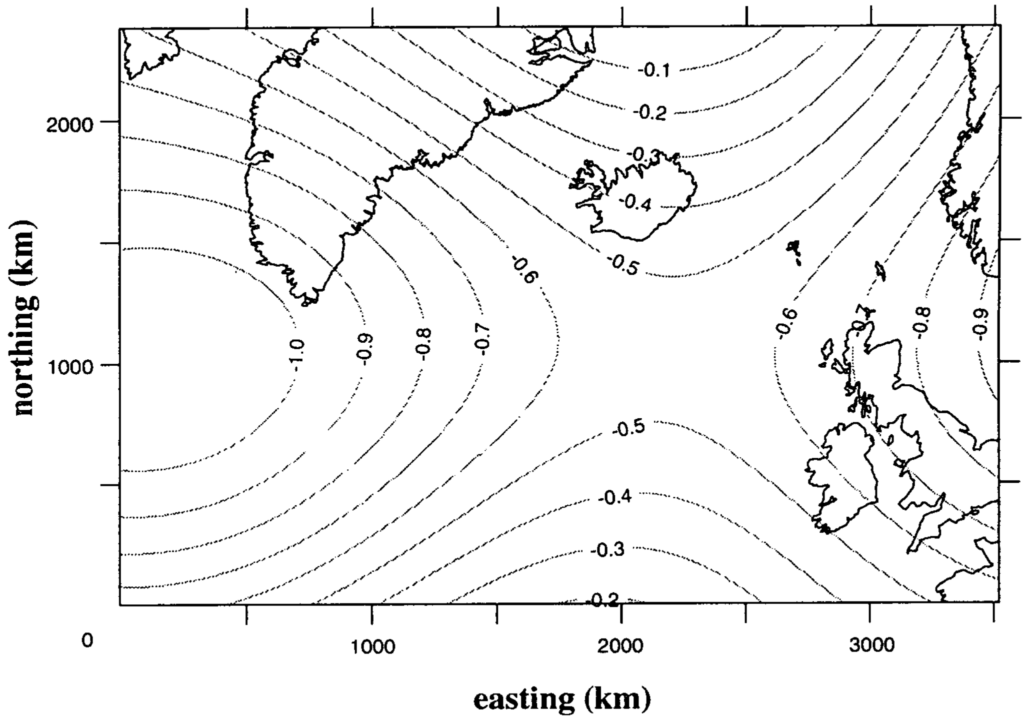

Figure 1.2. The sea surface topography in the North Atlantic Ocean as given by the OSU91A model to degree and order 15. Contours in metres.

whereby a spherical harmonic expansion of the geoid height or freeair anomaly is subtracted from the observed data before Fourier operations occur. After the data manipulation, the corresponding geopotential model may be added back to recover the total field. Spherical harmonic expansions are particularly suited to this approach, as they define both geoid height and gravity anomaly at all points on the surface of the Earth.

The OSU91A model

The geopotential model used in this study is the OSU91A model to degree and order 360 [Rapp et al. (1991)]. The harmonic coefficients for degrees 2 to 50 were calculated from a combination of global 0.5° mean gravity anomaly data and the coefficients from the GEM-T2 geopotential model. The coefficients from degree 51 to 360 were calculated from a global set of adjusted gravity anomalies.

The coefficients for a harmonic expansion of the sea surface topography (the deviation of the sea level from the geoid, see §1.5.2) up to degree and order 15 (approximately 2600 km wavelength) have also been calculated. This surface is shown in fig 1.2.

The cumulative undulation commission errors for the geoid model to degree 10, 50, and 360 were 5 cm, 25 cm, and 49 cm respectively. The largest error was 4.3 cm at degree 30 ($\lambda \approx 1300$ km). The errors show the accuracy of the geoid model at certain wavelengths. The RMS difference with Geosat geoid undulation (after orbit and sea surface topography correction) was 34 cm.

1.4 Isostasy and the gravity field

1.4.1 Gravity anomalies

Anomalies in the gravity field reflect the presence of density contrasts at all depths within the Earth. Marine geophysicists often study the topography of the geoid to determine subsurface structure, grouping anomalies according to their wavelength.

The longest wavelength geoid anomalies (>3000 km) largely reflect dynamic processes in the mantle, such as the density differences between rising and sinking convective cells. It is suggested though that the geoid anomalies in this range are not systematically correlated with the part of mantle convection which is coupled to plate motions [Vogt (1986)]. Exceptions do exist, such as the large geoid high in the northeast Atlantic, which corresponds to a large area of anomalously shallow ocean crust associated with the Azores, Iceland and interlying hotspots. Modelling has suggested this high arises from sources at the core/mantle boundary [*ibid.*].

Intermediate wavelength anomalies (300-3000 km) generally correlate with thermal anomalies in the lithosphere and asthenosphere. These might arise at mid-ocean ridges, subduction zones, or be due to differences in crustal age (and thus density) within a plate [*ibid.*].

The short wavelength geoid anomalies (<300 km) are strongly correlated with seafloor topography, due to the large density contrast between the ocean and seabed [Sandwell (1992)]. Also present in this part of the geoid spectrum are anomalies arising from localised differences in crustal density and sediment loading. As the freeair anomaly is a derivative of the geoid height, this field highlights the short and intermediate wavelength anomalies. The correlation between the gravity fields and surface topography, and the relation of both to deep structure leads to the concept of isostasy: isostasy provides a physical model which relates topographic loads to the compensating buoyancy of the subsurface density distribution.

1.4.2 Isostasy

Isostasy was first postulated in the 19th Century, when it was observed that the deflection of the vertical in the Himalayas was less than would be generated by the visible topographic masses. Furthermore, the Bouguer anomaly over mountain ranges was found to be systematically large and negative: if the effect of the topographic masses had been properly removed, the Bouguer anomaly should exhibit only small fluctuations about zero. These observations suggest that beneath the mountains there exists a region of reduced density that supports their load in a state of hydrostatic equilibrium.

Two hypotheses were proposed to explain this isostatic compensation: the Airy model postulated a thickening of a constant density crust, displacing a higher density substratum, the mantle; while Pratt's hypothesis proposed lateral changes in crustal density and a constant depth to the fluid substratum [*e.g.* Fowler (1990)]. These models though are idealised extremes, and in reality isostatic compensation mechanisms are most probably a combination of the two, together with a model of *regional* compensation.

In contrast to the local compensation mechanisms of Airy and Pratt, regional compensation [Vening Meinesz (1931)] is described by a mechanically strong lithosphere 'floating' on a viscous, higher density asthenosphere. This later became the central element in plate tectonics.

The difference between the lithosphere and asthenosphere is rheological rather than compositional, largely dependent upon the temperature and pressure regimes present in the mantle. The asthenosphere comprises materials made up of minerals close to their melting point, so that they are easily deformable without being completely molten. The lithosphere consists of elastic material, generally about 80-100 km thick, but decreasing to zero thickness at mid-ocean ridges. The boundary between lithosphere and asthenosphere is marked approximately by the 1400°C isotherm [Cox and Hart (1986)].

The upper part of the lithosphere can contain both oceanic and continental crust, the continents having slightly lower densities but greater thicknesses than the oceanic crust. Below the crust is the mantle, which includes the lower lithosphere and the asthenosphere. While the lithosphere/asthenosphere boundary is marked by a change in rheology allowing relative motion, the crust/mantle boundary is compositional, marked by a large density contrast (from 2.8 to 3.3 $Mg.m^{-3}$ average) at the Mohorovičić discontinuity (Moho). There is no relative motion between crust and mantle. Thus, plate motion is determined by the generation and subduction of *lithosphere* at plate boundaries.

The lithosphere responds to long term loads by bending and displacing a volume of asthenosphere below it. The lateral and vertical scale (wavelength and amplitude) of the bending is determined by the lithosphere's *flexural rigidity*, D, a measure of its stiffness. The flexural rigidity is usually expressed in terms of an *elastic thickness*, T_e, in kilometres. The relationship between the two is given by

$$D = \frac{E T_e^3}{12(1 - \sigma_p^2)} \tag{1.35}$$

where E is Young's modulus, and σ_p is Poisson's ratio. The elastic thickness corresponds to the depth to which materials behave elastically on long timescales; it is much less than the thermal or seismic lithosphere thicknesses.

The lithosphere also increases its strength with age. This is borne out by the relationship between elastic thickness and the depth to the $450°C$ isotherm, which increases with lithosphere age [Watts (1992)]. The elastic thickness is 'frozen in' at the time of loading, and does not significantly change with time. This accounts for the low T_e associated with features formed at a mid-ocean ridge many millions of years ago, that are now emplaced in old, strong lithosphere with a comparatively high elastic thickness.

Loading can also occur within the interior of the plate, or at its bottom. This might be due to temperature changes in the lithosphere or asthenosphere, metamorphism, volcanic intrusions, or underplating. The strength of the lithosphere is also very susceptible to re-heating by thermal anomalies in the mantle, and there appears to be no empirical relationship between elastic thickness and general loading models [*ibid.*].

1.4.3 Isostatic admittance

Analyses of the relief (topography or bathymetry) of an area together with the freeair or Bouguer anomalies, can help to constrain the type of isostatic compensation present, the depth to compensating layer, and the flexural rigidity of the lithosphere. This might be done by assuming a compensation mechanism for the relief, calculating a gravity effect for this mechanism, and comparing the model with the observed field [Watts (1978)].

A more preferable method, and one which does not pre-suppose any compensation mechanism, is to examine the relationship of gravity and relief in the wavenumber domain, using the isostatic admittance, $Q(k)$. This is the response of the Earth's gravity field to the application of a point load on the lithosphere: thus it will contain information about the mechanism of isostatic compensation present in the region.

Admittances calculated from observed data can then be compared with admittance values calculated from theoretical models of a compensation mechanism.

In the following loading models, a load of density ρ_0 causes flexure of a lithospheric plate. The compensation for the applied load occurs at the Moho, the crust-mantle interface, at a depth z_m. The symbol G denotes the gravitational constant, and g is the acceleration due to gravity.

Airy compensation

A system in perfect isostatic equilibrium corresponds to Airy, or 'local', isostasy. In this case the lithosphere shears and can be represented by a plate with a flexural rigidity of zero. The Bouguer admittance function for this system is given by

$$Q_B(k) = -2\pi G \rho_0 e^{-kz_m} \tag{1.36}$$

[*e.g.* Karner and Watts (1983)].

Regional compensation

Regional compensation mechanisms have been modelled in two main forms: loading on the surface of the Earth, and loading from below, at the Moho [both Forsyth (1985)]. If the lithosphere is now represented by a thin elastic plate, it will have a finite flexural rigidity. When the loading is on the surface, the

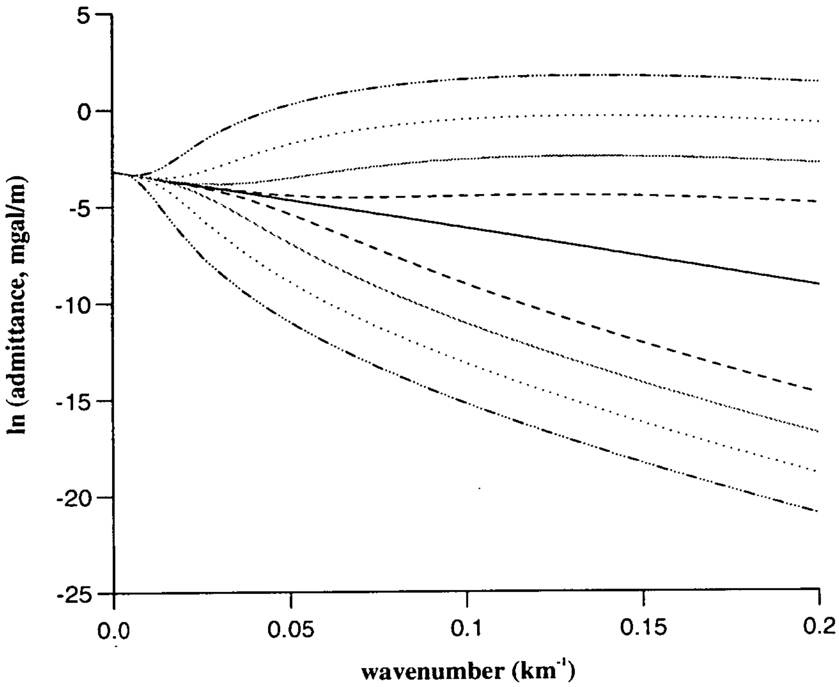

Figure 1.3. Theoretical admittance curves for z_m = 30 km. Curves for Airy isostasy (solid line), surface loading models (below Airy curve), and Moho loading models (above Airy curve). Elastic thicknesses are 5 km (dashed), 10 km (faint), 20 km (dotted) and 40 km (dot/dash).

admittance function becomes

$$Q_B(k) = -2\pi G\rho_0 e^{-kz_m} \big/ \xi \tag{1.37}$$

where

$$\xi = 1 + \frac{Dk^4}{\Delta\rho g} \quad . \tag{1.38}$$

Here, D is the flexural rigidity, given by eq.1.35, and $\Delta\rho$ is the density contrast at the Moho.

When the load is applied at the Moho, the admittance function for the system is given by

$$Q_B(k) = -2\pi G\rho_0 e^{-kz_m}\phi \tag{1.39}$$

where

$$\phi = 1 + \frac{Dk^4}{\rho_0 g} \quad . \tag{1.40}$$

Forsyth (1985) also examined a model for varying combinations of uncorrelated top and bottom loading. If the ratio of the weight of the applied load at

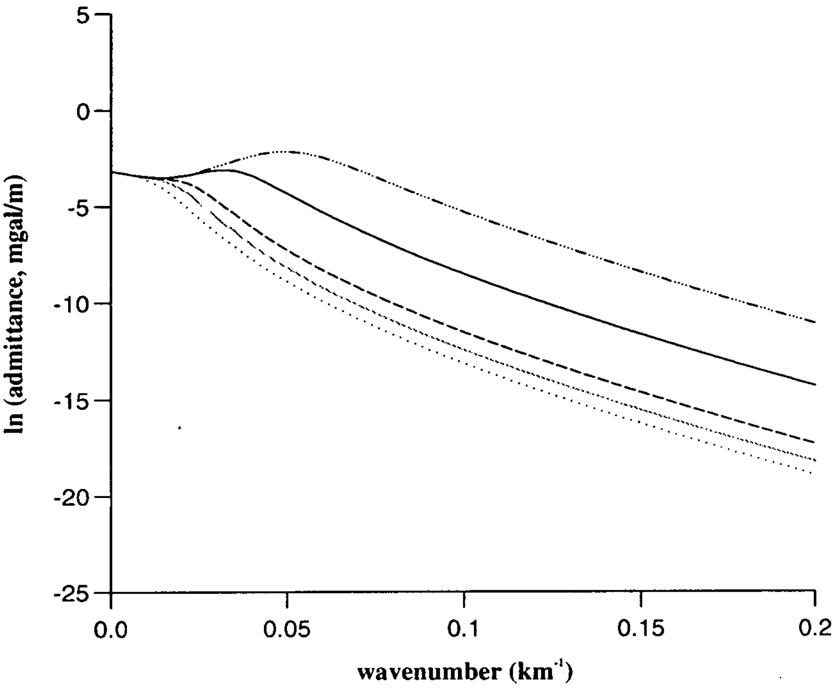

Figure 1.4. Theoretical admittance curves for $z_m = 30$ km and $T_e = 20$ km, and loading ratios of 0 (dotted), 0.5 (faint), 1 (dashed), 5 (solid) and 25 (dot/dash).

the Moho to the weight of the applied load on the surface is f, then

$$Q_B(k) = -2\pi G\rho_0 e^{-kz_m}\left[\frac{\phi\chi^2 + 1/\xi}{\chi^2 + 1}\right] \tag{1.41}$$

where

$$\chi = \frac{f\rho_0}{\xi\,\Delta\rho} \quad . \tag{1.42}$$

Note that eqs 1.37, 1.39 & 1.41 become the admittance function for Airy isostasy (eq.1.36) for a plate with zero flexural rigidity. Plots of $\ln|Q_B|$ against k for the above admittance functions are shown in figs 1.3 & 1.4. Fig 1.3 shows how the admittance varies with elastic thickness at constant depth to Moho, for surface loading models ($f = 0$), and for loading at the Moho ($f = 10^6$). Fig 1.4 shows the variation of $\ln|Q_B|$ with loading ratio, f. From eq.1.36 the initial slope of the curves in figs 1.3 & 1.4 depend only upon the Moho depth: larger values of z_m give a steeper initial gradient.

For short wavelength loads the admittance approaches zero: this is a result of the exponential decay of the Moho gravity signal for high k; and also because

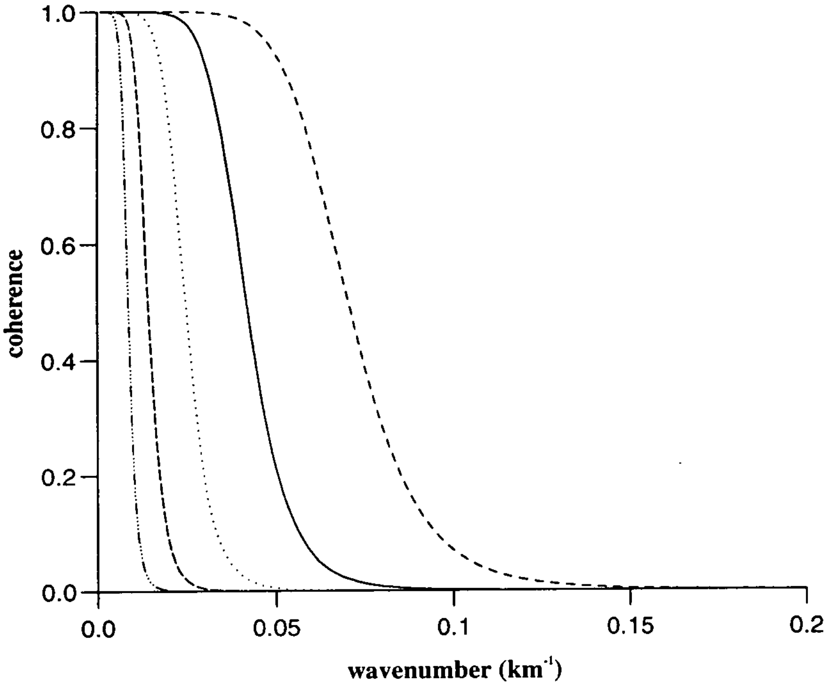

Figure 1.5. Theoretical coherence curves for $f = 1$ and elastic thicknesses of 80 km (dot/dash), 40 km (long dash), 20 km (dotted), 10 km (solid) and 5 km (short dash).

small loads can be adequately supported by an elastic plate without flexure occurring. At long wavelengths, both weak and strong plates will undergo flexure, and trend towards the Airy model.

1.4.4 Coherence

The use of admittance studies alone can, in certain cases, yield inaccurate values of the flexural rigidity. This arises from the non-uniqueness of solutions to gravity data, resulting in, for example, similar admittances for a weak plate loaded at the surface and a strong plate loaded at the Moho, with the top loading model giving too low a value of D [Forsyth (1985)].

A method that is less biased by the degree of surface and subsurface loading is the calculation of the coherence between the Bouguer gravity and the topography.

Consider an infinitely rigid plate: a load applied at the surface will have no compensating root, and a subsurface load will generate no surface topography. In the first case, the Bouguer gravity signature is zero and does not correlate with the topographic signature; in the second, the Bouguer gravity is negative while

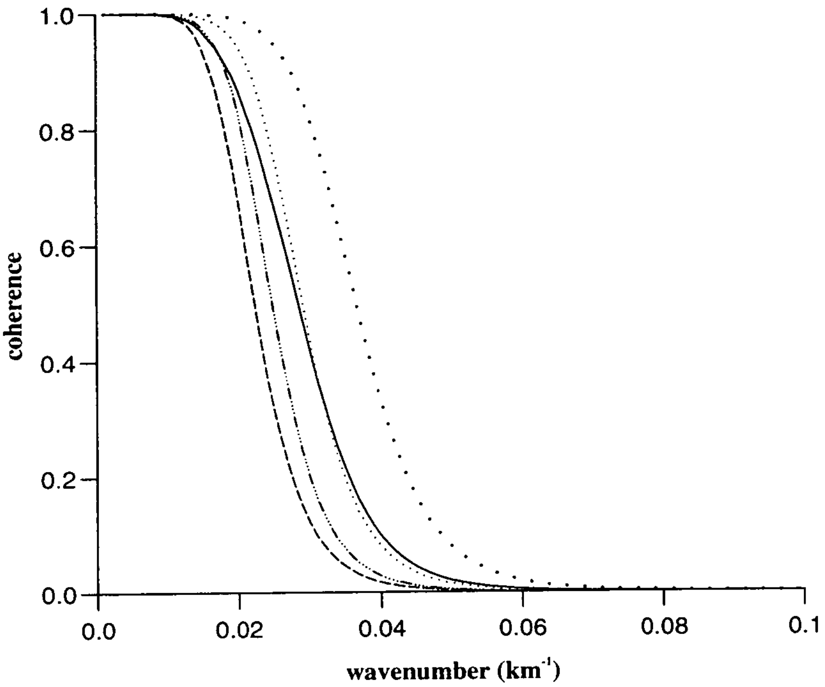

Figure 1.6. Theoretical coherence curves for $T_e = 20$ km and loading ratios of 0.1 (solid), 0.5 (dashed), 1 (dot/dash), 2 (dotted) and 5 (larger dotted).

the surface topography is zero. In both cases the degree of coherence between gravity and topography is zero and independent of the load location.

For a plate with zero flexural rigidity, a surface load generates a compensating root and a negative Bouguer anomaly, while a subsurface load creates surface topography and a similar gravity anomaly. Both scenarios are indistinguishable and the coherence is unity.

Thus for a plate with finite, non-zero rigidity, and with both surface and subsurface loading, the coherence will approach 1 at wavelengths long compared to the elastic thickness, and approach zero at short wavelengths (see fig 1.5). The transition from coherent to incoherent signatures will occur in the same wavelength range as the transition from compensated to uncompensated topography. The wavelength of the transition indicates the flexural rigidity of the plate [Forsyth (1985)].

The coherence calculated from observed data can be compared with a theoretical model, and the flexural rigidity obtained from the best-fitting curve. Forsyth

(1985) gives the coherence as

$$\gamma^2 = \frac{(1+\phi\xi\chi^2)^2}{(1+\chi^2)(1+\phi^2\xi^2\chi^2)} \tag{1.43}$$

where χ is given by eq.1.42, and ξ and ϕ by eqs 1.38 & 1.40 respectively. Note this expression is independent of the depth to the compensating stratum (z_m).

Fig 1.5 shows how theoretical coherence varies with plate elastic thickness: weaker plates have a shorter wavelength of transition from compensated to uncompensated topography. Fig 1.6 shows the variation of coherence with loading ratio for constant elastic thickness (20 km). Forsyth (1985) has shown that the coherence is fairly insensitive to uncertainty in f, also evident from this plot in the coincidence of the curves for $f = 0.1$ and $f = 2$.

1.5 Satellite altimetry

The advent of remote mapping of the ocean's surface in the 1970's through satellite altimetry has given geophysicists unprecedented global resolution of the Earth's gravity field. This information has been used to make maps of the sea bed topography, improve models of the structure of the Earth's lithosphere, and investigate the nature of convective processes in the mantle.

The altimeter indirectly measures the geoid height above a reference ellipsoid using a radar altimeter. The altimeter sends a short-pulse microwave signal to the sea surface below, which is reflected back to the satellite and the two-way traveltime recorded. The footprint diameter of the radar beam at the sea surface depends upon the design of the altimeter and the sea state at the reflection site. The footprint usually has a diameter of several kilometres. The position of the satellite is tracked from either the Earth's surface by laser ranging instruments, or through radar tracking, the most recent missions carrying an onboard GPS (Global Positioning System) receiver. Using these two pieces of information, the height of the satellite and its altimeter measurement, the (uncorrected) height of the sea surface above the reference ellipsoid can be deduced.

Corrections

There are various sources of error in an altimeter sea level measurement, which must be corrected to obtain the true sea surface topography. First there are signal delays in the onboard instrumentation: these can be modelled in the laboratory prior to launch. There are path length delays caused by local changes of the speed of light in the atmosphere. Models exist that correct for the delays caused by free electrons present in the ionosphere, and for the pressure effect of the dry air mass in the troposphere [Tapley et al. (1982)]. An onboard microwave radiometer measures and provides corrections for the amount of moisture in the troposphere.

Oceanographic corrections include the electromagnetic (EM) bias correction, which arises due to the radar backscatter cross section being larger at wave troughs than at the crests, resulting in an altimeter measurement biased towards the troughs. The inverse barometer correction accounts for the effect pressure systems (depressions and anti-cyclones) have upon sea level. A correction is also made for the noise in a measurement dependent upon the significant wave height at the ocean surface. Corrections must also be made for the gravitational effects of the sun and moon distorting the solid shape of the Earth and its oceans. [A good analysis of the errors present in Topex/Poseidon data is provided in Tsaoussi and Koblinsky (1994).]

One of the largest sources of error in altimeter measurements is the radial orbit error [Sandwell (1992)], the uncertainty in the height of the satellite above the reference ellipsoid. Orbits are computed from the satellite tracking data and from a long wavelength geopotential model. Uncertainties in these, and in the position of the centre of mass of the Earth were found to generate errors in Geosat data of up to 5 m at 40,000 km wavelength, and 1 m at 20,000 km [Sandwell and Zhang (1989)]. The use of a better geopotential model can dramatically reduce these errors [*e.g.* McAdoo (1990)]. Using the geoid gradient instead of the geoid height in the interpretation of satellite data can also reduce the long wavelength errors. This is discussed further in Chapter 3.

The application of these corrections to the altimeter measurement yields the height of the mean sea level above the reference ellipsoid. In order to recover the geoid height, corrections for ocean phenomena such as tides and currents must be applied (§1.5.2).

1.5.1 Satellite missions

Table 1.1 summarizes some of the capabilities of the various altimeter missions. The measurement precision is most easily evaluated in terms of the vertical deflection along the satellite profiles [Sandwell (1992)]. This precision depends primarily upon short-wavelength ($<$ 100 km) altimeter "noise" and to a lesser extent upon mesoscale (100-1000 km) ocean variability. 1 μrad of deflection error translates to 0.98 mgal of gravity anomaly error [*ibid.*]. The along-track resolution of the profiles is estimated by calculating the spectral coherence between independent repeat profiles, taking 50% coherence as the short-wavelength limit [Sandwell and McAdoo (1990)]. The overall resolution is of course limited by the groundtrack spacing.

Geos 3

Although the first spaceborne radar altimeter was used in 1973 (the Skylab space station carried an altimeter with an accuracy of a few metres) the first dedicated mission to record sea level height was the launch of Geos 3 in 1975, lasting for three years. The satellite had an orbit height of 843 km with groundtracks separated by 20-400 km at the equator. Marks and Sailor (1986) calculated the along-track resolution from repeat profiles to be 110 km, with an overall accuracy on its sea surface height measurements of 25 cm [Cheney and Marsh (1981)].

Seasat

The Seasat altimeter became operational in July 1978, but suffered instrument failure three months later. It still succeeded in collecting sea height readings between latitudes 72° N & S with an 8 cm accuracy [Cheney and Marsh (1981)], and a precision of 10 μrad [Sandwell (1992)]. The orbit groundtrack separation at the equator varied between 80 and 120 km owing to different repeat orbit configurations. Data were sampled ten times a second, but were also averaged over a second giving an effective distance between readings of 3.4 km. The along-track resolution was calculated at 50 km [Marks and Sailor (1986)].

Geosat

The Geosat altimeter was launched on 12th March 1985 to perform two missions: the first, lasting 18 months, collected classified military data along groundtracks spaced 4 km at the equator, at the same rate as the Seasat altimeter. The orbit altitude was 800 km, and the satellite operated between latitudes 72° N & S. The data from this Geodetic Mission (GM) south of 30° S were declassified by the U.S. Navy in 1990.

	GEOS-3	Seasat	Geosat/GM	Geosat/ERM	ERS-1	Topex/Poseidon
Launch year	1975	1978	1985	1986	1991	1992
Orbit altitude	843 km	800 km	800 km	800 km	782 km	1336 km
Latitude extremes	±65°	±72°	±72°	±72°	±82°	±66°
Equatorial groundtrack spacing	20-400 km	80-120 km	4 km	165 km	8 km	316 km
Altimeter noise level	60 cm	10 cm	4 cm	4 cm	4 cm	2 cm
Precision	30 μrad	10 μrad	6 μrad	<1 μrad	?	?
Along-track Resolution, λ	110 km	50 km	30 km	20 km	?	?

Table 1.1. Altimeter mission parameters [from Sandwell (1992), Fu et al. (1994), McAdoo and Marks (1992), Marks and Sailor (1986), Sandwell et al. (1995)] (? indicates no information available).

The second of Geosat's missions was the Exact Repeat Mission (ERM), primarily designed to measure oceanographic variations in the sea surface topography. It was manoeuvred into an orbit similar to the GM orbit, except groundtracks were repeated to within 1 km every 17 days. This gave an equatorial spacing of 165 km for adjacent groundtracks, and some 66 repeat orbits, until the mission ceased on 5^{th} January 1990. If repeat orbits are averaged (stacked), this removes most of the time-dependent oceanographic signals such as tides, eddies and storm signals. Sandwell and McAdoo (1990) calculated the along-track resolution from several pairs of repeat profiles to be 31 km; however when they averaged 44 repeats this decreased to 19 km. They also calculated the precision of the unstacked profiles at 6 μrad, while that for the average of 44 repeats was < 1 μrad at latitudes between 30° N & S, but 2-5 μrad at higher latitudes, largely due to sea ice contaminating the measurements.

ERS-1

The European Remote Sensing satellite, ERS-1, is currently providing unprecedented global resolution of the ocean surface topography. It was launched in October 1991, embarking on a 3-day repeat mission until April 1992, a 35-day repeat mission until December 1993, and is currently in a 176-day repeat orbit. With its latitude limits at ±82° , and the 176-day groundtracks spaced by 9 km at the equator, it is providing the scientific community with very high resolution data.

Topex/Poseidon

The Topex/Poseidon satellite was launched on 10^{th} August 1992 and is still operational. In addition to other instruments, it carries a dual frequency radar altimeter, and a single frequency solid-state radar altimeter. The dual frequency altimeter, Topex, was designed and built in the USA for NASA. It operates at 5.3 and 13.6 GHz, thus minimizing the errors caused by ionospheric free electrons [Fu et al. (1994)]. The single frequency altimeter, Poseidon, was designed by the French space agency (CNES), and operates at 13.65 GHz. The two altimeters share the same antenna, so cannot operate at the same time. Verification tests were performed in the mission's early stages to cross-check the two altimeters, and the Geophysical Data Records (GDR's) then commenced in late May 1993.

The satellite orbits the Earth at an altitude of 1336 km: this is a relatively high orbit for an oceanographic satellite, that was chosen to reduce atmospheric drag and gravity forces acting on the satellite. The inclination and repeat period of the orbit determine how the ocean is sampled by the satellite. The Topex/Poseidon satellite has an inclination of 66° to reduce undesirable aliased tidal frequencies, yet still provide good global coverage. A repeat period of approximately 10 days gives a high temporal resolution but a poorer spatial resolution, resulting in an equatorial groundtrack spacing of 316 km.

The RMS accuracy of a single-pass sea level measurement is 4.7 cm for the Topex system, and 5.1 cm for Poseidon. The altimeter noise level is given as 1.7 cm for Topex, and 2.0 cm for Poseidon. The radial orbit error is quoted as 3 cm. [All data Fu et al. (1994).]

1.5.2 Sea surface topography

Throughout this thesis the statement that satellite altimeters measure "the departure of the geoid from a reference ellipsoid" is used for simplicity, though this is not strictly true. The altimeter measures the height of the *sea surface* above the ellipsoid, and while the geoid signature forms the main part of this departure, with amplitudes ranging up to 100 m and anomalies occurring at all wavelengths, there is also a substantial signal due to permanent and time-dependent oceanographic effects. These are expressed as a 'dynamic topography', defined as the sea surface slope relative to the geoid [Cheney and Marsh (1981)].

The time-varying features include western boundary currents and eddies, which have wavelengths in the range 100-300 km and amplitudes of up to a metre. Also, there are currents, tides and pressure gradients which can distort the sea surface by up to 2 m from the geoid in deep ocean regions, with slopes greater than 1 μrad, but tend to have longer wavelengths [Cheney and Marsh (1981)]. These transient features can be reduced in amplitude by averaging repeat altimeter tracks [*e.g.* Sandwell and McAdoo (1990)].

However, it is harder to separate the permanent component of the dynamic topography from the geoid signal in an altimeter reading. This will not be so important in regional studies, as the permanent component has a relatively small amplitude (< 1 μrad) and consists primarily of long wavelengths (> 1000 km) [Sandwell and McAdoo (1990) and *cf* fig 1.2].

Many of the existing geopotential models, such as OSU91A and GEM-T2, incorporate a spherical harmonic expansion of the sea surface topography (§1.3).

The OSU91A model includes this information for wavelengths above 2600 km. Thus, subtraction of such a model from altimeter readings would remove the known long wavelength sea surface topography signal.

Another method of separation would be to develop a high accuracy geoid by independent methods; namely a dedicated satellite gravity mission that would measure either the gravity field or gravity gradient at orbit altitude. From upward continuation effects, the calculated geoid would be lacking in short wavelength information. However this geoid could be used to identify that part of the long wavelength spectrum of an altimeter signal that is only gravitational, thus indicating the part that is due to the long wavelength sea surface topography, assuming all other long wavelength errors are accounted for. Thus the combination of a dedicated gravity mission and regular altimetry would provide the community with unprecedented geodetic and oceanographic datasets. Such dedicated gravity missions have been proposed by the European Space Agency, *e.g.* STEP and ARISTOTELES, but are yet to be implemented.

Chapter 2

Data Sources

2.1 Introduction

There are many ways of determining the gravity field of the Earth. Direct measurements of the force at the Earth's surface are made using absolute or relative gravity meters or pendulum observations, and these can be reduced to give a freeair or Bouguer anomaly. The gravitational potential can also be determined by measuring the mean height of the sea surface (an approximation to the geoid) above a reference ellipsoid, which then can be transformed to gravitational acceleration. With the advent of satellite altimetry in the 1970's, this latter method has gained importance and is now widely used in constructing both global and regional scale gravity field maps over the oceans.

This thesis uses gravity data over the North Atlantic Ocean to construct a two-dimensional gridded geoid. Data from two satellite missions were used in the combination algorithm, those from the Geosat/ERM, and those from the recently launched Topex/Poseidon mission. Shipboard observations of the freeair anomaly were also used where available, as well as all available freeair anomaly data measured on land.

2.2 The study area

The study area used to demonstrate the gridding and combination algorithms is the North Atlantic Ocean. Gravity data were used that fell between 47° N and 72° N latitude, and between 68° W and 18° E longitude. Their positions were then converted to a Lambert conical conformal coordinate grid with two standard parallels (Appendix A).

To obtain a rectangular area, data were deleted that lay outside an area defined by -1760 km to 1755 km easting, and -1130 km to 1245 km northing. The resulting study area had dimensions of 3515 × 2375 km. This area, with the meridians and parallels, is shown in, *e.g.* fig 2.1, with the southwest corner assigned the coordinates (0,0).

All grids throughout this thesis have a 5 km spacing between nodes in both easting and northing.

2.3 Geosat/ERM data

The Geosat/ERM datasets used in the study were taken from the *Gravity CD-ROM* [NGDC (1992)]. The database on the CD consists of two separate files of ascending cycles and descending cycles, which were constructed from the average of 44 repeat cycles of the Geosat/ERM. Each data record contains the time and location of the record in latitude and longitude, and the geoid height, gravity anomaly, and uncertainty in the gravity anomaly at the record point. The averaging method and general data processing procedure is described in Sandwell and McAdoo (1990), who compiled this dataset.

Programs to extract areas of interest from the data were supplied with the CD-ROM. The data were extracted and their locations converted to the Lambert projection according to the area parameters given in §2.2. Two files were created: one of ascending cycle data and one of descending cycle data. Each contained the easting, northing, geoid height and latitude of the record. The latitude is required by the gridding algorithm (Chapter 3), and including it in the data record removes the need to convert the Lambert grid coordinates back to degrees during program run-time. The records in each of the files were then collated into continuous profiles, where the distance between adjacent records was no more than 6 km. The number of points in each profile preceded the profile as a "header".

The OSU91A geoid height model to harmonic degree and order 360 was then subtracted from the data records. The harmonic coefficients were tapered with a cosine-squared function between degrees 300 and 360 to reduce the Gibbs' effect, arising when spectra are sharply truncated [Kanasewich (1981)]. The OSU91A harmonic expansion of the sea surface topography was also subtracted from the satellite profiles. The coefficients in this model were tapered between degrees 12

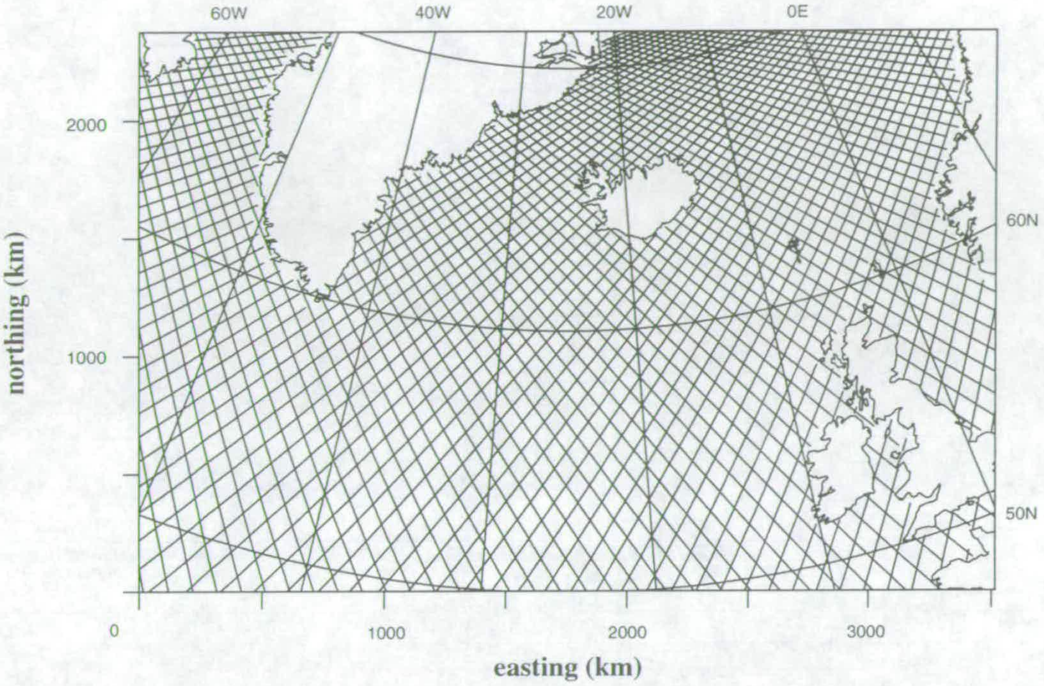

Figure 2.1. Geosat/ERM groundtracks in the North Atlantic study area.

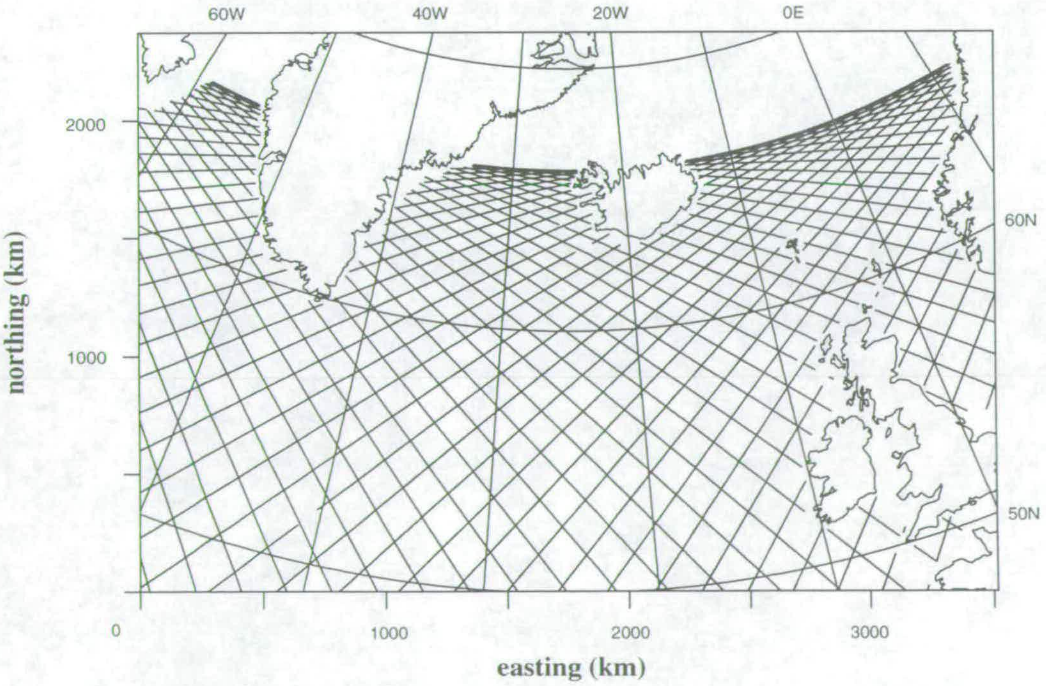

Figure 2.2. Topex/Poseidon groundtracks in the North Atlantic study area.

and 15. These models are discussed in §1.3.

The Geosat/ERM groundtracks in the North Atlantic Ocean study area are shown in fig 2.1.

2.4 Topex/Poseidon data

The Topex/Poseidon data used in the study were taken from the CD-ROMs supplied by AVISO (1992). The CD-ROMs contain the time, latitude and longitude for each data record, the altimeter orbit height and measured height above sea level, and a set of atmospheric and other geophysical corrections to be applied to the height value. A suite of programs was also supplied to extract the position, time and corrected sea surface height reading.

Unlike the Geosat/ERM dataset, the Topex/Poseidon data were not given in the averaged form, so this study used repeat cycles 11 to 40 inclusive (*AVISO* discs 6 to 20). The Topex/Poseidon data are referenced to a slightly different ellipsoid [AVISO (1992)] than the GRS80 ellipsoid used in the Geosat data, so it was necessary to convert the data to GRS80. Following the method for sorting the Geosat/ERM data, these were separated into ascending and descending passes, converted to the Lambert coordinate plane, and divided into continuous profiles.

Finally, the OSU91A geoid height and sea surface topography models were subtracted from the data records.

The Topex/Poseidon groundtracks in the North Atlantic Ocean study area are shown in fig 2.2.

2.5 Marine gravity measurements

The *GEODAS CD-ROM* [NGDC (1994)] provided all the available marine gravity observations. The CD comes with menu-driven software that extracts the type, date, and location of the data, and writes them out in a chronologically ordered sequence.

Most of the ship track freeair anomalies on the CD-ROM were referenced to the GRS80 international ellipsoidal gravity formula and the IGSN 71 reference system. However, a number of cruises used the International 1930 or IAG System 1967 ellipsoidal gravity formulae, and/or the Potsdam reference system. As this information was provided in the cruise header file, it was a straightforward task to reduce the data to GRS80/IGSN 71 [Moritz (1984)].

The data were then projected onto the Lambert conical conformal plane, and a rectangular area created as described in §2.2. It is then a simple task to sort the data into a series of along-track profiles with a maximum observation separation of 10 km; *i.e.* when the distance between two adjacent points exceeded this value, a new profile was started. As with the satellite data, the number of records in each profile preceded the profile records as a header, along with the cruise identifier and the survey year.

Finally, the OSU91A freeair gravity model to harmonic degree and order 360 was subtracted from the data records.

The ship tracks in the North Atlantic Ocean study area are shown in fig 2.3.

2.6 Land gravity data

The location of the terrestrial freeair anomaly measurements used in the thesis are shown in fig 2.4. The Bureau Gravimetrique International (BGI) supplied the data over Iceland (*pers. comm.* G. Balma, BGI, Toulouse, 1995). The Ireland data came from John Davies (*pers. comm.* J. Davies, Dublin Institute for Advanced Studies, Dublin, 1980).

The data over mainland Britain was taken from the British geoid/freeair gravity map compiled by Stewart and Hipkin (1990). Note from fig 2.4 that data from this geoid map extend into the waters surrounding the UK; these were used in the combination algorithm.

The location of each gravity measurement was converted to the Lambert projection, and a rectangular area created as described in §2.2. Then, the OSU91A freeair gravity model to harmonic degree and order 360 was subtracted from the data records.

2.7 Relief dataset

The topographic/bathymetric relief data were extracted from the ETOPO5 dataset [NGDC (1993)] on CD-ROM. This provides worldwide 5-minute gridded elevations/depths, which were easily interpolated onto the 5 km Lambert grid used in this study.

The relief dataset was also used to create a 'land/sea' grid, for use in the satellite data gridding algorithm (§3.4). Any gridnodes falling over landmasses were assigned a value of 1; those nodes falling over the sea were assigned a

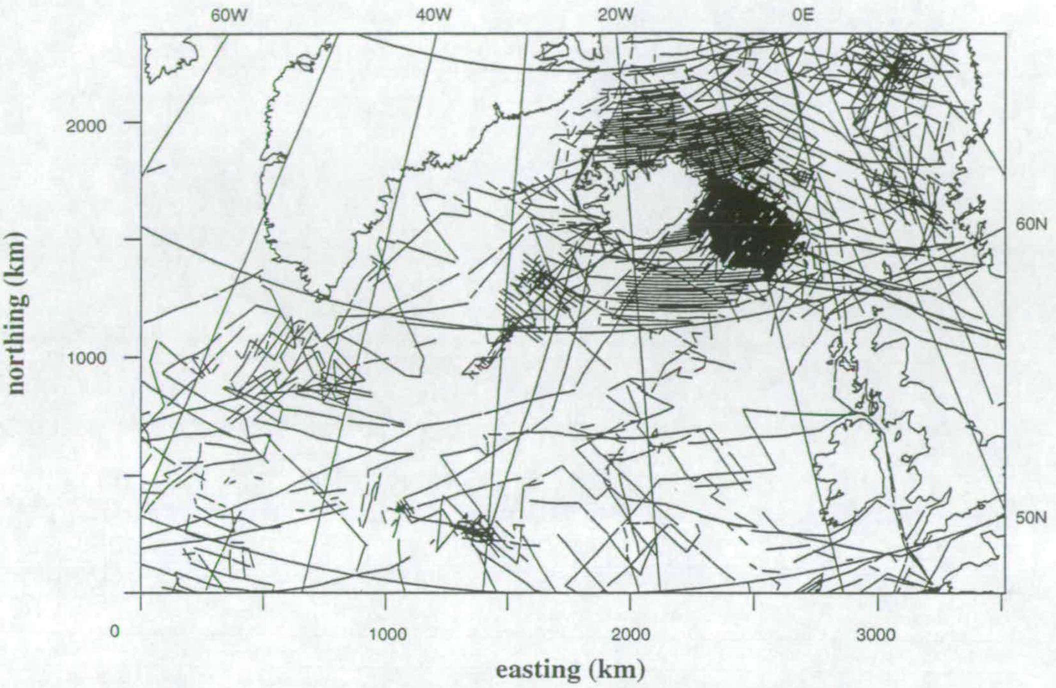

Figure 2.3. Ship tracks in the North Atlantic study area.

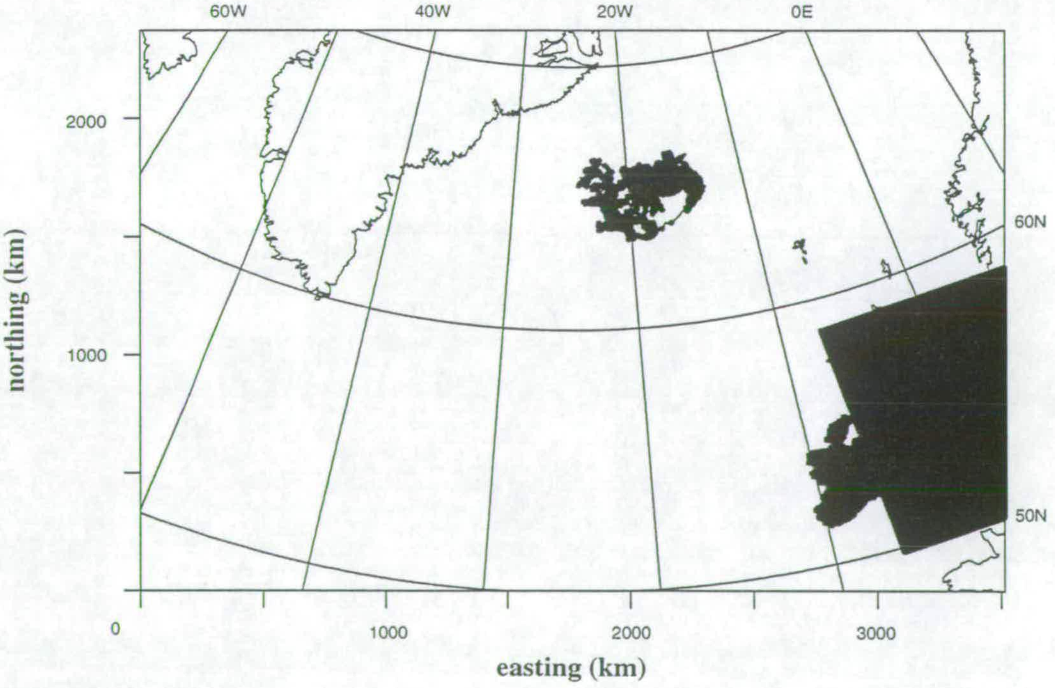

Figure 2.4. Land gravity data in the North Atlantic study area. (See text.)

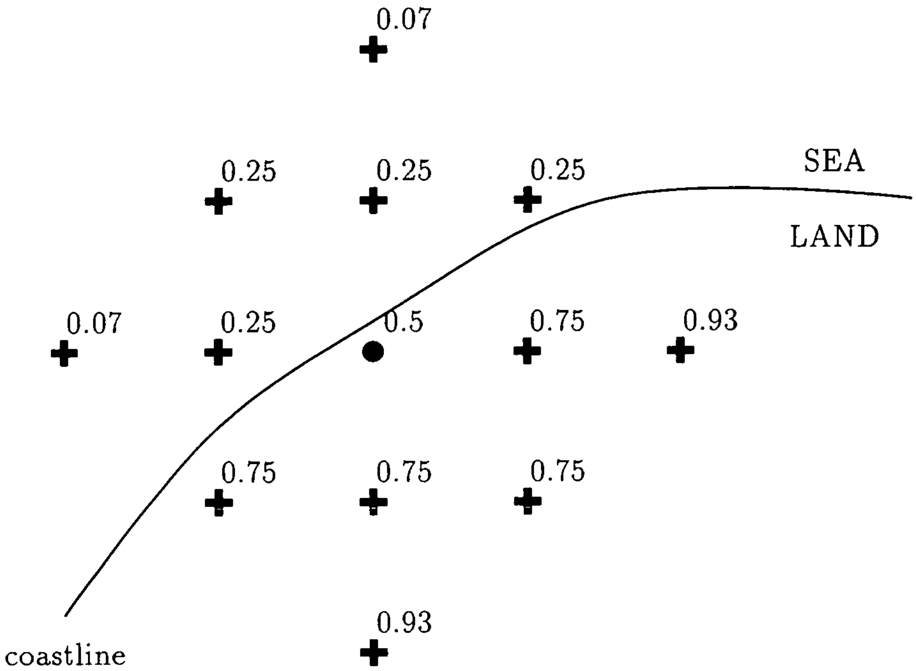

Figure 2.5. Tapering the coastline in the gridded land/sea file.

value of 0. The land/sea interface at the coastline was then tapered to ensure a smooth transition important in the Fourier transformation procedure. Adjacent gridnodes were identified where a change from 1 to 0 occurred, or vice versa. The gridnode with value 1 was then assigned a 0.5 value and deemed the coastline node (the • in fig 2.5). The node to its horizontal landward side was then assigned a value 0.75, and the node beyond this a value 0.93. The node to its horizontal seaward side was assigned a value 0.25, and the node beyond this a value 0.07. This procedure was repeated for the four vertically adjacent gridnodes. The four gridnodes diagonally adjacent to the coastline node were assigned values 0.75 or 0.25, depending whether they were landward or seaward.

2.8 The test dataset

In order to test the algorithm, a dataset is needed where both freeair gravity anomaly and the geoid height are accurately known everywhere, self-consistent, and fully interchangeable. Then, with simulated satellite and marine gravity measurements "lifted off" these datasets, the ability of the algorithm to interpolate between tracks can be tested against the gravity field variation of the real Earth.

The test model used involves freeair gravity and geoid height derived from surface gravity measurements made over the British Isles and North Sea, on a 2 km grid [Stewart and Hipkin (1990)]. The test model is a 500x500 km extract of both geoid and freeair anomalies, on a 5 km grid. It contains both short and long wavelength features, such as we would expect to find over both shallow marine and deep ocean environments. The geoid grid is shown in fig 2.6. The mean value of the geoid heights is 0.146 m, with a standard deviation of 0.184 m. The freeair grid is shown in fig 2.7. The mean value of the freeair anomalies is 0.360 mgal, with a standard deviation of 10.213 mgal. These values will later be compared with values calculated from the models derived from the simulated datasets using the presented gridding and combination algorithms.

A simulated altimetry dataset was constructed from the British geoid using coordinates of ascending and descending Geosat/ERM observations passing through a 500x500 km area in the North Atlantic, with the bottom-left corner having Lambert coordinates (-1700 km, -1100 km). The geometry of these observation points was then superimposed upon the British geoid, and the model geoid height determined by bicubic interpolation. This gave a simulated dataset of fictitious satellite passes over the test model area, which are shown superimposed upon the geoid grid in fig 2.6. The mean value of these passes is 0.138 m, with a standard deviation of 0.188 m.

A simulated ship track dataset was created in the same way, using the coordinates of ship tracks in the same North Atlantic area, superimposed upon the test model freeair anomaly. These are shown on the freeair anomaly grid in fig 2.7. The mean value of these track data is 2.878 mgal, with a standard deviation of 11.848 mgal.

Thus, as the two simulated datasets contain accurate information about the test model, we would hope to recover the test model geoid (or freeair gravity) upon their combination by the presented algorithm. In particular, we can test the effectiveness of the algorithm by comparing the model with the known gravity field in the unsampled regions between tracks.

In the following three chapters, the gridding and combination algorithms will be applied to the test model data, illustrating their usage and effectiveness.

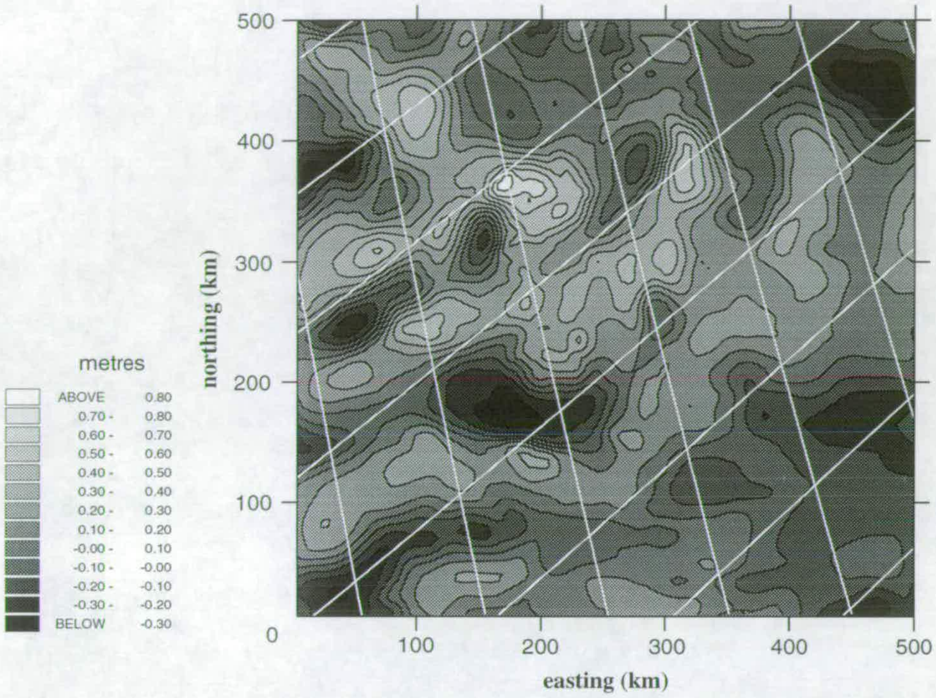

Figure 2.6. The test model geoid height showing simulated satellite groundtracks.

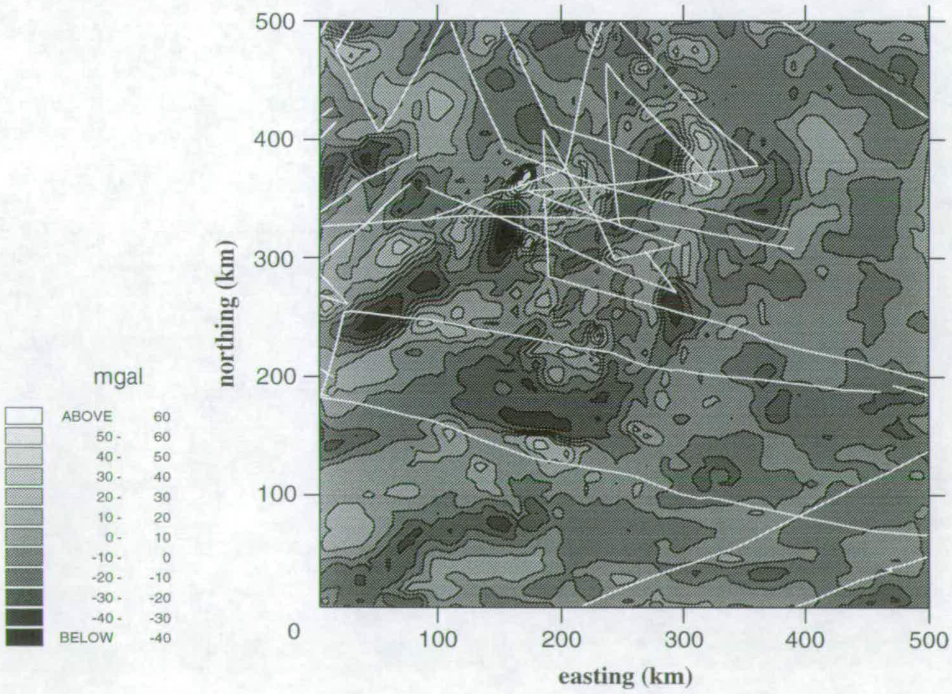

Figure 2.7. The test model freeair anomaly showing simulated ship tracks.

Chapter 3

Gridding Satellite Data

3.1 Introduction

The algorithm combining a satellite geoid with freeair anomalies observed on the Earth's surface makes use of fast Fourier transforms (FFTs). Although they greatly speed up operations, FFTs require the data to exist on a regular grid. Furthermore, in order to avoid the Gibbs' effect caused by sharp cutoffs at data boundaries, the data should be complete, with few gaps.

The almost global coverage provided by satellite altimeter missions gives an excellent starting point for the creation of a complete grid of geoid heights (ignoring for the time being the gaps occurring when the satellite passes over landmasses). The method presented here enables the combination of data from more than one satellite mission, thus producing a geoid model that has greater resolution, greater accuracy and greater coverage than such a model from only one mission.

The high along-track sampling rate of satellite altimetry data compared with the large track separation at the equator (§1.5.1) makes gridding these datasets a problem. Ideally, we would like to retain the along-track resolution, but also interpolate into the spaces between adjacent tracks so that a complete grid can be generated. However, as will be discussed later, the generation of a complete grid implies a degree of smoothing of the data and thus a loss of resolution along track. The gridding kernel chosen to interpolate the data should exhibit a "trade-off" between completeness and resolution, but priority should be given to the generation of a complete grid.

The along-track geoid slope is gridded up in preference to the geoid height:

the differentiation operation effectively removes the long wavelength radial orbit error (see §1.5), removing the large amplitude stripes that arise when a crossover analysis is performed [Sandwell (1992)]. Furthermore, the algorithm allows for the averaging, or stacking, of repeat profiles. This has the following benefits: first, it is much better procedure to average the geoid slope rather than the geoid height, as offsets are not introduced at data gaps [McAdoo (1990)]; second, the resolution capabilities of the mission are increased [Sandwell and McAdoo (1990)]; and third, time-variant oceanographic signals are reduced (§1.5.2).

However, the nature of the data distribution is such as to provide an underestimated geoid slope value, due to the strike of the groundtrack across sea surface anomalies. Only when the groundtrack lies perpendicular to an anomaly will a true value of the geoid slope be determined. In all other cases the slope value will be lower, leading to a gridded anomaly with lower amplitude than in reality. As this method cannot correct for this phenomenon, it must be acknowledged that errors in geoid anomaly amplitude could result.

Using this method, obtaining a gridded geoid model from along-track altimeter data is a two stage process, involving the generation of grids of along-track geoid slopes as an intermediate stage. Separate grids of geoid slopes from ascending passes and from descending passes are calculated for each satellite mission considered. These along-track slope grids are then combined using an approach similar to that employed by Sandwell (1984) and McAdoo (1990), to give a gridded geoid over the area.

3.2 The gridding kernel

The kernel chosen to grid altimeter data distributed on widely spaced groundtracks should conform to certain restrictions.

1. It should be rotationally symmetric (isotropic), ensuring no bias in any direction.

2. It should be of sufficient radius to ensure all grid nodes between adjacent groundtracks are assigned a slope value.

3. Acknowledging that while a complete grid is required, the kernel should smooth the altimeter data as little as possible.

4. It is not possible, and thus not necessary, to reproduce the short wavelength resolution in the areas between adjacent groundtracks. In these areas it is reasonable to suggest that the information provided by the altimeter measurements can only determine the intermediate and long wavelength structure of the gravity field. That is, short wavelength anomalies on the satellite track will have relatively little influence upon the short wavelength anomalies inter-track. This criterion removes any desire to design a "super-kernel".

In processing and interpreting satellite altimetry data, most studies use the track profiles without the construction of a grid [*e.g.* Sandwell and McAdoo (1988), Sandwell and McAdoo (1990)]. Other studies have produced 2D grids from altimeter profiles using bilinear interpolation [*e.g.* McAdoo and Marks (1992)], an unspecified inverse-squared distance kernel [McAdoo (1990)], and using a method known as "projection onto convex sets" [Sandwell (1992)]; these studies have also used vertical deflections coupled with a Fourier transform based approach to determine the geoid height, similar to that outlined in this thesis. Another study, by Sandwell (1984), used a kernel of the form $1/(1 + (x/a)^3)$ to grid vertical deflections.

Several designs of kernel satisfying the above requirements were tested on the simulated altimeter data. They are described in Appendix B. The kernel chosen to grid the altimeter data has the form of the function commonly known as the "Witch of Aganissi", or "Witches' Hat". Its formula is

$$\delta\omega(x,\phi) = \frac{1}{[\Phi(\phi)]^2} \cdot \frac{1}{1+(\frac{x}{a'})^2} \qquad |x| \leq R' \qquad (3.1)$$

for a point x kilometres from the observation whose geodetic latitude is ϕ. For a given observation point, the parameters $\Phi(\phi)$, R', and a' are constants; they are discussed later. Cross-sections through various forms of the kernel are shown in figs 3.1 & 3.2: the kernel is rotationally symmetrical about the axis $x = 0$.

This form was also chosen for its fast calculation by a computer: no intrinsic series approximation functions are called, resulting in a relatively fast CPU execution time.

Suppose we need to interpolate a set of values z_k observed at points (x_k, y_k) $(k = 1, \cdots, M)$ onto a regular grid, z^{ij}. For a particular observation point, P, with value z_P, the kernel is centred on P and an increment is added to all gridnodes within a certain distance of P, the *search radius* R'. The increment is the product of z_P with the value of the gridding kernel at the gridnode. Thus the gridnodes close to the observation point are weighted higher than those at the edge of the search radius. This procedure is carried out in a cumulative fashion for all the observation points M, resulting in a grid of cumulative interpolated observations. If the sum of the gridding kernel values at each gridnode is also stored, then the grid of interpolated observations can be normalised to give a final interpolated grid, z^{ij}, representing the original values z_k:

$$z^{ij} = \sum_k z_k \, \delta\omega_k^{ij} \Big/ \sum_k \delta\omega_k^{ij}. \tag{3.2}$$

Here, $\delta\omega_k^{ij}$ represents the value of the kernel at gridnode (i, j) for the particular observation k.

An additional problem with gridding satellite altimeter data in this way is that as the satellites near the turning points of a cycle (±72° latitude for Geosat) the groundtracks draw closer together and the observation density increases. Thus the gridding kernel needs only influence a smaller number of gridnodes than at lower latitudes; if this did not happen then over-smoothing of the interpolated field would result. Furthermore, as the search radius decreases, the shape of the kernel needs to be altered to preserve uniform gridding. The function $\Phi(\phi)$ is designed to take this into account.

$\Phi(\phi)$ is a function included to reflect the gradual decrease in separation of the satellite groundtracks with increasing latitude. Its form on a Lambert projection is

$$\Phi(\phi) = \frac{\phi_1 - \phi}{\phi_1 - \phi_0} \tag{3.3}$$

where, for a particular study area, ϕ_0 is lowest absolute latitude, and ϕ_1 is highest absolute latitude. Thus, as latitude increases, $\Phi(\phi)$ decreases proportionally. As shown in fig 3.2, it serves to reduce the search radius of the kernel and its halfwidth. It also modifies the overall amplitude of the kernel function: tests showed that as the width and search radius of the kernel decreased with increasing latitude, the gridnodes in this region of closely-spaced groundtracks were assigned too low a weight. Consequently, including the $1/\Phi^2$ term in eq.3.1 compensated for this effect and ensured a constant, latitude-independent integral (see Appendix C.2 and eq.C.14). Care must be taken though, when choosing the value of ϕ_1, to ensure it is greater than the maximum possible value of ϕ. If ϕ_0 is always taken as the

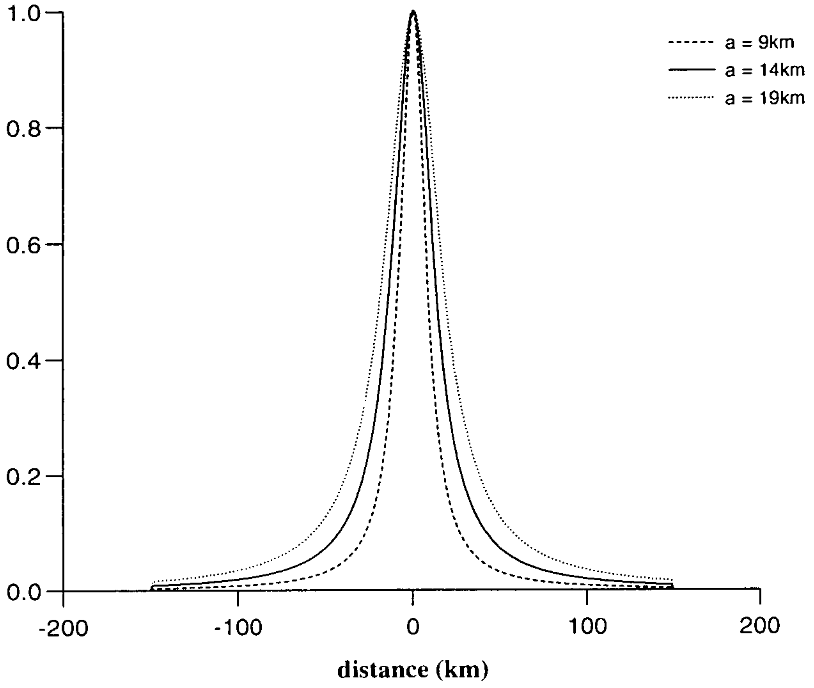

Figure 3.1. Cross-section of the Topex gridding kernel showing variation with halfwidth.

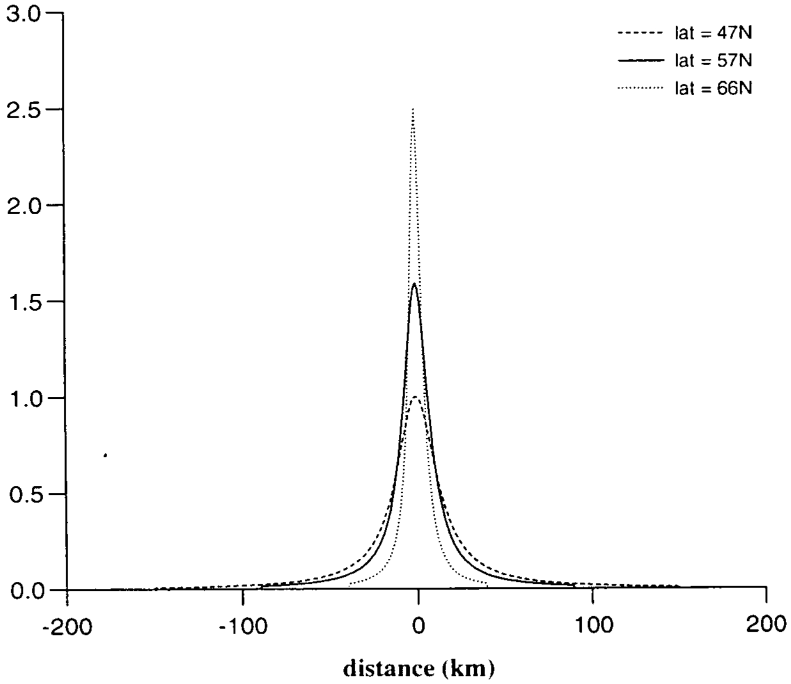

Figure 3.2. Cross-section of the Topex gridding kernel showing variation with latitude.

lowest absolute latitude in the survey area, and ϕ_{sat} is the latitude extreme of the satellite mission being gridded, then a good value of ϕ_1 is given by

$$\phi_1 = \phi_{sat} + (\phi_{sat} - \phi_0)/3 \quad . \tag{3.4}$$

Note Φ is linear in latitude, whereas the actual separation of satellite groundtracks in latitude and longitude is much more complex. A linear approximation was found to be adequate when compared with trigonometric functions, and also to be computationally much faster. The values of the parameters ϕ_0 and ϕ_1 used in the study are given in Appendix E.

R' is the search radius of the kernel at a particular latitude. If R_o is the maximum value of the search radius, then

$$R' = R_o \cdot \Phi \quad . \tag{3.5}$$

The dependence of R' on ϕ decreases the search radius as the observation density increases with increasing latitude. The value of R_o should be chosen so that it is slightly greater than half the separation between adjacent satellite groundtracks at the lowest latitude. A large value of R_o will smooth the resultant grid too much, while a small R_o will leave some gridnodes unassigned. The values of R_o used in the study are given in Appendix E.

a' is a factor determining the halfwidth of the kernel, higher values of a' giving a 'broader' shape, as shown in fig 3.1. Again this parameter is latitude dependent,

$$a' = a_o \cdot \Phi \quad , \tag{3.6}$$

the shape of the kernel being maintained as the latitude of the observation point changes. The value of a_o is linked to the search radius, R_o, as

$$a_o = Q \cdot R_o \qquad \text{with} \qquad Q = 0.175 \quad . \tag{3.7}$$

This value of Q was chosen from a range of values, by studying the shape of the kernel and the resulting interpolated grid of geoid slopes. For a fixed search radius of $R_o = 80$ km for Geosat data, studies were made for $a_o = 5$ to 36 km: values of $a_o > 18$ km had large discontinuities at the edge of the kernel, while kernel functions with $a_o < 9$ km were too narrow, gridnodes near the edge of the search radius not gaining enough weight. The kernel function with $a_o = 14$ km gave good weight to the inner nodes, while having only a small discontinuity at $x = R'$, hence the chosen value of Q.

3.3 Gridding along-track geoid slopes

To create a gridded model of the geoid height from satellite altimeter data, the first step is to produce separate grids of the ascending and descending along-track geoid slopes. The along-track gradient, ϵ, is calculated at the midpoint between two observations by the formula:

$$\epsilon_k = \frac{N_{k+1} - N_{k-1}}{\Delta \ell} \tag{3.8}$$

where N_k is the geoid height at observation k, and $\Delta \ell$ is the distance between observations $k - 1$ and $k + 1$.

The flow diagram in fig 3.3 illustrates how altimeter observations are interpolated onto a regular grid. The procedure follows the steps described in §3.2, with the along-track geoid slope, ϵ substituted for z in eq.3.2. Two grids are generated by the algorithm: a weighted mean grid of the along-track geoid slope; and a grid of the corresponding weights. The values of the weighting grid are normalized by the maximum cumulative weight, so that all values lie between 0 and 1. This removes the bias introduced when previously stacked datasets are to be combined with unstacked datasets of many repeat orbits. The gridding algorithm is performed separately on the ascending and descending passes of each satellite dataset considered.

This method of gridding satellite altimeter data also has the advantage of filtering the data. The action of differentiation followed by gridding with the described kernel adequately suppresses both long wavelength radial orbit errors and the short wavelength noise generated by the derivative operator. A study of the spectral characteristics of this gridding procedure is described in Appendix C.2.

For easy reference, this gridding procedure will be refered to as the "Witch gridding algorithm" throughout the thesis, after the name of the gridding kernel. The algorithm is coded in the subroutine GSGRID.F (Appendix E).

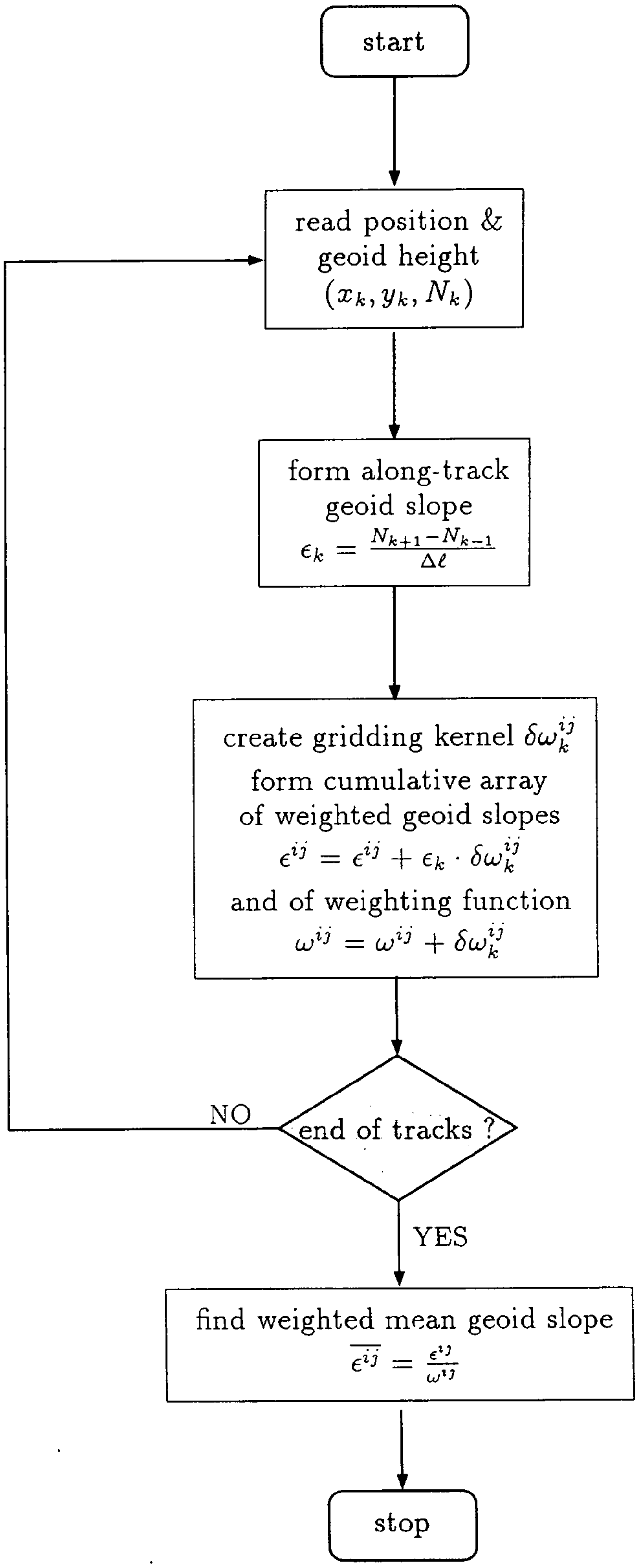

Figure 3.3. Flow diagram for gridding along-track geoid slope.

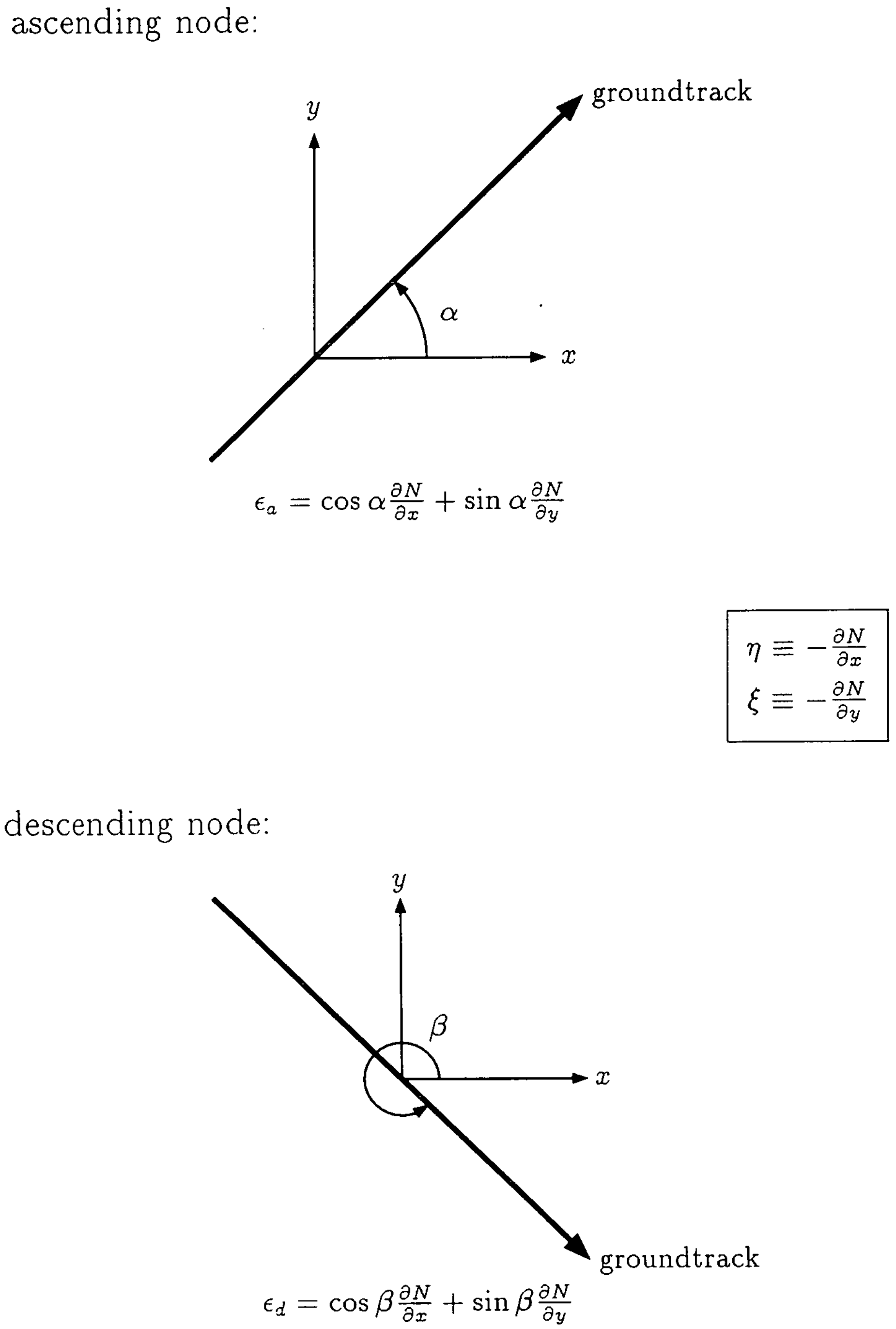

$$\epsilon_a = \cos\alpha\frac{\partial N}{\partial x} + \sin\alpha\frac{\partial N}{\partial y}$$

$$\boxed{\begin{aligned}\eta &\equiv -\frac{\partial N}{\partial x}\\ \xi &\equiv -\frac{\partial N}{\partial y}\end{aligned}}$$

$$\epsilon_d = \cos\beta\frac{\partial N}{\partial x} + \sin\beta\frac{\partial N}{\partial y}$$

Figure 3.4. Determination of east (η) and north (ξ) vertical deflections from the ascending and descending along-track geoid slopes ($\epsilon_{a/d}$).

3.4 Production of the altimeter geoid grid

3.4.1 Production of vertical deflection grids

Grids of ascending and descending along-track geoid slopes from any number of satellite missions may be combined to give one pair of east and north vertical deflection grids, as shown following.

Initially keeping the data from different missions separate, the grids of ascending (ϵ_a) and descending (ϵ_d) along-track geoid slopes are converted to grids of east (η) and north (ξ) vertical deflection (see §1.1). Fig 3.4 shows how a geometrical analysis of the satellite groundtrack on a map projection grid resolves the along-track geoid slope into components of the east and north vertical deflections. We have,

$$\epsilon_a = \cos\alpha\frac{\partial N}{\partial x} + \sin\alpha\frac{\partial N}{\partial y} \tag{3.9}$$

and

$$\epsilon_d = \cos\beta\frac{\partial N}{\partial x} + \sin\beta\frac{\partial N}{\partial y} \quad . \tag{3.10}$$

Rearranging and equating these, and remembering that geoid slope is the negative of vertical deflection (eq.1.11), we obtain equations for the east and north vertical deflections at all grid nodes:

$$-\eta = \frac{1}{\cot\alpha - \cot\beta}\left(\epsilon_a \mathrm{cosec}\,\alpha - \epsilon_d \mathrm{cosec}\,\beta\right) \tag{3.11}$$

and

$$-\xi = \frac{1}{\tan\alpha - \tan\beta}\left(\epsilon_a \sec\alpha - \epsilon_d \sec\beta\right) \quad . \tag{3.12}$$

α and β are the angles made with the positive x-axis by the ascending and descending groundtracks respectively. Since not all gridnodes are intersected by a groundtrack, values of α and β at these nodes may be calculated by bilinear interpolation (*e.g.* UNIRAS).

Now, any number of the vertical deflection grids from different missions may be combined in a weighted linear superposition, using the weighting grids generated by the Witch gridding algorithm, §3.3. Thus, for the east component,

$$\overline{\eta} = \frac{\eta_{topex}\omega_{topex} + \eta_{geosat}\omega_{geosat} + \cdots}{\omega_{topex} + \omega_{geosat} + \cdots} \tag{3.13}$$

and similarly for the north component, giving $\bar{\xi}$. The weighting grid, $\omega_{satellite}$, is obtained by averaging the ascending and descending weights for a particular satellite mission at each grid node.

At this stage, the fields $\bar{\eta}$ and $\bar{\xi}$ may be multiplied by the tapered landmass grid (§2.7). This ensures a smooth roll-off onto land areas from the satellite data over the sea, leaving minimal edge effects upon Fourier transforming, the basis of the next stage.

3.4.2 Production of the gridded geoid

The production of a gridded geoid from east and north vertical deflections uses the Fourier domain approximation of the inverse Vening-Meinesz transformation [McAdoo (1990)]. The forward Vening-Meinesz integrals yield the vertical deflection components from freeair anomalies [Heiskanen and Moritz (1967)]: a Fourier analysis of both forward and inverse transformations shows that they can be written in simple form in the wavenumber domain, using the flat-Earth approximation [Schwarz et al. (1990)]. As already described (§1.3), the subtraction of a long wavelength spherical harmonic model from the data minimizes the errors in assuming a plane representation of Laplace's equation. These errors are also reduced by the transformation of all data to a plane map projection (Appendix A). (See also Appendix D for further techniques for error reduction.)

The calculation of the gravity anomaly or geoid height now involves taking the Fourier transform of the east and north vertical deflections and combining them thus:

$$\widetilde{N} = \frac{i}{|\vec{k}|^2}\left(k_x\tilde{\eta} + k_y\tilde{\xi}\right) \quad , \tag{3.14}$$

[after McAdoo (1990)]. A grid of the freeair anomaly can also be obtained without leaving the wavenumber domain, using eq.1.24.

The production of the gridded freeair anomaly or geoid height from grids of the along-track geoid slope is implemented in the subroutine GS2GRAV.F (Appendix E).

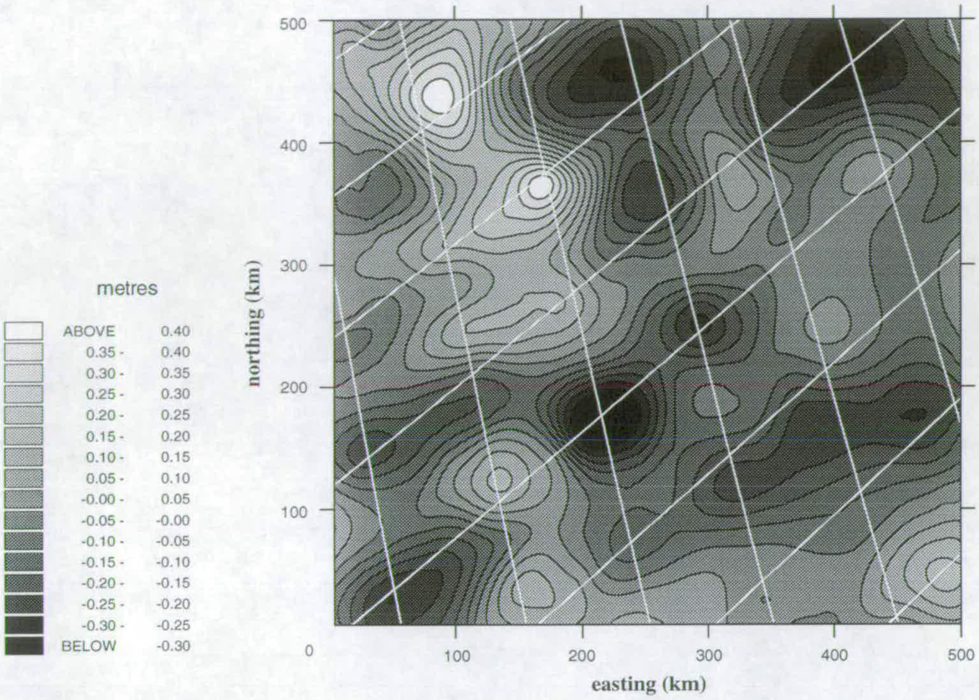

Figure 3.5. Geoid height from the simulated satellite tracks, showing location of simulated groundtracks (*cf* fig 2.6).

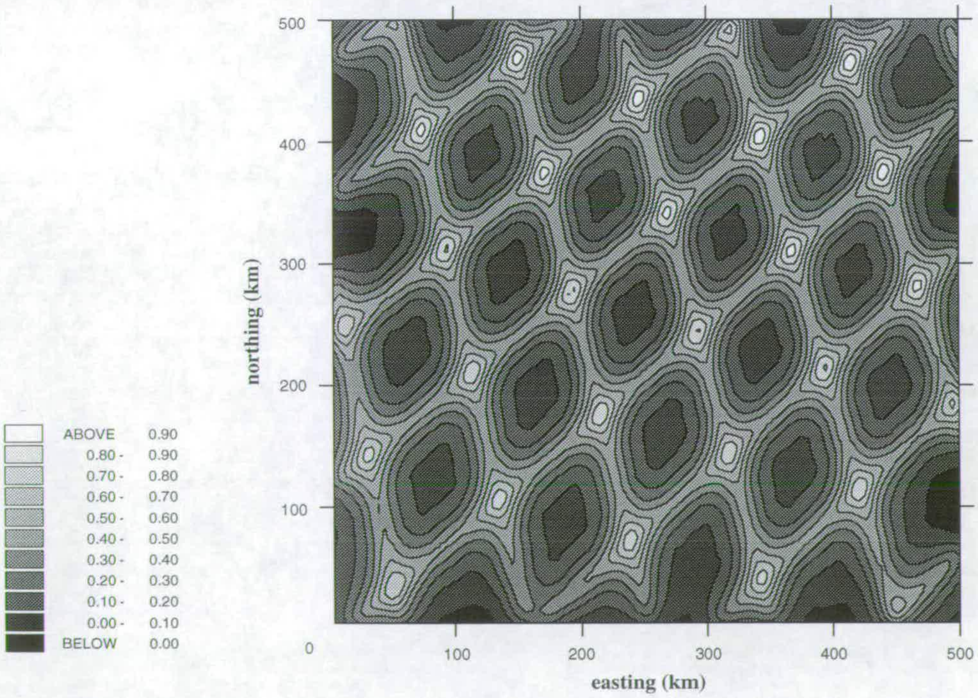

Figure 3.6. Weighting grid from the simulated satellite tracks.

3.5 Results on the test dataset

The algorithm was applied to the test dataset of simulated satellite altimeter readings (§2.8), and the generated models compared with the test models.

3.5.1 The algorithm-generated geoid grid

Fig 3.5 shows the grid of geoid heights generated by the algorithm from the simulated satellite profiles of the test dataset. The mean of these gridded values is -0.0067 m, with a standard deviation (spread) of 0.124 m. The mean of the test model geoid (fig 2.6) is 0.146 m with a standard deviation of 0.184 m, giving a mean difference between the grids of 0.153 m and a difference s.d. of 0.153 m (124% of the computed s.d.). The offset between the two grids is due to the preparation of the data for Fourier transformation: a least-squares plane is fitted to the data and subtracted, removing the residual very long wavelengths which are known to corrupt the Fourier transform.

Comparison of the test model with the generated model shows that while the algorithm has not reproduced the short wavelengths of the test model, the medium wavelength features are present, albeit with reduced amplitude due to the smoothing nature of the kernel (see Appendix C.2), and the method of taking along-track slopes (discussed in §3.1).

Fig 3.6 shows the weighting grid for this dataset.

Considering the freeair anomaly generated by the algorithm (not shown), the mean value of the grid is -0.191 mgal, with a standard deviation of 4.327 mgal. The mean and s.d. of the test model freeair anomaly (fig 2.7) are 0.360 mgal and 10.213 mgal respectively. This indicates a difference s.d. between the two grids of 8.723 mgal, or 202% of the computed grid s.d.

However, a more meaningful comparison of the test and computed fields is provided by studying the two at the satellite groundtrack locations, in the following two sections.

3.5.2 Accuracy of the Witch gridding algorithm

The accuracy of the gridding procedure (§3.3) in mimicking the along-track geoid slopes can be tested by comparing the slopes of the simulated profiles with the values of the slopes interpolated from the resulting grid at the equivalent spatial location. The lower the mean difference and standard deviation, the more accurate the model. Figs 3.7 & 3.8 show the simulated slopes (light curves), plotted against the values interpolated from the generated grid (dark curves), for ascending and descending profiles respectively.

The mean of the computed slopes is 0.375 μrad, that of the slopes of the simulated profiles is 0.357 μrad. The standard deviation of the computed slopes is 4.459 μrad, that of the slopes of the simulated profiles is 7.250 μrad, giving a difference s.d. of 3.582 μrad (80% of the computed s.d.).

Tables 3.1 & 3.2 show the mean differences and standard deviations between each pair of profiles in figs 3.7 & 3.8, (a) to (f). The mean differences are consistently less than 0.1 μrad. The highest standard deviation is 5.472 μrad for profile (c) fig 3.7. The lowest standard deviation is 1.972 μrad for profile (f) fig 3.8.

Interpolation using the Witch gridding algorithm smooths the data somewhat, evident from the profiles in figs 3.7 & 3.8, and from the power spectra in fig 3.11. These spectra are calculated by averaging the power spectra for each of the profiles (a) to (f) in figs 3.7 & 3.8 over discrete wavenumber intervals. It can be seen from fig 3.11 that application of the kernel in interpolation duplicates wavelengths down to approximately 125 km (*i.e.* light and dark curves are approximately coincident up to wavenumber ≈ 0.05 km^{-1}), whereas shorter wavelengths are not as well represented.

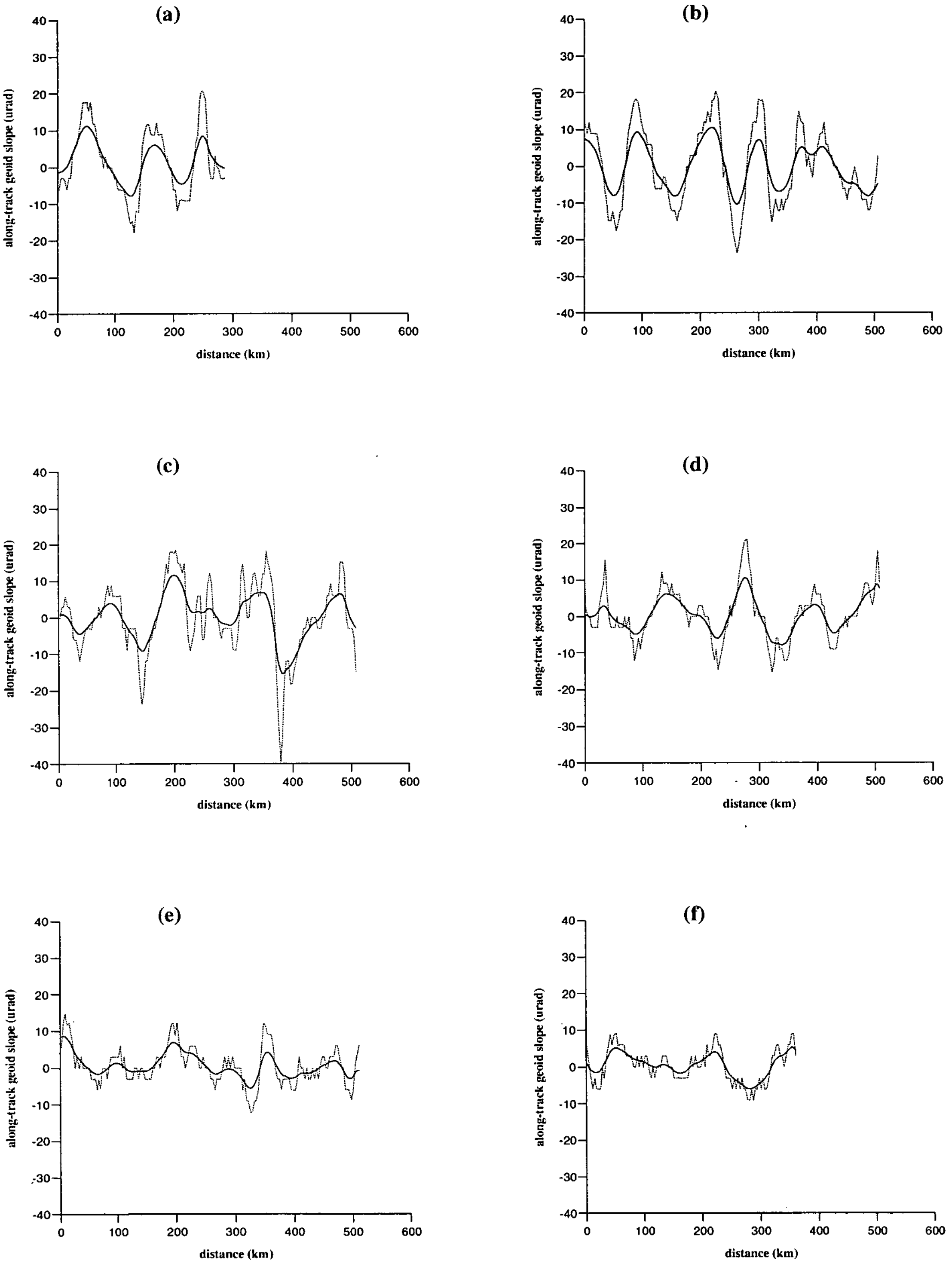

Figure 3.7. Comparison of ascending along-track geoid slopes from simulated satellite tracks (light curves) with values interpolated from the grid of slopes (dark curves). Difference values between the profiles in (a) to (f) shown in table 3.1.

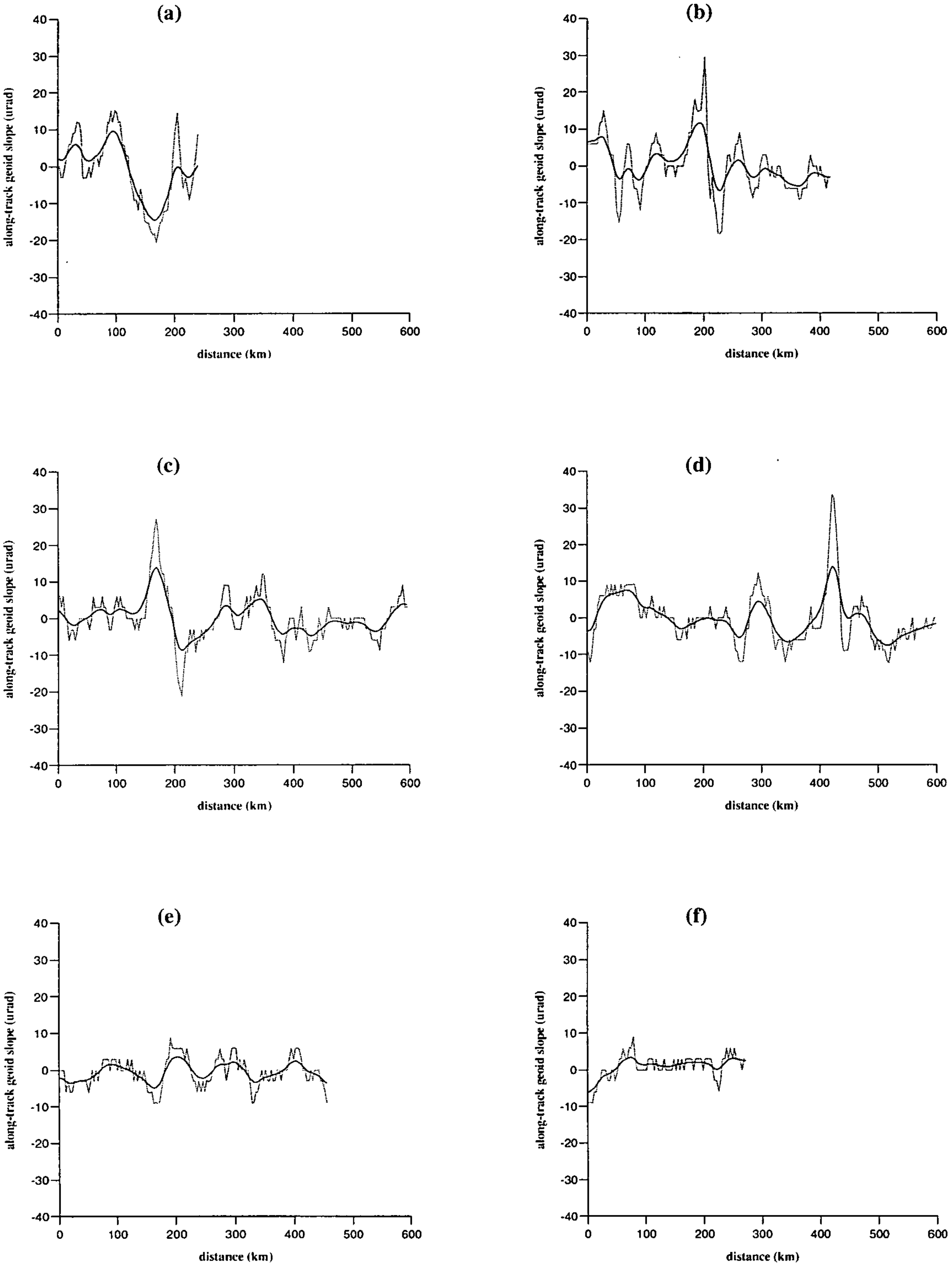

Figure 3.8. Comparison of descending along-track geoid slopes from simulated satellite tracks (light curves) with values interpolated from the grid of slopes (dark curves). Difference values between the profiles in (a) to (f) shown in table 3.2.

Profile	mean difference	standard deviation
(a)	-0.091 μrad	4.796 μrad
(b)	0.068 μrad	5.225 μrad
(c)	-0.031 μrad	5.472 μrad
(d)	0.047 μrad	3.457 μrad
(e)	0.044 μrad	2.922 μrad
(f)	-0.029 μrad	2.302 μrad

Table 3.1. Differences between the simulated and generated slopes in fig 3.7.

Profile	mean difference	standard deviation
(a)	-0.018 μrad	4.221 μrad
(b)	-0.006 μrad	4.563 μrad
(c)	0.023 μrad	3.364 μrad
(d)	-0.028 μrad	3.846 μrad
(e)	-0.013 μrad	2.352 μrad
(f)	-0.049 μrad	1.972 μrad

Table 3.2. Differences between the simulated and generated slopes in fig 3.8.

Profile	mean difference	standard deviation
(a)	0.167 m	0.102 m
(b)	0.070 m	0.097 m
(c)	0.218 m	0.101 m
(d)	0.257 m	0.101 m
(e)	0.106 m	0.124 m
(f)	0.184 m	0.061 m

Table 3.3. Differences between the simulated and generated geoid heights in fig 3.9.

Profile	mean difference	standard deviation
(a)	-0.005 m	0.146 m
(b)	0.209 m	0.076 m
(c)	0.223 m	0.104 m
(d)	0.156 m	0.140 m
(e)	0.170 m	0.088 m
(f)	0.075 m	0.049 m

Table 3.4. Differences between the simulated and generated geoid heights in fig 3.10.

3.5.3 Accuracy of the geoid gridding algorithm

In the same manner as above, the accuracy of the whole algorithm in generating a gridded geoid can be tested by comparing the simulated geoid heights with the values interpolated from the resulting grid, fig 3.5. Figs 3.9 & 3.10 show the comparisons for ascending and descending tracks respectively. The light curves represent the simulated test heights, the dark curves represent the heights interpolated from the resultant grid.

The mean and standard deviation of the computed geoid height profiles are -0.013 m, and 0.139 m respectively (*cf* 0.138 m and 0.188 m respectively for the simulated profiles). Thus, the mean and standard deviation of the differences with the simulated profiles are 0.151 m and 0.130 m (94% of the computed s.d.). This difference standard deviation is of the order of the s.d. of the simulated profiles, suggesting poor accuracy. However, comparisons of the simulated and computed profiles in figs 3.9 & 3.10 show that anomaly locations are preserved, albeit with a reduced amplitude, expected from this method of calculating and gridding the along-track geoid slopes.

Tables 3.3 & 3.4 show the mean differences and standard deviations between each pair of profiles in figs 3.9 & 3.10, (a) to (f). The mean offset between the profiles varies between -0.005 m for profile (a) fig 3.10, and 0.257 m for profile (d) fig 3.9. The mean offsets have a mean value of 0.153 m, evident from a glance at the profiles: with a few exceptions, the simulated profiles consistently have a higher bias than the generated profiles. The highest standard deviation is 0.146m for profile (a) fig 3.10. The lowest standard deviation is 0.049 m for profile (f) fig 3.10.

The power spectra of the simulated profiles and those interpolated from the resultant grid are plotted in fig 3.12. While divergence becomes apparent at wavenumbers larger than approximately 0.05 km^{-1}, as in fig 3.11, the magnitude of this difference is not as marked as that for the spectra of the along-track slopes. This large difference in the spectra in fig 3.11 is mainly due though to the relatively high power of the simulated slopes (light curve) at short wavelengths.

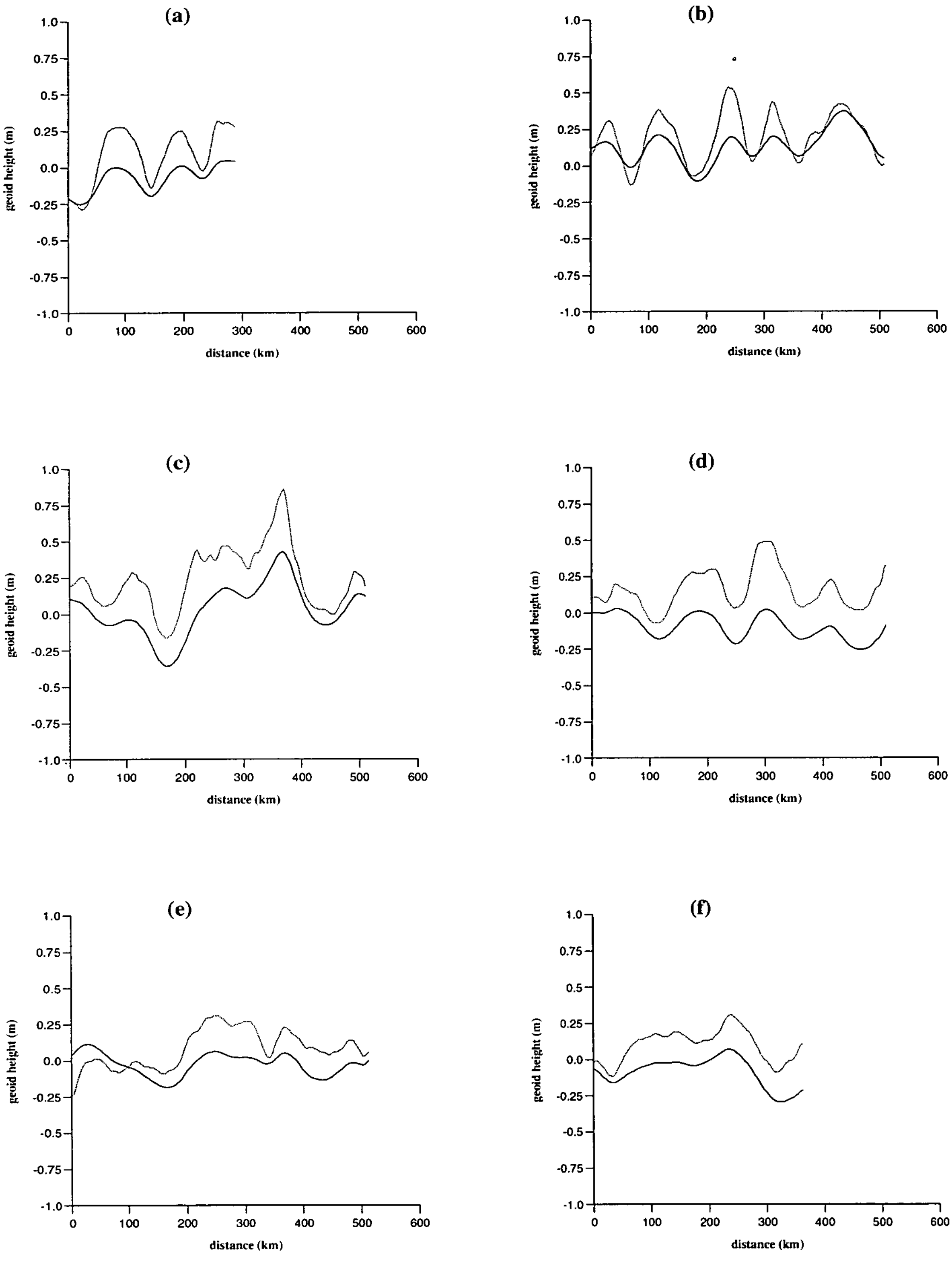

Figure 3.9. Comparison of the ascending simulated satellite tracks (light curves) with values interpolated from the generated grid, fig 3.5, (dark curves). Difference values between the profiles in (a) to (f) shown in table 3.3.

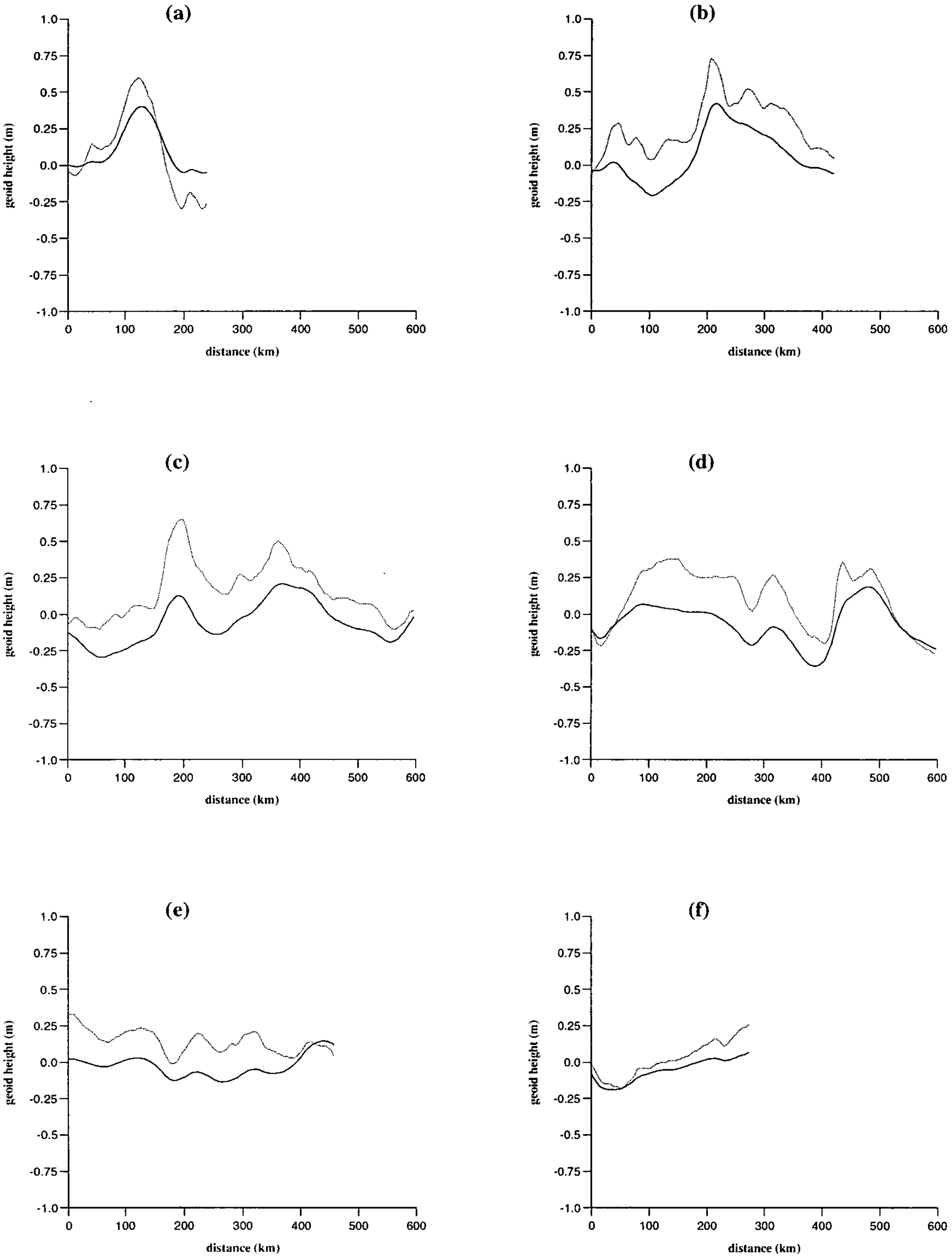

Figure 3.10. Comparison of the descending simulated satellite tracks (light curves) with values interpolated from the generated grid, fig 3.5, (dark curves). Difference values between the profiles in (a) to (f) shown in table 3.4.

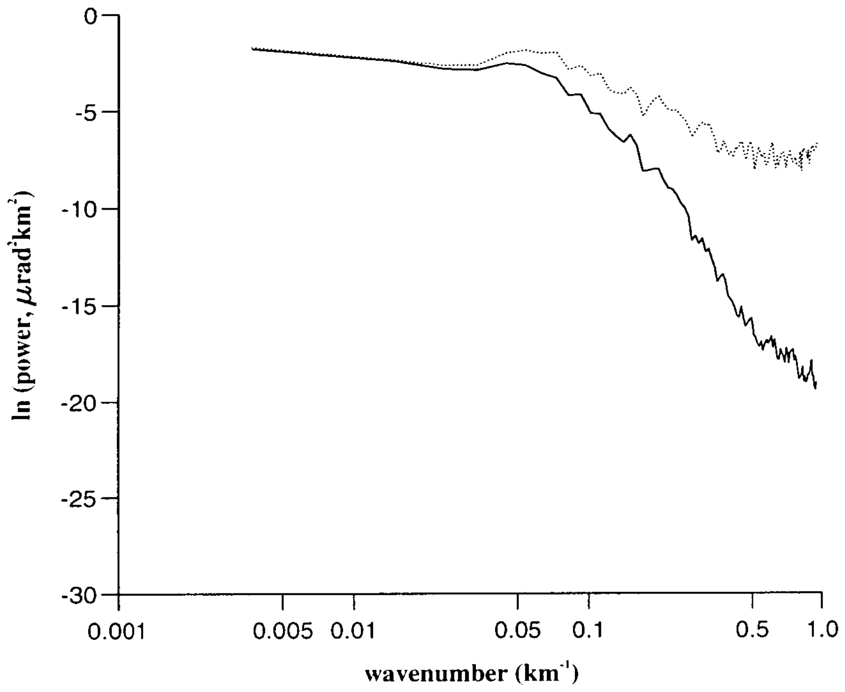

Figure 3.11. Power spectra of the simulated (light curve) & interpolated slopes (dark curve) in figs 3.7 & 3.8.

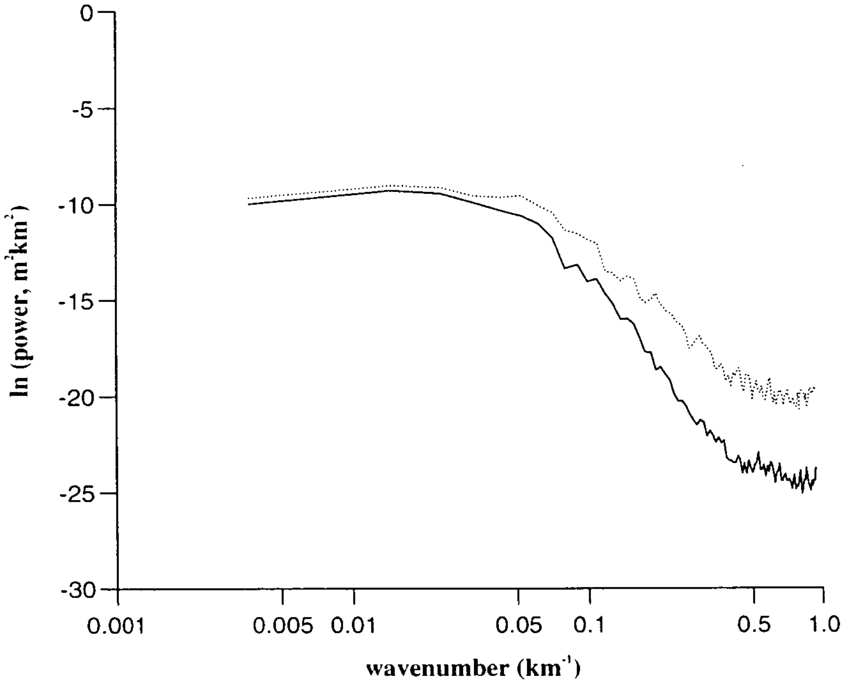

Figure 3.12. Power spectra of the simulated (light curve) & interpolated geoid height profiles (dark curve) in figs 3.9 & 3.10.

3.6 Results on the North Atlantic data

Fig 3.13 shows the gridded geoid height relative to the OSU91A geoid for the North Atlantic area, generated from the Geosat/ERM and Topex/Poseidon altimeter data. Fig 3.14 shows the equivalent freeair anomaly, again relative to the OSU91A freeair anomaly. A comparison with the combined field will be made in §5.5, with the features discussed in Chapter 6.

These grids are produced from Geosat/ERM along-track geoid slopes gridded using a kernel of maximum search radius 80 km, and Topex/Poseidon slopes gridded with a kernel of 150 km maximum search radius. The wavelength resolution of the geoid height grid is defined in Appendix C.2. At 47° N, the Geosat resolution is 49 km, and the Topex/Poseidon resolution is 92 km. At higher latitudes the groundtrack convergence increases the resolution of the geoid grid: the Geosat resolution at 72° N is 12 km, and the Topex/Poseidon resolution at 66° N is 27 km.

The overall accuracy of the gridded geoid in fig 3.13 can be estimated by comparing the along-track geoid slopes of the altimeter profiles with the corresponding slope values interpolated from the geoid grid at the equivalent spatial location. This removes the effect of orbit error, yielding a more reliable assessment of the error than would a comparison of geoid heights.

The mean value of the Geosat/ERM slopes (ascending and descending) is -0.20 μrad; their standard deviation is 10.66 μrad. The mean value of the computed slopes at the Geosat/ERM groundtrack locations is 0.006 μrad, with a standard deviation of 5.86 μrad. This gives a difference s.d. of 6.95 μrad, or 119% of the computed slope s.d.

The mean value of the Topex/Poseidon slopes (ascending and descending) is 0.044 μrad; their standard deviation is 9.13 μrad. The mean value of the computed slopes at the Topex/Poseidon groundtrack locations is 0.084 μrad, with a standard deviation of 3.99 μrad. This gives a difference s.d. of 6.75 μrad, or 169% of the computed slope s.d.

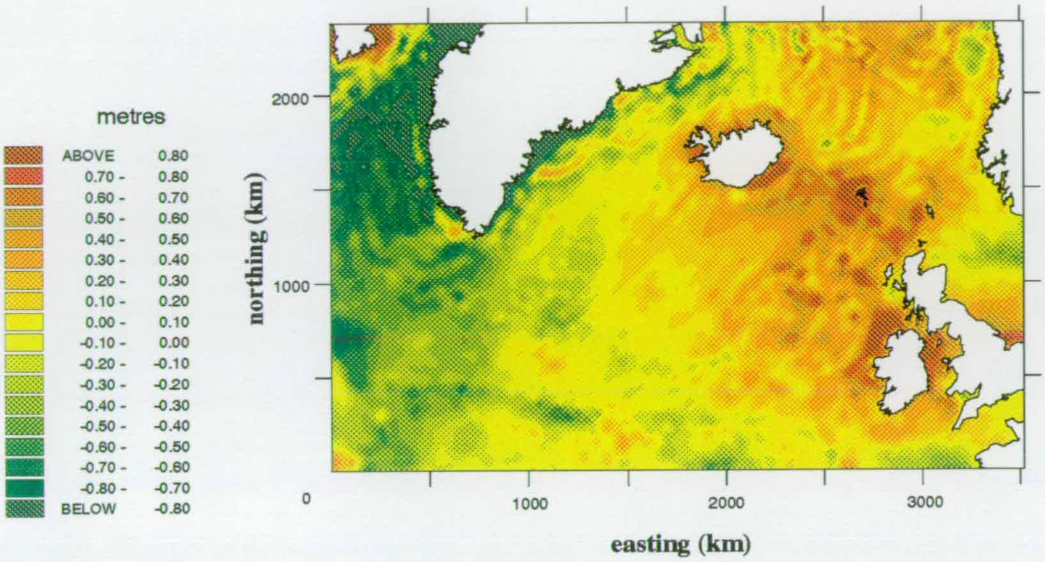

Figure 3.13. Atlantic geoid height from Geosat/ERM and Topex/Poseidon data, relative to the OSU91A geoid.

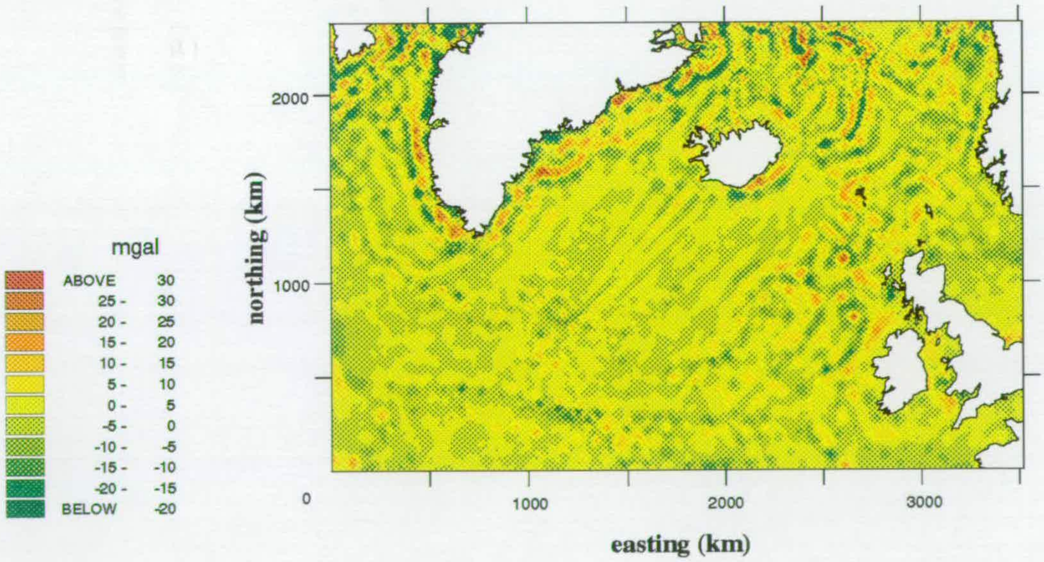

Figure 3.14. Atlantic freeair anomaly from Geosat/ERM and Topex/Poseidon data, relative to the OSU91A freeair anomaly.

Chapter 4

Gridding Marine & Land Gravity Data

4.1 Introduction

Large datum shifts are commonly present in compilations of marine gravity data due to the accumulation of gravity meter drift at points far from coastal base stations. These errors can be over 4 mgal in some older surveys [Armstrong (1978)]. They are conventionally reduced by a network analysis to minimise cross-over errors, a process which is computationally demanding. A new method for the gridding of marine freeair anomalies is presented here which removes the need for network adjustment.

The effect of the uncertain datum is reduced by taking along-track gravity gradients. However, due to a random directionality in the ship tracks, the method described in Chapter 3 for gridding satellite data cannot be used. Instead, the freeair field derived from altimetry measurements is introduced to constrain the shipboard observations. With satellite coverage now extending to ±82° latitude, only the polar regions of the Earth will be unmappable using this technique.

The algorithm assigns a value of gravity to the three gridnodes nearest to the ship observation point, based upon the local amplitude of the observations, the long wavelength mean of the altimetry gravity field, and the cross-track gradient of this altimetry field. This yields a grid of freeair anomalies containing both marine and satellite observations, and a corresponding grid of ship data weights. In contrast to the grid of altimeter measurements, it is not necessary for the grid of surface marine observations to be complete, due to the nature of the

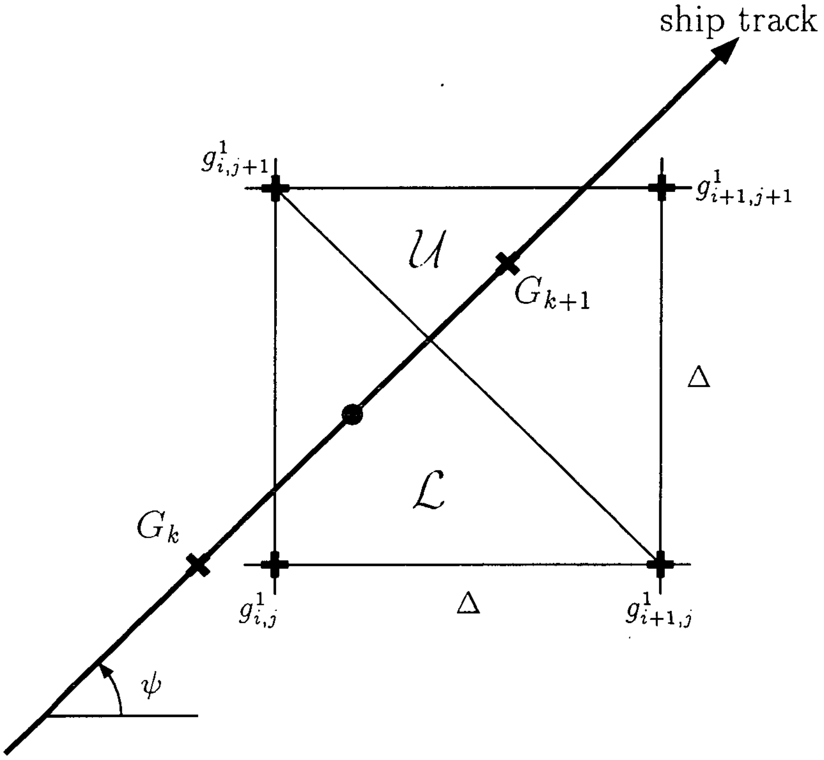

Figure 4.1. Gridding ship-track gravity data.

combination algorithm discussed in the next chapter. This obviates the difficulty in creating such a grid in areas of sparse ship coverage.

The gridding of land gravity data is more straightforward and is discussed in §4.3.

4.2 Gridding marine gravity data

Interpolation of the ship track gravity data onto a grid is a two-stage process. In the first stage, the observations are gridded, while in the second, the Witch gridding kernel is employed. The algorithm is coded in subroutine SHIPGRID.F (Appendix E).

4.2.1 Interpolation onto a grid

The marine gravity data must be available as point observations in chronological sequence as (x_k, y_k, G_k), with any gaps in the tracks larger than 10 km indicating the start of a new track. The gridding algorithm uses these point freeair anomalies together with the gridded altimetric freeair grid $g^0_{i,j}$, to estimate the new freeair grid including ship data, $g^1_{i,j}$.

Consider the situation in fig 4.1, with two consecutive ship observations G_k and G_{k+1} separated by a distance $\Delta\ell$. The interpolated grid has a cell size of Δ in both east (x) and north (y) directions. The angle between the positive x-axis and the ship track is ψ, with

$$\cos\psi = \frac{x_{k+1} - x_k}{\Delta\ell} \qquad \sin\psi = \frac{y_{k+1} - y_k}{\Delta\ell} \quad .$$

Take the case where the midpoint between the two observations (marked by a •) falls in the lower triangle ($\mathcal{L}$), and define the quantities:

- mean ship gravity at midpoint:

$$\overline{G} = \frac{1}{2}(G_{k+1} + G_k) \tag{4.1}$$

- along-track ship gravity gradient at midpoint:

$$\frac{\partial G}{\partial \ell} = \frac{G_{k+1} - G_k}{\Delta\ell} \tag{4.2}$$

- along-track gridded gravity gradient (n=0 or 1):

$$\frac{\partial g^n}{\partial \ell} \approx \left(\frac{g^n_{i+1,j} - g^n_{i,j}}{\Delta}\right)\cos\psi + \left(\frac{g^n_{i,j+1} - g^n_{i,j}}{\Delta}\right)\sin\psi \tag{4.3}$$

- cross-track gridded gravity gradient (n=0 or 1):

$$\frac{\partial g^n}{\partial c} \approx -\left(\frac{g^n_{i+1,j} - g^n_{i,j}}{\Delta}\right)\sin\psi + \left(\frac{g^n_{i,j+1} - g^n_{i,j}}{\Delta}\right)\cos\psi \quad . \tag{4.4}$$

The vector $\vec{\ell}$ has the direction of the part of the ship track between points k and $k+1$. The vector $\vec{c}$ is the cross-track vector perpendicular to $\vec{\ell}$.

In order to determine updated gravity estimates at the three grid points nearest to the midpoint ($g^1_{i,j}$, $g^1_{i+1,j}$, and $g^1_{i,j+1}$), three constraints are needed.

1. (Initially) preserve mean value of ship gravity data:

$$\overline{g^1} \equiv \frac{1}{3}\left(g^1_{i,j} + g^1_{i+1,j} + g^1_{i,j+1}\right) \approx \overline{G} \tag{4.5}$$

   This is only an approximation as the mean value of the new grid, $\overline{g^1}$, should of course be weighted by the position of the • relative to the three grid nodes.

   At the end of each ship track, the overall mean of all the amended $g^1_{i,j}$ values is adjusted to be the same as the overall mean of the same $g^0_{i,j}$ values, thereby preserving the *long wavelength* gravity mean of the gravity field derived from satellite altimetry.

2. Preserve along-track ship gravity gradient:

$$\frac{\partial g^1}{\partial \ell} = \frac{\partial G}{\partial \ell} \tag{4.6}$$

3. Preserve cross track altimetry gravity gradient:

$$\frac{\partial g^1}{\partial c} = \frac{\partial g^0}{\partial c} \tag{4.7}$$

These constraints are in effect three simultaneous equations enabling the unknowns, $g^1_{i,j}$, $g^1_{i+1,j}$, and $g^1_{i,j+1}$ to be determined. Substitute eq.4.3 into *constraint 2* (eq.4.6):

$$\Delta\frac{\partial G}{\partial \ell} = (g^1_{i+1,j} - g^1_{i,j})\cos\psi + (g^1_{i,j+1} - g^1_{i,j})\sin\psi \quad . \tag{4.8}$$

Substitute eq.4.4 into *constraint 3* (eq.4.7):

$$\Delta\frac{\partial g^0}{\partial c} = -(g^1_{i+1,j} - g^1_{i,j})\sin\psi + (g^1_{i,j+1} - g^1_{i,j})\cos\psi \quad . \tag{4.9}$$

Substituting $g^1_{i,j}$ from *constraint 1* (eq.4.5) into eq.4.8, gives

$$\Delta\frac{\partial G}{\partial \ell} = (2g^1_{i+1,j} + g^1_{i,j+1} - 3\overline{G})\cos\psi + (2g^1_{i,j+1} + g^1_{i+1,j} - 3\overline{G})\sin\psi \tag{4.10}$$

or, rearranging

$$\Delta\frac{\partial G}{\partial \ell} + 3\overline{G}(\cos\psi + \sin\psi) = (2\cos\psi + \sin\psi)g^1_{i+1,j} + (2\sin\psi + \cos\psi)g^1_{i,j+1} \quad . \tag{4.11}$$

Substituting $g^1_{i,j}$ from *constraint 1* (eq.4.5) into eq.4.9, gives

$$\Delta\frac{\partial g^0}{\partial c} = -(2g^1_{i+1,j} + g^1_{i,j+1} - 3\overline{G})\sin\psi + (2g^1_{i,j+1} + g^1_{i+1,j} - 3\overline{G})\cos\psi \qquad (4.12)$$

or, upon rearranging

$$\Delta\frac{\partial g^0}{\partial c} + 3\overline{G}(\cos\psi - \sin\psi) = (\cos\psi - 2\sin\psi)g^1_{i+1,j} + (2\cos\psi - \sin\psi)g^1_{i,j+1} \quad . \qquad (4.13)$$

Now multiply eq.4.11 by $(2\cos\psi - \sin\psi)$ and subtract from this eq.4.13 multiplied by $(2\sin\psi + \cos\psi)$. This simplifies to

$$g^1_{i+1,j} = \overline{G} + \frac{\Delta}{3}\frac{\partial G}{\partial \ell}(2\cos\psi - \sin\psi) - \frac{\Delta}{3}\frac{\partial g^0}{\partial c}(2\sin\psi + \cos\psi) \quad . \qquad (4.14)$$

Similarly, if eq.4.13 is multiplied by $(2\cos\psi + \sin\psi)$ and subtracted from eq.4.11 multiplied by $(\cos\psi - 2\sin\psi)$, the result simplifies to

$$g^1_{i,j+1} = \overline{G} + \frac{\Delta}{3}\frac{\partial G}{\partial \ell}(2\sin\psi - \cos\psi) + \frac{\Delta}{3}\frac{\partial g^0}{\partial c}(2\cos\psi + \sin\psi) \quad . \qquad (4.15)$$

Finally, an expression may be derived for $g^1_{i,j}$ by using eqs 4.14, 4.15, and *constraint 1* (eq.4.5):

$$g^1_{i,j} = \overline{G} - \frac{\Delta}{3}\frac{\partial G}{\partial \ell}(\cos\psi + \sin\psi) - \frac{\Delta}{3}\frac{\partial g^0}{\partial c}(\cos\psi - \sin\psi) \quad . \qquad (4.16)$$

However, if the midpoint falls in the upper triangle ($\mathcal{U}$ in fig 4.1), while the philosophy of the three constraints remains the same, the three nearest gridnodes are now $(i, j+1)$, $(i+1, j)$, and $(i+1, j+1)$, so new solutions must be derived, albeit using the same algebraic technique. These solutions are

$$g^1_{i+1,j+1} = \overline{G} + \frac{\Delta}{3}\frac{\partial G}{\partial \ell}(\cos\psi + \sin\psi) + \frac{\Delta}{3}\frac{\partial g^0}{\partial c}(\cos\psi - \sin\psi) \quad , \qquad (4.17)$$

$$g^1_{i+1,j} = \overline{G} + \frac{\Delta}{3}\frac{\partial G}{\partial \ell}(\cos\psi - 2\sin\psi) - \frac{\Delta}{3}\frac{\partial g^0}{\partial c}(2\cos\psi + \sin\psi) \quad , \qquad (4.18)$$

$$g^1_{i,j+1} = \overline{G} - \frac{\Delta}{3}\frac{\partial G}{\partial \ell}(2\cos\psi - \sin\psi) + \frac{\Delta}{3}\frac{\partial g^0}{\partial c}(\cos\psi + 2\sin\psi) \quad . \qquad (4.19)$$

In summary, depending on the position of the midpoint between two adjacent observations on a ship track, eqs 4.14, 4.15 and 4.16, or eqs 4.17, 4.18 and 4.19 are used to interpolate the marine freeair anomaly observations onto a regular grid.

However, *constraint 1* states that initially the two-point mean of the ship measurements ($\overline{G}$) must be used in the interpolation to retain *local* amplitude changes in the measured gravity field. But, to remove the uncertainty in the datum of shipboard measurements, at the end of a single ship track the gridnodes just amended must be adjusted to have the same overall mean as the corresponding nodes on the altimeter freeair anomaly field. This preserves the long wavelength gravity mean, more accurately known from the satellite field.

4.2.2 Using the gridding kernel

The gridding kernel introduced in §3.2 may be used on the interpolated grid values to spread their influence further, and also to generate of a grid of relative weights. However it is not necessary in this instance to have the latitude dependence that is necessary for gridding satellite data, as the ship track separation obviously does not have this dependence.

The kernel, then, has the form

$$\delta\omega(x) = \frac{1}{1+(\frac{x}{a_o})^2} \qquad |x| \leq R_o \quad . \tag{4.20}$$

It is applied in turn to each of the gridnodes affected by the interpolation procedure in the previous subsection, rather than to the original ship data; x is therefore the distance between one of these affected gridnodes and the gridnodes within the search radius of the kernel, R_o. The relationship between halfwidth, a_o, and search radius is the same as for the satellite data kernel, eq.3.7,

$$a_o = Q \cdot R_o \qquad \text{with} \qquad Q = 0.175 \quad . \tag{4.21}$$

For a search radius of 20 km, this gives a halfwidth of 3.5 km. These values were used for all ship data on this 5 km grid.

A grid of weights was produced simultaneously, but in contrast to the satellite procedure, these cumulative weights were not normalized by the maximum recorded weight, thus giving the weights an unlimited range. This places a bias towards the marine data in the combination algorithm, which is discussed in §5.2.

4.3 Gridding land gravity data

Gravity data collected on land may also be gridded by use of the Witch gridding kernel. Land gravity surveys are usually better constrained than their marine counterparts.

The available data can be edited by removal of obvious "spikes" in the freeair anomaly values, and then interpolated directly onto a grid, using the kernel in eq.4.20. This is applied to each of the observations, using a search radius that takes into account the mean station density over the area: gaps in the resultant grid are acceptable, so the search radius, R_o, should be approximately equal to half the mean station separation, but no greater than 30 km. The ratio of halfwidth to search radius, Q, is the same as for satellite and ship data, eqs 3.7 & 4.21.

The gridding procedure is then carried out as in §3.2, with the freeair gravity anomaly, Δg, replacing z in eq.3.2. A grid of weights is also generated, to be used in the combination algorithm (Chapter 5). As with the marine data, this grid of weights is not normalized by the maximum weight, lending more influence to the land data over areas where both land and altimeter data are available (for example, when the gridding kernel has extended land measurements over the coast).

The result of applying the gridding kernel to freeair anomaly data over Iceland is shown in fig 4.2. The kernel search radius was 20 km. The same data gridded using a UNIMAP bilinear interpolation routine are shown in fig 4.3. The data distribution is shown in fig 4.4. Given that the UNIMAP routine will interpolate into areas with no data measurements, the two maps are very similar. Moreover, and equally important, the Witch gridding algorithm generates a grid of weights for use in the combination algorithm.

The spectral characteristics of this gridding procedure are analysed in Appendix C.4, through the study of the transfer function.

The algorithm to grid land gravity data is coded in the subroutine LANDGRID.F (Appendix E).

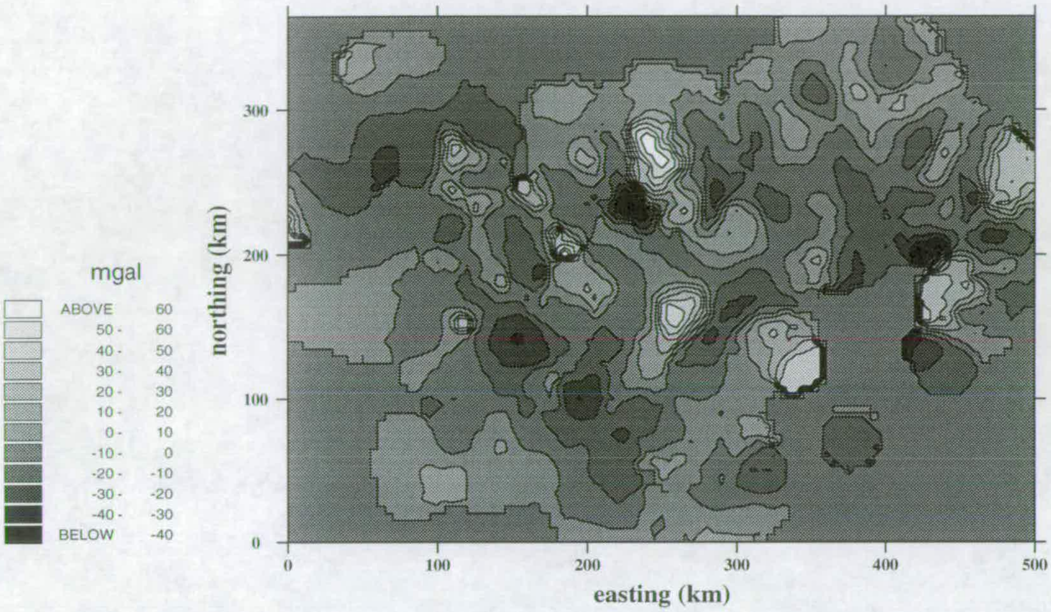

Figure 4.2. Freeair anomaly data over Iceland, gridded using the Witch kernel with a search radius of 20 km.

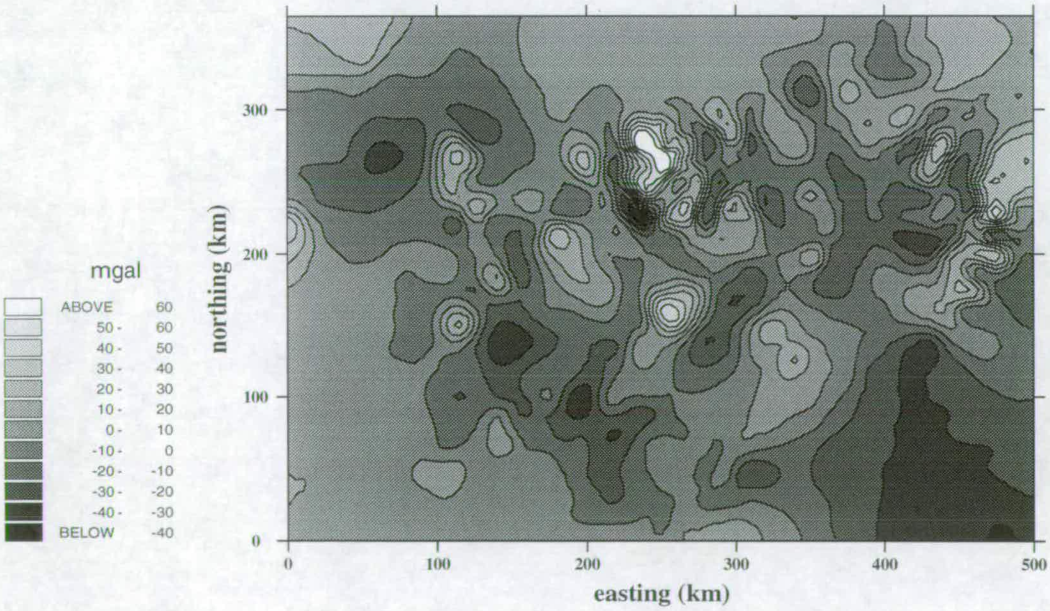

Figure 4.3. Freeair anomaly data over Iceland, gridded using UNIMAP bilinear interpolation.

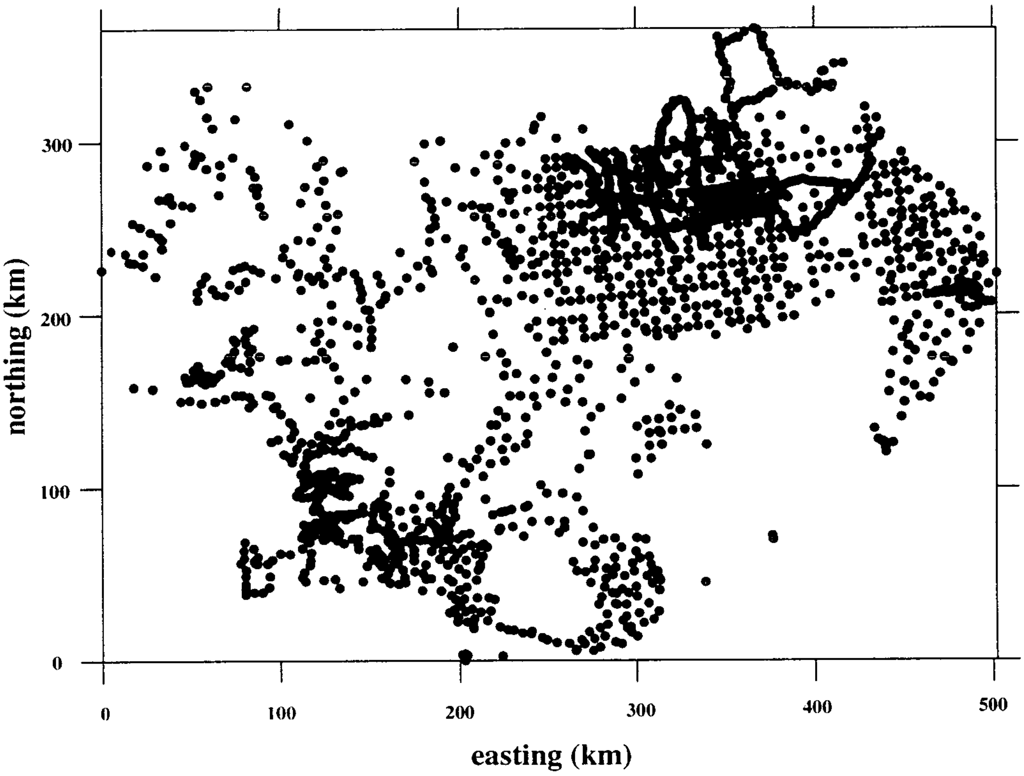

Figure 4.4. Location of freeair anomaly data in Iceland.

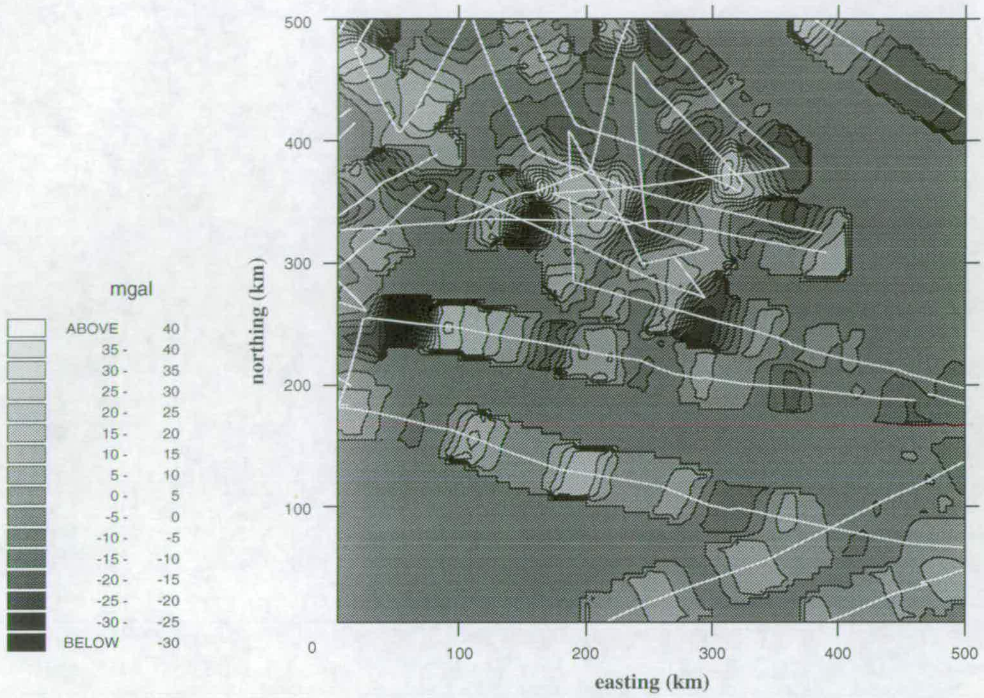

Figure 4.5. Freeair anomaly from the simulated ship tracks.

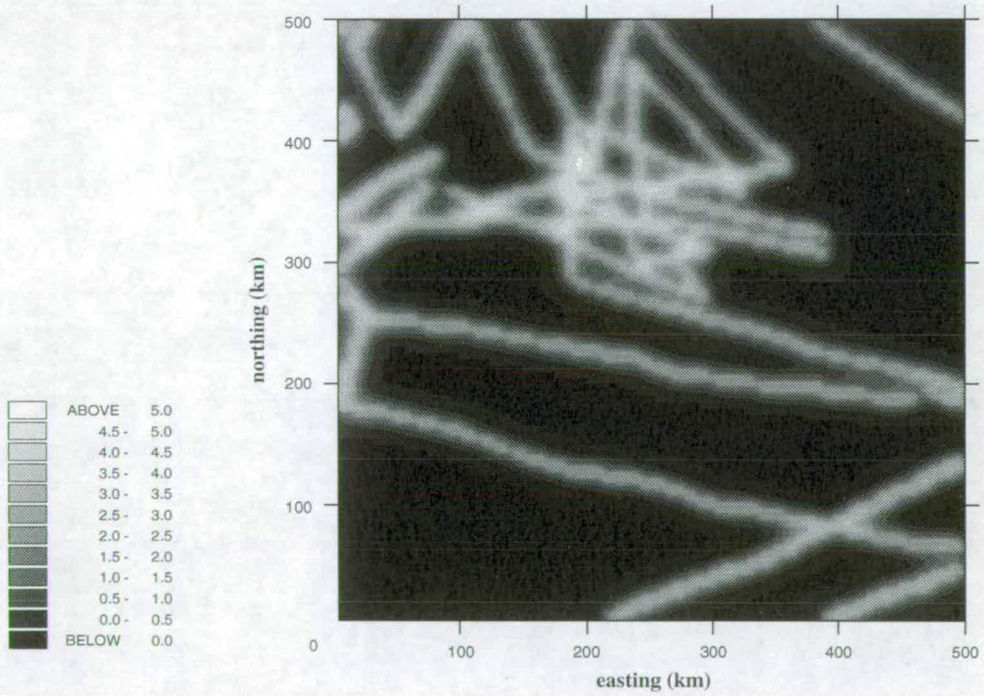

Figure 4.6. Weighting grid from the simulated ship tracks.

4.4 Results on the test dataset

Fig 4.5 shows the freeair anomaly as calculated by the gridding algorithm from the simulated ship gravity data, §2.8. Fig 4.6 shows the accompanying weighting grid. Note the absence of assigned grid values in the areas where no tracks are present.

The accuracy of the algorithm in reproducing the original along-track data can be assessed by comparing the simulated freeair anomaly profiles with values interpolated from the generated grid at the equivalent spatial location. The mean value and standard deviation of the simulated ship tracks are 2.878 mgal and 11.848 mgal respectively. The mean value and standard deviation of the computed profiles are 0.134 mgal and 9.876 mgal respectively. Thus, the mean difference between the ship data and the computed values is 2.744 mgal with a difference s.d. of 4.065 mgal (41% of the computed profile s.d.). As a comparison, profiles computed from the satellite-only freeair anomaly have a mean value of 0.182 mgal, and a standard deviation of 4.959 mgal, giving a difference s.d. of 10.500 mgal (212% of the satellite-only computed profile s.d.).

Fig 4.7 shows comparisons for six profiles, the light curves representing the simulated profiles, the dark curves representing the values interpolated from the grid in fig 4.5. Table 4.1 lists the mean differences and standard deviations between the two profiles in each of (a) to (f), fig 4.7. The mean offset between the profile pairs varies between -0.716 mgal for profile (e), and 3.214 mgal for profiles (c) and (d). The mean offsets have a mean value of 2.010 mgal. The highest standard deviation is 4.626 mgal for profile (d), the lowest is 0.887 mgal for profile (f).

An observation of the profiles reveals very good agreement between the generated values and the originals. The amplitudes are slightly reduced, but most of the short wavelength features, and certainly those of longer wavelength, are reproduced accurately in both position and shape.

Profile	mean difference	standard deviation
(a)	2.400 mgal	1.164 mgal
(b)	2.286 mgal	2.518 mgal
(c)	3.214 mgal	3.302 mgal
(d)	3.214 mgal	4.626 mgal
(e)	-0.716 mgal	4.117 mgal
(f)	1.667 mgal	0.887 mgal

Table 4.1. Differences between the simulated and generated freeair anomalies in fig 4.7.

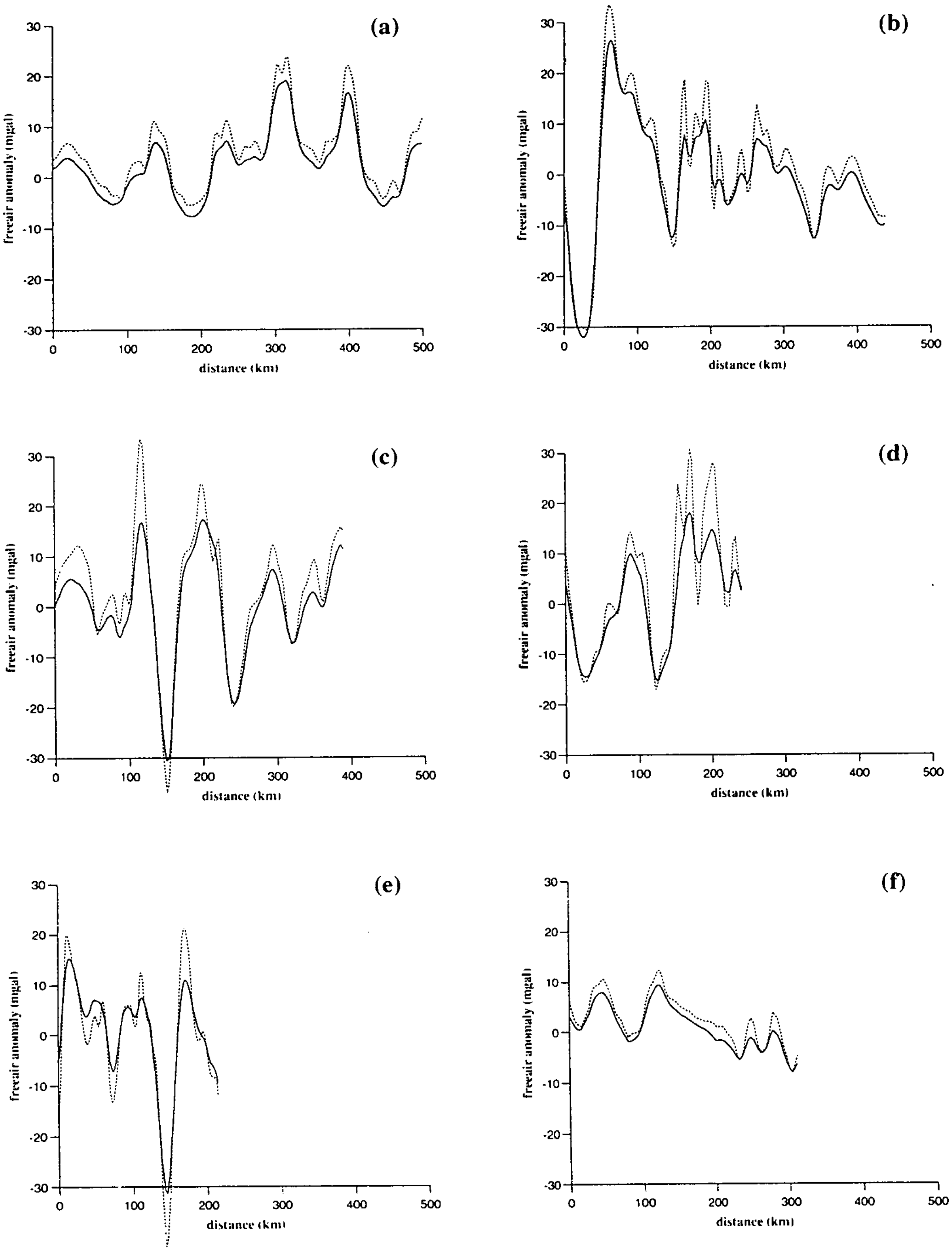

Figure 4.7. Comparison of simulated ship tracks (dashed curves) with values interpolated from the generated grid, fig 4.5, (solid curves). Difference values between the profiles in (a) to (f) shown in table 4.1.

Chapter 5

Combination of the Heterogeneous Datasets

5.1 Introduction

This chapter presents a new method for the combination of heterogeneous gravity datasets, improving upon existing methods in having a much reduced computation time. The algorithm makes use of the wavenumber domain relationship between geoid height, freeair anomaly, and other derivatives of the gravity field (§1.2.2), and can thus employ the fast Fourier transform (FFT) to carry out a rapid conversion between these various forms of gravity data.

A method extensively used today to combine heterogeneous gravity data is Least Squares Collocation (LSC). A study by Hwang and Parsons (1995) combined altimeter data with ship gravity data, generating a field with an average accuracy of 5.76 mgal. However, LSC is notoriously costly in CPU time. To combine N data points, a matrix of size $N \times N$ must be inverted; "inversions of this size obviously present time problems even on a supercomputer and results will suffer from round-off errors" [Schwarz et al. (1990)].

Proponents of the LSC method claim that the Fourier method is not easily adapted to include more than one type of potential field data [Hwang and Parsons (1995)]. It will be demonstrated here that this is not the case, and that the accuracy of the combined field is comparable to one generated by LSC. Furthermore, this method uses relatively little CPU time and memory, and can be easily implemented on a PC, on board an exploration ship for example. (CPU times for various runs of the algorithm are given in Appendix E.)

In the presented algorithm (which has been given the name IFC , for Iterative Fourier Combination), a provisional gravity model is created, and each different dataset integrated by means of a weighted superposition followed by the FFT conversion. The procedure is then iterated until the provisional model shows stability. Data arrays generated by any gridding algorithm may be used, but the gridding methods introduced in Chapters 3 and 4 have the advantage of additionally generating the grid of weights required in the combination.

5.2 The weighting grids

The IFC routine requires not only a grid of gravity values, but also a grid of weights for the dataset. This grid should reflect the relative influence which the corresponding gridnode on the gravity grid has in the dataset combination. This depends upon the distance of the node from the actual observation points. Due to the smooth topology of the Witch gridding kernel that generates the weighting grids, the grids themselves are smooth. This reduces the ringing effect of the Gibbs' phenomenon during wavenumber-domain operations.

The satellite data weighting grid is not used in the combination stage. This is because the field generated by the satellite gridding algorithm (Chapter 3) was generated using the relative weights, and thus already has this information included. Furthermore, as the satellite-only fields contain predominantly longer wavelength information, their values are deemed representative of the long wavelength gravity field at all marine locations. This field is then enhanced using the ship and land gravity data.

The ship data weighting grid is not required to be complete. The freeair anomaly generated from satellite data is used as the template in the IFC routine, to which the ship data is added. It would also be unreasonable to generate a complete ship grid in areas where only one ship track passes through many hundreds of square kilometres. As mentioned in §4.2.2, the ship data weights are not normalized by the maximum weight. This gives a bias towards this dataset in the combination with the satellite field, which will hopefully lead to a better refinement of the gravity field.

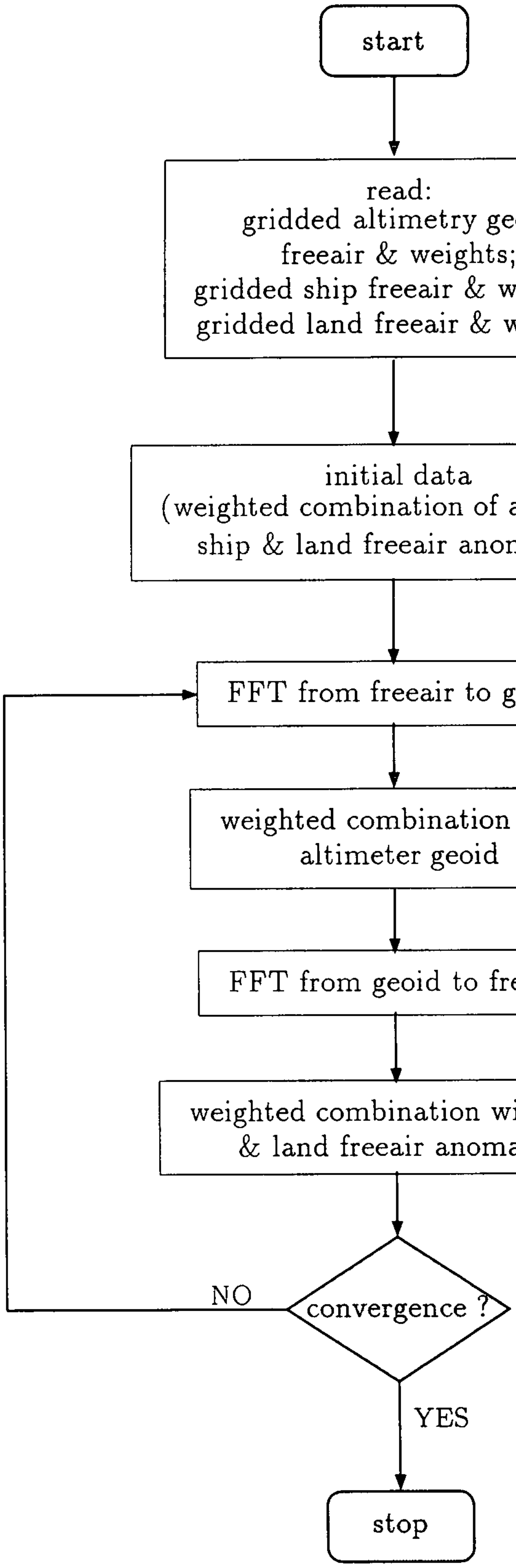

Figure 5.1. Flow diagram for the IFC routine, combining altimeter & surface data.

5.3 The combination procedure

The IFC algorithm creates a provisional gravity field model, h_*, which is improved upon in successive iterations of a weighted superposition with grids of geoid or freeair anomaly measurements. While h always represents the provisional model, the $*$ indicates whether the current model is geoid (g) or freeair anomaly (f), and also the iteration number in the algorithm. For example, h_{g2} indicates that the current provisional model is a geoid height field in the second iteration of the combination algorithm.

The datasets considered here are the geoid and freeair anomaly grids generated by the satellite data gridding algorithm, N_{sat} and Δg_{sat} respectively (§3.4); the incomplete grid of shipboard freeair anomaly measurements, Δg_{ship}, and the associated weighting grid, ω_{ship} (§4.2.2); and the gridded land gravity dataset, Δg_{land}, and its grid of weights, ω_{land} (§4.3).

The first step in the combination routine is to create a complete grid of freeair anomalies, the provisional freeair model, h_{f1}:

$$h_{f1} = \frac{\omega_{sea}\Delta g_{sat} + \omega_{ship}\Delta g_{ship} + \omega_{land}\Delta g_{land}}{\omega_{sea} + \omega_{ship} + \omega_{land}} \quad , \tag{5.1}$$

where ω_{sea} is the tapered landmass grid (§2.7). This provisional model now has no data gaps, which could generate edge effects through the Gibbs' phenomenon, and so can be converted to a grid of geoid heights, h_{g2}, using the FFT operation introduced in §1.2.2, eq.1.24:

$$h_{g2} = \mathcal{F}^{-1}\left\{\widetilde{h_{f1}}/\gamma k\right\} \quad , \tag{5.2}$$

where γ is the mean value of the normal gravity field over the grid, and k the magnitude of wavenumber (see §1.2.2). This new provisional model is then combined with the satellite-derived geoid height grid, N_{sat}, to give an updated provisional geoid model, h'_{g2}:

$$h'_{g2} = \frac{1}{2}(h_{g2} + N_{sat}) \quad . \tag{5.3}$$

This provisional geoid model is then converted back to a freeair anomaly,

$$h_{f3} = \mathcal{F}^{-1}\left\{\widetilde{h'_{g2}} \cdot \gamma k\right\} \tag{5.4}$$

and a weighted superposition carried out with the original land and shipboard freeair gravity grids:

$$h'_{f3} = \frac{h_{f3} + \omega_{ship}\Delta g_{ship} + \omega_{land}\Delta g_{land}}{1 + \omega_{ship} + \omega_{land}} \quad . \tag{5.5}$$

This procedure, from eqs 5.2 to 5.5, can be iterated any number of times, with h'_{f3} replacing h_{f1} in eq.5.2, and so on until the provisional model, h_*, stabilises. Stabilisation occurs at the iteration count when the RMS difference between successive 'like' provisional models (*e.g.* the RMS of $h'_{f3}-h_{f1}$, or $h'_{g4}-h'_{g2}$) reaches a previously specified value, indicating convergence. Figure 5.1 is a flow diagram illustrating the combination procedure.

The major source of error in tests of the IFC algorithm lay in the divergence of successive provisional models. This divergence was found primarily to be due to errors occuring during FFT operations; these errors, and procedures to reduce them are discussed in Appendix D.

5.4 Results on the test dataset

The algorithm to combine the satellite, ship and land gravity grids is coded in subroutine IFC.F (Appendix E).

Grids

Fig 5.2 shows the geoid height created by combining the grids generated from the simulated satellite altimeter data and the simulated ship gravity data. Convergence to less than 1 cm was obtained after only 3 iterations of the IFC algortithm. Fig 5.4 shows the RMS difference between successive provisional geoid models in the IFC procedure, with an RMS difference at 24 iterations of 6×10^{-8} m.

Comparing IFC model with the test model geoid, fig 5.3, good agreement is seen in areas where ship tracks are at their most dense, the short wavelength features being successfully reproduced. Even in areas with sparse ship data, the IFC geoid shows an improvement over the altimeter-only solution.

The mean of the IFC model is 0.004 m with a standard deviation (spread) of 0.143 m (*cf* the mean and s.d. of the test model geoid are 0.146 m and 0.184 m respectively). This gives a mean difference of 0.142 m, with a difference s.d. of 0.149 m (103% of the computed grid s.d.). This represents a marginal improvement upon the 124% difference for the satellite-only solution (§3.5.1), but is still of the order of the spread of the test model values.

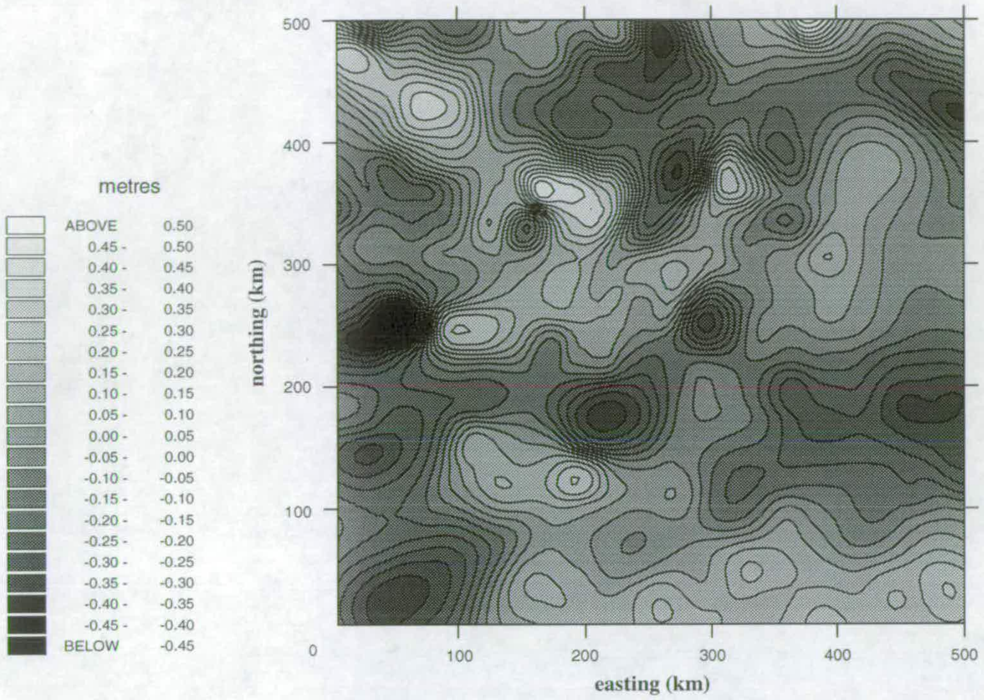

Figure 5.2. Geoid height from the simulated satellite and ship data.

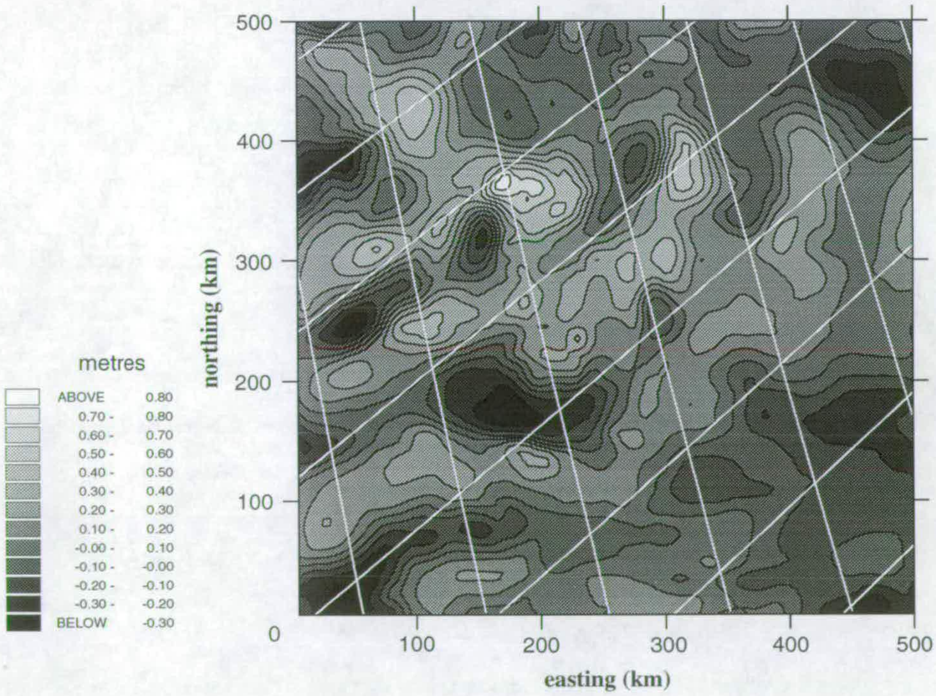

Figure 5.3. The test model geoid height showing simulated satellite ground-tracks.

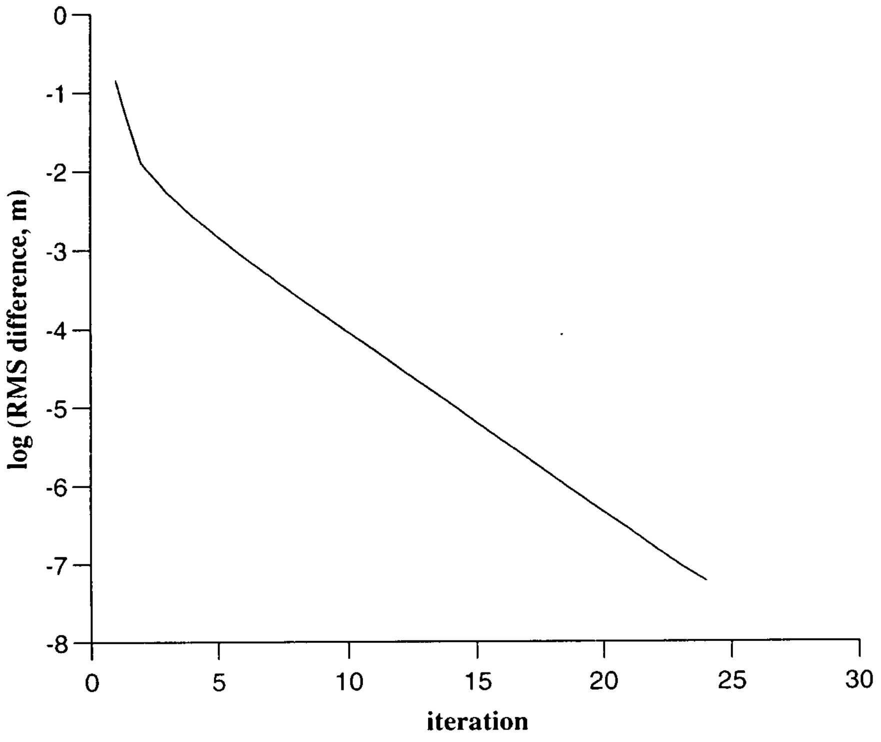

Figure 5.4. The logarithm of the RMS difference between successive provisional geoid models in the IFC procedure.

Comparing the IFC freeair anomaly, fig 5.5, with the test model freeair anomaly, fig 5.6, shows the ability of the algorithm to reproduce the very short wavelength information in the data, geoid maps predominantly highlighting the medium to long wavelength anomalies. Again, in areas with no shipboard measurements, the short wavelength features are not resolved, the model relying on any satellite information present. In areas with a high density of ship tracks though, these short wavelength anomalies have been successfully resolved, in equivalent locations and with a comparable amplitude.

The mean value of the IFC freeair anomaly is -0.050 mgal, with a standard deviation of 6.157 mgal (*cf* the mean and s.d. of the test model freeair anomaly are 0.360 mgal and 10.213 mgal respectively). This gives a mean difference of 0.410 mgal, with a difference s.d. of 7.309 mgal (119% of the computed grid s.d.). This does indicate some degree of improvement upon the satellite-only freeair anomaly, where the difference s.d. formed 202% of the computed grid s.d. (§3.5.1).

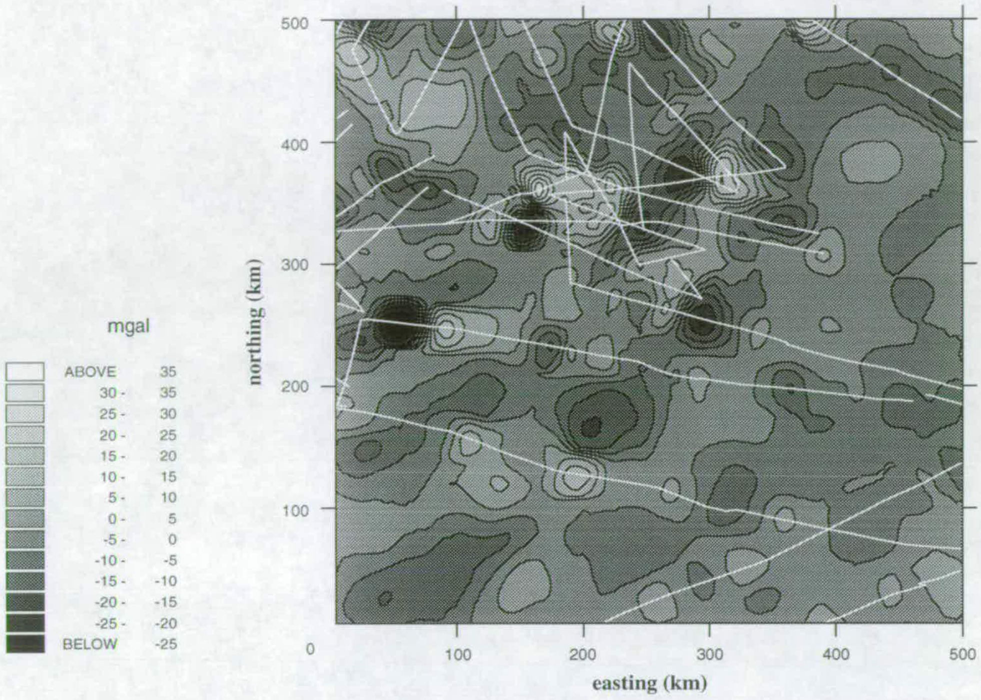

Figure 5.5. Freeair anomaly from the simulated satellite and ship data, showing location of ship tracks.

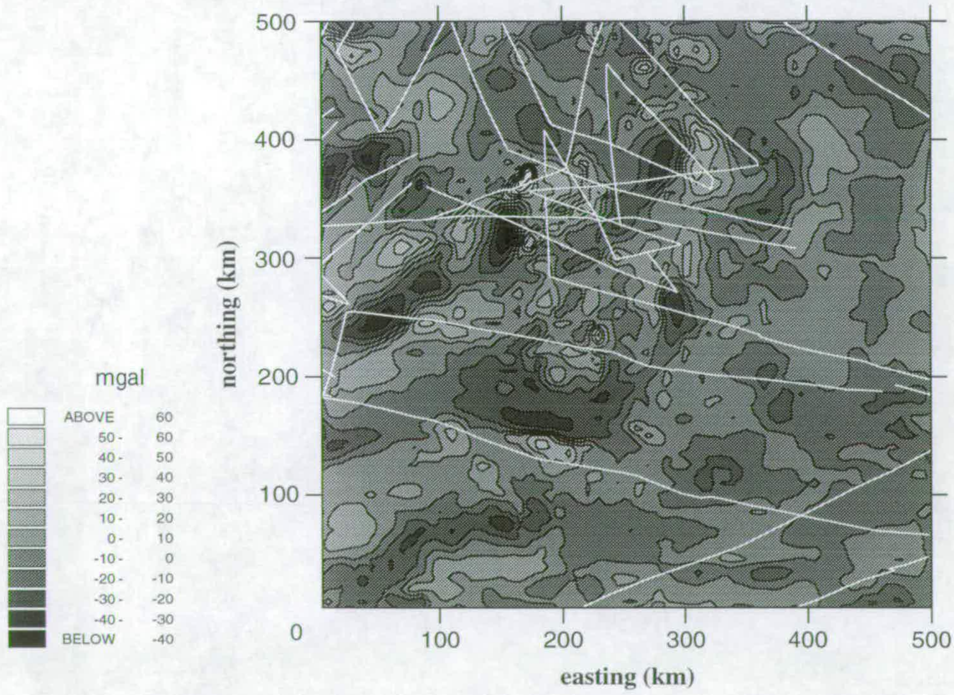

Figure 5.6. The test model freeair anomaly showing simulated ship tracks.

Profiles

The profiles in figs 5.7 & 5.8 show the simulated ascending and descending satellite track geoid heights respectively (light curves), plotted with the geoid height interpolated from the IFC model, fig 5.2. This indicates how well the gridding and combination algorithms have reproduced the original simulated data.

The mean and standard deviation of the computed geoid height profiles are -0.0029 m and 0.155 m respectively (*cf* 0.138 m and 0.188 m respectively for the simulated profiles). Thus, the mean and standard deviation of the differences with the simulated profiles are 0.141 m and 0.139 m (90% of the computed s.d.). This actually shows almost no improvement upon the satellite-only computed profiles, where the difference s.d. formed 94%; however a visual comparison of the profiles in figs 3.9 & 3.10, with figs 5.7 & 5.8 does show an improvement in anomaly location and amplitude, even though the computed profiles do not exactly mimic the simulated profiles. This improvement will be due to the inclusion of ship gravity data.

Tables 5.1 and 5.2 show the mean differences and standard deviations between the profile pairs in each plot. The mean offset between the profile pairs varies between 0.024 m for profile (a) fig 5.8, and 0.303 m for profile (b) fig 5.8. The highest standard deviation is 0.153 m for profile (a) fig 5.8. The lowest standard deviation is 0.060 m for profile (f) fig 5.8.

As mentioned in §3.5.1, this mean offset between the two datasets is due to the preparation of the data for Fourier transformation: a least squares plane is removed giving the data a zero mean.

The profiles in fig 5.9 show six of the longest simulated ship track freeair anomaly profiles (light curves), plotted against the profiles interpolated from the IFC freeair anomaly model (dark curves), fig 5.5.

The mean and standard deviation of the computed ship gravity profiles are 0.379 mgal and 8.992 mgal respectively (*cf* 2.878 mgal and 11.848 mgal for the simulated profiles). This gives the mean and standard deviation of the difference profiles as 2.499 mgal and 4.536 mgal (forming 50% of the computed s.d.). As a comparison, profiles computed from the satellite-only freeair anomaly have a mean value of 0.182 mgal, and a standard deviation of 4.959 mgal, giving a difference s.d. of 10.500 mgal (212% of the satellite-only computed profile s.d.). This shows that inclusion of the ship data has improved the computed gravity fields without adversely affecting the contribution from the satellite data. This accuracy of 4.536 mgal also compares favourably with the accuracy of 5.76 mgal quoted for the LSC method [Hwang and Parsons (1995)].

Table 5.3 shows the mean differences and standard deviations between the profile pairs in each plot. The mean offset between the profile pairs varies between -0.990 mgal for profile (e), and 2.863 mgal for profile (c). The mean offsets have a mean value of 1.698 mgal. The highest standard deviation is 5.428 mgal for profile (d), and the lowest is 1.180 mgal for profile (f).

The new algorithm could not reproduce the resolution of the real gravity field in regions with no observational data, but it very significantly improved the representation compared with the satellite only model in those regions with even sparse ship track coverage.

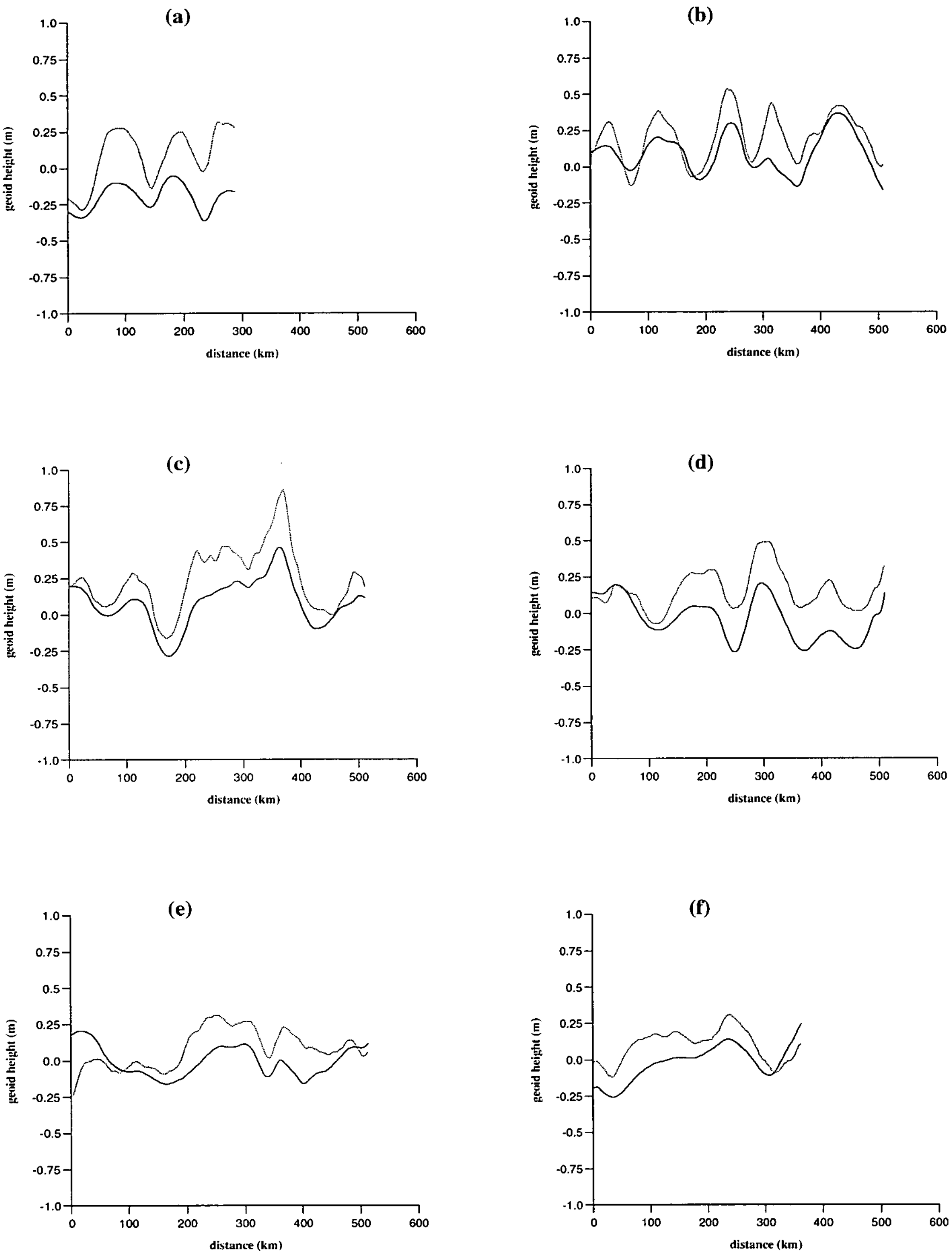

Figure 5.7. Comparison of the ascending simulated satellite tracks (light curves) with values interpolated from the IFC geoid grid, fig 5.2, (dark curves). Difference values between the profiles in (a) to (f) shown in table 5.1.

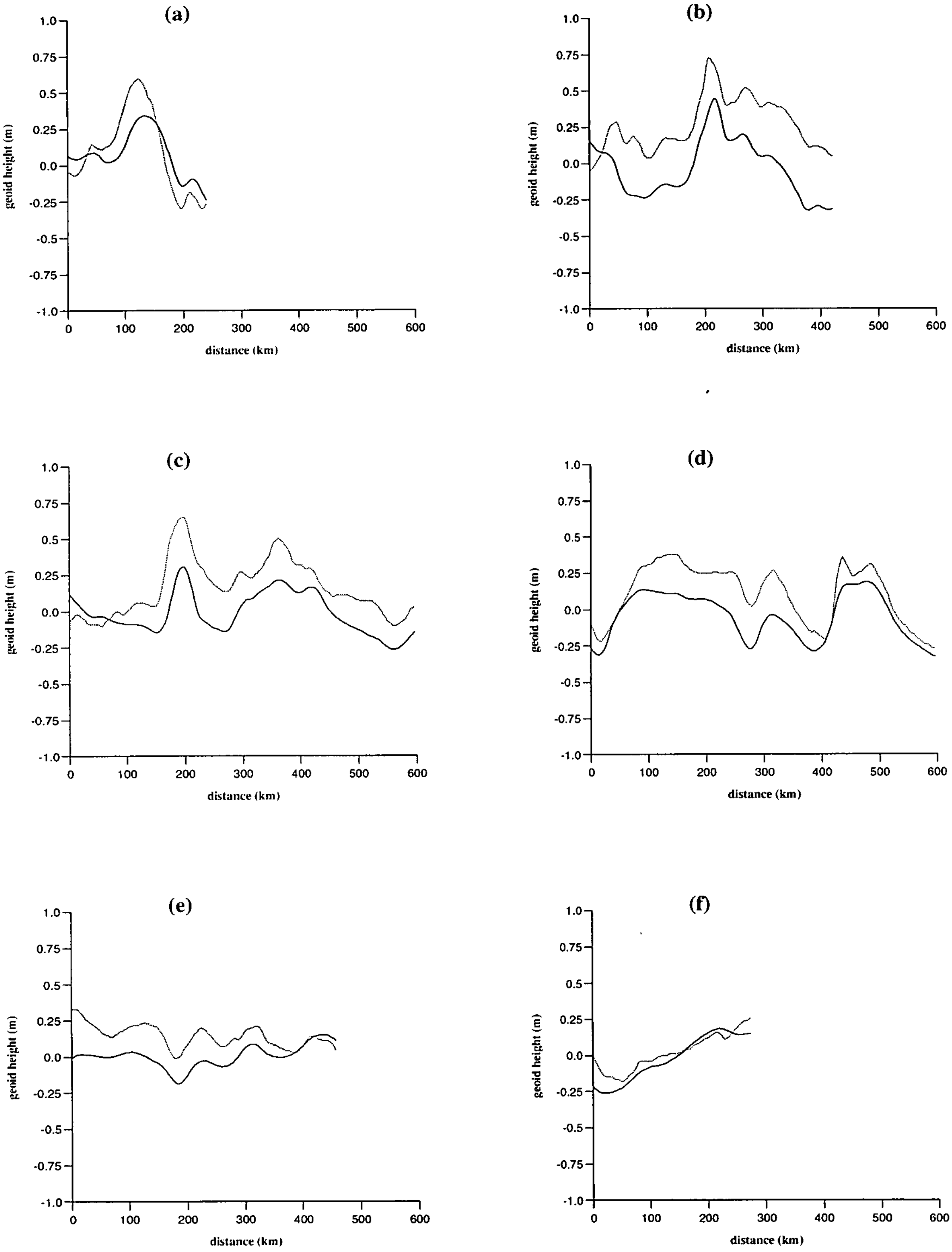

Figure 5.8. Comparison of the descending simulated satellite tracks (light curves) with values interpolated from the IFC geoid grid, fig 5.2, (dark curves). Difference values between the profiles in (a) to (f) shown in table 5.2.

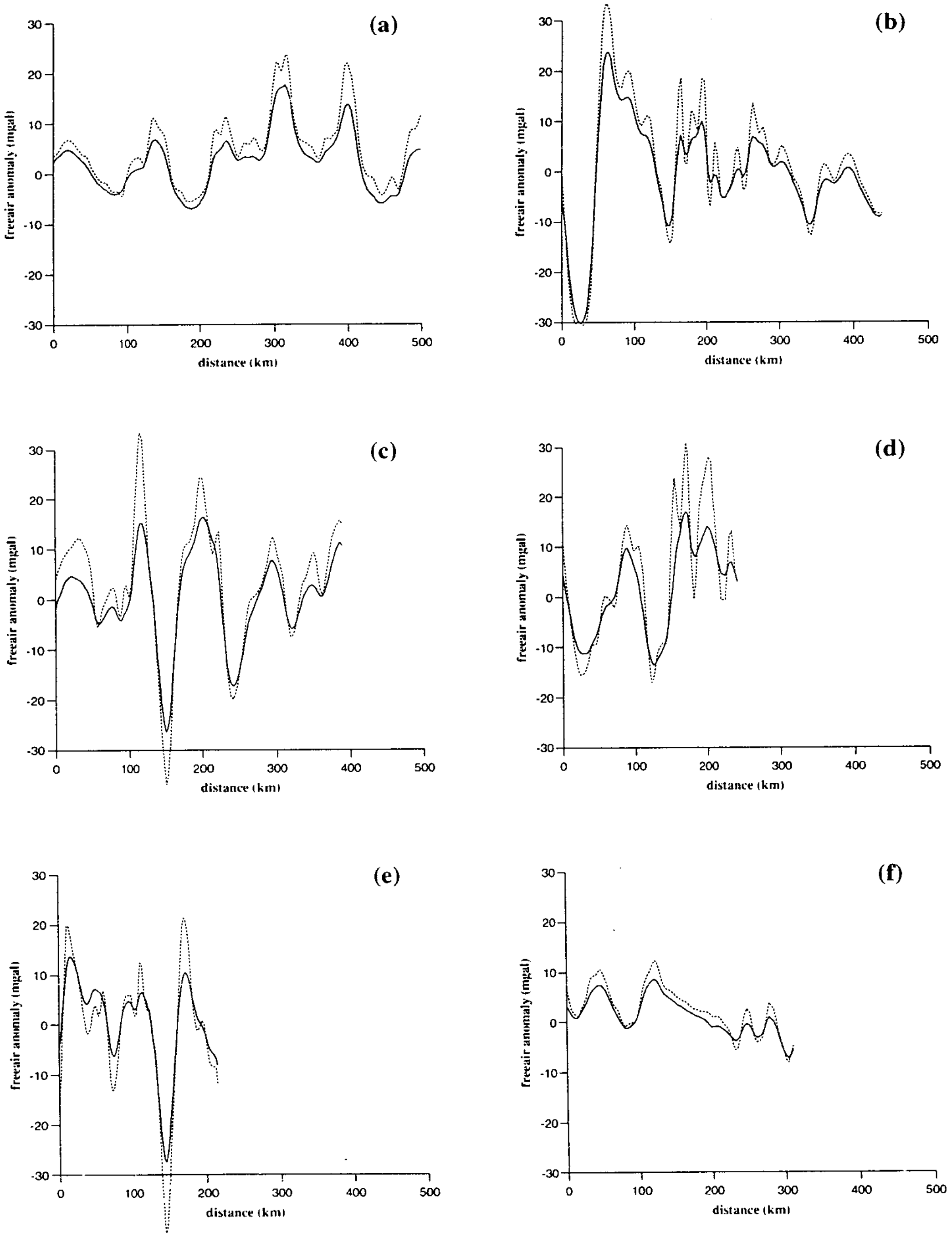

Figure 5.9. Comparison of simulated ship tracks (dashed curves) with values interpolated from the IFC freeair grid, fig 5.5, (solid curves). Difference values between the profiles in (a) to (f) shown in table 5.3.

Profile	mean difference	standard deviation
(a)	0.289 m	0.129 m
(b)	0.108 m	0.101 m
(c)	0.165 m	0.093 m
(d)	0.198 m	0.117 m
(e)	0.086 m	0.146 m
(f)	0.121 m	0.095 m

Table 5.1. Differences between the simulated satellite and IFC geoid height profiles in fig 5.7.

Profile	mean difference	standard deviation
(a)	0.024 m	0.153 m
(b)	0.303 m	0.129 m
(c)	0.176 m	0.122 m
(d)	0.146 m	0.098 m
(e)	0.141 m	0.091 m
(f)	0.041 m	0.060 m

Table 5.2. Differences between the simulated satellite and IFC geoid height profiles in fig 5.8.

Profile	mean difference	standard deviation
(a)	2.545 mgal	1.804 mgal
(b)	1.929 mgal	3.139 mgal
(c)	2.863 mgal	4.142 mgal
(d)	2.570 mgal	5.428 mgal
(e)	-0.990 mgal	4.823 mgal
(f)	1.270 mgal	1.180 mgal

Table 5.3. Differences between the simulated ship and IFC freeair anomaly profiles in fig 5.9.

5.5 Results on the North Atlantic data

Fig 5.10 shows the gridded geoid height relative to the OSU91A geoid for the North Atlantic area, generated from the altimeter, shipboard and terrestrial gravity measurements. Fig 5.11 shows the equivalent freeair anomaly. Both fields were obtained after two iterations of the IFC routine.

A visual comparison of the satellite-only (fig 3.13) and IFC geoids, shows immediately that inclusion of the ship track gravity data has improved the resolution of the marine geoid, and that the available land gravity data has been combined without discontinuities at the coastlines. The improvement is largely in the short wavelength features, though the longer wavelengths in the altimeter geoid have been altered too. A spectral comparison of the satellite-only and IFC freeair anomaly fields is shown in fig 5.12.

The short wavelength features stand out more in the freeair anomaly maps. Compare the altimeter-only freeair anomaly (fig 3.14) with the IFC field. The tectonic features will be identified and described in the next chapter, but it is evident that the signatures of the Reykjanes Ridge (southwest from Iceland) and the fracture zones south of this are much clearer in the IFC field. It is possible to see ship tracks in the IFC freeair anomaly. However these are only prominent in areas of low track density, such as around coordinates (1500,200) km (see fig 2.3). This is expected, especially if the shipboard gravity reading is very different from the altimeter-only field in the region. In areas with a high density of ship tracks, such as the seas off the north, east and south coasts of Iceland, individual ship tracks are not visible, and the gravity field has been greatly improved.

As in §3.6, the overall accuracy of the gridded geoid in fig 5.10 can be estimated by comparing the along-track geoid slopes of the altimeter data with the corresponding slope values interpolated from the geoid grid at the equivalent spatial location. The mean value of the Geosat/ERM slopes (ascending and descending) is -0.20 μrad; their standard deviation is 10.66 μrad. The mean value of the computed slopes at the Geosat/ERM groundtrack locations is 0.03 μrad, with a standard deviation of 6.47 μrad. This gives a difference s.d. of 6.81 μrad, or 105% of the computed slope s.d. The mean value of the Topex/Poseidon slopes (ascending and descending) is 0.044 μrad; their standard deviation is 9.13 μrad. The mean value of the computed slopes at the Topex/Poseidon groundtrack locations is -0.16 μrad, with a standard deviation of 5.33 μrad. This gives a difference s.d. of 6.56 μrad, or 123% of the computed slope s.d.

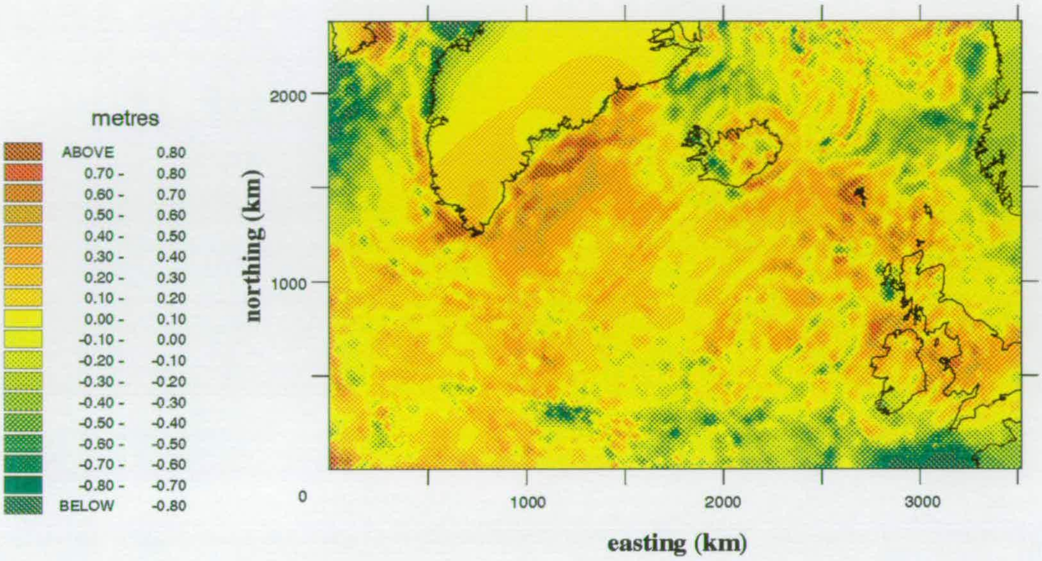

Figure 5.10. Atlantic geoid height from altimeter, ship and land data, relative to the OSU91A geoid.

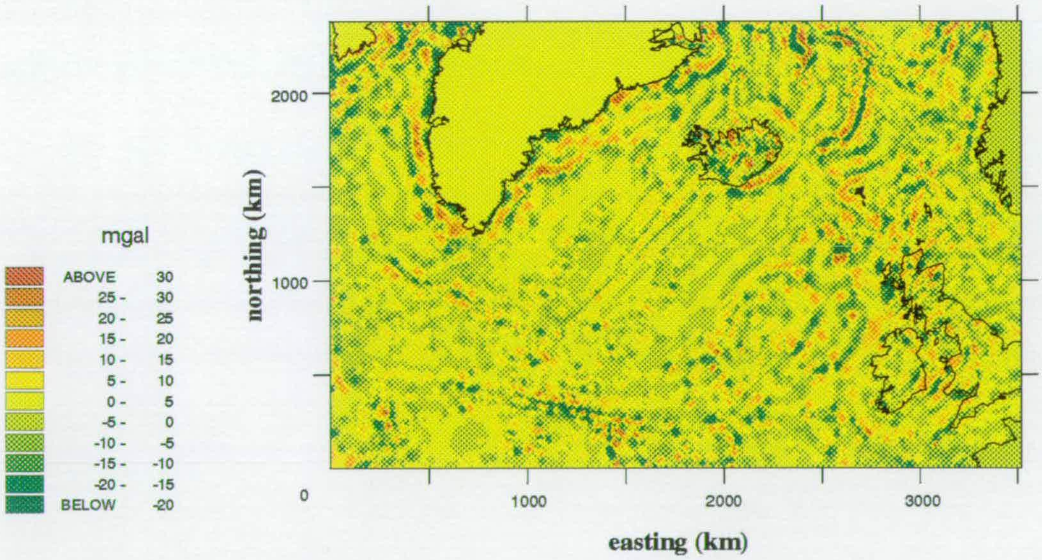

Figure 5.11. Atlantic freeair anomaly from altimeter, ship and land data, relative to the OSU91A freeair anomaly.

The accuracy of the gridded freeair anomaly in fig 5.11 can be assessed in a similar manner with the original ship track data, but using the gravity anomaly rather than its slope. The mean value of the ship gravity profiles was 2.79 mgal; their standard deviation was 16.35 mgal. The mean and standard deviation of the gravity profiles computed from the IFC field were -0.05 mgal and 10.07 mgal respectively. Thus the difference s.d. was 10.17 mgal, forming 101% of the computed s.d..

However, the mean value of the gravity profiles computed from the satellite-only solution (fig 3.14) was 0.08 mgal, and their standard deviation was 6.63 mgal, giving a difference s.d. of 13.41 mgal, or 202% of the computed s.d.. This indicates that the inclusion of the ship track data has increased the accuracy of the satellite field.

It is interesting to compare the ship gravity data with freeair anomaly fields generated using altimeter data that have not been corrected for the OSU91A sea surface topography model (§1.3). As the gravity data do not contain a sea surface topography expression, this tests by how much this correction, when applied to the altimeter data, has improved the resulting model, and whether its long-wavelength signature has contaminated the Fourier transformation procedure. Comparing an uncorrected IFC model with the ship track data resulted in a mean difference of 2.88 mgal, and a standard deviation of 10.27 mgal. The mean difference for the uncorrected satellite-only grid is 2.66 mgal, and the standard deviation is 13.41 mgal. These figures do not show any improvement upon those above. This suggests that the removal of a long-wavelength sea surface topography model from satellite altimeter profiles does not improve the final model.

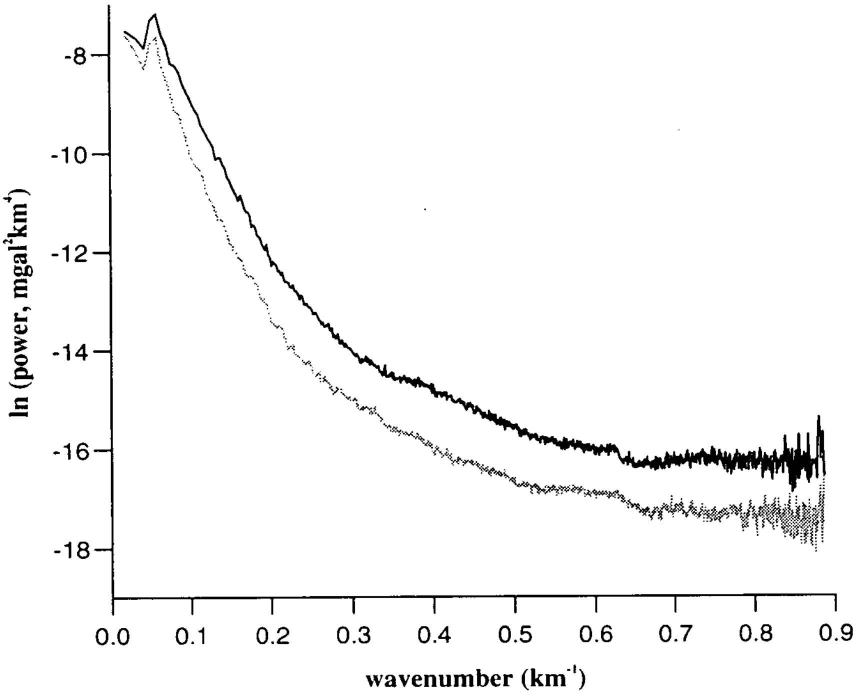

Figure 5.12. Power spectra of IFC (dark curve) and satellite-only (light curve) freeair anomalies.

Chapter 6

The North Atlantic Ocean

6.1 Introduction

This chapter presents the freeair anomaly over the North Atlantic generated by the algorithm described earlier, and compares it with a field generated by Sandwell et al. (1995). Although this thesis is concerned primarily with development and application of the IFC combination algorithm, and with the gridding of satellite and ship gravity data, a brief description of the tectonic environment of the study area follows. However, the North Atlantic Ocean exhibits many different tectonic provinces, some with unusual properties, and it is beyond the aims of this study to provide models to describe these.

A method will be introduced that uses two-dimensional gravity maps to investigate the method of isostatic compensation present in a region, as well as providing estimates of the flexural rigidity of the oceanic lithosphere in the area. The results obtained will be compared with the findings of previous studies, and with a sample one dimensional admittance analysis from a single ship profile.

6.2 Tectonic setting

From analysis of the magnetic anomaly stripes in the Atlantic Ocean, the oldest recorded geomagnetic anomaly is M25, occurring off the east coast of North America and off the northwest coast of Africa. This indicates that the ancient continents of west Gondwana and Laurentia started separating to form the central Atlantic Ocean around 160 million years ago (Ma), in the mid-Jurassic [Fowler (1990)]. In fact, seafloor rocks have been discovered in the central Atlantic that have been dated at 175 Ma, though these probably arise from early Jurassic rifting, rather than actual plate spreading [Van der Voo (1993)].

Geomagnetic anomaly M11 has been recorded in the South Atlantic, indicating that Africa and South America started separating around 135 Ma, at the Jurassic-Cretaceous boundary.

In the North Atlantic, anomaly 34 is the oldest recorded anomaly, dated at around 84 Ma, occurring off Newfoundland and the U.K. continental shelf. However, from 118 to 84 Ma (anomalies M0 to 34), the Cretaceous Quiet Zone has rendered all palaeomagnetic evidence ambiguous, suggesting that separation between North America and Eurasia could have started as early as 118 Ma [Van der Voo (1993)].

As the spreading ridge gradually migrated northwards, it veered west between North America and Greenland, forming the Labrador Sea (see fig 6.1). This ridge was probably the main active ridge in the area from about 55 to 43 Ma, with magnetic anomalies 24 to 19 identifiable on the seafloor. The Reykjanes Ridge must also have been active at this time, as anomaly 24 can be seen off the coast of Greenland and off the Rockall Bank. Then in the early Oligocene, the Labrador Sea ridge became inactive, and plate spreading became confined to the Reykjanes Ridge, as it stands today.

The Reykjanes Ridge is not typical of slow-spreading mid-ocean ridges, despite its 13.4 mm/yr spreading rate [Van der Voo (1993)]. Slow-spreading ridges are usually characterised by an axial rift valley, about 1-2 km deep, whereas fast spreading ridges (with rates up to 150 mm/yr) have an axial topographic high. However the Reykjanes Ridge posesses an axial high from Iceland down to latitude 59° N, where it changes to an axial valley. This change in the ridge can be seen on both gravity and bathymetry, and is due to the presence of convective upwelling of the mantle below Iceland enhancing crustal production. Chen and Morgan (1990) have developed a model that accounts for this change in structure, that is dependent on spreading rates, but also upon mantle temperature and the variation of viscosity within the lithosphere.

Furthermore, the ridge is flanked by a series of "chevrons", also visible on bathymetry and gravity maps [*e.g.* Vogt (1983)]. One model that explains this phenomenon, described by Vogt (1971), involves melt material from the Iceland mantle plume pulsing down the ridge axis at regular intervals. This would explain the convergence of these flanking highs, as points further down the ridge would receive these pulses later and diminished in amplitude. Vogt and Johnson (1975)

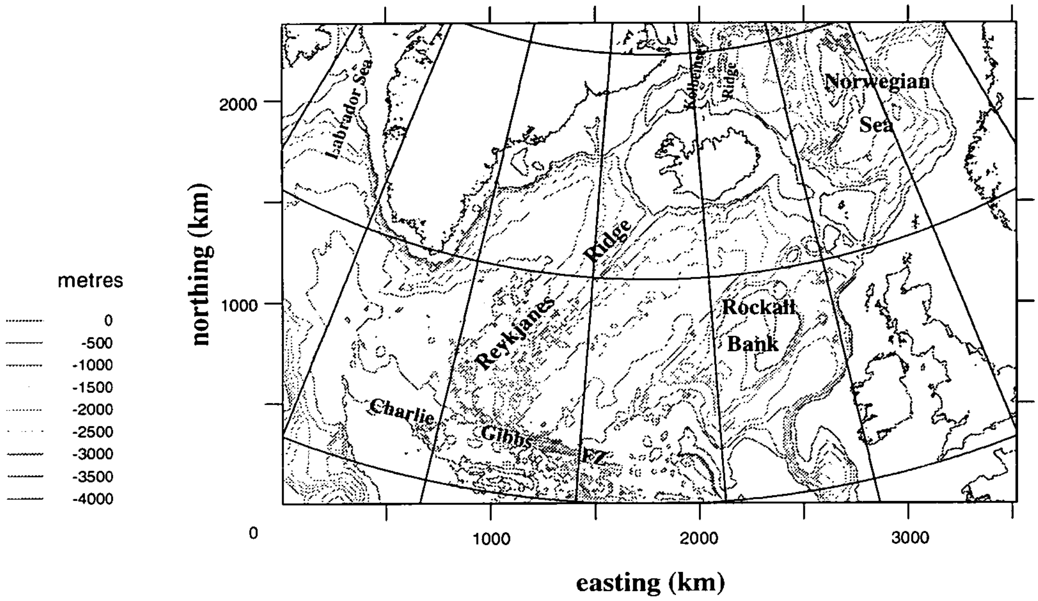

Figure 6.1. Bathymetry of the North Atlantic Ocean, showing major features.

go on to describe what happens when such material encounters the damming effect of a fracture zone (FZ), as occurs at the Bight fracture zone (crossing the Reykjanes Ridge at around 57° N), and the Tjörnes FZ (crossing the Kolbeinsey Ridge just off the north coast of Iceland).

6.3 The gravity field

The procedure to grid and combine the various forms of gravity data began by subtracting a long-wavelength spherical harmonic model of the geoid/freeair anomaly from the original data. The model used was the OSU91A geopotential model to degree and order 360 (§1.3). This was done to reduce errors caused by long wavelengths in Fourier transformation. To recover the total gravity field (or geoid), this harmonic model must be added back to the combined model field.

With regard to the dynamic topography, the strong signature of the Gulf Stream does not extend into this study area [Cheney and Marsh (1981)], and the time-variant effects have been reduced by using repeat cycle averages of the altimeter data (§1.5.2).

Fig 6.2 shows the total freeair anomaly over the North Atlantic, obtained by combining satellite altimeter measurements of the geoid height, and shipboard and terrestrial measurements of the freeair anomaly, using the IFC method, and with the OSU91A model added back.

The Sandwell field The accuracy of this model can be tested by comparison with a similar gravity field. The gravity field generated by Sandwell et al. (1995) is used for this purpose, shown in fig 6.3. This field is a regridded version (5 km spacing) of the original, which had a 2' longitude spacing. The original grid was generated from the along-track vertical deflections of altimeter profiles, converted to geoid height using a previously calculated reference field. This reference field was created using a vertical deflection method similar to that used in this thesis (Chapter 3), described in Sandwell (1992). The new geoid height profiles were then gridded using a minimum curvature algorithm with added tension [Smith and Wessel (1990)].

The Sandwell field has a much higher resolution than the IFC field: in addition to Geosat/ERM and Topex/Poseidon data, Sandwell used ERS-1 altimeter data, having an equatorial track spacing of only 8 km. [This high sampling density lends itself to the gridding method he used.] Bearing this in mind, the IFC field shows very good agreement with the Sandwell field.

As the Sandwell field does not contain data on land areas, a quantitative comparison between the two fields should not include the landmasses. Thus, the mean value of the Sandwell field is 15.90 mgal, with a standard deviation of 21.10 mgal. The mean value of the IFC field is 15.25 mgal, with a standard deviation of 19.84 mgal. Therefore, the difference s.d is 8.84 mgal, which forms 45% of the IFC field s.d..

It is also useful to compare the power spectra of the datasets. These are shown in fig 6.4. At long wavelengths the power is similar for both datasets, but from wavenumber 0.051 km^{-1} (123 km wavelength) to 0.339 km^{-1} (18.5 km wavelength), the Sandwell spectrum holds more power. Then from this point the IFC spectrum is considerably larger. It is also interesting to note the abrupt decrease in both spectra at approximately 0.63 km^{-1} wavenumber. This is a result of the grid representation of the data: on a 5 km grid, the Nyquist wavenumber in easting and northing is 0.628 km^{-1} (10 km wavelength). The fields are unable to represent data accurately above this wavenumber.

The similarities between the IFC and Sandwell gravity fields are striking. One of the most interesting features are the "chevrons" flanking the Reykjanes Ridge, clearly visible in both fields. These are discussed briefly in §6.2.

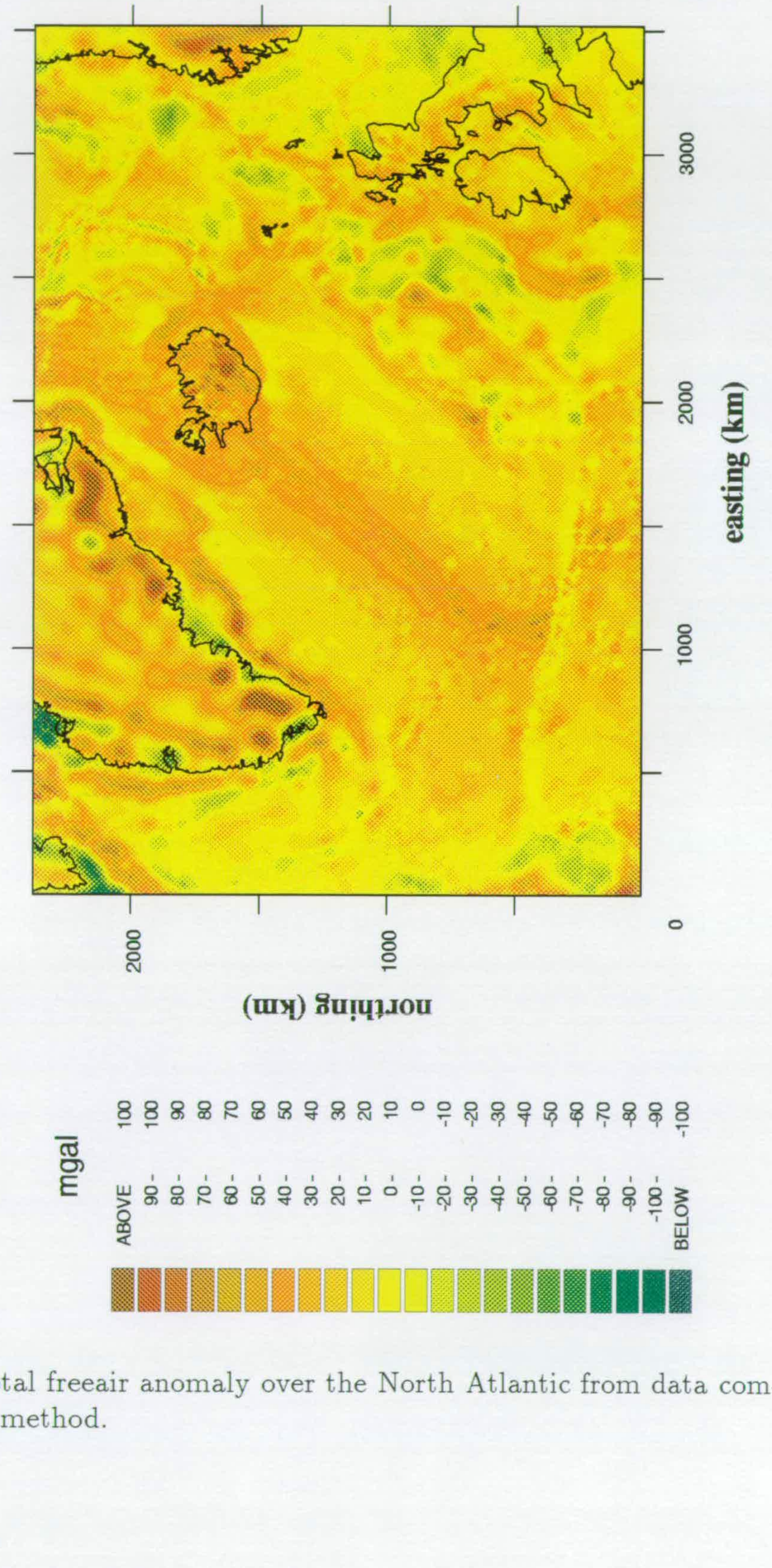

Figure 6.2. The total freeair anomaly over the North Atlantic from data combined using the IFC method.

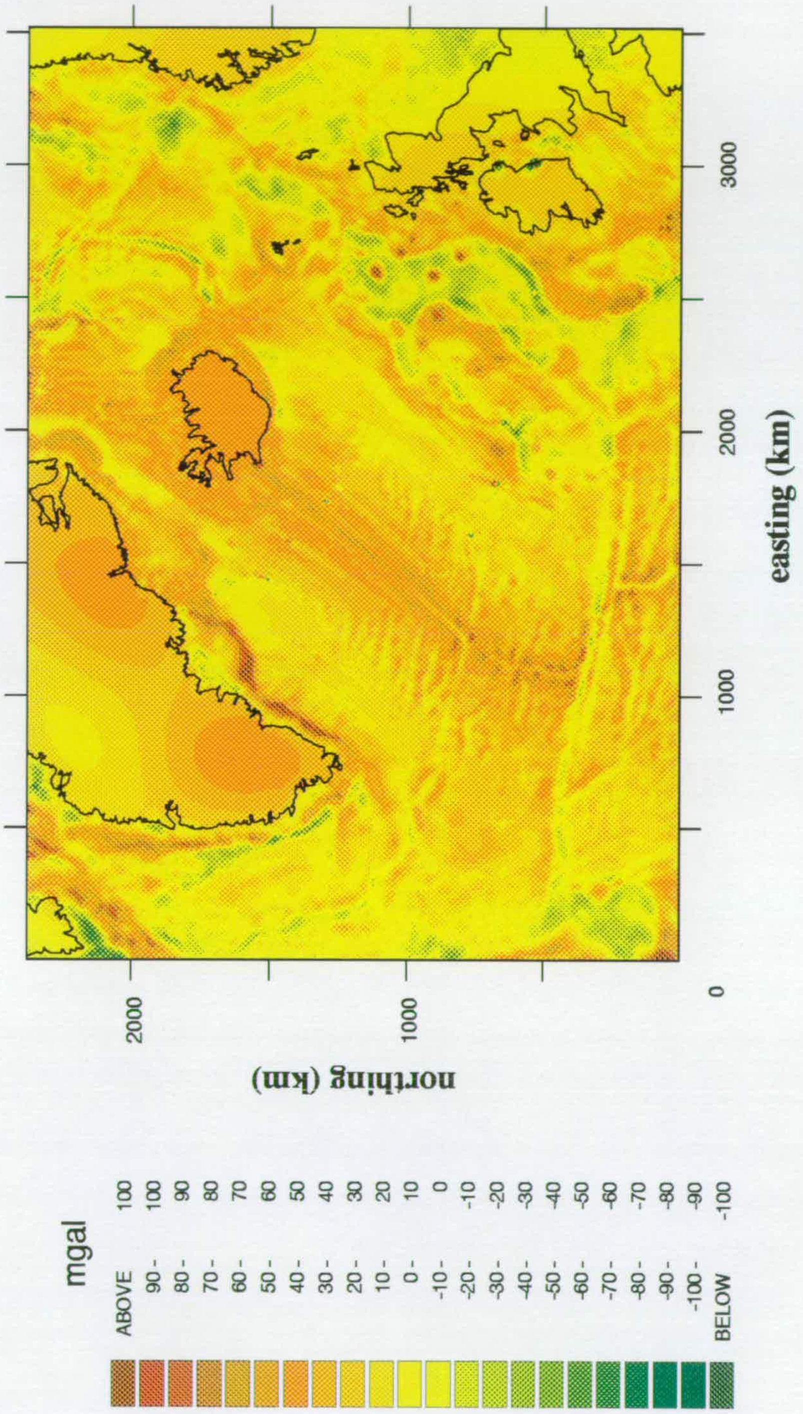

Figure 6.3. The total freeair anomaly over the North Atlantic, from Sandwell et al. (1995).

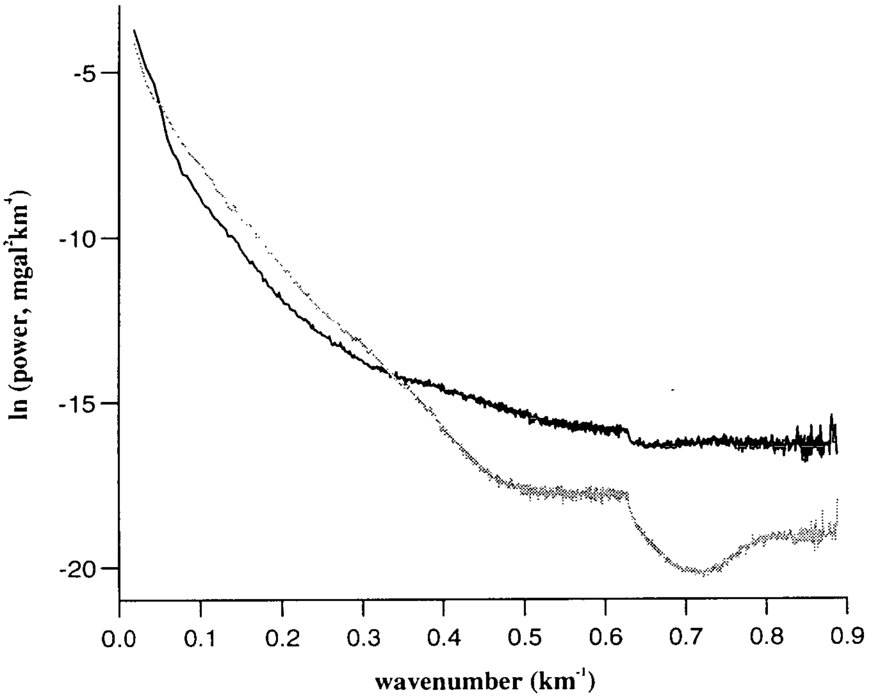

Figure 6.4. Power spectra of IFC (dark curve) and Sandwell (light curve) freeair anomalies.

Moving southwards down the ridge, the chevrons taper together, and the axial gravity high changes to an axial valley at coordinates (1400,1000). An explanation for this can be found in §6.2. This low is then cut by the Bight FZ at approximately (1200,800); this FZ can be seen on the IFC model by the break in the axial low, and by the anomaly at (700,900) to the west, with a visible trend between the two. The Bight FZ is clearer in the Sandwell field, due to its higher resolution, and the low density of ship track data in the IFC field.

The Reykjanes Ridge then changes direction slightly to meet the Charlie-Gibbs FZ at (1100,300) (see also fig 6.1). This feature is clearly visible in the IFC field, extending from (400,400) to (1600,250), with the area of increased thickness of ridge volcanics at (1200,300) postulated by Vogt and Johnson (1975) even being resolved. The double-valley nature of this fracture zone, a feature 45 km across [Whitmarsh and Calvert (1986)], is also resolved in both fields. The Mid Atlantic Ridge is offset at the Charlie-Gibbs FZ, and can be seen trending south from coordinates (1400,200). The IFC field signature of the ridge here is slightly 'lumpy'. This is due to the low density of satellite and ship tracks in the area (see figs 2.1, 2.2 & 2.3).

The failed spreading centre in the Labrador Sea can also be resolved on both maps. It can be seen to start at the "doughnut" shaped anomaly at the western end of the Bight FZ. The gravity valley, flanked by highs, can be followed trending northwest (map reference) along "doglegs", until it straightens and leaves the map at (1600,0). Note this feature has been resolved from satellite data only, but has a rather weak signature due to the large thickness of overlying sediment [Rabinowitz and Jung (1986)].

The seas surrounding Iceland have been extensively surveyed by ships (fig 2.3), and this is reflected in the similarity of the two datasets in this area. The Kolbeinsey Ridge gravity high can be seen arcing northwards from the north coast of Iceland, where the signature stops at the Spar FZ at (2050,2100). The Jan Mayen FZ can just be seen as a west-east trending gravity low at (2200,2400). This trends southeastwards to beyond a 'T'-junction with the Aegir Ridge which arcs southwest to the eastern tip of Iceland. These features are very clear in both datasets.

Other interesting similarities include the resolution of the passive continental margins at the edges of the Rockall Bank and Greenland. The gravity-high shield is very prominent off Greenland, and again off the Rockall Bank. Both fields have resolved seamounts in the Rockall Trough, and structure in the North Sea.

The differences between the marine areas of the IFC and Sandwell datasets are predominantly in the short wavelength features, as expected from the inclusion of ERS-1 data by Sandwell. Most striking are the small fracture zones trending almost perpendicular to the Reykjanes Ridge. The IFC field does exhibit some localised anomalies coinciding with these fracture zones, but the Geosat/ERM and Topex/Poseidon tracks are too sparse to resolve the trends. Also visible in the Sandwell field but absent from the IFC map are the northwest-southeast trending lows at the western end of the Charlie-Gibbs FZ.

An obvious difference, in favour of the IFC field, is the inclusion of terrestrial gravity data over the British Isles and Iceland. This data merges without discontinuities with the surrounding marine data. No gravity data were available for Greenland or Scandinavia, so the field shown in fig 6.2 over these areas is the OSU91A gravity field.

6.4 Tectonic interpretation

Some quantitative information about the rheology and density structure of the lithosphere in the North Atlantic can be determined by analysis of the isostatic

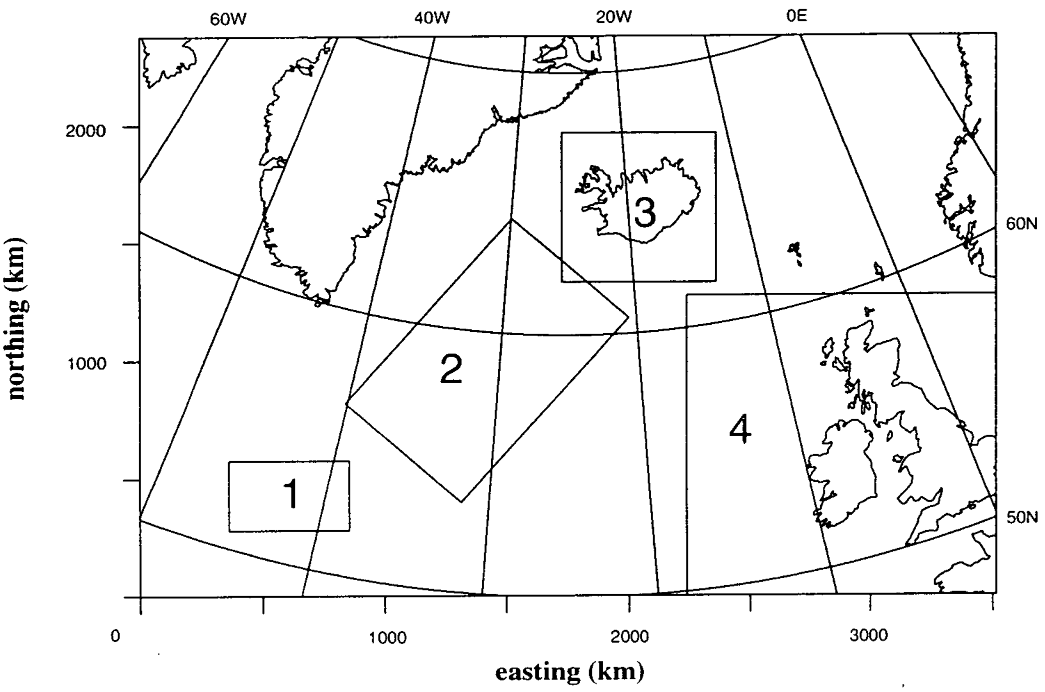

Figure 6.5. Location of the sub-areas for admittance studies.

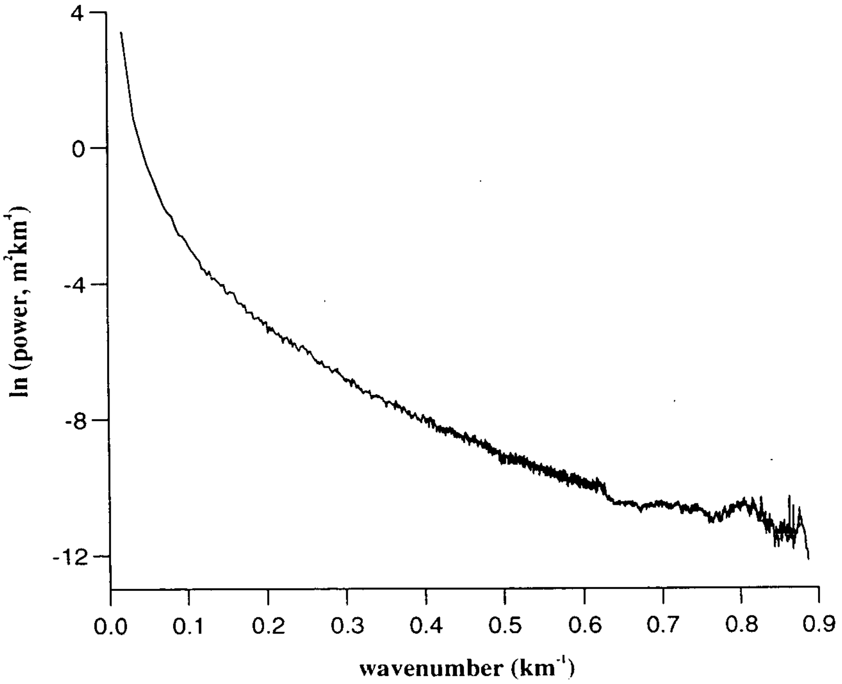

Figure 6.6. Power spectra of Atlantic topography.

admittance and coherence, introduced in §1.4.2.

Calculating the isostatic admittance for the whole of the North Atlantic area may not yield a meaningful depth to Moho or elastic thickness value, as there are many different tectonic regimes operating. Therefore, four smaller areas of different tectonics were chosen to test the admittance. The locations of these sub-areas are shown in fig 6.5. The sub-areas were chosen to have uniform internal tectonics. However, to obtain accurate information from admittance and coherence analyses, it is preferable to have large areas with many values of the gravity field and topography. Thus a 'trade-off' exists between having enough points to gain accurate information, and having an area small enough to ensure a good degree of tectonic consistency.

Area 1 takes in the fossil transform of the Charlie-Gibbs fracture zone, to the west of the Reykjanes Ridge intersection. Area 2 includes most of the Reykjanes Ridge without including the Iceland hot spot or the Charlie-Gibbs FZ. Area 3 comprises Iceland and the surrounding ocean; and Area 4 includes the British Isles and the continental shelf to the west.

Of these areas, the British Isles perhaps contains the most varied tectonic provinces. This presents problems in that admittances calculated in areas containing both oceanic and continental crust will not reflect the relative proportion of these provinces in the area. This arises from eqs 1.41, 1.38 & 1.40: a load emplaced on oceanic crust will produce a deflection different from the same load on continental crust by an amount proportional to combinations of both the fourth and inverse fourth power of the load wavelength. This phenomenon is noted but not accounted for quantitatively in this thesis.

IFC gravity data were available for all four sub-areas, taken from the field shown in fig 6.2. As a comparison, admittance and coherence analyses were also performed on gravity data taken from the Sandwell field in sub-areas 1 and 2, the Charlie-Gibbs FZ and Reykjanes Ridge.

The ETOPO5 topographic dataset was used in admittance and coherence studies (§2.7, with bathymetry shown in fig 6.1). A power spectrum for the re-gridded data is shown in fig 6.6. As mentioned previously (§2.7), the ETOPO5 dataset was given on a 5-minute grid, thus is limited to this degree of resolution. Furthermore, much of the dataset was complied from grids of the marine freeair anomaly derived from satellite altimetry: thus the process of correlating the IFC and Sandwell gravity fields with the ETOPO5 bathymetry should be treated with caution, and may in fact lead to erroneous results. For this reason, a one dimensional admittance analysis was performed upon gravity and bathymetry data from a ship track over the Reykjanes Ridge (§6.4.2).

6.4.1 The isostatic admittance

Calculation

Examination of the correlation between the topography and gravity field as a function of wavelength indicates the component of the gravity field that is generated by the sub-surface mass anomalies compensating the applied load [Forsyth (1985)].

Although the effect of the compensating mass on the gravity field is nonlinear, it is only slightly so, and can be represented by a linear response function [Dorman and Lewis (1970)]. If the linear system is the Earth, with response function $q(\vec{x})$, let the input be the load σ due to the topography z:

$$\sigma(\vec{x}) = \begin{cases} \rho_0 \, z(\vec{x}) & : \quad z > 0 \\ (\rho_0 - \rho_w) \, z(\vec{x}) & : \quad z < 0 \end{cases} \tag{6.1}$$

where ρ_0 is the density of the topographic masses on land, and ρ_w is the density of water. The output from the system is then the component of the Bouguer gravity anomaly which is due to the resulting compensation, together with the geological "noise", ν: that is, the part of the field which is not correlated with topography:

$$\Delta g_B = q_B * \sigma + \nu \quad . \tag{6.2}$$

Because ν does not correlate with the load, it will be eliminated from the cross-correlation of Δg_B and σ. If eq.6.2 is transformed to the wavenumber domain, convolution becomes multiplication, giving

$$G_B(\vec{k}) = Q_B(\vec{k})\Sigma(\vec{k}) + N(\vec{k}) \quad , \tag{6.3}$$

and cross-correlation becomes multiplication with the complex conjugate:

$$\langle G_B \Sigma^* \rangle = Q_B \langle \Sigma\Sigma^* \rangle + \langle N\Sigma^* \rangle \quad , \tag{6.4}$$

where the $\langle \, \rangle$ denote averaging around annuli in the wavenumber domain. As mentioned earlier (§1.4.3), q_B is the response of the Earth's gravity field to the application of a point load on the lithosphere, and is axially symmetric. The averaging procedure is performed around annuli for this reason, and is necessary to remove the $N\Sigma^*$ term in eq.6.4, since N, the geological noise spectrum, does not correlate with load. This term averages out to zero, and the admittance function is thus:

$$Q_B(k) = \frac{\langle G_B \Sigma^* \rangle}{\langle \Sigma \Sigma^* \rangle} \ . \tag{6.5}$$

The admittance may be calculated directly from the freeair anomaly. The relationship between freeair and Bouguer anomalies,

$$\Delta g_B = \Delta g_F - 2\pi G \sigma \ , \tag{6.6}$$

may be transformed and substituted into eq.6.5, giving

$$Q_B = \frac{\langle G_F \Sigma^* \rangle}{\langle \Sigma \Sigma^* \rangle} - 2\pi G \ . \tag{6.7}$$

Admittance values are calculated using a "load", σ, instead of the topography, z, as in eq.6.1, with a Bouguer reduction density on land of 2.67 gcm^{-3}. A Bouguer admittance is calculated using eq.6.7, with averaging performed around equal area annuli in the wavenumber domain. Outputted graphs are plotted as $\ln|Q_B|$ versus k. These may then be compared with curves generated from theoretical models. Note that these curves (§1.4.3) are calculated for a symmetrical response function, and may not be used for asymmetrical models.

An example, for the U.K. area, is shown in fig 6.7. According to the theoretical curves in fig 1.4, the data should decrease rapidly with increasing wavenumber ($Q_B(k) \longrightarrow 0$ as $k \longrightarrow \infty$) as the correlation between Bouguer anomaly and topography diminishes. However the values in fig 6.7 tend to the value $\ln(2\pi G)$. This occurs because, below a certain wavelength related to the track spacing, the satellite derived gravity spectrum is negligible, and from eq.6.7, for $G_F = 0$, $Q_B = -2\pi G$. The wavenumber at which this occurs, k_{max}, can be found by a spectral analysis of the kernel used to generate the gravity field maps. This is done in Appendix C. The value of k_{max} was chosen to be the highest wavenumber at which the transfer functions for Geosat or Topex/Poseidon data fall to half their maximum value. Bearing in mind the lower resolution at the south of the study area, a conservative value of $k_{max} = 0.11\text{km}^{-1}$ (approximately 60 km wavelength) was chosen as this limit. Thus, only the small wavenumber part of the admittance will contribute usefully to the tectonic interpretation.

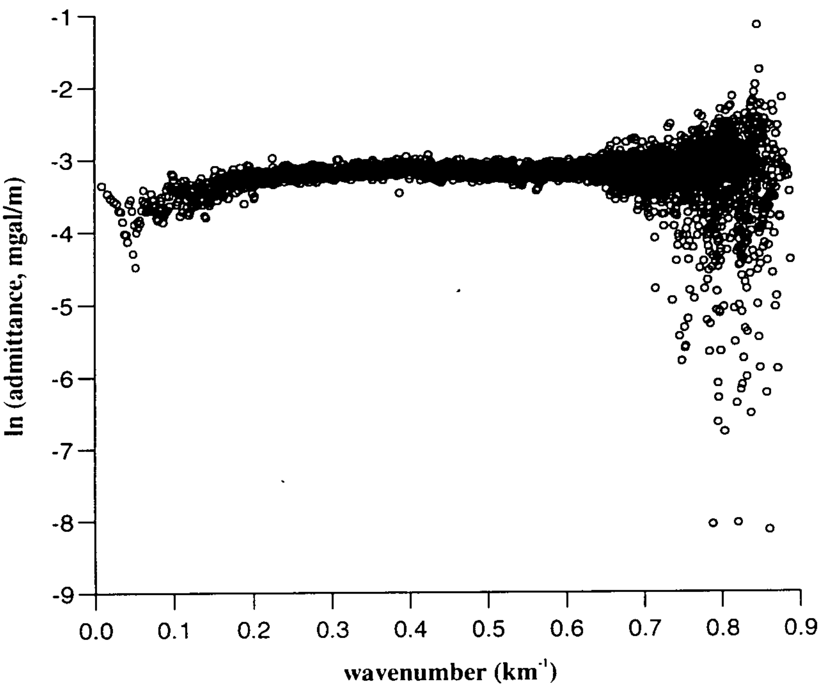

Figure 6.7. Admittance of the U.K. area.

The high wavenumber end of fig 6.7 is typical of plots of spectral data for this study, in that a high degree of noise is exhibited above a wavenumber of approximately 0.63 km^{-1}. This is a result of the Nyquist wavenumber for the gridded data, discussed in §6.3.

Admittance plots

The admittance data are fitted to the combined model of loading at the surface and at the Moho (eq.1.41), in a least-squares sense up to a wavenumber k_{max}. The standard error of the difference between real and theoretical values, α_d, is calculated for combinations of a range of values of depth to Moho (z_m), elastic thickness (T_e), and Moho-to-surface loading ratio (f). This was done in a program which varied f from 0 to 10 in units of 0.1, then 0 to 100 in units of 1; and varied T_e and z_m from 0 to 50 km in 0.5 km steps. Table 6.1 shows the values of the three parameters that gave the curve with the best fit (smallest α_d) to the IFC and Sandwell admittance data in the four areas.

Fig 6.8 shows the admittance data up to k_{max} for the four sub-areas (IFC and Sandwell data), and the best fitting theoretical curve given by the values in table 6.1. The error bars are a formal precision from the procedure of averaging

Area	min. α_d, log(mgal/m)	z_m (km)	T_e (km)	f
Charlie-Gibbs FZ	0.0273	24.5	7.0	17
CGFZ (Sandwell)	0.0388	25.0	4.5	100
Reykjanes Ridge	0.0159	10.0	3.0	100
Reykjanes (Sandwell)	0.0508	20.0	3.5	100
Iceland	0.0171	16.5	4.5	6
U.K.	0.0204	22.5	6.0	14

Table 6.1. Best values of z_m, T_e and f from admittance data.

around annuli in the wavenumber domain. The theoretical curves have the value $\ln(2\pi G)$ at zero wavenumber; this fits the data in figs 6.8(b), (e) & (f) very well. These plots also show good agreement between the initial gradients of the data and curve: recall (§1.4.3) that the low wavenumber gradient of the admittance data gives the depth to Moho. Therefore the z_m values for the Charlie-Gibbs FZ (Sandwell data), Iceland and the U.K. are likely to be more reliable than the Moho depth given for the Charlie-Gibbs FZ (IFC data) and Reykjanes Ridge (IFC data), which show a poor fit at low wavenumbers (figs 6.8(a) & (c) respectively).

At higher wavenumbers (0.05 to 0.1 km^{-1}), the effects of elastic plate thickness and loading ratio dominate the admittance spectrum (figs 1.3 & 1.4). Take the U.K. area, fig 6.8(f): comparing this with fig 1.3, it would seem that bottom loading models ($f > 1$) are required to explain the increase in $\ln|Q_B|$ from wavenumber 0.05 km^{-1}. Then a comparison with fig 1.4 suggests bottom loading ($f > 1$) again to explain the decrease at wavenumber 0.09 km^{-1}.

The problem with this least-squares curve fitting procedure is that outlying points contribute to the fit, when in fact they could be erroneous. Therefore, some data were deleted from the graphs in fig 6.8 and the curve fitting algorithm was re-run. For the Charlie-Gibbs FZ IFC data, fig 6.8(a), the three low-admittance points around 0.04 km^{-1} wavenumber were deleted, giving a best fit model of $z_m = 15.0$ km, $T_e = 5.0$ km and $f = 6$, with $\alpha_d = 0.0119$. For the Charlie-Gibbs FZ Sandwell data, fig 6.8(b), the three low-admittance points around 0.04 km^{-1} wavenumber were deleted, giving a best fit model of $z_m = 20.5$ km, $T_e = 3.5$ km and $f = 100$, with $\alpha_d = 0.0287$. For the Reykjanes Ridge Sandwell data, fig 6.8(d), the five low-admittance points between 0.07 and 0.09 km^{-1} wavenumber were deleted, giving a best fit model of $z_m = 19.0$ km, $T_e = 3.5$ km and $f = 100$, with $\alpha_d = 0.0347$.

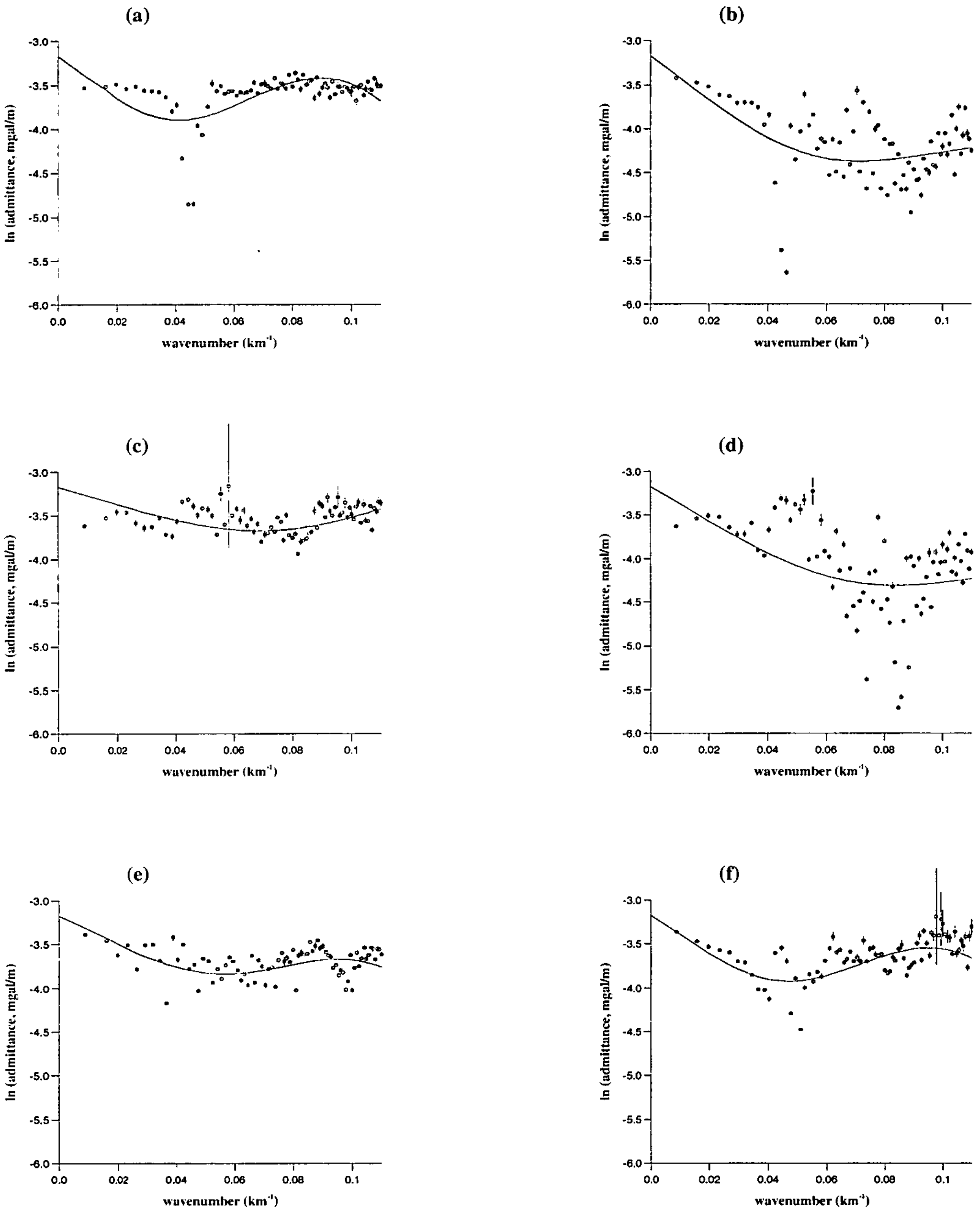

Figure 6.8. Admittance plots for (a) Charlie-Gibbs FZ, (b) Charlie-Gibbs FZ (Sandwell data), (c) Reykjanes Ridge, (d) Reykjanes Ridge (Sandwell data), (e) Iceland, and (f) U.K. areas. The plots also show the best fit theoretical curve given by the parameters in table 6.1.

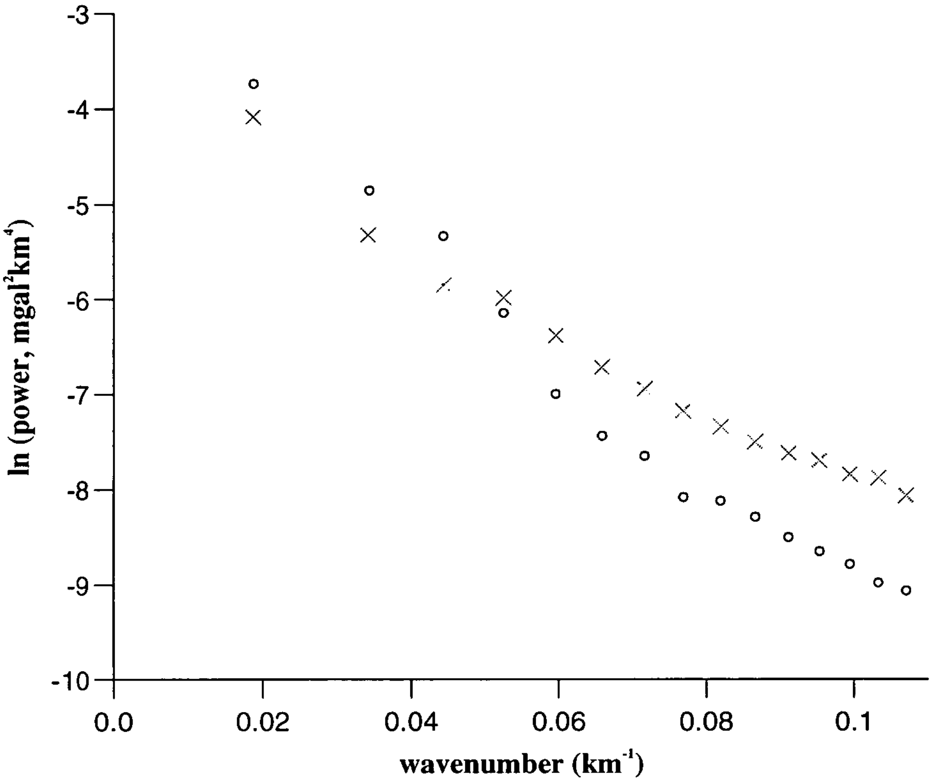

Figure 6.9. Power spectra of the IFC (circles) and Sandwell (crosses) gravity fields.

In short, comparing the above values with their equivalent in table 6.1, except for the Moho depth of the Charlie-Gibbs FZ IFC data, the estimates of z_m, T_e and f were not significantly altered by deleting outlying points.

Observation of the admittance data in the plots in fig 6.8, show the Sandwell data to have much lower admittances over wavenumbers 0.05 to 0.11 km^{-1}. This can be explained by the power spectra in fig 6.9, which is a blow-up of fig 6.4 over wavenumbers 0 to 0.11 km^{-1}. The IFC field has less power over wavenumbers 0.05 to 0.11 km^{-1} than the Sandwell field. This results in a comparatively poor correlation between gravity and topography, and a value of $\ln|Q_B|$ that is closer to $\ln(2\pi G)$, as described earlier.

$f - z_m - T_e$ plots

Figs 6.10 to 6.15 show the degree of fit of curves generated from all values of f, z_m and T_e to the admittance data for the four sub-areas (IFC and Sandwell data). The (a) graphs show how α_d varies with z_m and T_e, with f fixed at the best value. The (b) graphs fix T_e at its best value, and plot the variation of α_d for f versus z_m; and the (c) graphs fix z_m and plot α_d for f versus T_e. This is a convenient way of showing how a parameter varies in three dimensions.

Analysis of the $T_e - z_m$ plots shows the best solutions lying either on a straight line (*e.g.* figs 6.11, 6.12 & 6.13), or more localised in a truncated version of a straight line (*e.g.* figs 6.10, 6.14 & 6.15). The former solutions suggest more leeway in the elastic thickness and Moho depth values while still preserving the linear relationship between the two. The latter plots indicate a more constrained set of values. In all cases, the Airy compensation mechanism ($T_e = 0$) does not provide the best solutions.

The $f - T_e$ and $f - z_m$ plots show how insensitive the admittance is to variations in loading ratio for $f > 1$. Take fig 6.10(c): at $T_e = 7.0$ km and $f = 17$, $\alpha_d = 0.0273$, while at $T_e = 7.0$ km and $f = 100$, α_d is only 0.0352. Similarly in fig 6.12(b), for $z_m = 10.0$ km and $f = 100$, $\alpha_d = 0.01587$. But at $z_m = 10.0$ km and $f = 10$, α_d is 0.01590. However, the lowest values of α_d lie above the line $f = 1$ for all areas, implying predominantly bottom loading solutions are required.

Note also the differences between the solutions for areas where gravity data from the Sandwell field is available. First, table 6.1 shows that the Sandwell admittance curves have a poorer fit than the IFC curves. Looking at the Charlie-Gibbs FZ, the z_m solutions are almost identical, while the T_e solutions are smaller by almost a half for the Sandwell data. The f solutions are radically different, but this can be explained by the insensitivity of the solution to any loading ratio significantly larger than 1: for the Sandwell data with $z_m = 25$ km, $T_e = 4.5$ km, but $f = 17$, $\alpha_d = 0.0390$ compared to 0.0388 for $f = 100$. For the Reykjanes Ridge, the IFC Moho depth solution is half that of the Sandwell data solution, while the elastic thicknesses and loading ratios are virtually the same.

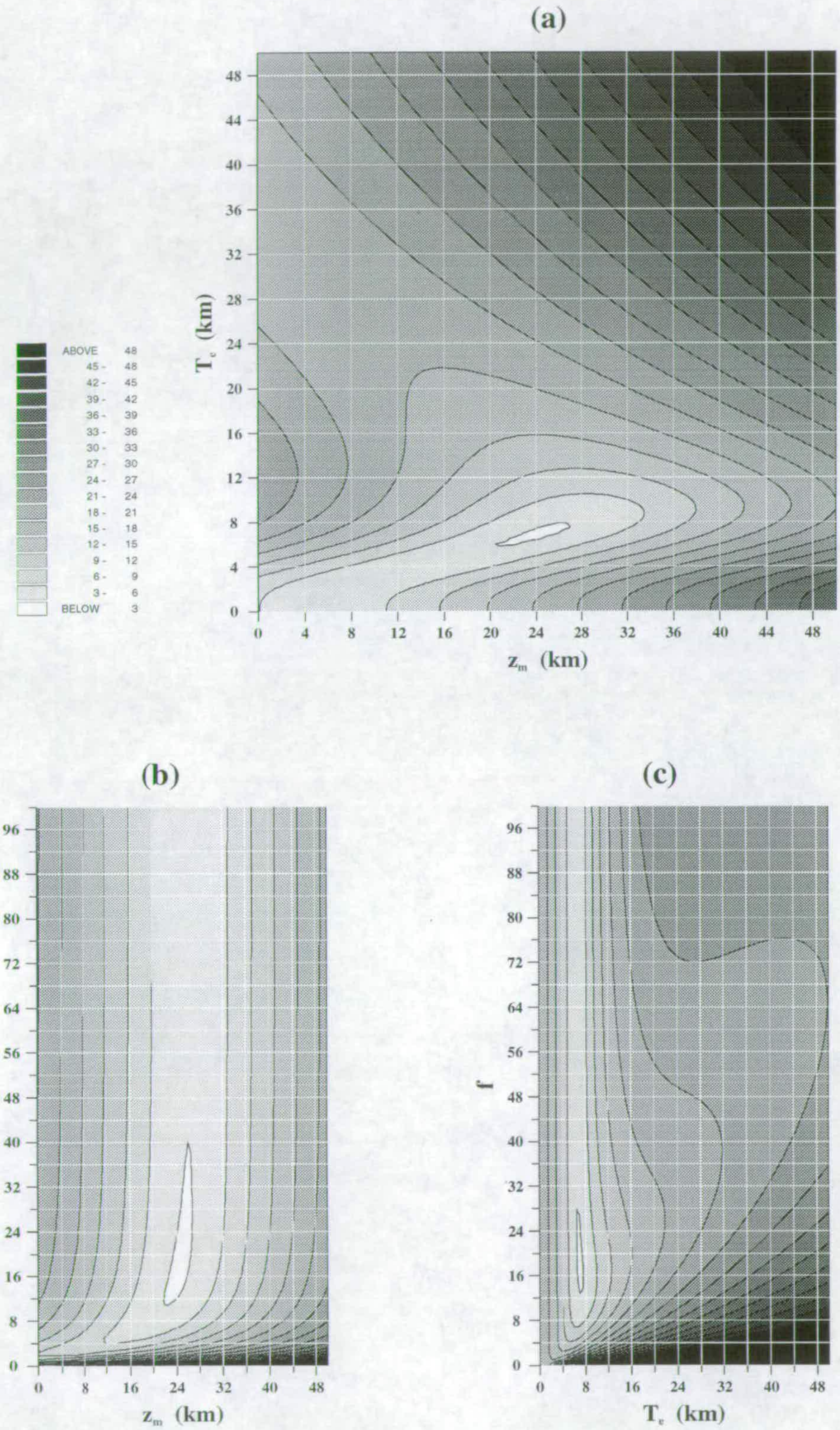

Figure 6.10. Charlie-Gibbs FZ (area 1). Plots of $\alpha_d \times 10^2$ from admittance data for (a) T_e vs z_m for $f = 17$; (b) f vs z_m for $T_e = 7.0$ km; (c) f vs T_e for $z_m = 24.5$ km.

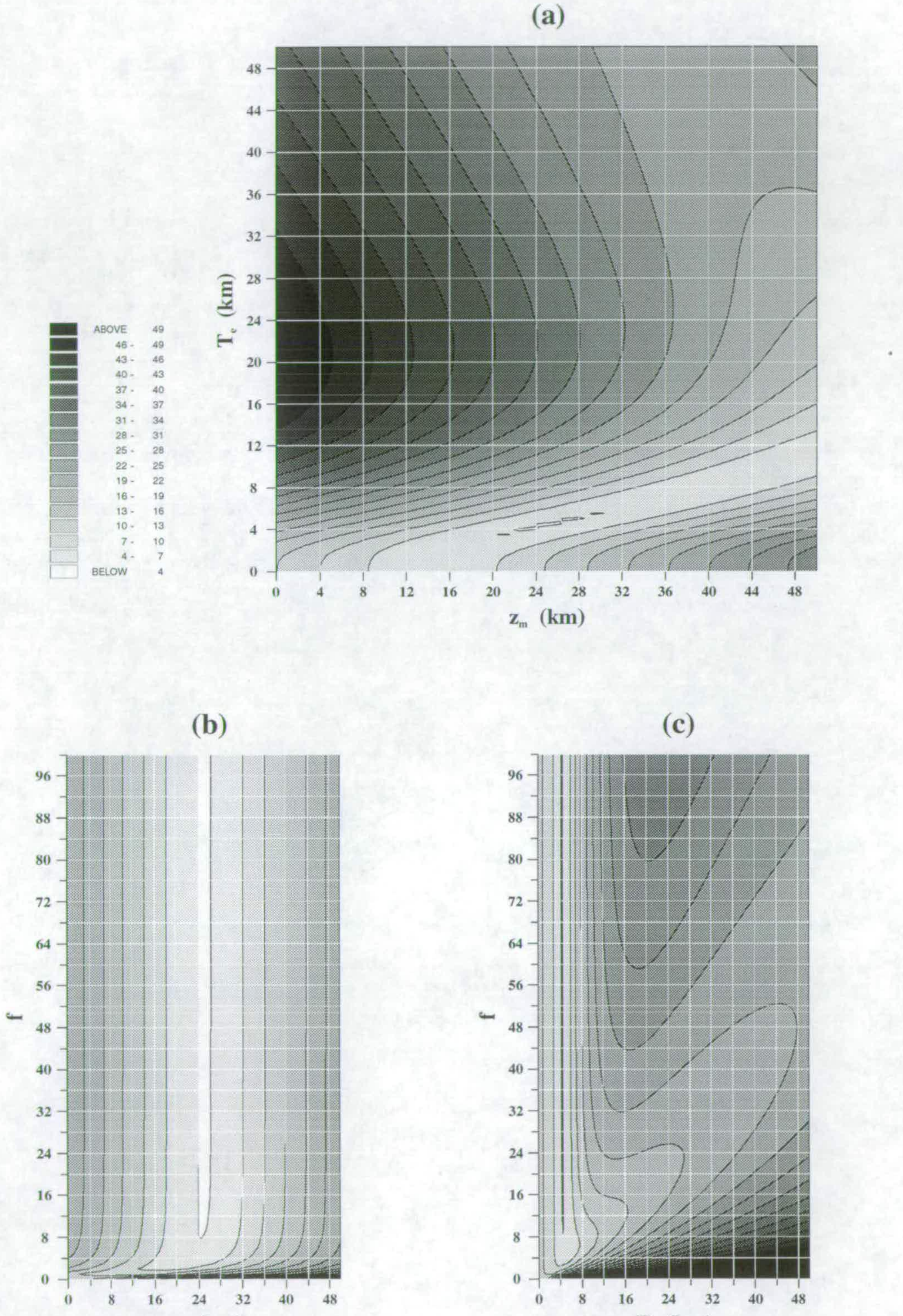

Figure 6.11. Charlie-Gibbs FZ (area 1), Sandwell data. Plots of $\alpha_d \times 10^2$ from admittance data for (a) T_e vs z_m for $f = 100$; (b) f vs z_m for $T_e = 4.5$ km; (c) f vs T_e for $z_m = 25.0$ km.

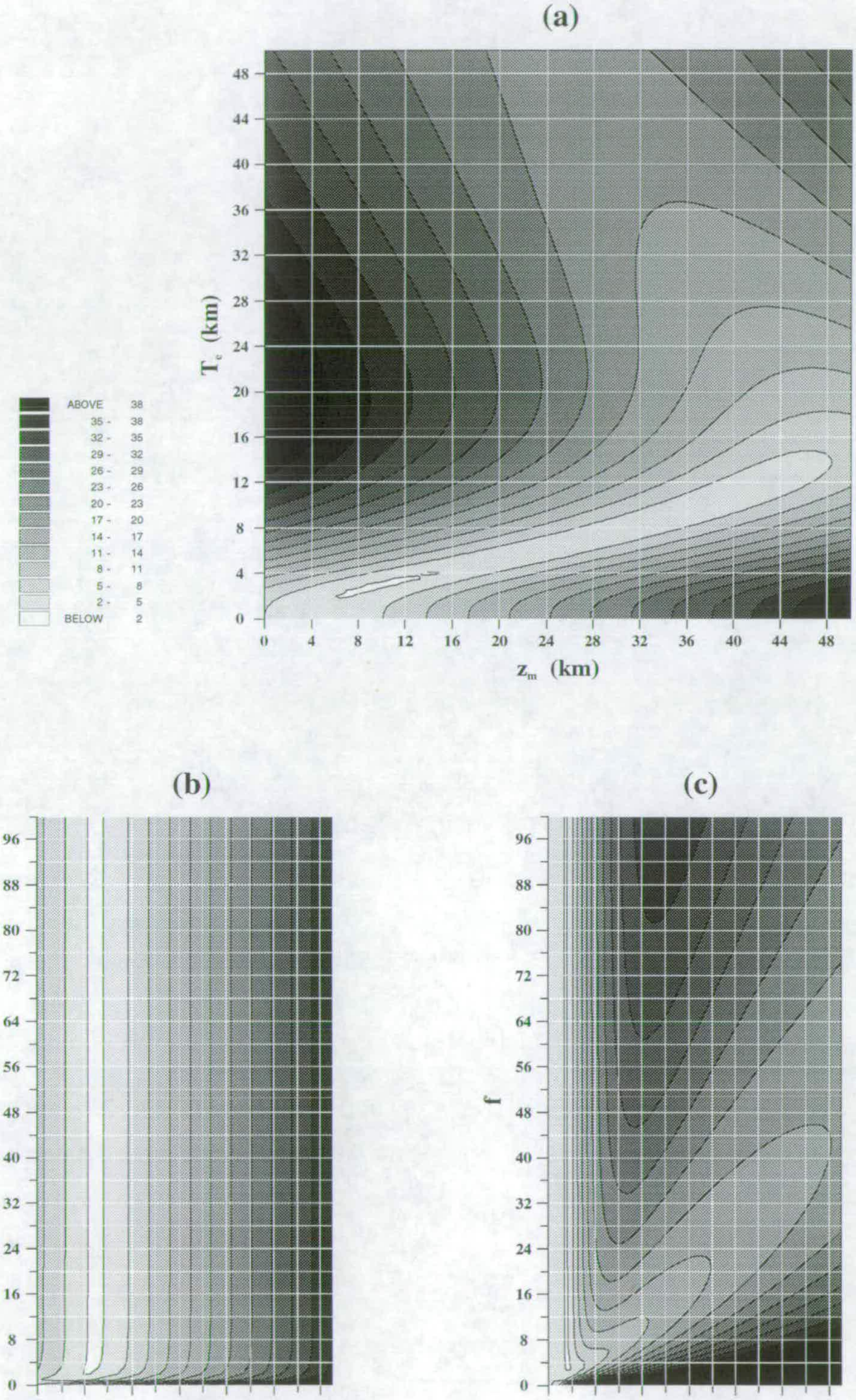

Figure 6.12. Reykjanes Ridge (area 2). Plots of $\alpha_d \times 10^2$ from admittance data for (a) T_e vs z_m for $f = 100$; (b) f vs z_m for $T_e = 3.0$ km; (c) f vs T_e for $z_m = 10.0$ km.

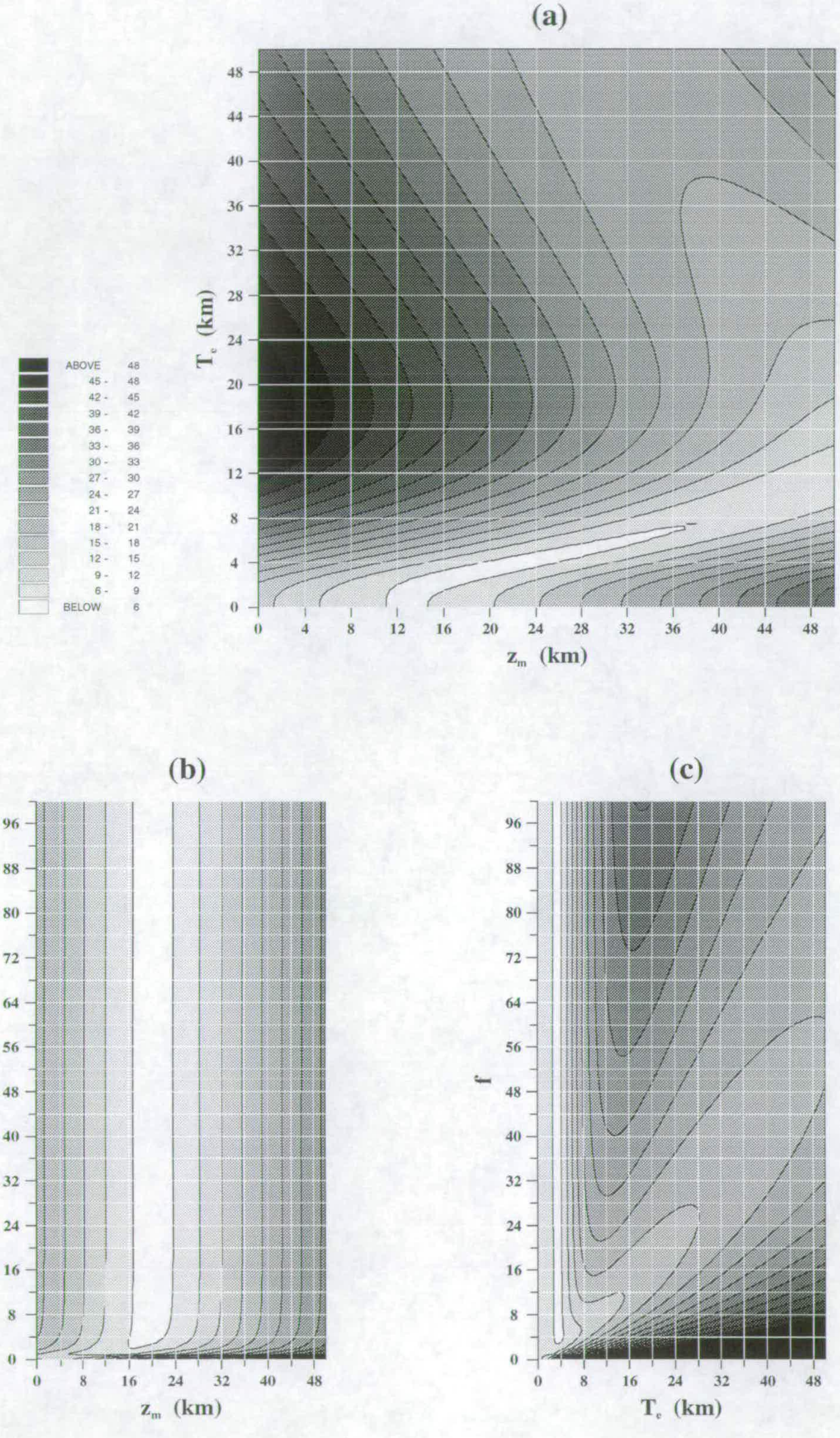

Figure 6.13. Reykjanes Ridge (area 2), Sandwell data. Plots of $\alpha_d \times 10^2$ from admittance data for (a) T_e vs z_m for $f = 100$; (b) f vs z_m for $T_e = 3.5$ km; (c) f vs T_e for $z_m = 20.0$ km.

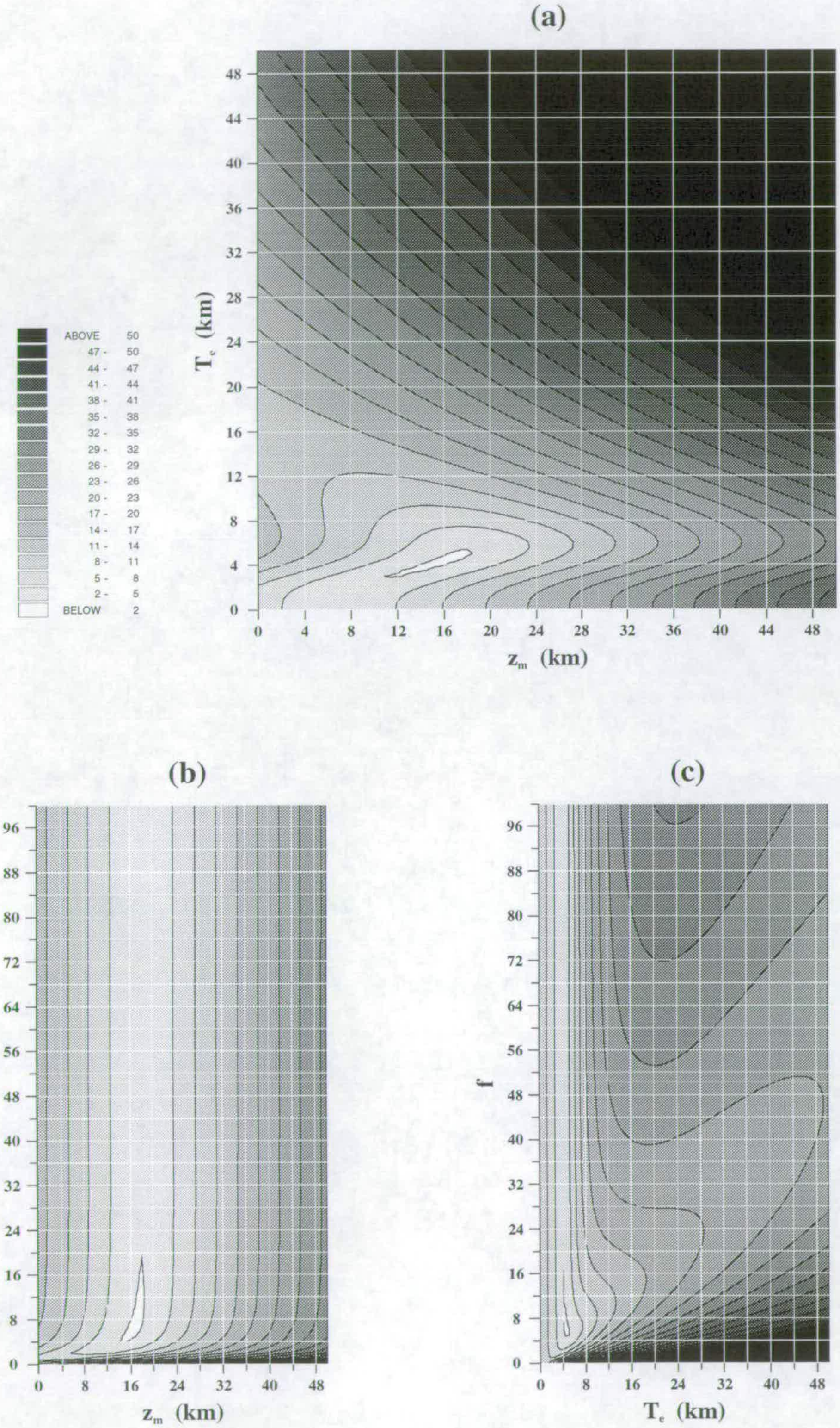

Figure 6.14. Iceland (area 3). Plots of $\alpha_d \times 10^2$ from admittance data for (a) T_e vs z_m for $f = 6$; (b) f vs z_m for $T_e = 4.5$ km; (c) f vs T_e for $z_m = 16.5$ km.

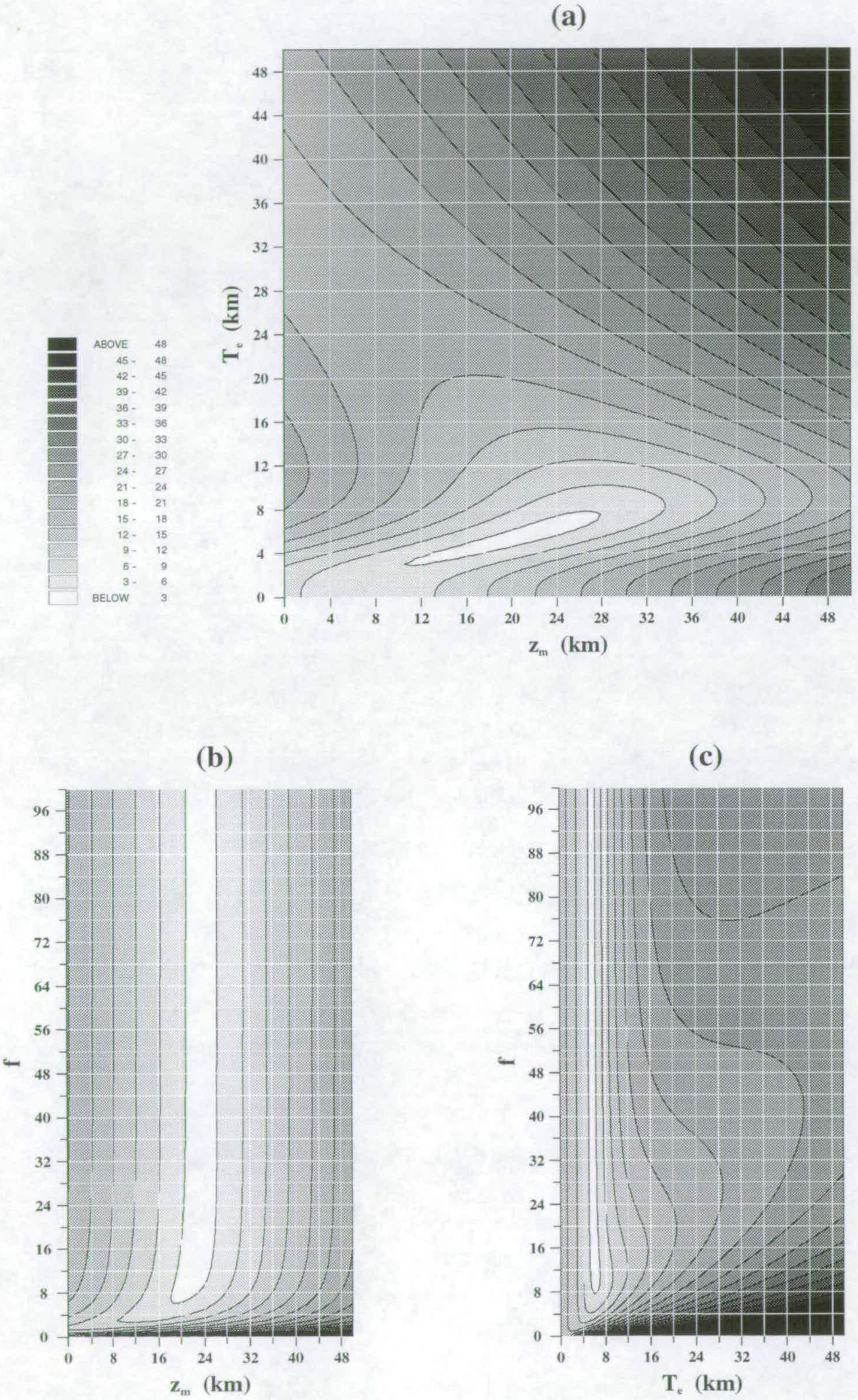

Figure 6.15. U.K. (area 4). Plots of $\alpha_d \times 10^2$ from admittance data for (a) T_e vs z_m for $f = 14$; (b) f vs z_m for $T_e = 6.0$ km; (c) f vs T_e for $z_m = 22.5$ km.

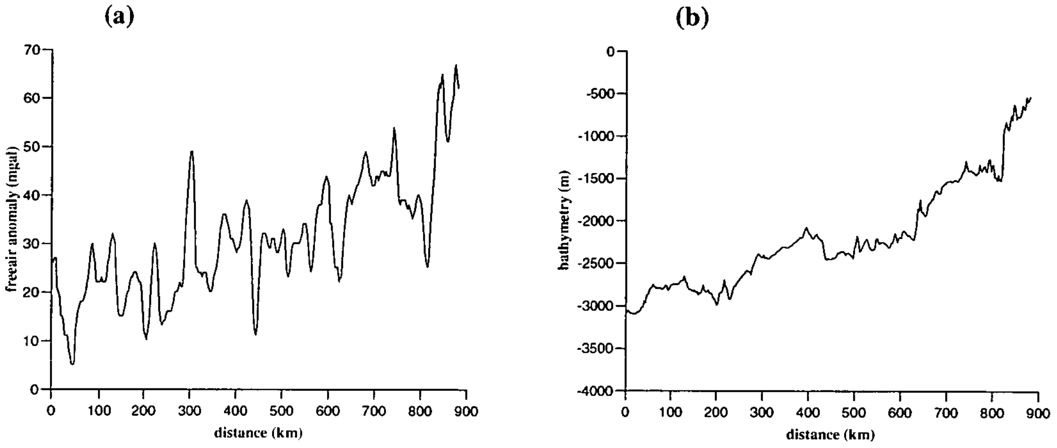

Figure 6.16. (a) Freeair anomaly and (b) bathymetry for the test ship profile.

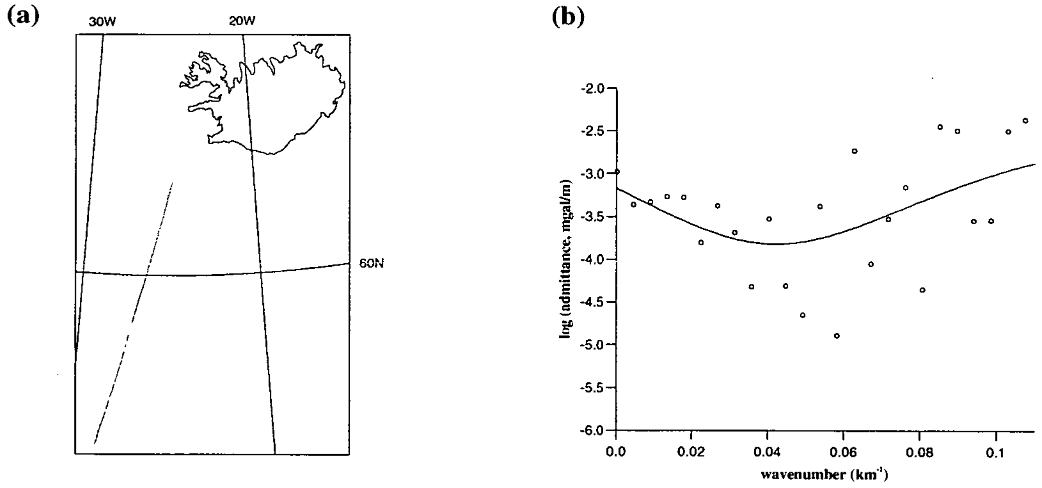

Figure 6.17. (a) Location and (b) isostatic admittance of the test ship profile (circles) and theoretical admittance curve for $z_m = 21.5$ km, $T_e = 6.5$ km, and $f = 100$.

6.4.2 One-dimensional admittance

As the ETOPO5 dataset was partly generated from altimeter gravity data [NGDC (1993)], it will correlate with such a field. For this reason, a one-dimensional admittance analysis was performed upon gravity and bathymetry data from a sample ship profile passing over the Reykjanes Ridge. The ship track is part of one leg from the Discovery cruise, DI84L1-2, extracted from the *GEODAS CD-ROM* [NGDC (1994)]. The freeair anomaly and bathymetry are shown in fig 6.16(a) & (b) respectively. These were re-interpolated along-track at regular intervals to enable their Fourier transformation. Fig 6.17(a) shows the location of the profile.

In the 1-D analysis, admittances were calculated using the equation

$$Q_B = \frac{G_F \Sigma^*}{\Sigma\Sigma^*} - 2\pi G \ , \tag{6.8}$$

where G_F is here the 1-D Fourier transform of the freeair anomaly profile, and Σ the 1-D transform of the load.

The 1-D analysis yielded a mean depth to Moho of 21.5 km, an elastic thickness of 6.5 km, and a Moho to surface loading ratio of 100. Fig 6.17(b) shows the isostatic admittance for the profile (circles), with the best-fit least squares theoretical admittance curve for $z_m = 21.5$ km, $T_e = 6.5$ km, and $f = 100$.

6.4.3 Coherence

Calculation

The coherence between the Bouguer anomaly and the topography of an area reveals the scale at which loading on the Moho (whether from above or below) changes from being compensated to being supported without flexure (§1.4.4). It is calculated in the wavenumber domain by

$$\gamma^2 = \frac{\langle G_B \Sigma^* \rangle^2}{\langle G_B G_B^* \rangle \langle \Sigma\Sigma^* \rangle} \cdot \tag{6.9}$$

where G_B is the Fourier transform of the Bouguer anomaly, and Σ that of the load. An example is shown in fig 6.18: this is the coherence for the Reykjanes Ridge. Note again the noise above the ordinate/abscissa Nyquist wavenumber, as discussed in §6.3.

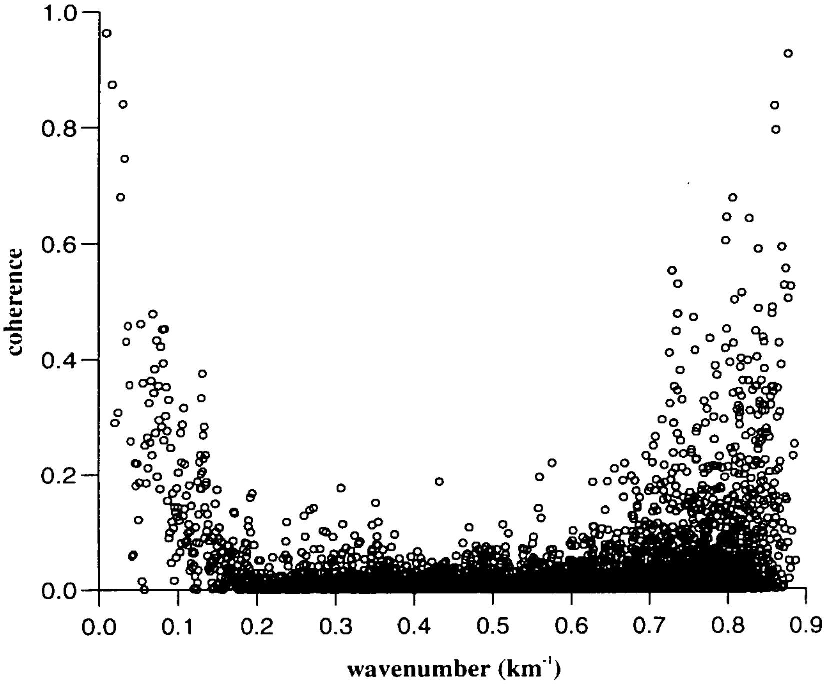

Figure 6.18. Coherence of the Reykjanes Ridge (IFC data).

Coherence plots

Following the method for calculating the best-fit curve to admittance data (§6.4.1), the standard error of the difference between real and theoretical coherences, α_d, was calculated for combinations of f varying from 0 to 1 in steps of 0.01, then 0 to 100 in units of 1; and T_e varying from 0 to 50 km in steps of 0.5 km, then 0 to 100 km in steps of 1 km. The formula for the theoretical curves is given by eq.1.43: note they are not dependent upon the depth to compensating layer (z_m). The curves were fitted for three values of k_{max}: 0.11 km^{-1}, 0.15 km^{-1} and 0.3 km^{-1}. Table 6.2 shows the results only for k_{max} = 0.11km^{-1}, as surprisingly, the T_e and f values for k_{max} = 0.15 and 0.3 km^{-1} were found to be identical, only with a lower standard error of fit.

The elastic thickness and loading ratio figures in table 6.2 show excellent consistency in areas with both Sandwell and IFC data, with the IFC data showing a slightly better degree of fit. However, the values for the loading ratio are consistently around 0.16. This seems unusual considering the supposed tectonic differences between the areas, but can be explained by the relative insensitivity of the coherence to variations in f (discussed in §1.4.4, and the next subsection).

The graphs in fig 6.19 show the coherence data for all areas and datasets, with

Area	min. α_d	T_e (km)	f
Charlie-Gibbs FZ	0.0293	26.0	0.17
CGFZ (Sandwell)	0.0432	23.0	0.16
Reykjanes Ridge	0.0282	12.5	0.15
Reykjanes (Sandwell)	0.0305	12.5	0.15
Iceland	0.0311	5.5	0.15
U.K.	0.0243	9.5	0.16

Table 6.2. Best values of T_e and f from coherence data.

the best least-squares fit theoretical curve generated from the values in table 6.2. The coherence data for the Charlie-Gibbs FZ, figs 6.19(a) & (b), obviously do not match the expected theoretical model. If the data are reliable, this suggests that the approach of fitting the model of eq.1.43 by a least-squares method is not applicable in this area. Studying the plots by eye, it is difficult to find a curve of the form of eq.1.43 that does fit the data. While this suggests that the model does not accurately represent the tectonics of the area, this area is the smallest of the four sub-areas, and thus contains less power at long wavelengths. This would imply poorer resolution at this end of the spectrum, so the low coherence exhibited in figs 6.19(a) & (b) could be due to this phenomenon, rather than any physical relationship between gravity and topography.

The fit of the curves to the data in figs 6.19(c) and (d), the Reykjanes Ridge, is very good at wavenumbers less than 0.05 km^{-1} (approximately 125 km wavelength). It is also good for the Iceland and U.K. areas, figs (e) and (f), if the data below wavenumber 0.05 km^{-1} and 0.04 km^{-1} respectively, are ignored.

$f - T_e$ plots

Figs 6.20 to 6.25 show the degree of fit of curves generated from all values of f and T_e to the coherence data for the four sub-areas (including Sandwell data). The most striking aspects of these plots are the extent of the area over which there is very little change in α_d, and that α_d is very low in this region of the plot. These support the observation that coherence is insensitive to variations in loading ratio. However, they also suggest that coherence is insensitive to variations in plate elastic thickness, a hypothesis seemingly in contradiction with the studies of Forsyth (1985). Take the Charlie-Gibbs FZ sub-area for example. A curve with a 26 km elastic thickness and 0.17 loading ratio give $\alpha_d = 0.0293$;

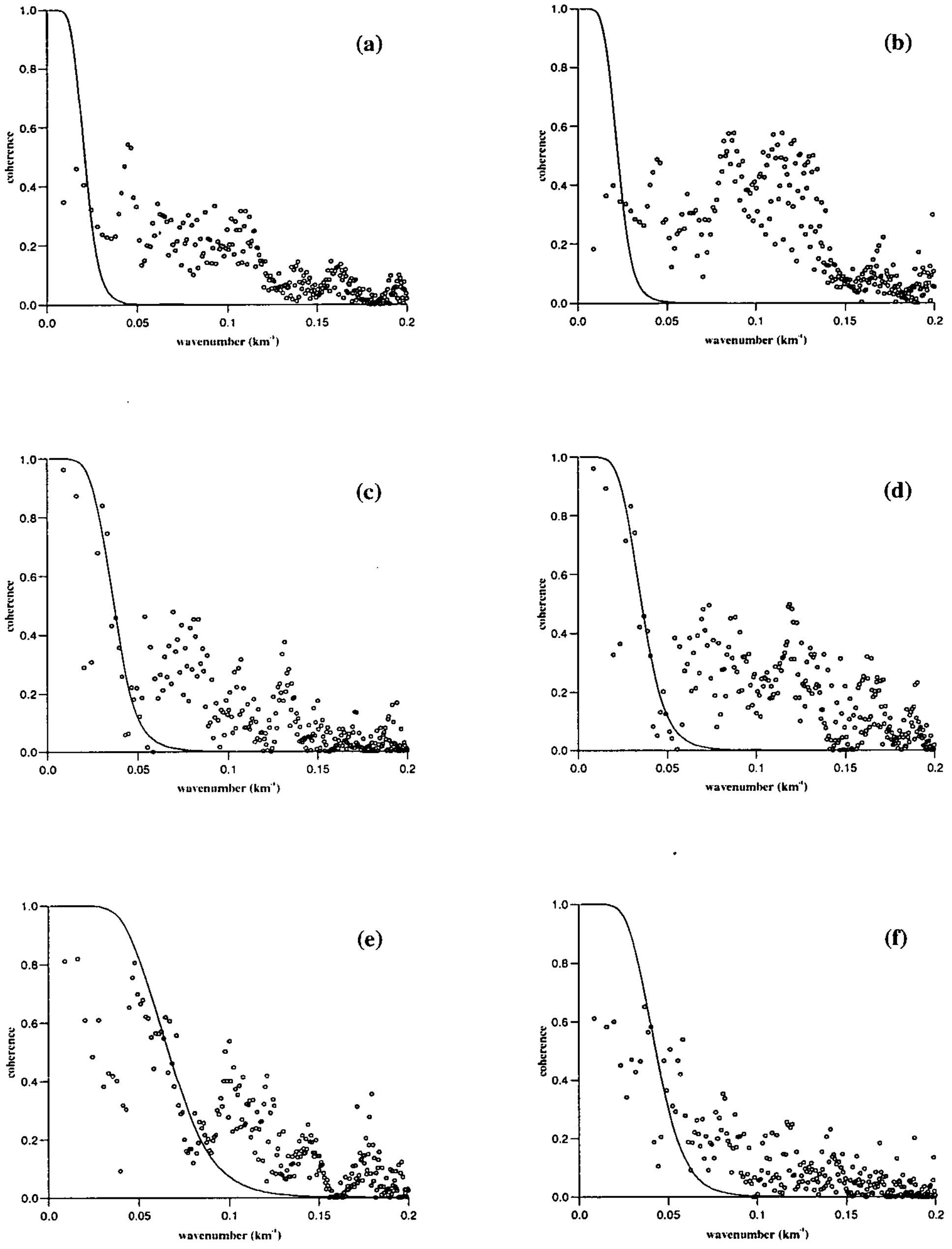

Figure 6.19. Coherence plots for (a) Charlie-Gibbs FZ, (b) Charlie-Gibbs FZ (Sandwell data), (c) Reykjanes Ridge, (d) Reykjanes Ridge (Sandwell data), (e) Iceland, and (f) U.K. areas. The plots also show the best fit theoretical curve given by the parameters in table 6.2.

but a curve with $T_e = 50$ km and $f = 10$ give $\alpha_d = 0.0299$. The other sub-areas show a better degree of constraint on the lowest error solutions, but while the lower values of elastic thickness have high errors of fit, there is still considerable leeway in fitting curves with high values of T_e.

Another reason for the variations in good solutions could be poor data. However in the light of the reasonably well-constrained solutions from admittance studies, this seems not to be the case.

It is more likely that this kind of least-squares fit procedure is not the best way to calculate elastic thickness from coherence data. Whereas admittance fits are constrained only at one point (the ordinate intercept), Forsyth's coherence model constrains the curves at both the ordinate intercept and the large-k asymptote. Given the distribution of the coherence data in the plots in fig 6.19, it can be understood how a least-squares solution can give similar values of fit error for a wide range of curves.

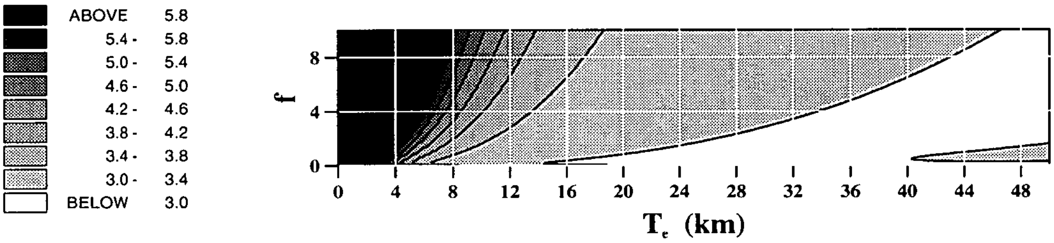

Figure 6.20. $f - T_e$ plot of $\alpha_d \times 10^2$ for Charlie-Gibbs FZ from coherence data.

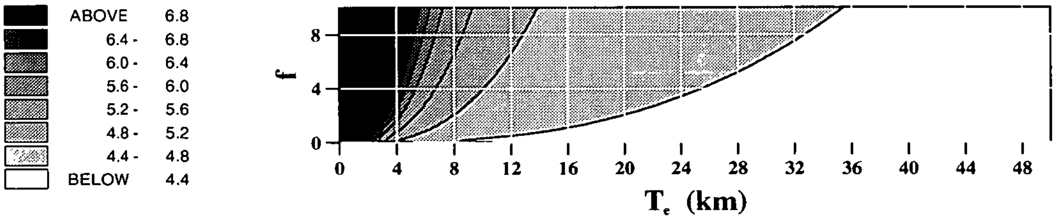

Figure 6.21. $f - T_e$ plot of $\alpha_d \times 10^2$ for Charlie-Gibbs FZ (Sandwell) from coherence data.

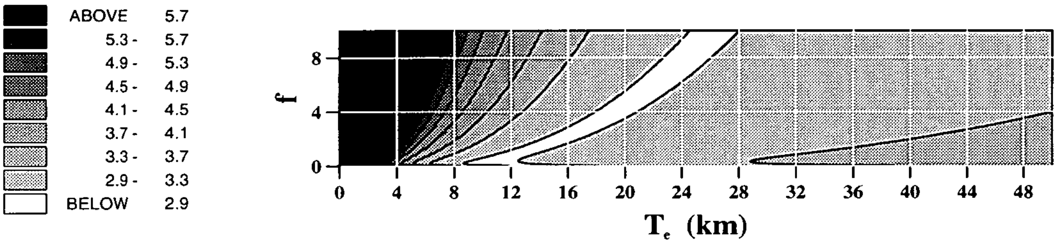

Figure 6.22. $f - T_e$ plot of $\alpha_d \times 10^2$ for Reykjanes Ridge from coherence data.

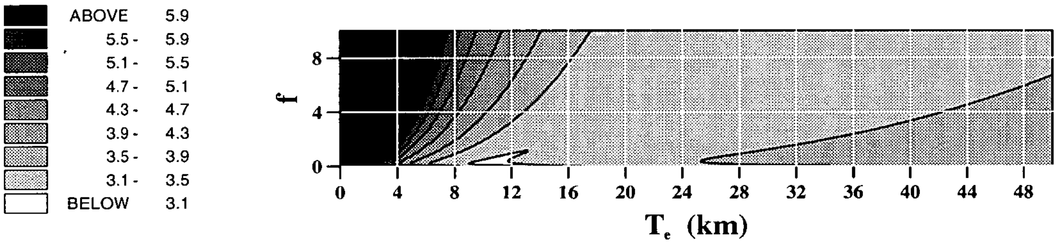

Figure 6.23. $f - T_e$ plot of $\alpha_d \times 10^2$ for Reykjanes Ridge (Sandwell) from coherence data.

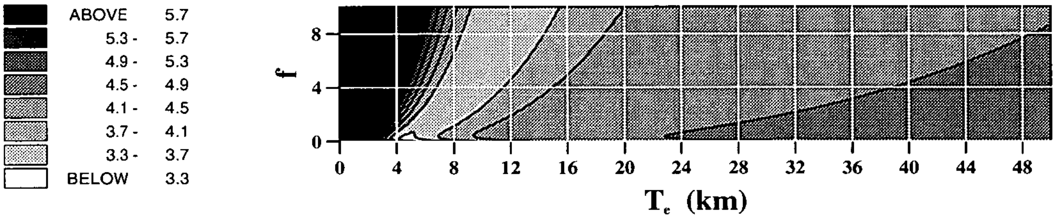

Figure 6.24. $f - T_e$ plot of $\alpha_d \times 10^2$ for Iceland area from coherence data.

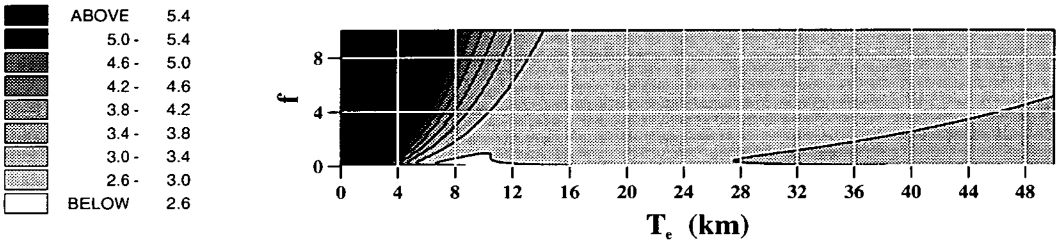

Figure 6.25. $f - T_e$ plot of $\alpha_d \times 10^2$ for U.K. area from coherence data.

6.5 Discussion

An initial analysis of tables 6.1 and 6.2 indicate a large difference between the values of elastic thickness and loading ratio returned by admittance and coherence studies. The estimates of T_e from the coherence analyses are uniformly lower than those from admittances. Furthermore, estimates of f from coherences imply loading occurs predominantly at the surface in all sub-areas, while admittance studies suggest the opposite is true, and give a wider spread of values. It was suggested (§6.4.3) that the least-squares fitting of a theoretical curve constrained at two points to the coherence data is not a good method of determining elastic thickness. Furthermore, the degree of fit of the curves to the data was found to be very insensitive to variations in the Moho to surface loading ratio, for values greater than 1. Thus we would expect the coherence estimates to be less reliable.

To test the validity of the 2-D approach, and also the use of the ETOPO5 dataset, a 1-D admittance analysis was performed on a single ship track. This track lay at the northern end of the Reykjanes Ridge, extending into the seas close to Iceland. The result from this analysis is discussed in the sub-section on the Reykjanes Ridge, and in the summary at the end of the chapter.

The results of Moho depth and elastic thickness from the admittance and coherence analyses follow, together with some values measured in previous studies. As a prelude, a summary of studies of crustal thicknesses from seismic refraction surveys by White et al. (1992), found the mean thickness of normal oceanic crust to be 7.1 km.

Bear in mind that the variable z_m in eq.1.41 is the *mean* depth to the compensating density contrast over the whole area, as far as this concept is viable.

This has been taken as the depth to the Moho, the crust/mantle boundary. Furthermore, z_m is the depth below sea level, which in oceanic areas will be larger than the crustal thickness by up to 4 km. Most of the following cited references have found the Moho depth using seismic methods, which detect differences in the velocity of seismic waves through strata. As this velocity is largely dependent upon the rock density, the seismic depth to the Moho will be equivalent to the gravitationally determined depth.

Charlie-Gibbs FZ

Taking the Charlie-Gibbs FZ IFC data, the admittance method yields an elastic thickness of 7 km and a Moho depth of 24.5 km, though if the outlying points are deleted (§6.4.1), these figures become 5 km and 15 km respectively. The Sandwell admittance data return an elastic thickness of 4.5 km and a Moho depth of 25 km, but omitting the outliers results in values of 3.5 km and 20.5 km respectively. The coherence data yield elastic thicknesses of 26 km from the IFC data, and 23 km from the Sandwell data. The mean ocean depth in this area is approximately 3.5 km: Moho depth values should be reduced by this figure to obtain a crustal thickness.

A seismic refraction survey of the active transform of the Charlie-Gibbs FZ by Whitmarsh and Calvert (1986) yielded crustal thicknesses between 3.5 and 5 km, with the crust thickening to 8 km due south of the FZ. However, an admittance analysis of gravity and bathymetry profiles across a number of Atlantic FZs by Kogan and Kostoglodov (1981), found a best fitting crustal thickness of 28 km for an Airy model of compensation, but 5 km for a flexure model with an elastic thickness of 6 km. The summary study by White et al. (1992) found the crust at fracture zones to be generally thinner than the normal oceanic crust, with a mean value of 4.0 km.

These estimates of crustal thickness differ greatly from the values found in this study, both for the IFC and Sandwell data. These latter values, of over 15 km, are much too high for normal oceanic crust, and especially the anomalous crust at a fracture zone. The estimate of elastic thickness from the IFC field admittance study does show good agreement with the estimate by Kogan and Kostoglodov (1981) however.

Reykjanes Ridge

Admittance studies on the Reykjanes Ridge yield an elastic thickness of 3 km and a Moho depth of 10 km, from the IFC field, while the Sandwell field generates values of 3.5 km and 20 km respectively. Both datasets indicate the load to be almost exclusively applied at the Moho. Coherence studies give an elastic thickness of 12.5 km from both fields. The mean ocean depth in this area is approximately 2 km.

The 1-D admittance analysis estimated the mean depth to Moho as 21.5 km, with a plate elastic thickness of 6.5 km. These figures show close agreement with those from the Sandwell gravity field.

Estimates of the elastic thickness of the lithosphere at the Reykjanes Ridge, from admittance studies by Cochran (1979), found T_e to lie in the range 2-6 km. A seismic study of the ridge at 60° N by Bunch and Kennett (1980), gave crustal thicknesses of 7 km at the ridge axis, and 10 km at the 9 Ma line (around 80 km from the axis). The White et al. (1992) paper quotes a mean crustal thickness from seismic studies of 10.3 km for oceanic crust affected by the Iceland mantle plume. They state that the influence of this plume can extend up to 1000 km from the plume core, thus incorporating all of this sub-area.

These values for z_m and T_e show fair agreement with the IFC data admittance analysis results, but surprisingly do not for the Sandwell data. However, the results from the 1-D admittance analysis support the estimates from the Sandwell field. This is discussed later.

Iceland

Elastic thicknesses from admittance and coherence data are more in agreement, being 4.5 km and 5.5 km respectively. Admittance studies give a Moho depth of 16.5 km, and a Moho to surface loading ratio of 6.

This depth to Moho might appear to be too low compared to the value obtained in southwest Iceland by Bjarnason and Menke (1993) of 20-24 km. Further still, seismic velocity studies by Gebrande et al. (1980) postulated the Moho at 30 km depth below central Iceland, though they acknowledge the petrology of this material (an ultrabasic melt from around 15 to 30 km depth) could imply a region of anomalous mantle.

However, around two-thirds of the Iceland study area is surrounding ocean, which White et al. (1992) assign a mean crustal thickness of 10.3 km (and which has a mean depth of 750 m). This would decrease the estimates of Moho depth and elastic thickness over the whole area somewhat, but certainly not as much as implied by the admittance studies.

U.K.

Finally, admittance and coherence analyses of the data over the U.K. area give the elastic thickness as 6 km and 9.5 km respectively. The admittance study gives the Moho depth as 22.5 km with $f = 14$.

Dewey (1982) gives the typical crustal thickness of the British Isles as 31 km. Regional seismic surveys give values close to this figure: the LISPB-IV profile from Cape Wrath to Derbyshire [Bamford et al. (1978)] found the Moho depth to vary between 30 and 35 km; a seismic refraction survey over Cornwall and on a profile from Ireland to Brittany by Holder and Bott (1971), found a Moho reflector at 27 km; a survey of the North Sea by Barton and Wood (1984) found the crust generally to be 32 km thick, thinning to 20 km at the Central Graben; and multichannel seismic profiles over the Rockall passive margin by Fowler et al. (1989) found the Moho deepening from 15 to 27 km across the margin.

Barton and Wood (1984) also put an upper limit of the elastic thickness over the North Sea of 5 km. And a study by Watts (1992) gives the elastic thickness of the Rockall plateau as 5 km.

All the areas in the above surveys are included in Area 4, rendering any estimate of a mean Moho depth or elastic thickness dubious.

Summary

In general, the estimates of Moho depth and elastic thickness returned by the admittance and coherence studies do not show good agreement with values obtained from previous surveys. Theoretical admittance curves in fig 6.8 show a poor fit to the data, especially in the Charlie-Gibbs FZ and Reykjanes Ridge sub-areas; while the coherence curves in fig 6.19 show a poor fit for all areas. The discrepancy in the coherence method results has been suggested as arising from the least-squares method being inappropriate, in that there are two constrained points. However, the admittance method should give better results as only one point is constrained.

In the Charlie-Gibbs FZ, the IFC field has a poor resolution due to the large separation between satellite groundtracks, and the scarcity of ship track data.

Thus, while we would expect a poor result in this case, it is surprising that the Sandwell model gives similar estimates of z_m and T_e from both admittance and coherence studies, as this field is of much higher resolution. One possible cause of this discrepancy is the presence of an altimeter-derived component in the ETOPO5 model contaminating the correlation. Furthermore, this sub-area is relatively small, meaning that although the internal tectonics should be uniform, there is comparatively little data to perform an accurate analysis.

Over the Reykjanes Ridge, the Moho depths from admittance analyses of the IFC and Sandwell data are very different. The IFC estimates of z_m are too low, while those from the Sandwell field are too high. Interestingly, the estimate of Moho depth from the 1-D analysis almost exactly agree with the estimate from the Sandwell field. As the 1-D gravity is not derived from altimeter data, and the 1-D bathymetry is an independent dataset, we would expect estimates from this method to be the most accurate, assuming that the admittance algorithms are in order. A comparison between 1-D and 2-D methods should be investigated further.

In the Iceland and U.K. sub-areas, it is probably incorrect to compare the estimates of Moho depth and elastic thickness from admittance analyses with the values from the literature. These sub-areas have large amounts of heterogeneous crust, rendering a mean value of z_m and T_e difficult to determine from a spectral approach. However, the results are not so inaccurate as to be discarded out of hand. A Moho depth of 16.5 km for the Iceland sub-area is reasonable given the large amount of oceanic crust in the area. Furthermore, as the U.K. sub-area is largely continental crust, the estimated Moho depth of 22.5 km is close to those values determined in previous studies. Finally, it should be pointed out that there exists no inherent correlation between the gravity and ETOPO5 datasets in the land areas, as there was at sea.

The misfits between the admittance and coherence estimates, and those from previous studies could suggest incorrect modelling of the loading regimes in certain provinces. However, as previously mentioned, the discrepancy is most probably due to the ETOPO5 grid, but it is possible that the assumption of a symmetrical isostatic response function is generating the errors. This, again, should be investigated further.

Chapter 7

Summary and conclusions

The aim of the thesis was to develop an algorithm to combine heterogeneous datasets using the fast Fourier transform, and apply the method to data in a large, predominantly marine area of the Earth, with the intent of generating accurate geoid and gravity models.

The requirement of the FFT that input data should exist on a regular grid, has resulted in the development of two new gridding routines, for satellite and ship gravity data.

The along-track geoid slope of the altimeter profiles is calculated. This removes the effects of long-wavelength orbit error and sea surface topography, meaning no cross-over error analysis is needed. However, it also underestimates the true slope value of the anomaly. The application of a specifically designed gridding kernel spreads out a slope value to create a complete grid, yet retains a degree of the along-track resolution. The gridding procedure also allows for the averaging of colinear repeat passes, which removes the time-variant oceanographic noise. Further still, the spectral characteristics of the gridding routine lead to a smoothing of the data, reducing the high amplitude short-wavelength noise generated by the along-track differencing.

An altimeter geoid/freeair anomaly grid was created using a Fourier domain representation of the inverse Vening-Meinesz transformation, that allows for the combination of data from multiple altimeter missions.

Interpolating the ship gravity data onto a grid also involves differencing along the track profile. This removes the long-wavelength gravity meter drift, and the uncertainty in the datum that often arises. It also removes the need to perform computationally demanding cross-over error adjustments. The freeair anomaly field generated from altimeter data is used to constrain the mean value of gravity along a ship track.

Previous studies using Fourier domain techniques have tended to use ship gravity data as a non-contributing verification of the gravity field from satellite data. Here, the ship data are combined with the altimeter gravity field resulting in a much improved model. Furthermore, the IFC algorithm is able to include terrestrial freeair anomaly data, and, owing to the simple mathematical relationships between the geoid height, gravity anomaly, and their spatial derivatives of any order, these data can also be combined in the iteration scheme.

In comparison, the least squares collocation method of heterogeneous data combination, while having proven accuracy, must invert matrices of size $N \times N$, for N data points. This requires the use of powerful computers and a long run-time. In contrast, the IFC algorithm, with its FFT processing, is able to process large datasets in a very short time. A new technique was developed to reduce the errors arising from the Fourier transformation of a truncated dataset. This involved increasing the dataset size by 'mirroring' 10% of the edges and tapering this border.

The intrinsic accuracy of the gridding and IFC algorithms was determined by testing the ability of the algorithm to reproduce accurately determined, self-consitent geoid and freeair anomaly fields, using simulated data extracted from the fields. This was assessed by comparing the simulated data with values interpolated from the generated grids at the equivalent spatial location. The standard deviation between the simulated ship freeair anomalies and the values interpolated from the altimeter-only freeair anomaly grid was 10.50 mgal; that between the simulated freeair anomalies and the values interpolated from the combined freeair anomaly grid was 4.54 mgal, showing an improvement upon the altimeter-only solution, and comparing favourably with the 5.76 mgal accuracy of a LSC grid.

A 5 km gridded model of the gravity field of the North Atlantic was then created from Geosat/ERM and Topex/Poseidon altimeter data, and marine and land freeair anomaly datasets. The accuracy of the altimeter geoid was assessed by comparing the along-track slopes of the altimeter profiles with values obtained by interpolation of the model grid at the equivalent locations. The standard deviation of the difference between Geosat slopes and the altimeter-only slopes was 6.95 μrad; while that for Topex/Poseidon data was 6.75 μrad. The standard deviation of the difference between Geosat slopes and the IFC geoid slopes was 6.81 μrad; that for Topex/Poseidon data was 6.56 μrad. Comparing the freeair anomalies of the ship tracks with values interpolated from the model fields gave a standard deviation of 13.4 mgal for the altimeter-only field, and 10.2 mgal for the IFC field. While these figures show a slight improvement of the IFC over the altimeter-only models, a spectral and visual comparison immediately confirms the improvement.

Finally, the OSU91A model was added back to the IFC freeair anomaly grid, and this was compared with a grid produced by Sandwell et al. (1995). The mean difference between the fields was -0.67 mgal with a standard deviation of 8.74 mgal. The IFC model compares very well with the Sandwell model, especially considering the latter was generated from much more densely spaced ERS-1 altimeter data.

The isostatic admittance and coherence was calculated for four sub-areas in the IFC and Sandwell models: the western fossil transform of the Charlie-Gibbs fracture zone, the Reykjanes Ridge, the Iceland hot spot, and the U.K. and its continental shelf. The topographic/bathymetric relief data was selected from the ETOPO5 dataset. The admittance and coherence studies yielded estimates of the Moho depth, lithospheric elastic thickness, and ratio of Moho to surface loading, by fitting curves from a range of theoretical models to the data. The model that gave the best least-squares fit was deemed to be representative of the actual isostatic compensation mechanism. The results from the admittance studies showed some agreement with values obtained from earlier seismic surveys in the Iceland and U.K. regions, but poor agreement for the Reykjanes Ridge, and very poor agreement for the Charlie-Gibbs fracture zone from both the IFC gravity data and the high-resolution Sandwell data. Except for one case, the Iceland area, the coherence estimates of elastic thickness were too large when compared with both previous studies and the admittance results. This general lack of correlation between values was proposed as having a variety of sources: errors in the topographic model; the failure of least-squares regression to determine the best fitting model; the inappropriate use of a symmetrical isostatic response function; or incorrect assumptions about the physics of the compensation mechanisms in certain regions.

In conclusion, this thesis has produced algorithms

1. that grid and combine altimeter measurements of the geoid height from many satellite missions;

2. that grid shipboard measurements of the freeair anomaly; and,
3. that can combine heterogeneous potential field data, processing large datasets very rapidly.

The resulting gravity field can be used to determine the crustal and elastic thicknesses in a region approximately, though it is proposed that the sources of error mentioned above must be investigated further. The method can also be applied to small areas. Given a satellite mission with a dense groundtrack spacing, and many shipboard observations, the algorithms could be applied to the data for exploration purposes or local geophysical surveys.

I suggest that, despite the global availability of high density altimeter datasets such as ERS-1 and Geosat/GM, they will never supercede the use of shipboard measurements of the gravity field. First, shipboard gravity meters can make point observations at very small track spacings, whereas altimeter measurements presently have an along-track resolution of at least 20 km. The increasing accuracy of marine gravity surveys, and the gridding procedure described here, can remove most errors that have been characteristic of marine surveys in the past. Second, marine surveys measure the gravity field directly, which of course contains no sea surface topography expression. The accuracy of satellite altimeter determinations of the geoid will always be limited by the accuracy to which the sea surface topography is known.

Appendix A

The Lambert conical conformal projection

When using the flat-Earth approximation to Laplace's equation it is desirable to have minimal coordinate scale distortion throughout the area of study. Consider data given on a latitude/longitude grid, separated by one degree in both coordinates. Adjacent gridpoints on the same parallel (line of latitude) at the equator have a separation of 111 km, whereas the adjacent gridpoints at 70° N have only a 38 km separation. Yet a Fourier analysis of the data would consider this pair of adjacent points as though they had an equal separation, thus misinterpreting the wavelengths of anomalies present.

The transformation of the coordinate system from ellipsoidal or spherical to planar using map projections can dramatically reduce these distance distortion errors. The projection used in this study is the Lambert conical conformal with two standard parallels. To quote from Dorman and Lewis (1970): "The difference between distances measured on the spherical Earth and those measured on a Lambert conformal map are slight; hence we expect little distortion due to using the plane approximation in transforming into the frequency domain."

A conformal projection is one which maintains correct representation of shapes (angles); the scale distortion is the same in every direction, an important property for the geodesist. The Lambert projection is particularly suited to areas with a large east-west extent, such as the North Atlantic. Another useful conformal projection is the transverse Mercator, best suited for areas with a large north-south but limited east-west extent.

In the Lambert projection, geographical coordinates are mapped onto a cone intersecting the reference ellipsoid at two parallels within the study area and with its apex on the rotational axis of the ellipsoid. The resulting coordinates on the plane are called 'eastings' and 'northings'. The central meridian of the study area forms the zero easting axis. The coordinate scale distortion, a measure of the accuracy of the projection, is dependent only upon latitude: at the standard parallels the distortion is zero.

In this study, the standard parallels are at $53\frac{1}{3}$° N and $66\frac{2}{3}$° N. The central meridian is at 25° W. The projection used the Geodetic Reference System 1980 (GRS80) reference ellipsoid, with a semi-major axis of 6378137.0 m and a flattening of 1/298.257. The scale distortion at the lower latitude limit of the study area (47° N) is 1.017343, that at 60° N is 0.993227, while the distortion at the higher latitude limit (72° N) is 1.018172.

The equations used for the coordinate transformation are given in Richardus and Adler (1972).

Appendix B

Comparison of gridding kernels

The simulated ascending altimeter profiles (§2.8) were gridded using the kernels listed below. Profiles were interpolated from the computed slope grids at the locations of the simulated satellite tracks ("on-track"), and also at "mid-tracks" lying between the simulated tracks (see fig B.1). These were then compared with the along-track slopes of the simulated dataset, and of the geoid slope along the mid-tracks (interpolated, using a bicubic interpolator, from the test model geoid grid, fig 2.6). The standard deviation of the on-track slopes is 7.81 μrad, that for the mid-track simulated slopes is 7.49 μrad.

In all cases the search radius of the kernel was 65 km. Cross-sections through the kernels are shown in fig B.2. The distance of an influenced gridnode from the observation location is x.

1. The "Witch of Aganissi":

   $$\delta\omega(x) = \frac{1}{1 + (\frac{x}{a_o})^2} \quad , \tag{B.1}$$

   with the halfwidth $a_o = 11.375$ km. This is shown in fig B.2 as the solid, dark curve. Fig B.3(a) and (b) show the resulting slopes (dark curves) when this kernel is applied to the simulated profiles.

2. An inverse cubic function used by Sandwell (1984):

   $$\delta\omega(x) = \frac{1}{1 + (\frac{x}{a_o})^3} \quad , \tag{B.2}$$

   with the halfwidth $a_o = 11.375$ km. This is shown in fig B.2 as the dashed curve. Fig B.4(a) and (b) show the resulting slopes (dark curves) when this

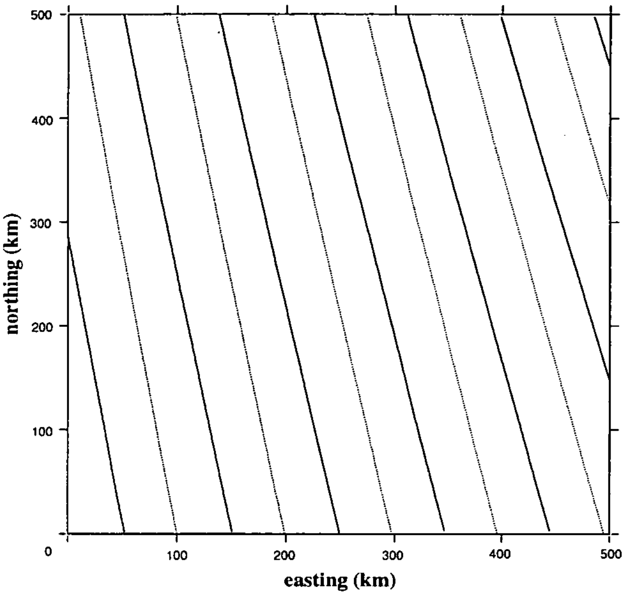

Figure B.1. Location of the simulated on-track (dark) and the mid-track altimeter profiles (light).

kernel is applied to the simulated profiles.

3. Gaussian function:

$$\delta\omega(x) = e^{-x^2/\alpha^2} \quad , \tag{B.3}$$

with $\alpha = 13.667$ km, chosen so that the kernel has the same halfwidth as the above two kernels. This is shown in fig B.2 as the solid, light curve. Fig B.5(a) and (b) show the resulting slopes (dark curves) when this kernel is applied to the simulated profiles.

4. Sinc function:

$$\delta\omega(\delta x, \delta y) = \frac{1}{\Delta x\, \Delta y} \, \frac{\sin(\pi\, \delta x/\Delta x)}{\pi\, \delta x/\Delta x} \, \frac{\sin(\pi\, \delta y/\Delta y)}{\pi\, \delta y/\Delta y} \quad , \tag{B.4}$$

from Vermeer (1992), where $x = \sqrt{\delta x^2 + \delta y^2}$, and $\Delta x, \Delta y$ are the target grid spacings. This is shown in fig B.2 as the dotted curve. Fig B.6(a) and (b) show the resulting slopes (dark curves) when this kernel is applied to the simulated profiles.

5. UNIMAP bilinear interpolation. The on-track simulated slopes were gridded using the UNIMAP bilinear interpolation package. Fig B.7(a) and (b) show the resulting slopes (dark curves) when this kernel is applied to the

Kernel	*On-track*		*Mid-track*	
	computed	*difference*	*computed*	*difference*
Witch	4.34	4.19	2.21	7.15
inverse cubic	5.46	3.24	2.39	7.10
gaussian	6.03	2.87	4.77	7.45
sinc	9.37	4.09	409	409
UNIMAP bilinear	6.45	2.79	2.79	7.14

Table B.1. Standard deviations in μrad of the slopes interpolated from a grid computed using the stated gridding kernels, and the standard deviations of the difference between the simulated slopes and the computed slopes, at the on-track and mid-track locations. For comparison, the s.d. of the simulated on-track slopes is 7.81 μrad, that of the simulated mid-track slopes is 7.49 μrad.

simulated profiles.

While the Witch gridding kernel gives the largest difference of computed versus simulated slopes on-track, it is the only gridding routine that does not involve calling external routines, thus saving on computer run-time. The inverse cubic kernel calls the square root function, the gaussian kernel calls the exponential function, the sinc kernel calls the sine function, while the UNIMAP bilinear interpolator requires the user having access to the UNIRAS software.

Regarding execution time for the kernels, the inverse cubic kernel takes around 1.1 times longer than the Witch kernel, the gaussian kernel took 1.7 times as long, while the sinc kernel took 3.5 times longer.

Given that the algorithm should be self-contained, the UNIMAP interpolator was discarded, also because no weighting grid is produced from this method.

While the sinc function is theoretically the best interpolator, a conjecture borne out by the coincidence of the simulated and computed profiles in fig B.6(a), fig (b) shows that it does not reproduce the slope values at all well elsewhere. This arises from the truncation of the kernel in the space domain. This kernel was therefore discarded also.

In the mid-track locations, none of the kernels can mimic the slope values. From table B.1, the spread of the differences is of the order of the spread of the simulated slopes in all cases, except for the sinc function where it is far greater.

[This appendix was included after the oral examination. With hindsight, the gaussian kernel yields the best results with no significant increase in computing time.]

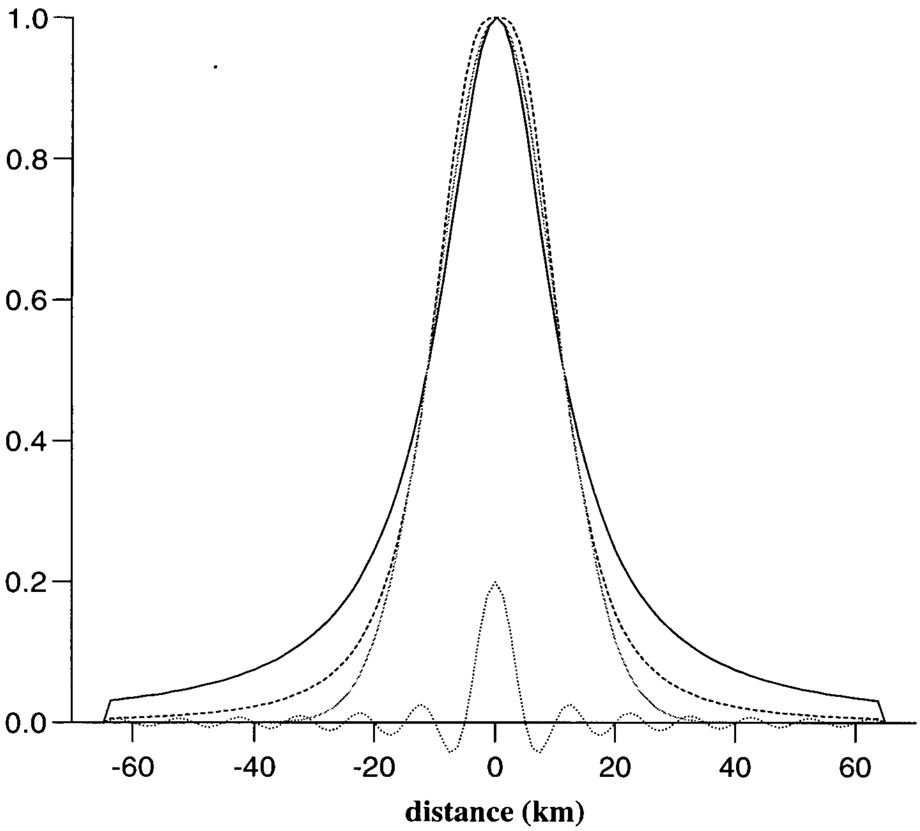

Figure B.2. The gridding kernels used in the comparison: Witch (solid, dark); inverse cubic (dashed); Gaussian (solid, light); sinc (dotted).

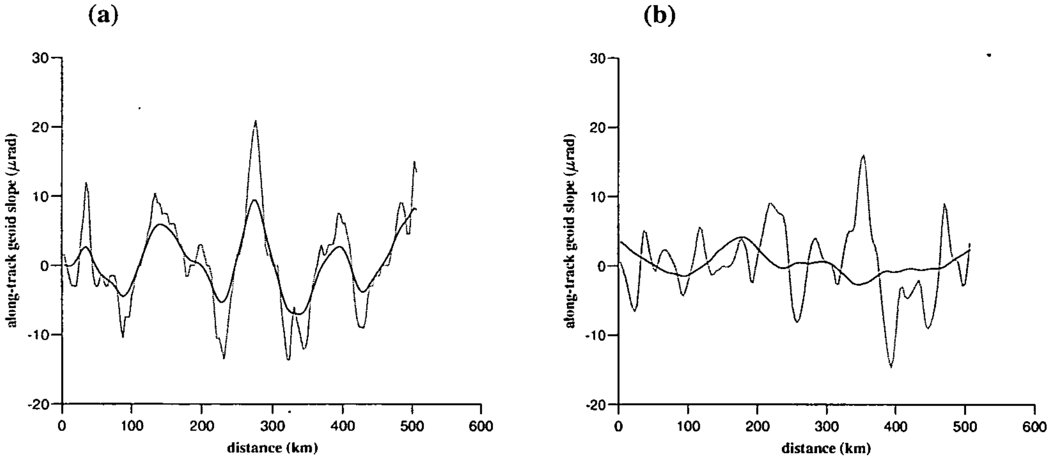

Figure B.3. Slope comparison from simulated satellite tracks (light curves), with values interpolated from the grid of slopes (dark curves) computed using the Witch kernel (eq.B.1). (a) shows values on-track, (b) the values at the mid-track.

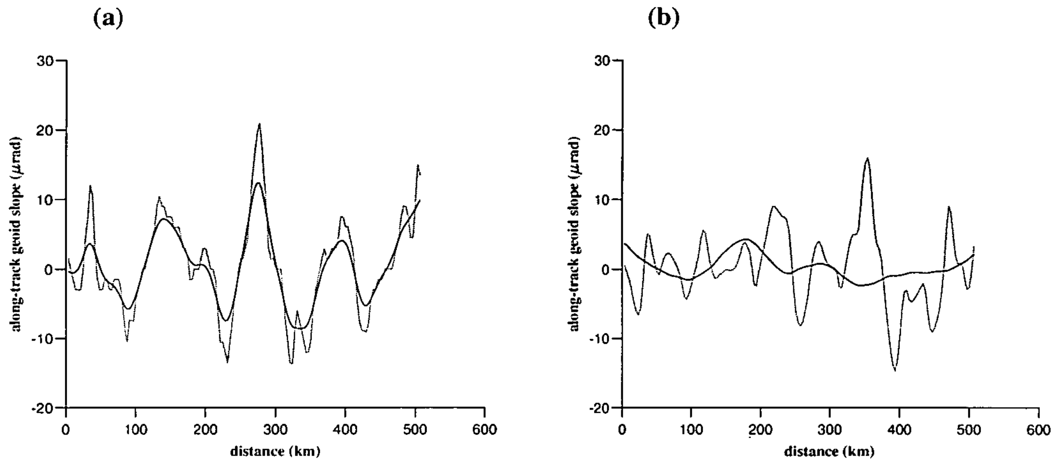

Figure B.4. As fig B.3, for the inverse cubic kernel (eq.B.2).

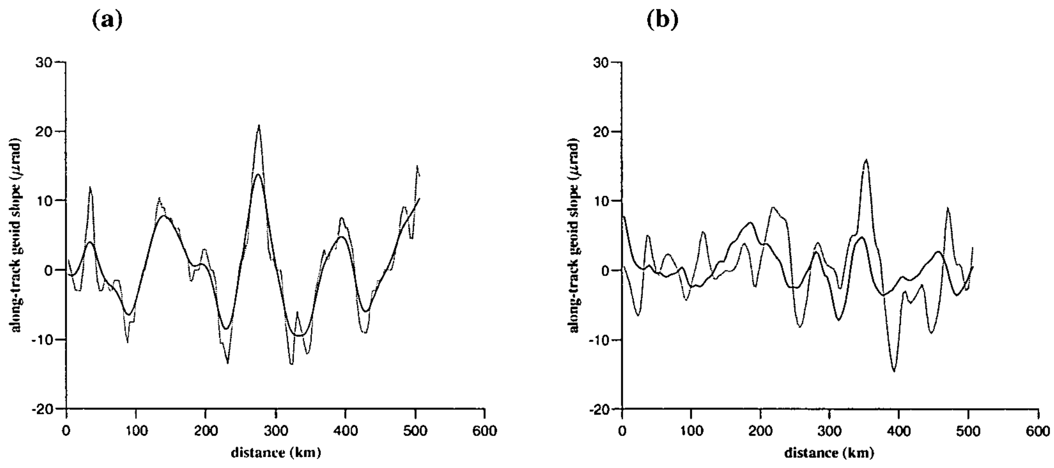

Figure B.5. As fig B.3, for the gaussian kernel (eq.B.3).

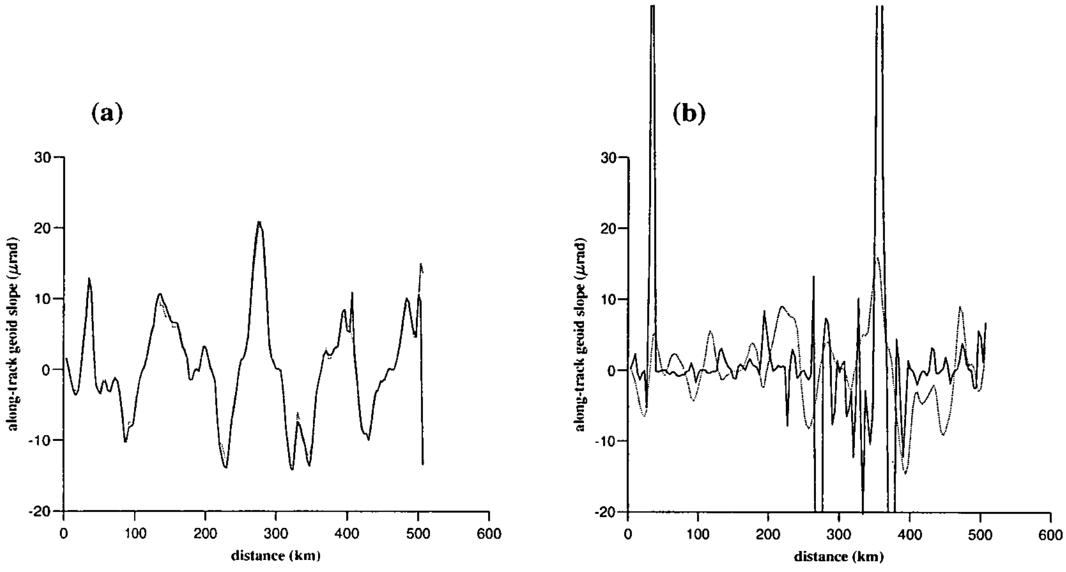

Figure B.6. As fig B.3, for the sinc kernel (eq.B.4).

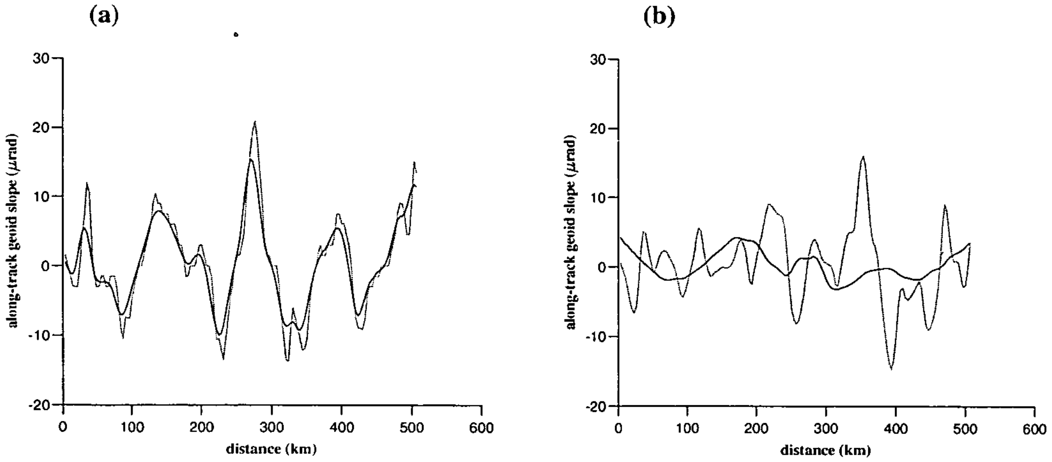

Figure B.7. As fig B.3, for UNIMAP bilinear interpolation.

Appendix C

Transfer function of the gridding kernel

C.1 Introduction

The gridding kernel introduced in §3.2 can be regarded as a 'filter' in its action of transcribing point data onto a regular grid. The effect the gridding procedure has upon the altimeter, ship and land data (§3.3, §4.2.2, & §4.3 respectively) can be analysed by studying the form of the gridding kernel in the wavenumber domain. This can be done quantitatively using a transfer function [Bracewell (1965) and *e.g.* Sandwell and Zhang (1989)]. If an input signal with Fourier transform $A(k)$ is fed into a linear system which gives an output signal with transform $B(k)$, the transfer function is defined as

$$T(k) = \frac{B(k)}{A(k)} \tag{C.1}$$

which is a function only of the properties of the system.

The input and output datasets are normally required to be isotropic, which the data considered in this study are not. Satellite data exist on widely spaced groundtracks; ship data can be densely collected in some regions, while sparsely, or not at all in others, the same being true for land data. Thus, while a rigorous calculation of the transfer function cannot be performed, a good estimate can be obtained by assuming that the wavenumber content of the point data are an accurate representation of the wavenumber content of the field over the whole area.

The "Witches' Hat" gridding kernel has the basic form

$$\delta\omega(\vec{x}_2-\vec{x}_1) = \frac{1}{1+(\frac{\vec{x}_2-\vec{x}_1}{a_o})^2} \quad . \tag{C.2}$$

Its action upon a set of observations, $A(\vec{x}_1)$, can be regarded as a convolution in the space domain of the kernel with the observations. This is true due to the even symmetry of the kernel function, the convolution's 'folding' operation leaving the kernel unchanged. The resultant interpolated grid, $B(\vec{x}_2)$, is then given by

$$B(\vec{x}_2) = \frac{\int\!\!\int A(\vec{x}_1)\,\delta\omega(\vec{x}_2-\vec{x}_1)\,d^2\vec{x}_1}{\int\!\!\int \delta\omega(\vec{x}_2-\vec{x}_1)\,d^2\vec{x}_1} \equiv \frac{I_1}{I_2} \quad . \tag{C.3}$$

The denominator integral, I_2, can be shown to be wavenumber-independent (eq.C.14), thus contributing a constant term in eq.C.3, affecting only the amplitude. Therefore, the Fourier transform of eq.C.3 can be taken, and using the equivalence of convolution in the space domain and multiplication in the wavenumber domain [Sheriff and Geldart (1983)], we have

$$\tilde{B}(\vec{k}) = \frac{\tilde{A}(\vec{k})\,\widetilde{\delta\omega}(\vec{k})}{I_2} \quad . \tag{C.4}$$

This equation will be used as the basis for determining the transfer function in the following cases.

C.2 Altimeter data

The gridding 'filter' for altimeter data is the successive action of derivative and interpolation operations upon geoid height data (§3.3). Thus if we let the input field $A(\vec{x}) = \epsilon(\vec{x})$, the along-track geoid slope, in eq.C.3, we can use the relationship between the Fourier transforms of a function and its horizontal derivative [Sheriff and Geldart (1983)]:

$$\tilde{A}(\vec{k}) \equiv \tilde{\epsilon}(\vec{k}) \equiv \mathcal{F}\left\{\frac{\partial N}{\partial \vec{x}}\right\} = i\left|\vec{k}\right|\tilde{N}(\vec{k}) \quad . \tag{C.5}$$

Substituting this into eq.C.4, the transfer function for the system becomes (from eq.C.1)

$$T(k) = \frac{\tilde{B}(k)}{\tilde{N}(k)} = \frac{i\,k\,\widetilde{\delta\omega}(k)}{I_2} \quad , \tag{C.6}$$

for an input $N(\vec{x})$, the geoid heights, and output $B(\vec{x})$, the new grid of geoid heights.

Now, the Fourier transform of the gridding kernel is

$$\widetilde{\delta\omega}(\vec{k},\phi) = \frac{1}{2\pi}\int\!\!\int_{-\infty}^{\infty} \delta\omega(\vec{x},\phi)\, e^{-i\vec{k}\cdot\vec{x}}\, d^2\vec{x} \quad . \tag{C.7}$$

While convolution integrals (eq.C.3) are normally evaluated over an infinite range, the gridding kernel has a finite extent. If a conversion is made to a cylindrical coordinate system (r,θ), the r-integral is now evaluated from 0 to R', the latitude-dependent search radius. However, to account for the variation of the kernel's shape with latitude (ϕ), it is convenient to introduce a scaled cylindrical coordinate system (ρ,θ), where

$$\rho = r/\Phi \quad . \tag{C.8}$$

and $\Phi(\phi)$ is given by eq.3.3. That is, instead of the kernel decreasing in size with increasing latitude, the kernel retains its shape while the coordinate system expands. The kernel function now becomes

$$\delta\omega(\rho,\phi) = \frac{1}{1+(\frac{\rho}{a_\circ})^2} \qquad |\rho| \le R_\circ \tag{C.9}$$

which is ϕ-independent. The wavenumber coordinates transform similarly,

$$\kappa = k\cdot\Phi \quad . \tag{C.10}$$

Thus,

$$\begin{aligned}
\widetilde{\delta\omega}(\kappa,\phi) &= \frac{1}{2\pi}\int\limits_{\rho=0}^{R_\circ}\int\limits_{\theta=0}^{2\pi} \frac{a_\circ^2}{a_\circ^2+\rho^2}\, e^{-i\kappa\rho\cos(\theta-\theta_0)}\,\rho\, d\rho\, d\theta \\
&= \frac{1}{2\pi}\int\limits_{\rho=0}^{R_\circ} \frac{a_\circ^2}{a_\circ^2+\rho^2}\left\{\int\limits_{\theta=0}^{2\pi} \cos[\kappa\rho\cos(\theta-\theta_0)] - i\sin[\kappa\rho\cos(\theta-\theta_0)]\, d\theta\right\}\rho\, d\rho \quad .
\end{aligned} \tag{C.11}$$

The θ-integrals are standard forms, given in Gradshteyn and Ryzhik (1980) (eqs 3.715.18 and 3.715.13) as

$$\int_0^{2\pi} \cos[z\cos\psi]\,d\psi = 2\pi\,J_0(z) \qquad\qquad \int_0^{2\pi} \sin[z\cos\psi]\,d\psi = 0 \quad ,$$

where $J_0(z)$ is a Bessel function of zero order. Thus

$$\widetilde{\delta\omega}(\kappa,\phi) = a_o^2 \int_0^{R_o} \frac{\rho\,J_0(\kappa\rho)}{a_o^2+\rho^2}\,d\rho \quad , \tag{C.12}$$

the integral having a numerical solution only.

The denominator integral I_2 in eq.C.6, is solved in the same coordinate space:

$$\begin{aligned} I_2 &= \int_{\rho=0}^{R_o} \int_{\theta=0}^{2\pi} \frac{1}{1+\frac{\rho^2}{a_o^2}}\,\rho\,d\rho\,d\theta \\ &= 2\pi \int_0^{R_o} \frac{1}{1+\frac{\rho^2}{a_o^2}}\,\rho\,d\rho \quad . \end{aligned} \tag{C.13}$$

This is solved by the sustitution $u = \rho^2/a_o^2$ to give

$$I_2 = \pi\,a_o^2\,\ln\Big[1+(R_o/a_o)^2\Big] \quad , \tag{C.14}$$

which is latitude-independent, indicating that the area under the gridding kernel is a constant no matter where its location in a region.

So in the expanded coordinate space, from eqs C.6, C.12 and C.14, the transfer function is

$$T(\kappa) = \frac{i\,\kappa}{\pi} \int_0^{R_o} \frac{\rho\,J_0(\kappa\rho)}{a_o^2+\rho^2}\,d\rho \Big/ \ln\Big[1+(R_o/a_o)^2\Big] \quad . \tag{C.15}$$

Transforming back to real coordinate space using eqs C.8 & C.10, the transfer function of the combined derivative/kernel filter is

$$T(k) = \frac{i\,k\,\Phi}{\pi} \int_0^{R'} \frac{r\,J_0(kr)}{a'^2+r^2}\,dr \Big/ \ln\Big[1+(R_o/a_o)^2\Big] \quad . \tag{C.16}$$

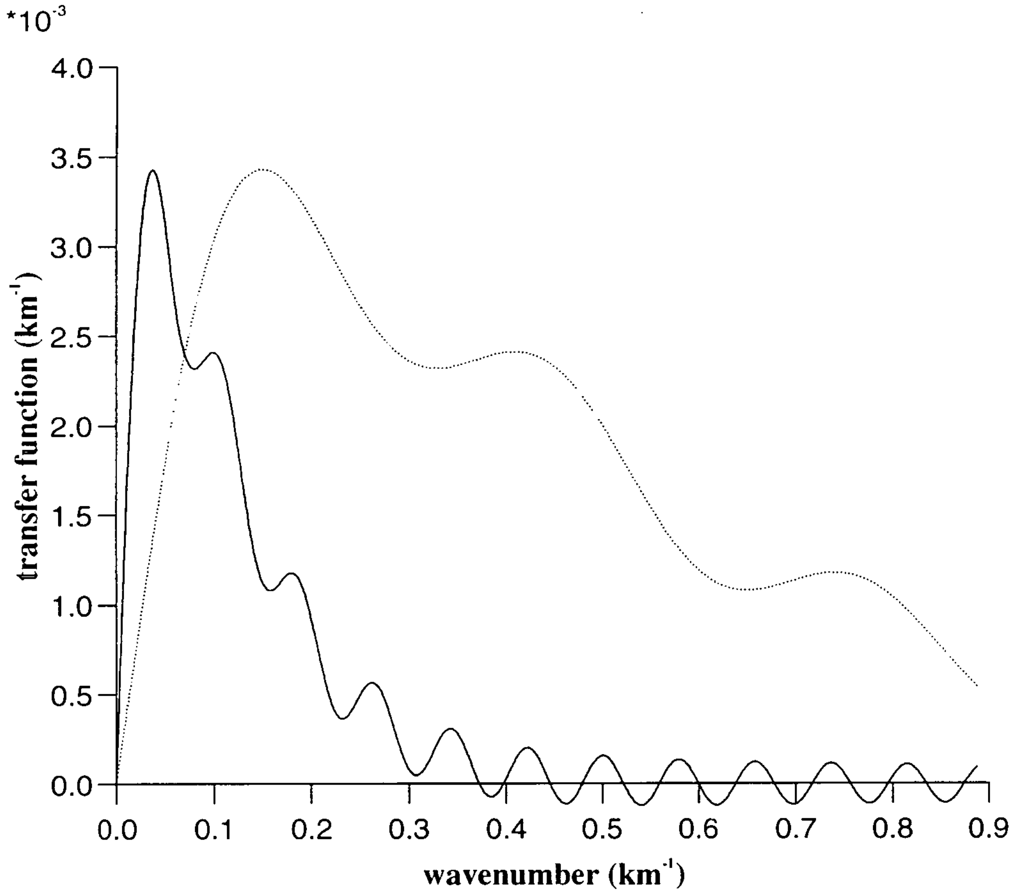

Figure C.1. The transfer function for the gridding operations on Geosat/ERM data at 47° N (R_o=80 km, dark curve) and 72° N (R_o=20 km, light curve).

Fig C.1 shows the magnitude of this transfer function for the Geosat/ERM data at 47° N (R_o=80 km, dark curve) and 72° N (R_o=20 km, light curve). Fig C.2 shows the magnitude of the transfer function for the Topex/Poseidon data at 47° N (R_o=150 km, dark curve), and at 66° N (R_o=44 km, light curve). These plots show how the resolution of the gridded fields increases as the track spacing decreases. If the resolution limit at short wavelength is taken as the half-amplitude wavenumber, then the Geosat geoid has a resolution of 49 km at 47° N, and 12 km at 72° N. The Topex/Poseidon geoid has a resolution of 92 km at 47° N, and 27 km at 66° N, though reproduces the geoid with a smaller amplitude than Geosat.

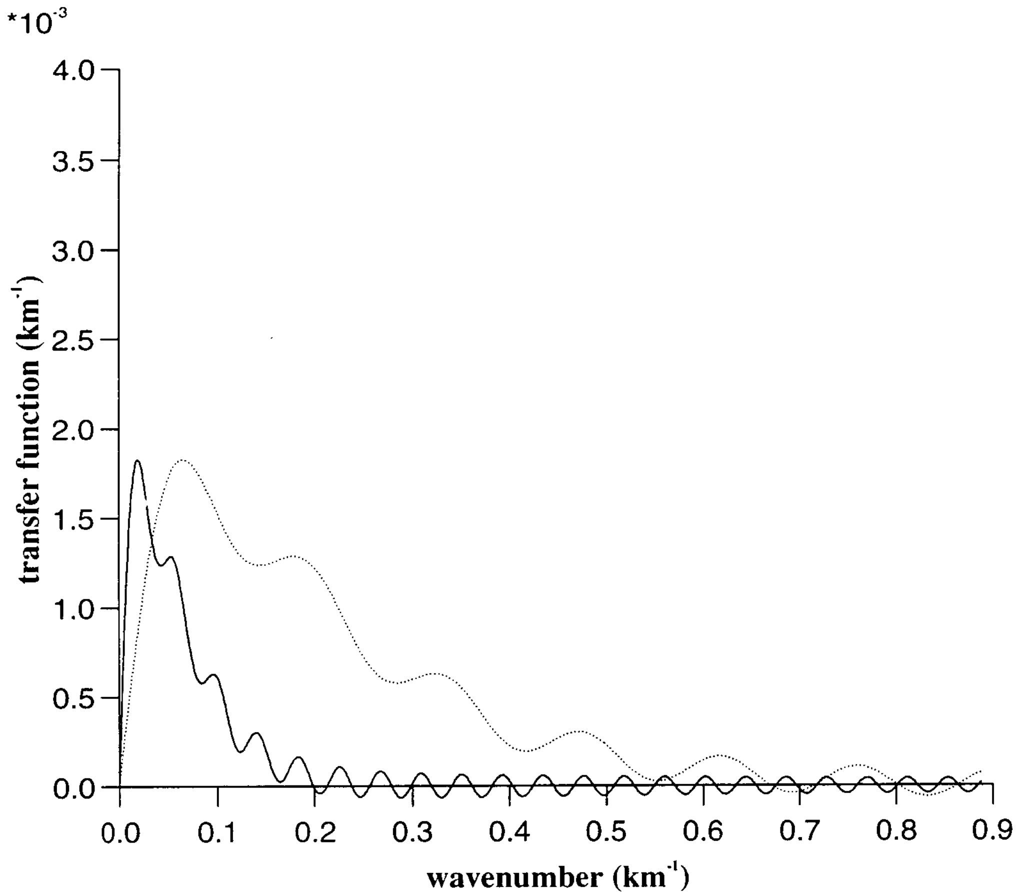

Figure C.2. The transfer function for the gridding operations on Topex/Poseidon data at 47° N (R_o=150 km, dark curve) and 66° N (R_o=44 km, light curve).

C.3 Ship data

A transfer function for the ship data gridding algorithm has not been calculated, owing to the complex nature of the gridding equations, eqs 4.14 to 4.19.

C.4 Land data

Land gravity data is gridded by the direct application of the kernel

$$\delta\omega(r) = \frac{1}{1+(\frac{r}{a_o})^2} \tag{C.17}$$

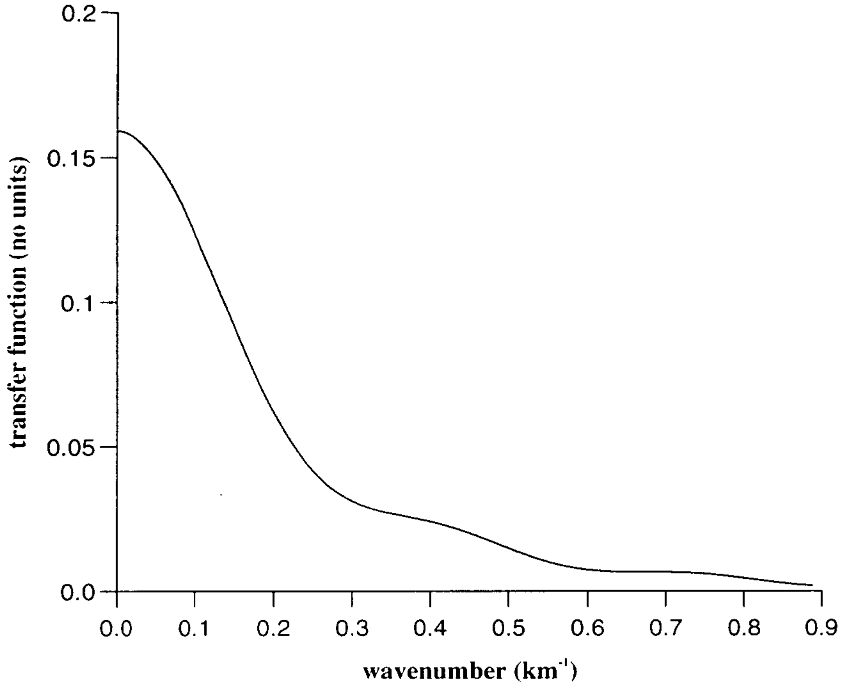

Figure C.3. The transfer function for the land data gridding operation, R_o=20 km.

to the point freeair anomaly data, $\Delta g(\vec{x})$. Thus, from eq.C.4, the transfer function for this system can be derived from

$$\tilde{B}(\vec{k}) = \frac{\widetilde{\Delta g}(\vec{k})\,\widetilde{\delta\omega}(\vec{k})}{I_2} \quad , \tag{C.18}$$

where $B(\vec{x})$ is the output grid of interpolated freeair anomalies.

The method of calculating $\widetilde{\delta\omega}(k)$ and I_2 is similar to the steps in §C.2, but without the latitude-dependence and coordinate expansion. It is therefore a straightforward task to derive the transfer function

$$T(k) = \int_0^{R_o} \frac{r\,J_0(kr)}{a_o^2 + r^2}\,dr \Bigg/ \pi \ln\left[1 + (R_o/a_o)^2\right] \quad . \tag{C.19}$$

A plot of this function is shown in fig C.3. The short-wavelength resolution of the gridded land data, using the definition applied to the satellites (§C.2), is 37 km for a gridding kernel with radius 20 km.

Appendix D

Fourier transform error reduction

It has been shown [*e.g.* Schwarz et al. (1990)] that taking a discrete Fourier transform (DFT) of a dataset introduces 'spectral leakage', which is due to the finite length of the dataset. This occurs first, because the DFT cannot resolve wavelengths longer than the dataset size; and second, as the dataset is periodic in the Fourier domain, any large amplitude anomalies at the dataset edge will influence the opposite edge.

The errors caused by the first effect are commonly reduced by fitting a least-squares plane through the data and subtracting it. However as this technique removes valuable information from the data, a better method is to remove an accurate long wavelength geopotential model before Fourier transformation, which is then added back to the grid generated at the end of the program (the 'remove-restore' technique, §1.3).

The errors due to the second effect are usually reduced by the application of a taper to the edges of the dataset. However, the reduction in data quality caused by edge tapering was not deemed acceptable, and other methods were tested.

The data manipulation techniques listed below were applied to the data immediately before the Fourier transformations in the IFC routine (§5.3).

1. no manipulation technique applied;
2. a border of 100 × 100 zeros added to the data;
3. a least-squares plane subtracted from the data;
4. a least-squares plane subtracted and a zero border applied;

5. 5% of the dataset edges tapered with a cosine-squared function;
6. a least-squares plane subtracted, a 10% cosine-squared taper applied to the edges, and a zero border applied;
7. extrapolating the dataset by 10% at each side using a cosine-squared function that falls off from the edge gridnode value to zero;
8. a "mirrored" border consisting of 10% of the dataset edges added around the dataset;
9. a mirrored border added as above, which was then tapered with a cosine-squared function.

The datasets used were the simulated altimeter and ship track data (§2.8). The results after many iterations of the routine for each of the above methods are shown in figs D.1 to D.9, together with a graph of the logarithm of the RMS difference between successive 'like' provisional models, indicating the degree of convergence.

With no manipulation techniques applied, illustrated in fig D.1, the IFC models converge to give a reasonable geoid, a somewhat unexpected result. Equally surprising was that the conventional technique of adding a zero border (figs D.2, D.4 & D.6) led to rapidly diverging solutions. And while detrending the grids on each iteration did not produce divergent models, convergence was much slower with the solution after 24 iterations showing signs of instability (fig D.3(a)).

The 5% taper solution exhibited good convergence, but with the sacrifice of the data quality at the edges (fig D.5). The cosine-squared extrapolation method (fig D.7) yielded a comparitively good geoid model, but had a lower rate of convergence than both of the mirroring techniques. These mirrored models showed the best results, with a similar degree of convergence and similar resultant geoids. Although no difference is apparent from a comparison of figs D.8(a) and D.9(a), the tapered mirror technique was chosen as the best method due to the good results from the 5% taper technique.

Thus, the tapered mirror technique was applied to all datasets before their Fourier transformation.

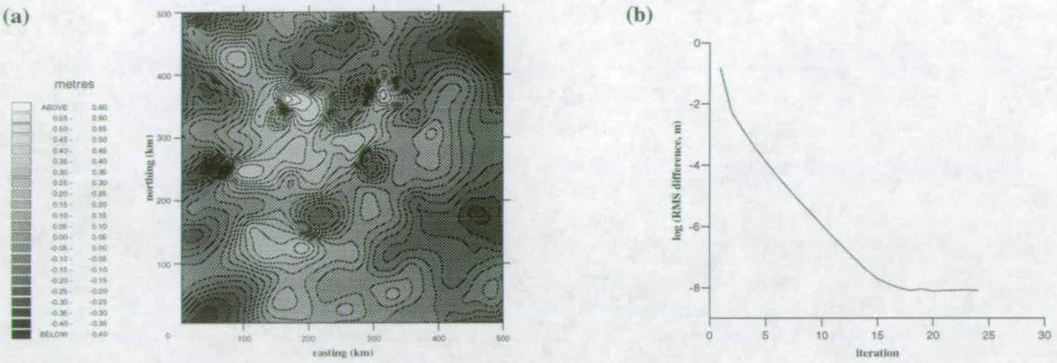

Figure D.1. (a) Geoid after 24 IFC iterations with no manipulation techniques applied. (b) Convergence of provisional model in successive iterations.

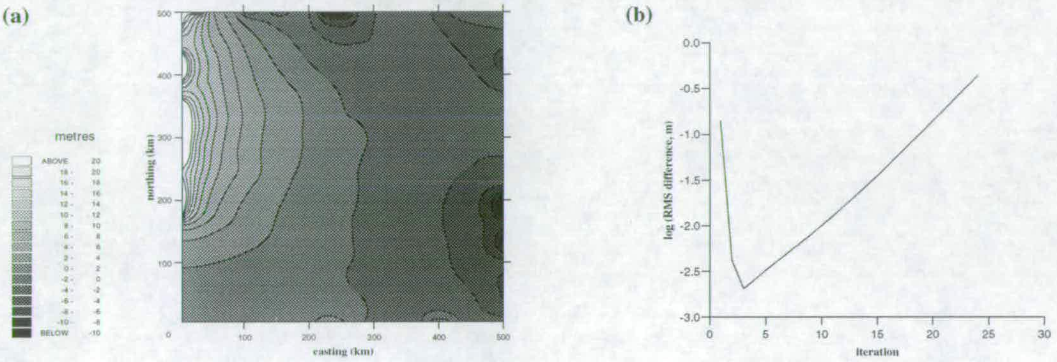

Figure D.2. (a) Geoid after 24 IFC iterations with border of 100 × 100 zeros applied. (b) Convergence of provisional model in successive iterations.

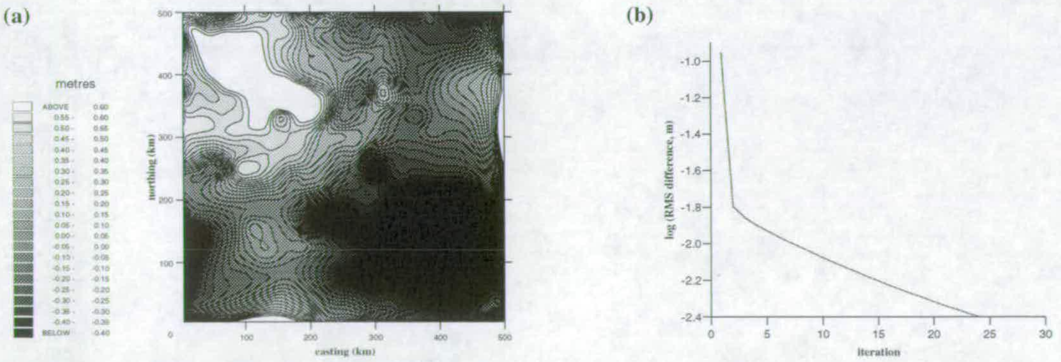

Figure D.3. (a) Geoid after 24 IFC iterations with detrending applied. (b) Convergence of provisional model in successive iterations.

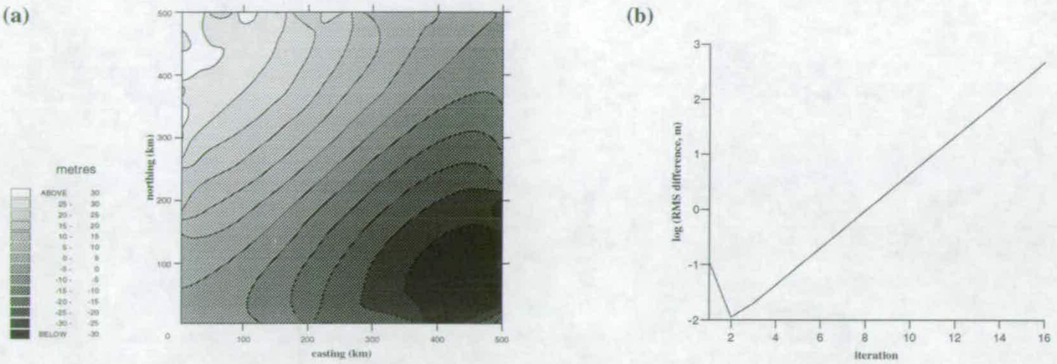

Figure D.4. (a) Geoid after 16 IFC iterations with zero border and detrending applied. (b) Convergence of provisional model in successive iterations.

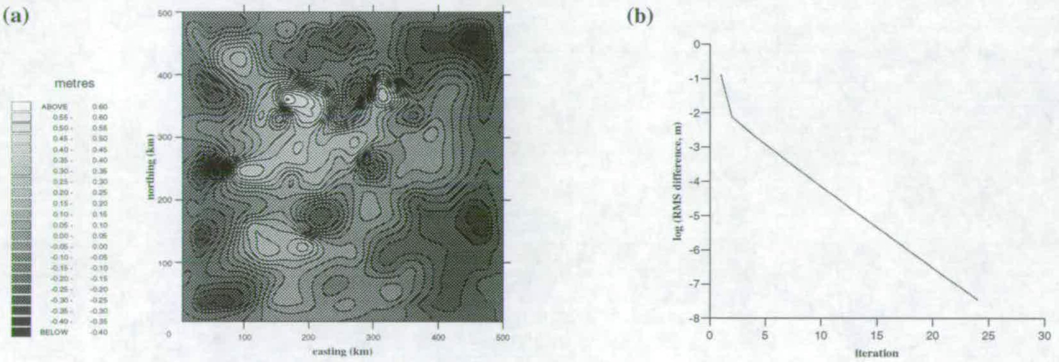

Figure D.5. (a) Geoid after 24 IFC iterations with 5% taper applied. (b) Convergence of provisional model in successive iterations.

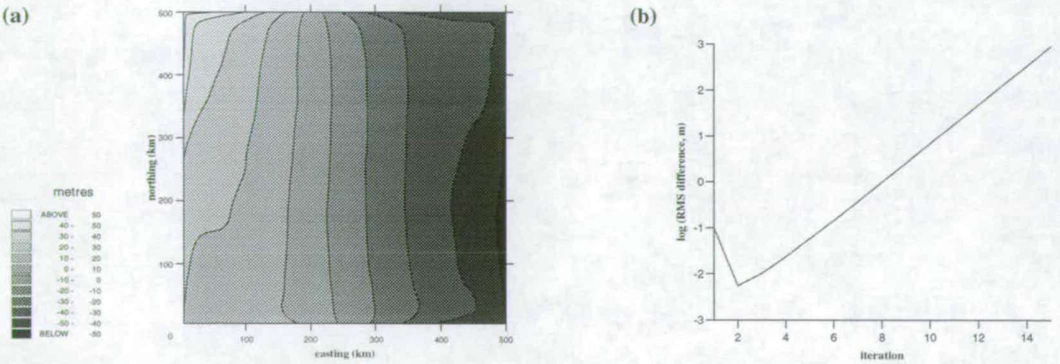

Figure D.6. (a) Geoid after 15 IFC iterations with zero border, detrending and 10% taper applied. (b) Convergence of provisional model in successive iterations.

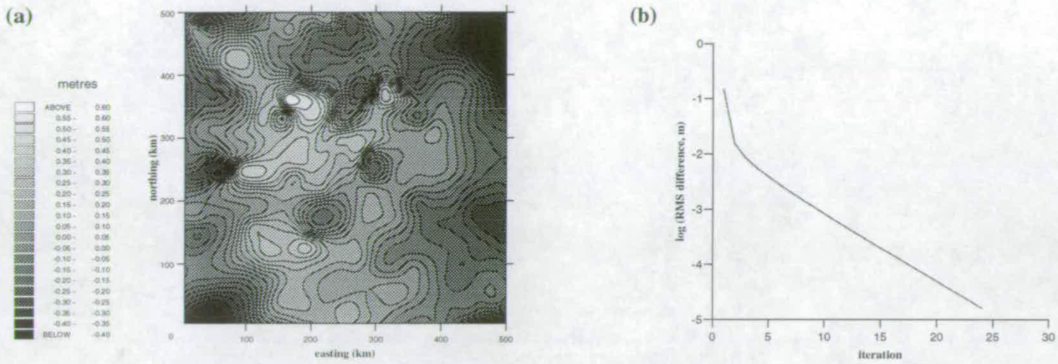

Figure D.7. (a) Geoid after 24 IFC iterations with $\cos^2$ extrapolation applied. (b) Convergence of provisional model in successive iterations.

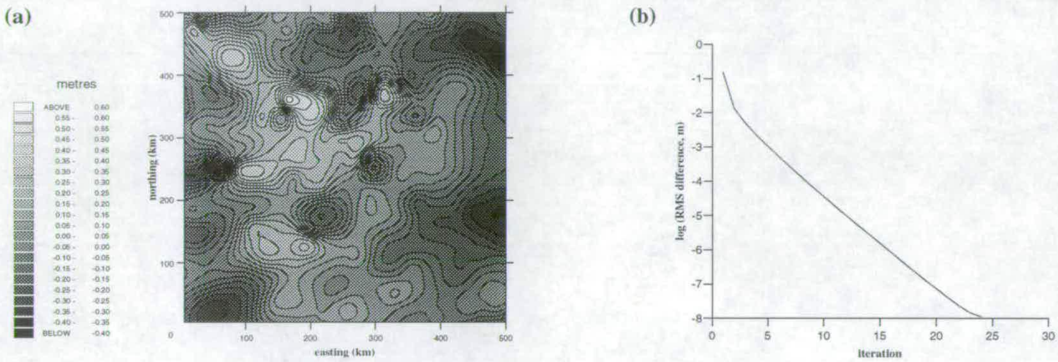

Figure D.8. (a) Geoid after 24 IFC iterations with mirrored border applied. (b) Convergence of provisional model in successive iterations.

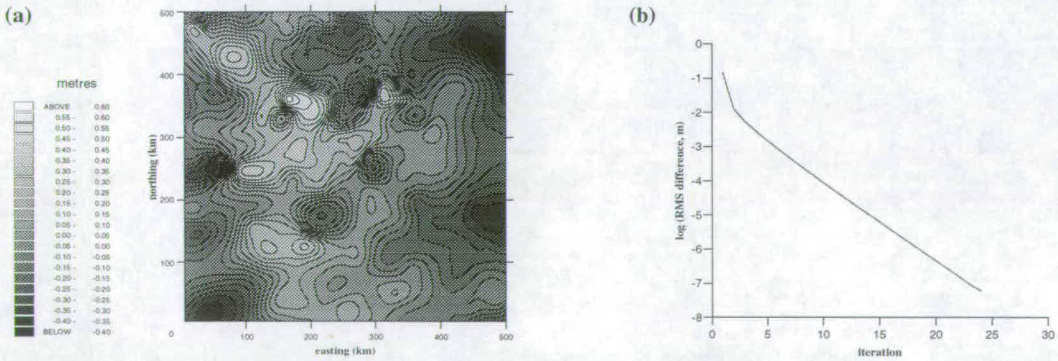

Figure D.9. (a) Geoid after 24 IFC iterations with tapered mirrored border applied. (b) Convergence of provisional model in successive iterations.

Appendix E

The FORTRAN program TOTAL.F

The FORTRAN program TOTAL.F is listed. This program incorporates the following subroutines, which may be used as individual programs with slight modification.

GSGRID.F This subroutine grids the along-track geoid slope using the Witch gridding kernel, following the procedure in §3.3. Input is one file for all ascending passes of a mission, one file for all the descending passes, for each mission. Input file must be in "track format":

$$\begin{array}{llll} N & & & \\ east_1 & north_1 & geoid_1 & lat_1 \\ \dots & \dots & \dots & \dots \\ east_N & north_N & geoid_N & lat_N \\ M & & & \\ east_1 & north_1 & geoid_1 & lat_1 \\ \dots & \dots & \dots & \dots \\ east_M & north_M & geoid_M & lat_M \end{array} \tag{E.1}$$

The program creates a grid of slopes and a grid of weights for each input file. Values for the parameters in the program were:

	Topex	Geosat
R	150 km	80 km
ϕ_0	47° N	47° N
ϕ_1	74° N	80° N

GS2GRAV.F The along-track geoid slope and weighting grids from GSGRID.F are passed to this subroutine. External input grids are

1. a grid of the angle made by the satellite groundtrack with the positive easting axis: one per input slope grid. UNIMAP bilinear interpolation was used to grid the angles;
2. the tapered landmass grid (§2.7).

From these, grids of the geoid height and freeair anomaly are created (§3.4).

SHIPGRID.F The subroutine grids data according to the procedure described in §4.2. The data must be in "track format":

$$\begin{array}{lll} N & \mathrm{cruise_A} & iyear \\ east_1 & north_1 & freeair_1 \\ \dots & \dots & \dots \\ east_N & north_N & freeair_N \\ M & \mathrm{cruise_B} & iyear \\ east_1 & north_1 & freeair_1 \\ \dots & \dots & \dots \\ east_M & north_M & freeair_M \end{array} \tag{E.2}$$

A search radius of 20 km was used in application of the Witch gridding kernel. Two grids are created, one of the gridded freeair anomaly, and one of the weights.

LANDGID.F Land gravity data are interpolated directly onto a grid using the Witch kernel, with a search radius of 20 km. The data format is

$$\begin{array}{lll} east_1 & north_1 & freeair_1 \\ east_2 & north_2 & freeair_2 \\ \dots & \dots & \dots \\ east_N & north_N & freeair_N \end{array} \tag{E.3}$$

Grids of the freeair anomaly and weights are created.

IFC.F The gravity and weighting grids created by GS2GRAV.F, SHIPGRID.F and LANDGRID.F are passed to this subroutine. They are combined iteratively according to the procedure in §5.3. The RMS difference between successive provisional models is calculated, and the subroutine exited when this begins to increase. A grid of either the combined geoid height or freeair anomaly can be generated.

The program was run on a Sun SPARC 1000 with 4 processors and 192 Mbytes RAM. It requires 136 kbytes of memory.

Two datasets were gridded and combined:

1. The test dataset (§2.8) consisted of 1670 simulated satellite observations, and 1853 simulated ship track observations. The working grid within the program was 128 × 128 gridnodes, and the program wrote to two files, each of 100 × 100 gridnodes. The CPU time was 18 seconds.

2. The North Atlantic dataset consisted of 68,391 Geosat/ERM observations, 483,068 Topex/Poseidon observations, 133,677 ship gravity observations, and 182,292 land gravity readings. The working grid within the program was 1024 × 1024 gridnodes, and the program wrote to two files, each of 704 × 476 gridnodes. The CPU time was 81 minutes.

```
* Program total.F
* version 16 - 7/12/1995
*
* Written by Jonathan Kirby,
*            Department of Geology & Geophysics,
*            University of Edinburgh.
*
* Calls the mixed-radix fast fourier transform algorithm by
* R.C. Singleton, Stanford Research Institute, Sept 1968.
*
* Array sizes and no. of satellite missions altered in "total.h"
* Parameters read in from "total.com"
************************************************************************

      include "total.h"
      character*32 fileout

      open(20,file='total.com')

*-----------------------------------------------------------------------
* area parameters :

      read(20,*) nx0
      read(20,*) ny0
      read(20,*) x0
      read(20,*) y0
      read(20,*) delta
      read(20,*) gn

      ibord1=nx0*0.1
      ibord2=ibord1
      jbord1=nx0*0.1
      jbord2=jbord1

      nx=nx0+ibord1+ibord2
      ny=ny0+jbord1+jbord2

      x0=x0*1.d3            !
      y0=y0*1.d3            ! now in metres
      delta=delta*1.d3      !

      x0=x0-(ibord1*delta)
      y0=y0-(jbord1*delta)

      write(*,601) n1,n2
      write(*,602) nx,ny
  601 format('n1 =',i5,3x,'n2 =',i5)
  602 format('nx =',i5,3x,'ny =',i5)
      if (nx.gt.n1.or.ny.gt.n2) then
        write(*,*) 'n1,n2 too small for data size'
        stop
      endif

*-----------------------------------------------------------------------
      write(*,*) 'gridding satellite data ...'

      do 10, k=1,2*nsat
       call gsgrid(k)
   10 continue

*-----------------------------------------------------------------------
      write(*,*) 'producing gridded geoid ...'
      call gs2grav

*-----------------------------------------------------------------------
      write(*,*) 'gridding ship data ...'
      call shipgrid

*-----------------------------------------------------------------------
      write(*,*) 'gridding land data ...'
      call landgrid

```

```
      write(*,*) 'combining satellite & ship datasets ...'
      call ifc

*-----------------------------------------------------------------------
* output geoid or freeair field :

      read(20,*) fileout
      write(*,*) 'writing to ',fileout
      open(1,file=fileout)

      do 20, j=1,ny0
       l=j+jbord1
       do 20, i=1,nx0
        k=i+ibord1
        write(1,'(f8.3)') real(h(k,l))
   20 continue

      close(1)
      close(20)

      stop
      end


************************************************************************
* The subroutine gsgrid
* Constructs 2D grids of ascending and descending along-track geoid
* slopes for each satellite mission, and their weighting grids.
* Input is easting, northing, geoid height and latitude for each
* record in an individual track.
* Each track must be preceded by the number of records.
* Interpolation is carried out by a distance-weighted average
* method, using the Witch gridding kernel.
************************************************************************

      subroutine gsgrid(iset)
      include "total.h"
      parameter (nmax=2000)
      double precision east(nmax),north(nmax),geoid(nmax),lat(nmax),
     # latt,latb
      character*32 filein

      deltasq=delta*delta

*-----------------------------------------------------------------------
* dataset parameters :

      read(20,*) filein
      read(20,*) idata
      read(20,*) rsearch0
      read(20,*) latt
      read(20,*) latb

      rsearch0=rsearch0*1.d3   ! metres
      a0=rsearch0*ratio
      alpha0=a0/dsqrt(log(2.d0))

      f0=latt-latb

*-----------------------------------------------------------------------
* read in satellite sea-surface height data and form geoid slope :

      open(1,file=filein)

    5 read(1,*,end=40) npts
      do 10, k=1,npts
       read(1,*) east(k),north(k),geoid(k),lat(k)
       east(k)=east(k)*units                           ! metres
       north(k)=north(k)*units                         !
   10 continue

      do 30, k=2,npts-1
```

```
       de=east(k+1)-east(k-1)
       dn=north(k+1)-north(k-1)

       dl=dsqrt(de*de+dn*dn)
       gds=(geoid(k+1)-geoid(k-1))/dl            ! gds in radians

       inode0=nint((east(k)-x0)/delta+1.)            ! nearest node
       jnode0=nint((north(k)-y0)/delta+1.)           !

       f=(latt-lat(k))/f0
       fsq=f*f

       rsearch=rsearch0*f
       ksearch=int(rsearch/delta)
       if (ksearch.lt.1) ksearch=1
       rsearch2=ksearch*ksearch*deltasq
       ksearch=ksearch+1

       asq=a0*a0*fsq
       alphasq=alpha0*alpha0*fsq

*-----------------------------------------------------------------------
* interpolation within the search radius :

       do 20, n=-ksearch,ksearch
        j0=jnode0+n
        y=y0+(j0-1)*delta
        do 20, m=-ksearch,ksearch
         i0=inode0+m
         if (i0.lt.1.or.i0.gt.n1.or.j0.lt.1.or.j0.gt.n2) goto 20
         x=x0+(i0-1)*delta

         distx=x-east(k)
         disty=y-north(k)
         distsq=distx*distx+disty*disty

         dw=1.d0/(1.d0+distsq/asq)
c        dw=dexp(-distsq/alphasq)

         dw=dw/fsq
         if (rsearch2-distsq.lt.1.d-4) dw=zero
         wt(iset,i0,j0)=wt(iset,i0,j0)+dw
         slope(iset,i0,j0)=slope(iset,i0,j0)+gds*dw
   20  continue

   30 continue

      goto 5

   40 close(1)

*-----------------------------------------------------------------------
* find maximum weight value to normalise all weights :

      wmax=zero
      do 50, j=1,ny
       do 50, i=1,nx
        if (wt(iset,i,j).gt.wmax) wmax=wt(iset,i,j)
   50 continue

* normalize the grid values by the weights :

      do 60, j=1,ny
       do 60, i=1,nx
        if (wt(iset,i,j).gt.zero) then
          slope(iset,i,j)=slope(iset,i,j)/wt(iset,i,j)
          wt(iset,i,j)=wt(iset,i,j)/wmax
        endif
   60 continue

*-----------------------------------------------------------------------
      return
```

```


************************************************************************
* The subroutine gs2grav
* Converts ascending and descending along-track geoid slope grids
* into grids of east & north geoid slopes. These are then combined
* into a single grid of either geoid heights or freeair anomalies.
* Angles are measured anticlockwise from the positive x-axis, and
* must have already been gridded.
* Complex array a() doubles up as east deflections and geoid,
* b() as north deflections and freeair.
************************************************************************

      subroutine gs2grav
      include "total.h"
      complex gtemp,imag
      character*32 fileangA,fileangD,filesea,fileout,output*1

      twopi=8.d0*datan(1.d0)
      imag=(0.,1.)

*-----------------------------------------------------------------------
      do 5, i=1,nz
       za(i)=0.
    5  zb(i)=0.

*-----------------------------------------------------------------------
* form grids of east & north geoid slopes :

      do 20, ksat=1,nsat

       read(20,*) fileangA
       read(20,*) fileangD
       open(3,file=fileangA)
       open(4,file=fileangD)

       do 10, j=1,ny0
        l=j+jbord1
        do 10, i=1,nx0
         k=i+ibord1

         atsA=slope(2*ksat-1,k,l)
         atsD=slope(2*ksat,k,l)
         read(3,*) angA
         read(4,*) angD

         if (angA.eq.zero.and.angD.ne.zero) then
           cosD=dcos(angD)
           sinD=dsin(angD)
           tanD=sinD/cosD
           tempe=atsA
           tempn=(-atsA+(atsD/cosD))/tanD

         else if (angD.eq.zero.and.angA.ne.zero) then
           cosA=dcos(angA)
           sinA=dsin(angA)
           tanA=sinA/cosA
           tempe=atsD
           tempn=((atsA/cosA)-atsD)/tanA

         else if (angA.eq.zero.and.angD.eq.zero) then
           tempe=atsA
           tempn=zero

         else
           cosA=dcos(angA)
           sinA=dsin(angA)
           cosD=dcos(angD)
           sinD=dsin(angD)
           tanAD=(sinA/cosA)-(sinD/cosD)
           cotAD=(cosA/sinA)-(cosD/sinD)
           if (tanAD.eq.zero.or.cotAD.eq.zero) then
```

```
             tempn=zero
           else
             tempe=((atsA/sinA)-(atsD/sinD))/cotAD
             tempn=((atsA/cosA)-(atsD/cosD))/tanAD
           endif

         endif

         wtA=wt(2*ksat-1,k,l)
         wtD=wt(2*ksat,k,l)
         wtAD=(wtA+wtD)/2.d0          ! combining the asc & desc weights
         wsat(k,l)=wsat(k,l)+wtAD

         a(k,l)=a(k,l)+(tempe*wtAD)     ! east deflection
         b(k,l)=b(k,l)+(tempn*wtAD)     ! north deflection

   10  continue

       close(3)
       close(4)

   20 continue

* read landmass file and multiply deflection grids by sea() to taper :

      read(20,*) filesea
      open(1,file=filesea)

      do 30, j=1,ny0
       l=j+jbord1
       do 30, i=1,nx0
        k=i+ibord1
        read(1,*) rland
        sea(i,j)=1.d0-rland
        if (wsat(k,l).gt.zero) then
          a(k,l)=a(k,l)*sea(i,j)/wsat(k,l)
          b(k,l)=b(k,l)*sea(i,j)/wsat(k,l)
          wsat(k,l)=wsat(k,l)*sea(i,j)/nsat
        endif
   30 continue

      close(1)

*-----------------------------------------------------------------------
* interpolation between real data and edge :

      call mirror(a)
      call mirror(b)

*-----------------------------------------------------------------------
* fourier transform the east & north arrays :

      ierr=0
      call fft(za,za(2),n12,n1,n1,2,ierr)
      call fft(za,za(2),n12,n2,n12,2,ierr)

      call fft(zb,zb(2),n12,n1,n1,2,ierr)
      call fft(zb,zb(2),n12,n2,n12,2,ierr)

*-----------------------------------------------------------------------
* wavenumber parameters :

      dx=delta         ! metres
      dy=delta         !

      nxhalf=n1/2+2
      nyhalf=n2/2+2
      dkx=twopi/(n1*dx)
      dky=twopi/(n2*dy)

*-----------------------------------------------------------------------
* create freeair anomaly & geoid :
```

```
      do 40, j=1,n2
       ywvn=(j-(j/nyhalf)*n2-1)*dky
       do 40, i=1,n1
        xwvn=(i-(i/nxhalf)*n1-1)*dkx
        wvnsq=xwvn*xwvn+ywvn*ywvn
        wvn(i,j)=dsqrt(wvnsq)                         ! in (1/m) units

        gtemp=xwvn*a(i,j)+ywvn*b(i,j)
        if (i*j.ne.1) a(i,j)=gtemp*imag/wvnsq             ! F{geoid}
        if (i*j.ne.1) b(i,j)=gtemp*imag*gn/wvn(i,j)       ! F{freeair}
   40 continue

      a(1,1)=(0.,0.)
      b(1,1)=(0.,0.)

* inverse fourier transform :

      call fft(za,za(2),n12,n1,n1,-2,ierr)
      call fft(za,za(2),n12,n2,n12,-2,ierr)

      call fft(zb,zb(2),n12,n1,n1,-2,ierr)
      call fft(zb,zb(2),n12,n2,n12,-2,ierr)

      do 50, j=1,n2
       do 50, i=1,n1
        a(i,j)=a(i,j)/n12                          ! geoid
        b(i,j)=b(i,j)/n12                          ! freeair
   50 continue

*-----------------------------------------------------------------------
* optional output of satellite geoid :

      read(20,*) output
      read(20,*) fileout
      if (output.eq.'y') then
        write(*,*) 'writing to ',fileout
        open(2,file=fileout)

        do 60, j=1,ny0
         l=j+jbord1
         do 60, i=1,nx0
          k=i+ibord1
          write(2,'(f9.3)') real(a(k,l))*sea(i,j)
   60   continue
        close(2)
      endif

      return
      end


***********************************************************************
* The subroutine shipgrid
* Input must be a header of no. of points in track, cruise identifier,
* and cruise year, followed by the records in the track: easting,
* northing, and freeair anomaly.
* dimension of dw() is for ksearch=4 (20 km on a 5 km grid).
***********************************************************************

      subroutine shipgrid
      include "total.h"
      parameter (nmax=70000)
      double precision g2(n1,n2),x(nmax),y(nmax),faa(nmax),dw(9,9)
      integer num(n1,n2),num2(n1,n2)
      character*32 fileship,cruise*8

*-----------------------------------------------------------------------
* read ship track data, and interpolate onto grid :

      read(20,*) fileship
      open(1,file=fileship)
```

```
      do 10, k=1,npts
       read(1,*) x(k),y(k),faa(k)
       x(k)=x(k)*units               ! metres
       y(k)=y(k)*units               !
   10 continue

      do 20, k=1,npts-1
       dx=x(k+1)-x(k)
       dy=y(k+1)-y(k)
       deltal=dsqrt(dx*dx+dy*dy)
       if (deltal.le.0.1d0) goto 20
       cospsi=dx/deltal
       sinpsi=dy/deltal

       xm=x(k)+dx/2.                ! midpoint coords
       ym=y(k)+dy/2.                !

       atgrad=(faa(k+1)-faa(k))*delta/(3.*deltal)

       gsbar=(faa(k+1)+faa(k))/2.
       sumgsbar=sumgsbar+gsbar

       inode=(xm-x0)/delta+1
       jnode=(ym-y0)/delta+1

       g01=real(b(inode,jnode))
       g02=real(b(inode+1,jnode))
       g03=real(b(inode,jnode+1))
       g04=real(b(inode+1,jnode+1))

* test whether midpoint falls in upper or lower gridpoint triangle
* and calculate the 3 gridpoint values :

       if (xm-x0+ym-y0-(inode+jnode-1)*delta.le.zero) then

         ctgrad=-(g02-g01)*sinpsi+(g03-g01)*cospsi
         ctgrad=ctgrad/3.

         g0bar=(g01+g02+g03)/3.

         gshp1=gsbar-atgrad*(cospsi+sinpsi)-ctgrad*(cospsi-sinpsi)
         gshp2=gsbar+atgrad*(2*cospsi-sinpsi)-ctgrad*(cospsi+2*sinpsi)
         gshp3=gsbar-atgrad*(cospsi-2*sinpsi)+ctgrad*(2*cospsi+sinpsi)
         gshp4=zero

         num(inode,jnode)=num(inode,jnode)+1
         num(inode+1,jnode)=num(inode+1,jnode)+1
         num(inode,jnode+1)=num(inode,jnode+1)+1

       else
         ctgrad=-(g04-g03)*sinpsi+(g04-g02)*cospsi
         ctgrad=ctgrad/3.

         g0bar=(g02+g03+g04)/3.

         gshp1=zero
         gshp2=gsbar+atgrad*(cospsi-2*sinpsi)-ctgrad*(2*cospsi+sinpsi)
         gshp3=gsbar-atgrad*(2*cospsi-sinpsi)+ctgrad*(cospsi+2*sinpsi)
         gshp4=gsbar+atgrad*(cospsi+sinpsi)+ctgrad*(cospsi-sinpsi)

         num(inode+1,jnode)=num(inode+1,jnode)+1
         num(inode,jnode+1)=num(inode,jnode+1)+1
         num(inode+1,jnode+1)=num(inode+1,jnode+1)+1

       endif

       sumg0bar=sumg0bar+g0bar

       gshp(inode,jnode)=gshp(inode,jnode)+gshp1
       gshp(inode+1,jnode)=gshp(inode+1,jnode)+gshp2
       gshp(inode,jnode+1)=gshp(inode,jnode+1)+gshp3
       gshp(inode+1,jnode+1)=gshp(inode+1,jnode+1)+gshp4
```

```
   20 continue

* end of track ...

      sumgsbar=sumgsbar/(npts-1)
      sumg0bar=sumg0bar/(npts-1)

      do 30, j=1,ny
       do 30, i=1,nx
        if (num(i,j).ne.0) then
          gshp(i,j)=gshp(i,j)/num(i,j)
          gshp(i,j)=gshp(i,j)-sumgsbar+sumg0bar
          g2(i,j)=g2(i,j)+gshp(i,j)
          num2(i,j)=num2(i,j)+1
          gshp(i,j)=zero
          num(i,j)=0
        endif
   30 continue

      sumgsbar=zero
      sumg0bar=zero

      goto 5                 ! new ship track

   40 close(1)

*-----------------------------------------------------------------------
* construct weighting grid :

      rsearch=20.d0*1.d3      ! metres
      ksearch=int(rsearch/delta)

      deltasq=delta*delta
      rsearch2=ksearch*ksearch*deltasq

      a0=rsearch*ratio
      asq=a0*a0

      do 50, n=-ksearch,ksearch
       do 50, m=-ksearch,ksearch
        distsq=(m*m+n*n)*deltasq
        dw(m,n)=1.d0/(1.d0+distsq/asq)
        if (rsearch2-distsq.lt.1.d-4) dw(m,n)=zero
   50 continue

*-----------------------------------------------------------------------
* extend influence of ship track data using weighting grid :

      do 70, j=1,ny
       do 70, i=1,nx
        if (num2(i,j).eq.0) goto 70
        g2(i,j)=g2(i,j)/num2(i,j)

        do 60, n=-ksearch,ksearch
         jn=j+n
         do 60, m=-ksearch,ksearch
          im=i+m
          if (im.lt.1.or.im.gt.n1.or.jn.lt.1.or.jn.gt.n2) goto 60
          wshp(im,jn)=wshp(im,jn)+dw(m,n)
          gshp(im,jn)=gshp(im,jn)+g2(i,j)*dw(m,n)
   60   continue

   70 continue

      return
      end


***********************************************************************
* The subroutine landgrid
* Input is series of easting, northing, and freeair anomaly for
* each record.
```

```
586   * Search radius (rsearch) of witch kernel is 20 km.
587   ***********************************************************************
588
589         subroutine landgrid
590         include "total.h"
591         double precision north
592         character*32 fileland,data*1
593
594         rsearch=20.d0*1.d3       ! metres
595         a0=rsearch*ratio
596         ksearch=int(rsearch/delta)
597
598         deltasq=delta*delta
599         rsearch2=ksearch*ksearch*deltasq
600         asq=a0*a0
601
602         read(20,*) data
603         read(20,*) fileland
604         if (data.eq.'n') return
605
606   *----------------------------------------------------------------------
607   * read gravity data :
608
609         open(1,file=fileland)
610
611       5 read(1,*,end=20) east,north,faa,boug
612         east=east*units            ! metres
613         north=north*units          !
614
615         inode=(east-x0)/delta+1
616         jnode=(north-y0)/delta+1
617
618         do 10, n=-ksearch,ksearch
619          j0=jnode+n
620          y=y0+(j0-1)*delta
621          do 10, m=-ksearch,ksearch
622           i0=inode+m
623           if (i0.lt.1.or.i0.gt.n1.or.j0.lt.1.or.j0.gt.n2) goto 10
624           x=x0+(i0-1)*delta
625           distsq=(x-east)*(x-east)+(y-north)*(y-north)
626           dw=1.d0/(1.d0+distsq/asq)
627           if (rsearch2-distsq.lt.1.d-4) dw=zero
628           wlnd(i0,j0)=wlnd(i0,j0)+dw
629           glnd(i0,j0)=glnd(i0,j0)+faa*dw
630      10 continue
631         goto 5
632
633      20 close(1)
634         return
635         end
636
637
638   ***********************************************************************
639   * The subroutine ifc
640   * Combines grids of satellite, ship and land data, using their
641   * weighting grids.
642   * Subroutine exits upon divergence of provisional model.
643   * Commemt out line 751 ("rmstemp=rms") if full iteration count
644   *  is required.
645   * Writes the rms differences between successive provisional models
646   *  to file rms.dat
647   ***********************************************************************
648
649         subroutine ifc
650         include "total.h"
651         complex htemp(n1,n2)
652
653         open(3,file='rms.dat')
654         rmstemp=999.
655
656   *----------------------------------------------------------------------
657         do 5, i=1,nz
```

```
659
660   *----------------------------------------------------------------------
661   * first iteration is to combine the gridded ship dataset with the
662   * satellite-derived freeair anomaly :
663
664         do 10, j=1,ny
665          do 10, i=1,nx
666           wsum=sea(i,j)+wshp(i,j)+wlnd(i,j)
667           if (wsum.gt.zero) then
668             h(i,j) = b(i,j)*sea(i,j) + gshp(i,j) + glnd(i,j)
669             h(i,j)=h(i,j)/wsum
670           endif
671      10 continue
672
673   *----------------------------------------------------------------------
674   * iteration loop, outputting geoid/freeair grid :
675
676         read(20,*) iteration
677         if (iteration.lt.2) goto 60
678
679         itmod=mod(iteration,2)
680
681         do 50, l=2,iteration
682
683          write(*,*) 'iteration #',l
684          lmod=mod(l,2)
685
686          call mirror(h)
687
688   *----------------------------------------------------------------------
689   * conversion between geoid & freeair gravity anomalies :
690
691          ierr=0
692          call fft(zh,zh(2),n12,n1,n1,2,ierr)
693          call fft(zh,zh(2),n12,n2,n12,2,ierr)
694
695          wvn(1,1)=1.d0
696
697          if (lmod.eq.0) then                        ! faa to geoid
698            do 20, j=1,n2
699             do 20, i=1,n1
700      20      h(i,j)=h(i,j)/(wvn(i,j)*gn)
701          else                                        ! geoid to faa
702            do 25, j=1,n2
703             do 25, i=1,n1
704      25      h(i,j)=h(i,j)*wvn(i,j)*gn
705          endif
706
707          wvn(1,1)=zero
708          h(1,1)=(0.,0.)
709
710          call fft(zh,zh(2),n12,n1,n1,-2,ierr)
711          call fft(zh,zh(2),n12,n2,n12,-2,ierr)
712
713          do 30, j=1,n2
714           do 30, i=1,n1
715            h(i,j)=h(i,j)/n12
716      30  continue
717
718   *----------------------------------------------------------------------
719          if (l.eq.iteration) goto 60
720
721   * over-writing the array h() :
722
723          if (lmod.eq.0) then                      ! adding on satellite data
724            do 40, j=1,ny
725             do 40, i=1,nx
726              h(i,j)=(h(i,j)+a(i,j))/2.d0
727      40    continue
728          else                                     ! adding on freeair data
729            do 45, j=1,ny
730             do 45, i=1,nx
```

```
           h(i,j)=h(i,j)/(1.d0+wshp(i,j)+wlnd(i,j))
   45    continue
       endif

       if (lmod.eq.itmod) then
         call srms(h,htemp,rms)
         if (rmstemp.le.rms) then
           do 80, j=1,n2
            do 80, i=1,n1
             h(i,j)=htemp(i,j)
   80      continue
           goto 60
         else
           write(3,*) l/2,rms
           do 85, j=1,n2
            do 85, i=1,n1
             htemp(i,j)=h(i,j)
   85      continue
         endif
         rmstemp=rms             ! comment out for full iteration count
       endif

   50 continue

*-----------------------------------------------------------------------
   60 close(3)
      return
      end


************************************************************************
* subroutine srms
* Returns the bias-free rms difference between two gridded datasets.
* f is the new transformed data, fcomp is the original data to be
* compared with.
************************************************************************

      subroutine srms(f,fcomp,stdev)
      include "total.h"
      double precision mean
      complex f(n1,n2),fcomp(n1,n2)

      npts=nx0*ny0
      sumd=0.d0
      sumd2=0.d0

      do 10, j=1,ny0
       l=j+jbord1
       do 10, i=1,nx0
        k=i+ibord1
        d=real(f(k,l)-fcomp(k,l))
        sumd=sumd+d
        sumd2=sumd2+d*d
   10 continue

      mean=sumd/npts
      variance=sumd2/npts-mean*mean
      stdev=dsqrt(variance)
      stdev=log10(stdev)

      return
      end


************************************************************************
* subroutine mirror
* Increases the inputted dataset size by reflecting a number of nodes
* of the data at the edges in the dataset boundary.
* ie, it pads out the dataset with semi-real data.
* This border is then tapered with a cos-squared function.
************************************************************************

      include "total.h"
      complex f(n1,n2),ftemp(n1,n2)
      pi=4.*atan(1.)

* mirror edge in border :

      nxturn=nx0+ibord1
      nyturn=ny0+jbord1

      do 10, j=0,ny-1
       l=abs(j-jbord1-2*(j-nyturn+1)*(j/nyturn))+1
       l=l+jbord1
       do 10, i=0,nx-1
        k=abs(i-ibord1-2*(i-nxturn+1)*(i/nxturn))+1
        k=k+ibord1
        ftemp(i+1,j+1)=f(k,l)
   10 continue

* taper the mirrored borders :

      nedge1=ibord1+1
      nedge2=jbord1+1
      pedge1=pi/nedge1
      pedge2=pi/nedge2

      nx1=nx+1
      do 20, j=1,ny
       do 20, i=1,nedge1
        temp=(1.-cos(pedge1*(i-1)))*0.5
        ftemp(i,j)=ftemp(i,j)*temp
        ftemp(nx1-i,j)=ftemp(nx1-i,j)*temp
   20 continue

      ny1=ny+1
      do 30, j=1,nedge2
       temp=(1.-cos(pedge2*(j-1)))*0.5
       do 30, i=1,nx
        ftemp(i,j)=ftemp(i,j)*temp
        ftemp(i,ny1-j)=ftemp(i,ny1-j)*temp
   30 continue

      do 40, j=1,n2
       do 40, i=1,n1
        f(i,j)=(0.,0.)
        f(i,j)=ftemp(i,j)
   40 continue

      return
      end
```

```
* Change :
*  n1,n2 = array dimensions (should be greater than 120% of
*           appropriate side),
*  nsat = the number of satellite missions being gridded.
*
* Parameter "units" is the conversion factor from Lambert projection
*  coordinates to metres.
* Parameter ratio is the ratio of a0 to rsearch for the Witch
*  gridding kernel.
************************************************************************

c     parameter (nsat=2,n1=1024,n2=1024,n12=n1*n2,nz=2*n12)
c     parameter (nsat=2,n1=306,n2=306,n12=n1*n2,nz=2*n12)
      parameter (nsat=1,n1=200,n2=200,n12=n1*n2,nz=2*n12)
      parameter (units=1.d4,ratio=0.175d0,zero=0.d0)
      implicit double precision (a-h,o-z)
      double precision slope(2*nsat,n1,n2),wt(2*nsat,n1,n2)
      double precision gshp(n1,n2),glnd(n1,n2),wvn(n1,n2)
      double precision wsat(n1,n2),wshp(n1,n2),wlnd(n1,n2),sea(n1,n2)
      real za(nz),zb(nz),zh(nz)
      complex a(n1,n2),b(n1,n2),h(n1,n2)
      equivalence (za,a),(zb,b),(zh,h)

      common /arrays/a,b,h,gshp,glnd,wsat,wshp,wlnd,wvn,sea,slope,wt
      common /nodes/nx,ny,nx0,ny0,ibord1,ibord2,jbord1,jbord2
      common /area/x0,y0,delta,gn
```

```
2
3     no. of gridnodes in x-direction
4     no. of gridnodes in y-direction
5     x origin (km)
6     y origin (km)
7     x grid spacing (km)
8     y grid spacing (km)
9     normal gravity value
10     ascending satellite track data filename
11     1=Topex, 2=Geosat
12     search radius (km)
13     highest latitude
14     lowest latitude
15     descending satellite track data filename
16     1=Topex, 2=Geosat
17     search radius (km)
18     highest latitude
19     lowest latitude
20    **REPEAT ABOVE 10 LINES FOR EACH SATELLITE MISSION**
21     ascending angles filename
22     descending angles filename
23    **REPEAT ABOVE 2 LINES FOR EACH SATELLITE MISSION**
24    filename of tapered landmass data (1's on land to 0's at sea)
25    output satellite geoid (y/n) ?
26    filename for satellite geoid (include even if not desired)
27    filename for ship track data
28    land data exists (y/n) ?
29    filename for land gravity data (include even if not desired)
30    no. of IFC iterations (even=geoid output, odd=freeair output)
31    filename for output combined geoid/freeair grid
```

Bibliography

Armstrong, E. J. (1978). 1:250,000 Bouguer Anomaly Map Compilation, *Marine Geophysics 096*, British Geological Survey.

AVISO (1992). *AVISO User Handbook: Merged TOPEX/POSEIDON products, Rep.AVI-NT-02-101-CN*, 2nd edn, CNES, Toulouse, France.

Bamford, D., Nunn, K., Prodehl, C. and Jacob, B. (1978). LISPB-IV. Crustal structure of northern Britain, *Geophysical Journal of the Royal Astronomical Society* **54**: 43–60.

Barton, P. and Wood, R. (1984). Tectonic evolution of the North Sea basin: crustal stretching and subsidence, *Geophysical Journal of the Royal Astronomical Society* **79**: 987–1022.

Bjarnason, I. T. and Menke, W. (1993). Tomographic image of the Mid-Atlantic plate boundary in southwestern Iceland, *Journal of Geophysical Research* **98**(B4): 6607–6622.

Bracewell, R. (1965). *The Fourier Transform and its Applications*, McGraw-Hill, New York.

Bunch, A. W. H. and Kennett, B. L. N. (1980). The crustal structure of the Reykjanes Ridge at 59° 30' n, *Geophysical Journal of the Royal Astronomical Society* **61**: 141–166.

Cazenave, A., Houry, S., Lago, B. and Dominh, K. (1992). Geosat-derived geoid anomalies at medium wavelength, *Journal of Geophysical Research* **97**(B5): 7081–7096.

Chen, Y. and Morgan, W. J. (1990). Rift valley/no rift valley transition at mid-ocean ridges, *Journal of Geophysical Research* **95**(B11): 17571–17581.

Cheney, R. E. and Marsh, J. G. (1981). Seasat altimeter observations of dynamic topography in the Gulf Stream region, *Journal of Geophysical Research* **86**(C1): 473–483.

Cochran, J. R. (1979). An analysis of isostasy in the world's oceans, 2. midocean ridge crests, *Journal of Geophysical Research* **84**(B9): 4713–4729.

Cox, A. and Hart, R. B. (1986). *Plate Tectonics: How It Works*, Blackwell Scientific Publications, Palo Alto, CA.

Dewey, J. F. (1982). Plate tectonics and the evolution of the British Isles, *Journal of the Geological Society* **139**: 371–412.

Dorman, L. M. and Lewis, B. T. R. (1970). Experimental Isostasy 1: Theory of the determination of the Earth's isostatic response to a concentrated load, *Journal of Geophysical Research* **75**: 3357–3365.

Forsyth, D. W. (1985). Subsurface loading and estimates of the flexural rigidity of continental lithosphere, *Journal of Geophysical Research* **90**(B14): 12623–12632.

Fowler, C. M. R. (1990). *The Solid Earth: An Introduction to Global Geophysics*, Cambridge University Press, Cambridge.

Fowler, S. R., White, R. S., Spence, G. D. and Westbrook, G. K. (1989). The Hatton Bank continental margin - II. Deep structure from two-ship expanding spread seismic profiles, *Geophysical Journal* **96**: 295–309.

Fu, L.-L., Christensen, E. J., Yamarone, C. A., Lefebvre, M., Menard, Y., Dorrer, M. and Escudier, P. (1994). Topex/Poseidon mission overview, *Journal of Geophysical Research* **99**(C12): 24369–24381.

Gebrande, H., Miller, H. and Einarsson, P. (1980). Seismic structure of Iceland along RRISP profile I, *Journal of Geophysics* **47**: 239–249.

Gradshteyn, I. S. and Ryzhik, I. M. (1980). *Table of Integrals, Series and Products*, 4th edn, Academic Press, London.

Heiskanen, W. A. and Moritz, H. (1967). *Physical Geodesy*, W. H. Freeman, San Francisco.

Holder, A. P. and Bott, M. H. P. (1971). Crustal structure in the vicinity of south-west England, *Geophysical Journal of the Royal Astronomical Society* **23**: 465–489.

Hwang, C. and Parsons, B. (1995). Gravity anomalies derived from Seasat, Geosat, ERS-1 and TOPEX/POSEIDON altimetry and ship gravity: a case study over the Reykjanes Ridge, *Geophysical Journal International* **122**: 551–568.

Kanasewich, E. R. (1981). *Time Sequence Analysis in Geophysics*, 3rd edn, University of Alberta Press, Edmonton.

Karner, G. D. and Watts, A. B. (1983). Gravity anomalies and flexure of the lithosphere at mountain ranges, *Journal of Geophysical Research* **88**(B12): 10449–10477.

Kogan, M. G. and Kostoglodov, V. V. (1981). Isostasy of fracture zones in the Atlantic Ocean, *Journal of Geophysical Research* **86**(B10): 9248–9258.

Marks, K. M. and Sailor, R. V. (1986). Comparison of Geos-3 and Seasat altimeter resolution capabilities, *Geophysical Research Letters* **13**(7): 697–700.

McAdoo, D. C. (1990). Gravity field of the southeast Central Pacific from Geosat Exact Repeat Mission data, *Journal of Geophysical Research* **95**(C3): 3041–3047.

McAdoo, D. C. and Marks, K. M. (1992). Gravity fields of the Southern Ocean from Geosat data, *Journal of Geophysical Research* **97**(B3): 3247–3260.

Moritz, H. (1984). Geodetic Reference System 1980, *in* C. C. Tscherning (ed.), *Bulletin Géodésique: the Geodesist's Handbook*, Vol. 58, No. 3, IAG, Paris, pp. 388–398.

NGDC (1992). *Gravity: Earth System Data, CD-ROM User's Manual*, U.S. Dept of Commerce, National Geophysical Data Center, Boulder.

NGDC (1993). *Global Relief Data CD-ROM*, U.S. Dept of Commerce, National Geophysical Data Center, Boulder.

NGDC (1994). *GEODAS: Marine Geophysical Data CD-ROM, version 3*, U.S. Dept of Commerce, National Geophysical Data Center, Boulder.

Rabinowitz, P. D. and Jung, W.-Y. (1986). Gravity anomalies in the western North Atlantic Ocean, *in* P. R. Vogt and B. E. Tucholke (eds), *The Geology of North America, Volume M, the Western North Atlantic Region*, The Geological Society of North America, Boulder, USA, pp. 205–214.

Rapp, R. H. and Pavlis, N. K. (1990). The development and analysis of geopotential coefficient models to spherical harmonic degree 360, *Journal of Geophysical Research* **95**(B13): 21885–21911.

Rapp, R. H., Wang, Y. M. and Pavlis, N. (1991). The Ohio State 1991 geopotential and sea surface topography harmonic coefficient models, *Technical Report 410*, Department of Geodetic Sciences and Surveying, Ohio State University, Columbus, USA.

Richardus, P. and Adler, R. K. (1972). *Map Projections for Geodesists, Cartographers and Geographers*, North-Holland, Amsterdam.

Sandwell, D. T. (1984). A detailed view of the South Pacific geoid from satellite altimetry, *Journal of Geophysical Research* **89**(B2): 1089–1104.

Sandwell, D. T. (1992). Antarctic marine gravity field from high-density satellite altimetry, *Geophysical Journal International* **109**: 437–448.

Sandwell, D. T. and McAdoo, D. C. (1988). Marine gravity of the Southern Ocean and Antarctic margin from Geosat, *Journal of Geophysical Research* **93**(B9): 10389–10396.

Sandwell, D. T. and McAdoo, D. C. (1990). High-accuracy, high resolution gravity profiles from 2 years of the Geosat Exact Repeat Mission, *Journal of Geophysical Research* **95**(C3): 3049–3060.

Sandwell, D. T. and Zhang, B. (1989). Global mesoscale variability from the Geosat Exact Repeat Mission: correlation with ocean depth, *Journal of Geophysical Research* **94**(C12): 17971–17984.

Sandwell, D. T., Smith, W. H. F. and Yale, M. M. (1995). Gravity anomaly profiles from ERS-1, Topex and Geosat altimetry, *EOS trans. AGU Spring Meeting* **76**(17): S89.

Schwarz, K. P., Sideris, M. G. and Forsberg, R. (1990). The use of FFT techniques in physical geodesy, *Geophysical Journal International* **100**: 485–514.

Sheriff, R. E. and Geldart, L. P. (1983). *Exploration Seismology volume 2: Data-processing and Interpretation*, Cambridge University Press, Cambridge.

Smith, W. H. F. and Wessel, P. (1990). Gridding with continuous curvature splines in tension, *Geophysics* **55**(3): 293–305.

Stewart, M. P. and Hipkin, R. G. (1990). A high resolution, high precision geoid for the British Isles, *in* H. Suenkel and T. Baker (eds), *IAG Symposia 104: Sea Surface Topography and the Geoid*, Springer-Verlag, New York, pp. 39–46.

Tapley, B. D., Born, G. H. and Parke, M. E. (1982). The Seasat altimeter data and its accuracy assessment, *Journal of Geophysical Research* **87**(C5): 3179–3188.

Tsaoussi, L. S. and Koblinsky, C. J. (1994). An error covariance model for sea surface topography and velocity derived from TOPEX/POSEIDON altimetry, *Journal of Geophysical Research* **99**(C12): 24669–24683.

Van der Voo, R. (1993). *Paleomagnetism of the Atlantic, Tethys and Iapetus Oceans*, Cambridge University Press, Cambridge.

Vening Meinesz, F. A. (1931). Une nouvelle méthode pour la réduction isostatique régionale de l'intensité de la pesanteur, *Bulletin Géodésique* **29**: 33.

Vermeer, M. (1992). A frequency domain approach to optimal geophysical data gridding, *manuscripta geodaetica* **17**: 141–154.

Vogt, P. R. (1971). Asthenosphere motion recorded by the ocean floor south of Iceland, *Earth and Planetary Science Letters* **13**: 153–160.

Vogt, P. R. (1983). The iceland mantle plume: status of the hypothesis after a decade of new work, *in* M. H. P. Bott, S. Saxov, M. Talwani and J. Thiede (eds), *Structure and Develpoment of the Greenland-Scotland Ridge: New Methods and Concepts*, NATO Conference Series IV: Marine Sciences, Plenium Press, New York, pp. 191–213.

Vogt, P. R. (1986). Geoid undulations mapped by spaceborne radar altimetry, *in* P. R. Vogt and B. E. Tucholke (eds), *The Geology of North America, Volume M, the Western North Atlantic Region*, The Geological Society of North America, Boulder, USA, pp. 215–228.

Vogt, P. R. and Johnson, G. L. (1975). Transform faults and longitudinal flow below the midoceanic ridge, *Journal of Geophysical Research* **80**(11): 1399–1428.

Watts, A. B. (1978). An analysis of isostasy in the world's oceans: 1. Hawaiian-Emperor seamount chain, *Journal of Geophysical Research* **83**(B12): 5989–6004.

Watts, A. B. (1992). The effective elastic thickness of the lithosphere and the evolution of foreland basins, *Basin Research* **4**: 169–178.

White, R. S., McKenzie, D. and O'Nions, R. K. (1992). Oceanic crustal thickness from seismic measurements and rare earth element inversions, *Journal of Geophysical Research* **97**(B13): 19683–19715.

Whitmarsh, R. B. and Calvert, A. J. (1986). Crustal structure of Atlantic fracture zones - I. The Charlie-Gibbs fracture zone, *Geophysical Journal of the Royal Astronomical Society* **85**: 107–138.